



City Research Online

City, University of London Institutional Repository

Citation: Kabir, S. (2007). Finite element modelling of photonic crystal fibres. (Unpublished Doctoral thesis, City University London)

This is the accepted version of the paper.

This version of the publication may differ from the final published version.

Permanent repository link: <https://openaccess.city.ac.uk/id/eprint/8592/>

Link to published version:

Copyright: City Research Online aims to make research outputs of City, University of London available to a wider audience. Copyright and Moral Rights remain with the author(s) and/or copyright holders. URLs from City Research Online may be freely distributed and linked to.

Reuse: Copies of full items can be used for personal research or study, educational, or not-for-profit purposes without prior permission or charge. Provided that the authors, title and full bibliographic details are credited, a hyperlink and/or URL is given for the original metadata page and the content is not changed in any way.

Finite Element Modelling of Photonic Crystal Fibres

By

A.K.M Saiful Kabir

A thesis submitted to the City University in fulfilment of the
requirements for the Degree of Doctor of Philosophy

City University, London

Photonics Research Group
School of Engineering & Mathematical Sciences
Northampton Square, London EC1V 0HB, UK.

May 2007

To my beloved parents, my wife, my baby Alina, and all of my
family members

Table of Contents

Table of Contents	iii
List of Tables	viii
List of Figures	ix
Acknowledgements	xvi
Declaration	xvii
Abstract	xviii
Symbols	xix
Abbreviations	xx
1. Introduction of Optical fibre	1
1.1 Brief Introduction	1
1.2 Definition of Optical Fibre	2
1.3 Optical Fibre Communication System	3
1.3.1 Transmitter	4
1.3.2 Optical Fibre Cable	4
1.3.3 Optical Regenerator	4
1.3.4 Optical Receiver	5
1.4 Historical Development of Fibre Optic Technology	5
1.5 Structure of Optical Fibre	7
1.6 Types of Optical Fibre	9
1.6.1 Single-Mode Fibre	9
1.6.1.1 Characteristics of single-mode fibre	9
1.6.1.1.1 Monomode Step-index Fibre	10
1.6.2 Multimode Fibre	10
1.6.2.1 Characteristics of Multimode Fibre	10
1.6.2.1.1 Multimode Step-index Fibre	11
1.6.2.1.2 Multimode Graded-index Fibre	11
1.6.3 Plastic Optical Fibre (POF)	11
1.7 Physics of Total Internal Reflection	13
1.8 Fabrication of Optical Fibre	14
1.8.1 Making the Preform Blank	14
1.8.2 Drawing Fibres from the Preform Blank	16

1.8.3 Testing the Finished Optical Fibre	17
1.9 Materials of Optical Fibre	17
1.10 Advantages of Optical Fibre	18
1.11 Applications of Optical Fibre	21
1.12 Aims and Objectives of the Thesis	23
1.13 Structure of the Thesis	25
2. Photonic Crystal Fibre (PCF)	27
2.1 Brief Introduction	27
2.2 Definition of PCF	28
2.3 Historical Development of PCF	30
2.4 Structure of PCF	33
2.5 Light-guiding Mechanism of PCF	33
2.5.1 Index-guiding PCFs	33
2.5.2 Photonic Bandgap (PBG) Effect	34
2.6 Advantages over Conventional Fibre	36
2.7 Applications of PCFs	37
2.8 Fabrication of PCF	39
2.9 Novel Properties of PCF	41
2.9.1 Birefringence Properties of PCF	41
2.9.2 Polarization Properties of PCF	42
2.9.3 Dispersion of PCF	42
2.9.3.1 Intermodal Dispersion	43
2.9.3.2 Chromatic Dispersion	44
2.9.3.3 Polarization Mode Dispersion	44
2.9.4 Loss Mechanism	44
2.9.5 Endless Single-mode (ESM) PCF	45
2.9.6 Nonlinear Properties of PCF	46
2.10 Materials	46
2.11 Summary	47
3. Numerical Methods	48
3.1 Introduction	48
3.2 Full-vectorial Solution	49
3.3 Different Methods	50
3.3.1 Indirect Entire-domain Techniques	50
3.3.2 Direct Sub-domain or Space Domain Discretization Techniques	51
3.3.3 Field Tracking Techniques	51
3.4 Comparison of Different Methods	51
3.4.1 Effective Index Method	51
3.4.2 Plane Wave Expansion (PWE)	52
3.4.3 Localized Function Method	52
3.4.4 Multipole Method	53
3.4.5 Supercell Lattice Method	53
3.4.6 Finite Difference Method (FDM)	53
3.4.7 Finite Difference Time Domain (FDTD) Method	53
3.4.8 Transfer-Matrix Method (TMM)	54
3.4.9 Finite Element Method (FEM)	54
3.4.10 Beam Propagation Method (BPM)	55

3.4.11 Full-vectorial Finite Element Based Beam Propagation Method (VFEBPM)	55
3.4.12 Imaginary Distance Full-vectorial Finite Element Based Beam Propagation Method (IDVFEBPM)	56
3.5 Summary	56
4. The Finite Element Method	57
4.1 Introduction	57
4.2 Historical Background	58
4.3 The Basic Idea of the FEM	59
4.4 Characteristics of FEM	61
4.5 Applications of FEM	62
4.6 Application of FEM to Optical Waveguides	63
4.6.1 One and Two Dimensional Optical Waveguides	63
4.6.2 Arbitrary Cross-sectional Shaped Optical Waveguide	64
4.7 Fundamental Electromagnetic Field Equations	65
4.7.1 Maxwell's Equations	65
4.7.2 Boundary Conditions	66
4.8 Finite Element Formulations	68
4.8.1 Types of Variational Formulation	69
4.8.2 Characteristics of the Scalar Finite Element Method	69
4.8.3 Characteristics of the Vector Finite Element Method	70
4.8.3.1 Types of Vector Finite Element Method	71
4.8.3.2 Comparison among Vector Finite Element Methods	71
4.8.4 The Vector H-field formulation	73
4.8.5 Natural and forced boundary conditions	74
4.9 Finite Element Method Formulation	74
4.9.1 Finite Element Discretisation	74
4.9.2 Shape Functions	76
4.9.3 Assembly of Element and Global Matrices	81
4.10 Spurious Solution	84
4.11 Infinite Element Representation	87
4.12 Summary	88
5. The Beam Propagation Method	89
5.1 Introduction	89
5.2 Historical Background of BPM	90
5.3 Applications of BPM	91
5.4 Modelling Techniques of BPM	92
5.5 Numerical Techniques of BPM	93
5.5.1 Fast-Fourier Transform Beam Propagation Method (FFT-BPM)	93
5.5.1.1 Advantages of FFT-BPM	94
5.5.1.2 Limitations of FFT-BPM	94
5.5.2 Finite Difference Beam Propagation Method (FD-BPM)	94
5.5.2.1 Advantages of FD-BPM	95
5.5.2.2 Limitations of FD-BPM	95
5.5.3 Modal Propagation Based Beam Propagation Method	96
5.5.3.1 Advantages of Modal Propagation Based	

BPM	97
5.5.3.2 Limitations of Modal Propagation Based BPM	97
5.5.4 Finite Element Beam Propagation Method (FE-BPM)	97
5.5.4.1 Advantages of FE-BPM	98
5.6 Boundary Condition of BPM	98
5.6.1 The Perfectly Matched Layer (PML) Boundary Condition	99
5.7 Summary	103
6. Modal Solutions of Square Lattice Photonic Crystal Fibre	104
6.1 Introduction	104
6.2 Modelling of PCF	105
6.2.1 Why Rectangular Hole rather than Square Hole is Better?	105
6.3 Structure of the PCF	106
6.3.1 Square Lattice PCF with Square Air Holes	106
6.3.2 Square Lattice PCF with Rectangular Air Holes	107
6.4 Results of Square Lattice PCF with Square Air Holes	108
6.4.1 Effect of Mesh Refinement in both Full Structure and Two Fold Symmetry	108
6.4.2 Effects of Operating Wavelength	109
6.4.3 Effect of Separation	110
6.5 Results of Square Lattice PCF with Rectangular Air Holes	117
6.5.1 Effects of Operating Wavelength	117
6.6 Comparison Results of Square and Rectangular Air Holes	121
6.7 Summary	123
7. Characterization of Hexagonal Lattice PCF	124
7.1 Introduction	124
7.2 Modelling of Hexagonal Lattice PCF with Circular Air Holes	125
7.2.1 Symmetry Air Holes	125
7.2.1.1 Representation of Hole by Triangles	126
7.2.2 Asymmetry Air Holes	127
7.3 Numerical Results of Identical Hole PCF	128
7.3.1 Results of a PCF when d/Λ is Varying	128
7.3.2 Results of a PCF when Wavelength is Varying	130
7.3.2.1 Results of a PCF when $d/\Lambda = 0.50$	130
7.3.2.2 Comparison results of PCF when $d/\Lambda = 0.50$ and $d/\Lambda = 0.30$	135
7.3.3 Results of a PCF when Λ is Varying	138
7.4 Numerical Results of a PCF Structure With Unequal Hole Diameter	143
7.4.1 Results of a PCF when Wavelength is Varying	143
7.4.2 Results of a PCF when d_2/Λ is Varying	146
7.5 Group Velocity Dispersion (GVD) of PCF	149
7.5.1 Effect of Mesh Division when Wavelength is Varying	149
7.5.2 Effect of d/Λ when Wavelength is Varying	149
7.5.3 Effect of d_2/Λ when Wavelength is Varying	151
7.6 Summary	153

8. Birefringence Study of Photonic Crystal Fibre	154
8.1 Introduction	154
8.2 Modal Birefringence of PCF	155
8.3 Way of Making Highly Birefringent PCF	156
8.4 Modelling of Highly Birefringent PCF	157
8.5 Simulation Results for Birefringence	159
8.5.1 Results of a PCF when d/Λ is Varying	159
8.5.2 Results of a PCF when d_2/Λ is Varying	161
8.5.2.1 Results of a PCF where Height is Greater than Width	161
8.5.2.2 Results of a PCF where Width is Greater than Height	164
8.5.2.3 Comparison Results of Two Different Structural Asymmetry	171
8.5.3 Results of a PCF when Wavelength is Varying	173
8.5.4 Results of a PCF when Λ is Varying	175
8.6 Simulation Results for Leakage Loss	177
8.6.1 Result of Leakage Loss when Number of Ring is Varying	178
8.6.2 Result of Leakage Loss when d_2/Λ is Varying	179
8.6.3 Result of Leakage Loss when Wavelength is Varying	180
8.7 Summary	181
9. Conclusion and Future Research Direction	183
9.1 Conclusion	183
9.2 Future Research Directions	189
Appendix 1 Calculation of the Material (SiO_2) Dispersion	193
Appendix 2 Calculation of the Element Matrices	195
Appendix 3 Calculation of the Wave Equations	197
Appendix 4 List of Publications by the Author	200
References	206
Bibliography	225

List of Tables

Table 1.1: Characteristics of single mode and multimode fibre.

Table 1.2: Comparison among different types of transmission media.

Table 2.1: Guidance Mechanisms and Holey Fibre Types.

List of Figures

- Figure 1.1:** The basic point-to-point fibre optic transmission system.
- Figure 1.2:** Optical communication systems.
- Figure 1.3:** Structure of optical fibre.
- Figure 1.4:** A bundle of optical fibres.
- Figure 1.5:** Fibre strands.
- Figure 1.6:** Light rays incident on high to low refractive index interface.
- Figure 1.7:** MCVD process for making the preform blank.
- Figure 1.8:** Lathe used in preparing the preform blank.
- Figure 1.9:** Diagram of a fibre drawing tower used to draw optical glass fibres from a preform blank.
- Figure 1.10:** Finished spool of optical fibre.
- Figure 1.11:** Comparison between optical fibre and copper wire.
- Figure 1.12:** Comparison between fibre optic cable and metal cable.
- Figure 2.1:** Uniform cross-section of air-holes in a single material.
- Figure 2.2:** (a) Solid-core photonic crystal fibre (b) Hollow-core photonic crystal fibre.
- Figure 2.3:** High-index guiding fibre.
- Figure 2.4:** Low-index guiding fibre.
- Figure 2.5:** Array of hollow capillary silica tubes bundled around a pure silica rod replacing the centre capillary.
- Figure 2.6:** Preform construction.
- Figure 2.7:** Preform drawing down in furnace.
- Figure 2.8:** Chromatic dispersion in single-mode fibre.
- Figure 2.9:** Nonlinearity tailoring of PCF.

- Figure 4.1:** Optical waveguide (a) one-dimensional planar waveguide (b) two-dimensional waveguide.
- Figure 4.2:** Optical waveguide with arbitrary-shaped, with different materials.
- Figure 4.3:** Sketch of a boundary between two media.
- Figure 4.4:** Two dimensional finite elements.
- Figure 4.5:** Waveguide cross-section is subdivided into a finite number of triangular elements showing its nodes.
- Figure 4.6:** Pascal's triangle for complete polynomials in two dimensions.
- Figure 4.7:** Coordinates and node numbers of first order triangular element.
- Figure 4.8:** Two-fold symmetry of rectangular dielectric waveguide cross section discretised into orthodox and infinite elements.
- Figure 5.1:** Optical waveguide cross-section with different PML regions.
- Figure 6.1:** Structure of the square size air hole in a homogeneous silica background.
- Figure 6.2:** Square lattice PCF with missing core at the centre surrounded by air-holes in a homogeneous silica background.
- Figure 6.3:** Schematic diagram of a integrated optic PCF with rectangular air-holes where central hole is missing.
- Figure 6.4:** Variation of the effective indices with mesh.
- Figure 6.5:** Variation of the effective indices with the operating wavelength for a square-hole PCF.
- Figure 6.6:** Variation of the effective indices of quasi-TM modes with the separation between the air-holes for a square-hole PCF.
- Figure 6.7:** Variation of the modal hybridness and vector field components with the separation between the air-holes.
- Figure 6.8:** Variation of the modal hybridness with the separation between the air-holes.
- Figure 6.9:** The dominant H_y field profile of the fundamental quasi-TE (H_{11}^y) mode at $\lambda = 1.55 \mu\text{m}$, when separation between the holes (a) $S = 1 \mu\text{m}$ and (b) $S = 5 \mu\text{m}$.
- Figure 6.10:** Variation of the effective indices with separation between the air-holes.

- Figure 6.11:** (a) The dominant H_y field profile and (b) the 3-D view of the dominant H_y field profile of the fundamental quasi-TE (H_{11}^y) mode when separation between the holes, $S= 5 \mu\text{m}$ at $\lambda= 1.55 \mu\text{m}$.
- Figure 6.12:** (a) The dominant H_y field profile and (b) the 3-D view of the dominant H_y field profile of the fundamental quasi-TE (H_{11}^y) mode when separation between the holes, $S= 12 \mu\text{m}$ at $\lambda= 1.55 \mu\text{m}$.
- Figure 6.13:** Variation of the modal hybridness with the separation between the air-holes.
- Figure 6.14:** Variation of the effective indices with the wavelength for the rectangular air-holes PCF.
- Figure 6.15:** Variation of the spot-size with the operating wavelength.
- Figure 6.16:** Variation of the power confinement with the operating wavelength.
- Figure 6.17:** Variation of the modal hybridness with the wavelengths.
- Figure 6.18:** Variation of the beat length with the operating wavelength.
- Figure 6.19:** Variation of the effective indices with the wavelength for the square and rectangular air-holes PCF.
- Figure 6.20:** Variation of the GVD with the wavelength for square-hole and rectangular-hole PCFs.
- Figure 7.1:** Schematic diagram of a PCF with hexagonal array of air-holes where the middle hole is missing.
- Figure 7.2:** Shows the distance between the air-holes from their centre.
- Figure 7.3:** Representation of circular hole by number of triangles.
- Figure 7.4:** Representation of holes by rectangular blocks (each with two triangles) using a very fine mesh.
- Figure 7.5:** Illustrates the two-fold symmetry of the structure of the waveguide and its corresponding distances on the x and y axis.
- Figure 7.6:** The variation of the effective index and spot-size with the normalized hole diameter d/Λ .
- Figure 7.7:** The dominant H_y field profile of the fundamental quasi-TE mode for (a) $d/\Lambda = 0.3$ and (b) $d/\Lambda = 0.7$.

- Figure 7.8:** Variation of the effective indices of the fundamental modes with the wavelength for 120*120 and 80*80 meshes.
- Figure 7.9:** Variation of the effective indices of the fundamental and higher order modes with the wavelength for a circular air-hole PCF.
- Figure 7.10:** (a) The dominant H_y and (b) non-dominant H_x field profiles of the fundamental quasi-TE mode at operating wavelength of $\lambda = 0.50 \mu\text{m}$.
- Figure 7.11:** The dominant H_y field profiles of the fundamental quasi-TE mode at operating wavelength of (a) $\lambda = 0.5 \mu\text{m}$ and (b) $\lambda = 1.55 \mu\text{m}$.
- Figure 7.12:** Variation of the spot-size with the operating wavelength when $d/\Lambda = 0.50$.
- Figure 7.13:** The variation of the field magnitude and modal hybridness with the operating wavelength for $d/\Lambda = 0.50$.
- Figure 7.14:** The variation of the power confinement factor with the operating wavelength when $d/\Lambda = 0.50$.
- Figure 7.15:** Variation of the silica index and the effective indices with the wavelength for $d/\Lambda = 0.50$ and 0.30 .
- Figure 7.16:** The variation of the hybridness with the operating wavelength for H_{11}^y mode when $d/\Lambda = 0.30$ and $d/\Lambda = 0.50$.
- Figure 7.17:** The variation of the spot-size with the operating wavelength for $d/\Lambda = 0.50$ and 0.30 .
- Figure 7.18:** The variation of the effective indices with the pitch when $d/\Lambda = 0.50, 0.70,$ and 0.90 .
- Figure 7.19:** The variation of the effective index and spot-size with the pitch when $d/\Lambda = 0.50$ and $d/\Lambda = 0.90$.
- Figure 7.20:** Variations of the modal hybridness with the pitch length, Λ when $d/\Lambda = 0.40, d/\Lambda = 0.50,$ and $d/\Lambda = 0.60$.
- Figure 7.21:** The variation of the field with the normalized X/Λ .
- Figure 7.22:** Variation of the effective index with the wavelength for a circular air-hole PCF when $d_1 \neq d_2$.
- Figure 7.23:** (a) The dominant H^x field profile of H_{11}^x mode and (b) the dominant H^y field profile of the fundamental H_{11}^y mode at $\lambda = 0.50 \mu\text{m}$.

- Figure 7.24:** (a) The dominant H^x field profile of H_{11}^x mode and (b) the dominant H^y field profile of the fundamental H_{11}^y mode at $\lambda = 1.55 \mu\text{m}$.
- Figure 7.25:** The variation of the modal indices with the normalized diameter, d_2/Λ .
- Figure 7.26:** The variation of the spot-size and modal hybridness with the normalized diameter, d_2/Λ .
- Figure 7.27:** The variation of the power confinement factor with the value of d_2/Λ .
- Figure 7.28:** Variation of the GVD of the H_{11}^y mode with the wavelength for $d_1=d_2= \Lambda 0.50 \mu\text{m}$ when 120*120 mesh and 80*80 mesh.
- Figure 7.29:** Variation of the GVD with wavelength for H_{11}^x mode and H_{11}^y mode.
- Figure 7.30:** Variations of the GVD with the wavelength for $d/\Lambda = 0.50$ and 0.30 .
- Figure 7.31:** Variation of the GVD of the H_{11}^y mode with the wavelength for $d_2/\Lambda= 0.50 \mu\text{m}$ and $d_2/\Lambda= 0.95 \mu\text{m}$ when 120*120 mesh.
- Figure 7.32:** Variation of the GVD with the wavelength for H_{11}^x and H_{11}^y when $d_1/\Lambda=0.5$ and $d_2/\Lambda= 0.95$.
- Figure 7.33:** Variation of the GVD with the wavelength for H_{11}^y modes for different d_2 values.
- Figure 8.1:** Birefringent fibre.
- Figure 8.2:** Regular array of equal circular holes in a hexagonal lattice.
- Figure 8.3:** Array of unequal circular holes in a hexagonal lattice where diameter of two air holes are increased.
- Figure 8.4:** Array of unequal circular holes of (a) full structure, and (b) quarter of a full structure in a hexagonal lattice where four air holes are increased.
- Figure 8.5:** Variations of the effective index and spot-size with the normalized hole diameter d/Λ when $\Lambda= 2.0 \mu\text{m}$ and $2.2 \mu\text{m}$.
- Figure 8.6:** Schematic diagram of the hexagonal lattice PCF with unequal hole sizes in the first ring where two air holes are increased.

- Figure 8.7:** (a) Array of hexagonal lattice, where (b) two circular air-holes are increased.
- Figure 8.8:** Variation of the effective indices with the normalized d_1/Λ when $\Lambda = 1.1 \mu\text{m}$.
- Figure 8.9:** The variation of the spot sizes with the normalized d_1/Λ when $\Lambda = 1.1 \mu\text{m}$.
- Figure 8.10:** Schematic diagram of the hexagonal lattice PCF with unequal hole sizes in the first ring where four air holes are increased.
- Figure 8.11:** (a) Array of hexagonal lattice, where (b) four unequal circular holes are increased.
- Figure 8.12:** Variation of the modal indices with the normalized diameter, d_2/Λ .
- Figure 8.13:** The variation of the beat length and modal birefringence with the normalized diameter, d_2/Λ at the operating wavelength, $\lambda = 0.50 \mu\text{m}$.
- Figure 8.14:** The variation of the beat length and modal birefringence with the normalized diameter, d_2/Λ at the operating wavelength, $\lambda = 1.55 \mu\text{m}$ and $\lambda = 0.50 \mu\text{m}$.
- Figure 8.15:** Variation of the effective indices with the normalized d_2/Λ when $\Lambda = 1.1 \mu\text{m}$.
- Figure 8.16:** The variation of the spot sizes with the normalized d_2/Λ when $\Lambda = 1.1 \mu\text{m}$.
- Figure 8.17:** Variation of the modal birefringence with the normalized d_2/Λ for $\Lambda = 1.1 \mu\text{m}$ and $2.2 \mu\text{m}$.
- Figure 8.18:** Variation of the birefringence with two different structural asymmetry, d_i/Λ , $i = 1, 2$.
- Figure 8.19:** Variation of the modal birefringence and log-log plot with the operating wavelength when $\Lambda = 2.2 \mu\text{m}$, $d/\Lambda = 0.50$ and $d_2/\Lambda = 0.95$.
- Figure 8.20:** Variation of the GVD with the operating wavelength for equal and unequal hole.
- Figure 8.21:** Variation of the modal birefringence with the pitch.
- Figure 8.22:** Schematic diagram of a PCF of two rings of 18 air holes.
- Figure 8.23:** Confinement loss of a three-ring and two-ring PCF of H_{11}^y mode

in dB/m with the wavelength, λ when $d/\Lambda = 0.50$ and $d_2/\Lambda = 0.95$ at $\Lambda = 2.2 \mu\text{m}$.

Figure 8.24: Confinement loss of a three-ring PCF of H_{11}^y mode in dB/m with the d_2/Λ when $d/\Lambda = 0.50$ at $\lambda = 1.55 \mu\text{m}$, $1.35 \mu\text{m}$, and $1.15 \mu\text{m}$.

Figure 8.25: Confinement loss of a three-ring PCF for H_{11}^y and H_{11}^x modes with the operating wavelength, λ at $d/\Lambda = 0.50$ and $d_2/\Lambda = 0.80$.

Acknowledgements

I am deeply obliged to the many people who helped in the preparation of this thesis.

I wish to express my thanks, first of all, to my supervisor, **Professor B M A Rahman**, shared this long, difficult, but ultimately rewarding experience with me every step of the way. Throughout the venture of this project, **Professor Rahman** cooperated with me fully by allotting me sufficient time to undertaken this endeavor and from where I gained invaluable professional experience, the background that played a large role in my plans for this text. He was always available for consultation when problem arose. His contribution helped significantly to improve the material covered here.

I appreciate the valuable feedback from my Co-Supervisor **Dr. Muttukrishnan Rajarajan**.

I am deeply appreciative of the advice given by **Professor K T V Grattan**, who had provided constructive critiques of the text during the writing stage and also offered invaluable comments and suggestions.

Very special thanks to Dr. Niranthe Somasiri and Dr. Shah Alam who were kind enough to work out solutions to some problems I discussed with them.

My colleagues and friends: Keja, Arti, Riyadh, Femi, Morshed, Tanvir, Irfan, Issuru, Gagandeep, Yansley, Alie, David, Vesel, and Wanne at Photonics Research Group who stimulated me in developing this project. Their encouragement and constructive feedback introduced new topics and led, I trust, to the overall improvement of the project and the thesis. Also many thanks to the secretarial and technical staff of the Electrical, Electronic and Information Engineering Department, specially John Rivellini, who never denied offering any help.

Finally my deepest gratitude is devoted to my dearest mother, my wife Farzana, my sweet, lovely baby Alina, father-in-law, mother-in-law, brothers: Shaheen, Ripon, sisters, sister-in-law, brother-in-law, nephew, niece, and last but not the least all of other family members who have supported and encouraged me during my studies. Without their help and patience, it would not have been possible to do this research project.

Declaration

I grant powers of discretion to the University Librarian to allow this thesis to be copied in whole or in part without further reference to the author. The permission covers only single copies made for study purposes, subject to normal conditions of acknowledgement.

Abstract

Photonic crystal fibre (PCF), a new kind of optical fibre, has many air-holes in their cross-section and has potential applications to new optical communication systems. The main objective of this research is the modelling of photonic crystal fibre to identify the fundamental and higher order quasi-TE and TM modes with square, rectangular and circular air holes in a square and hexagonal matrix, by using a rigorous full-vectorial **H**-field based finite element method (FEM). Besides the modal solutions of the effective indices, mode field profiles, spot sizes, modal hybridness, polarization beat length and group velocity dispersion values for equal and unequal air holes; research was carried out to optimize and design highly birefringent PCF.

The variation of modal birefringence is shown through the effect of hole diameters, air hole arrangement, structural asymmetry, operating wavelength, and pitch-distance. Birefringence was enhanced by breaking the structural symmetry and this was verified by using unequal air holes. The diameter of two air holes and four air holes in the first ring was changed to break the rotational symmetry and a comparison between the two designs is made in this work. In this work, highly birefringent PCF is designed with higher operating wavelength, larger d_2/Λ value, lower pitch length for a given structural asymmetry. It is identified that birefringence value increases rapidly when d_2 is much larger than d . At lower pitch value, one of the highest birefringence values reported so far at wavelength of 1.55 μm for an asymmetric PCF using circular air holes. A single polarization guide PCF structure is also achieved. In this study, it has been identified that for fixed d/Λ and d_2/Λ value, as operating wavelength is increased, birefringence increases significantly. It can also be identified that for higher d/Λ values, birefringence changes rapidly with Λ as their corresponding cutoff condition also approaches. One important validation of this work is the existence of modal birefringence for PCF with six-fold rotational symmetry. It is shown that birefringence value of a simple PCF incorporating circular holes but of different diameters is high compared to polarization maintaining Panda or Bow-tie fibres.

This research also aims to investigate the modal leakage losses of PCF, by using a semi-vectorial beam propagation method (BPM) based on the versatile FEM. The robust perfectly matched layer (PML) boundary condition has been introduced to the modal solution approach. The effects of d_2/Λ , operating wavelength and number of air holes have been thoroughly detailed and explained. In this study, it has been identified that the confinement loss decreases significantly with the increased number of rings, lower operating wavelength and lower d_2/Λ value. For special case, PCF with large spot-size provides higher leakage loss.

Symbols

- α Attenuation Constant
- β Propagation Constant
- λ Wavelength in μm
- ϵ Permittivity
- μ Permeability
- π $\text{Pi} \cong 3.14159265$
- ω Radian (angular) Frequency
- Γ Confinement Factor in Silica
- d Diameter of the cladding air hole
- Λ Air hole pitch
- Ω Discretization Frequency
- σ Spot-size
- k_0 Free space wave number
- n Refractive index profile
- n_e Effective index
- **H** Magnetic field intensity (amperes/meter)
- **E** Electric field intensity (volts/meter)
- **D** Electric flux density (coulombs/meter²)
- **B** Magnetic flux density (webers/meter²)
- **J** Electric current density (amperes/meter²)
- ρ Electric charge density (coulombs/meter³)
- j The imaginary unit
- t The time

Abbreviations

1. ASPF	Absolutely Single Polarization Fiber
2. BPM	Beam Propagation Method
3. CSF	Conventional Single-Mode Fiber
4. DWDM	Dense Wavelength-Division Multiplexing
5. EIM	Effective Index Method
6. EPCF	Elliptical Air holes Photonic Crystal Fiber
7. FDM	Finite Difference Method
8. FDTD	Finite Difference Time Domain
9. FEM	Finite Element Method
10. FSM	Fundamental Space-Filling Mode
11. FWM	Four-wave mixing
12. HF	Holey Fiber
13. IDVFEBPM	Imaginary Distance Full-Vectorial Finite Element Based Beam Propagation Method
14. MPM	Multipole Method
15. NA	Numerical Aperture
16. PBG	Photonic Bandgap
17. PCF	Photonic Crystal Fiber
18. PDL	Polarization Dependent Loss
19. PMF	Polarization Maintaining Fiber
20. PML	Perfectly Matched Layer
21. PM-PCF	Polarization Maintaining Photonic Crystal Fiber
22. RMSE	Root Mean Square Error
23. SC	Supercontinuum
24. SMF	Single-Mode Fiber
25. SPSM	Single-Polarization Single-Mode
26. TE	Transverse Electric
27. TIR	Total Internal Reflection
28. TM	Transverse Magnetic
29. VBEM	Vector Boundary Element Method
30. WDM	Wavelength-Division Multiplexing

Introduction of Optical Fibre

1.1 Brief Introduction

Over the last few years, fibre optic technology has advanced at a tremendous rate, driven by the need for higher bandwidths on long distance backbone links. In recent years, it has become apparent that fibre-optics are steadily replacing copper wire as an appropriate means of communication signal transmission. They span the long distances between local phone systems as well as providing the backbone for many network systems. Other system users include cable television services, university campuses, office buildings, industrial plants, and electric utility companies.

Fibre optics is one of the newer buzzwords these days. Optical fibre has a number of advantages over the copper wire used to make connections electrically. For example, optical fibre is immune to electromagnetic

interference, such as is caused by thunderstorms. Optical fibre has a wider bandwidth and can therefore carry more information at one time, because light has a much higher frequency than any radio signal we can generate. Optical fibre has two very simple advantages over copper:

- (a) The ability to transmit data at higher transmission rates with lower losses, and
- (b) The ability to do this at lower error rates.

Although fibres can be made out of either transparent plastic or glass, the fibres used in long-distance telecommunications applications are always glass, because of the lower optical attenuation. Both multimode and single-mode fibres are used in communications, with multimode fibre used mostly for short distances (up to 500 m), and single-mode fibre used for longer distance links. Single-mode transmitters, receivers, amplifiers and other components are generally more expensive than multimode components, because of the tighter tolerances required to couple light into and between single-mode fibres.

A fibre-optic system is similar to the copper wire system that fibre-optics is replacing. The difference is that fibre-optics use light pulses to transmit information down fibre lines instead of using electronic pulses to transmit information down copper lines. Optical fibre is less susceptible to external noise than other transmission media, and is cheaper to make than copper wire, but it is much more difficult to connect. Optical fibres are difficult to tamper with (to monitor or inject data in the middle of a connection), making them appropriate for secure communications.

1.2 Definition of Optical Fibre

An optical fibre refers to the long, thin, and transparent medium that transmits information as light pulses along its axis by the process of total internal reflection. Optical fibre is usually made of very pure glass (silica) or plastic about the diameter of a human hair. Fibre optics is the branch of applied science and engineering concerned with such optical fibres.

Optical fibres consist of a denser core, in which light is confined, surrounded by a cladding or substrate layer. The core and the cladding layers are enclosed by a protective sheath or buffer coating. Light rays modulated into digital pulses with a laser or a light-emitting diode (as the carrier), move along the core without penetrating the cladding. To confine the optical signal in the core, the refractive index of the core must be greater than that of the cladding. The light stays confined to the core, because the cladding has a lower refractive index.

Optical fibre carries much more information than conventional copper wire. The optical fibre can be used as a medium because it is flexible and can be bundled as cables called optical cables and used to transmit light signals over long distances. Optical fibres are connected to terminal equipment by optical fibre connectors.

1.3 Optical Fibre Communication System

Fig. 1.1 shows the basic point-to-point fibre optic transmission system consisting of three basic elements: the optical transmitter, the fibre optic cable and the optical receiver.

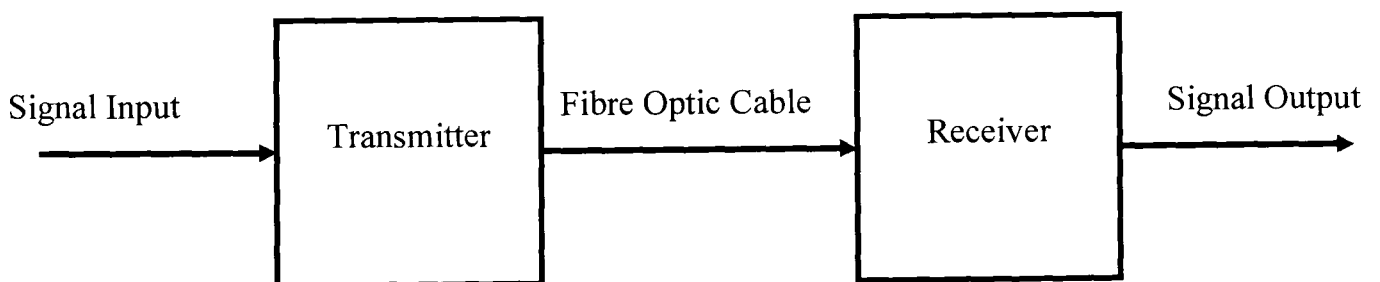


Fig. 1.1: The basic point-to-point fibre optic transmission system.

Fig. 1.2 shows fibre-optic relay systems, consisting of the following:

- **Transmitter** - Produces and encodes the light signals.
- **Optical fibre cable**- Conducts the light signals over a distance.
- **Optical regenerator or repeaters** - Necessary to boost the light signal (for long distances).
- **Optical receiver** - Receives and decodes the light signals

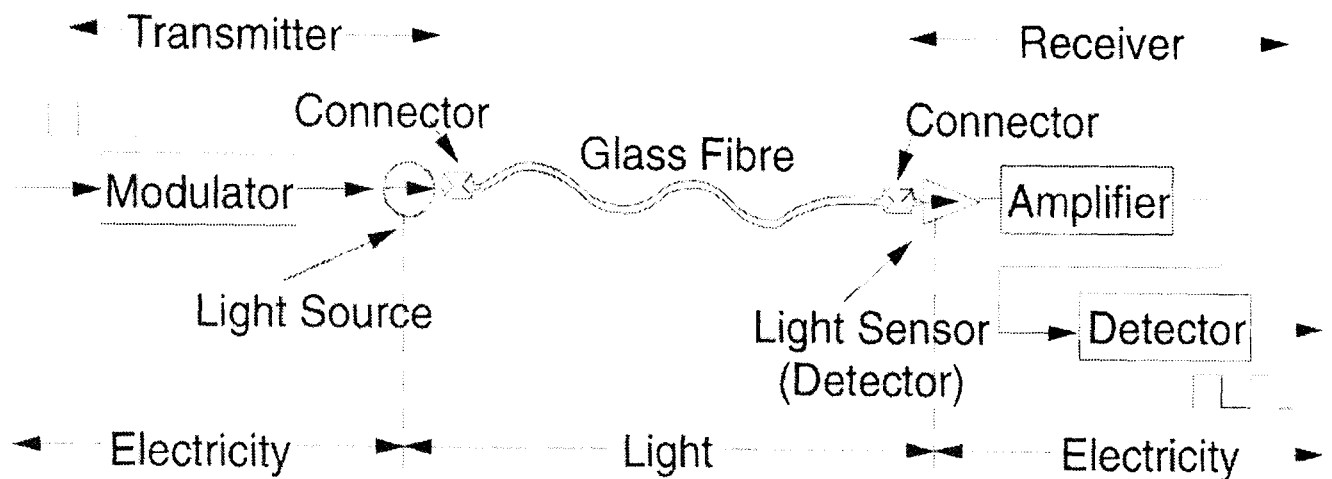


Fig. 1.2: Optical communication systems [Kolimbiris].

1.3.1 Transmitter

The transmitter converts an electrical signal into a corresponding optical signal or light pulses. At one end of the fibre optic system is a transmitter. This is the place of origin for information coming on to fibre-optic lines. The transmitter accepts coded electronic pulse information coming from copper wire. It then processes and translates that information into equivalently coded light pulses. The transmitter is physically close to the optical fibre and may even have a lens to focus the light into the fibre.

1.3.2 Optical Fibre Cable

The cable consists of one or more glass fibres, which act as waveguides or functions as a light guide for the optical signal, guiding the light introduced at one end of the cable through to the other end. Fibre optic cable is similar to electrical cable in its construction, but provides special protection for the optical fibre within. For systems requiring transmission over distances of many kilometers, or where two or more fibre optic cables must be joined together, an optical splice is commonly used. The generally accepted splicing method is arc fusion splicing, which melts the fibre ends together with an electric arc.

1.3.3 Optical Regenerator

Some signal loss occurs when the light is transmitted through the fibre, especially over long distances such as the fibre optic cable under the Atlantic Ocean from U.K to U.S.A. Therefore, one or more light strengtheners, called

repeaters or regenerators, are spliced along the cable to boost and refresh the degraded light signals.

1.3.4 Optical Receiver

The receiver converts the optical (light) signal back into a replica of the original electrical signal. It takes the incoming digital light signals, decodes them and sends the electrical signal to the other user's computer, TV or telephone. The receiver uses a photocell or photodiode to detect the light.

1.4 Historical Development of Fibre Optic Technology

Optical communication systems date back two centuries, to the "optical telegraph", invented by French engineer Claude Chappe in 1790s. His system was a series of semaphores mounted on towers, where human operators relayed messages from one tower to the next. By the mid-19th century it was replaced by the electric telegraph, leaving a scattering of "Telegraph Hills" as its most visible legacy [Hecht].

The Nineteenth Century [1800-1899]

In 1870, John Tyndall, using a jet of water that flowed from one container to another and a beam of sunlight, demonstrated that light used internal reflection to follow a specific path. The light followed a zigzag path inside the curved path of the water.

In 1880, Alexander Graham Bell patented an optical telephone system, named Photophone, which used free-space light to carry the human voice 200 meters. Bell believed this invention was superior to the telephone, his earlier invention, because photophone did not need wires to connect the transmitter and receiver.

The Twentieth Century [1900-1999]

Narinder Kapany, from the Imperial College of Science and Technology in London, first coined the term "fibre optics" in 1956 [Goff]. The development of fibre bundles for image transmission, with the primary application being the

medical endoscope, was patented by Basil Hirschowitz, C. Wilbur Peters, and Lawrence E. Curtiss, researchers at the University of Michigan, in 1956. In the process of developing the endoscope, Curtiss produced the first glass-clad fibres.

The development of laser technology was the next important step in the establishment of the industry of fibre optics. In 1957, Gordon Gould, as a graduate student at Columbia University, described the laser as an intense light source [Goff]. In 1965, Charles K. Kao and George A. Hockham of a British company the Standard Telecommunication Laboratory were the first to recognize that attenuation of contemporary fibres was caused by impurities, which could be removed, rather than fundamental physical effects such as scattering [Kao and Hockham,].

Intrigued by Kao and Hockham's proposal, glass researchers began to work on the problem of purifying glass. In 1970, the first practical optical fibre (with a loss of 17 dB/km by doping silica glass with titanium) for communications was invented by researchers Robert D. Maurer, Donald Keck, Peter Schultz, and Frank Zimar of the American based glass maker Corning. It was the purest glass ever made [Goff]. On 22 April, 1977, General Telephone and Electronics sent the first live telephone traffic through fibre optics, at 6 Mbit/s, in Long Beach, California.

In 1986, David Payne of the University of Southampton, and Emmanuel Desurvire at Bell Laboratories, invented the erbium-doped fibre amplifier, which reduced the cost of long-distance fibre systems by eliminating the need for repeaters. In 1991, the emerging field of photonic crystals led to the development of photonic crystal fibre [Russell, 2003]. In 1995, Prof. Philip Russell and his research team created the world's first working photonic crystal fibre, which became commercially available in 1996 [Knight, 1997].

The Twenty-First Century and Beyond [2000 and Beyond]

As the demand for data bandwidth increases, driven by the phenomenal growth of the Internet, the move to optical networking is the focus of new

technologies. An important factor in these developments is the increase in fibre transmission capacity, which has grown by a factor of 200 in the last decade.

There are extraordinary possibilities for future fibre optic applications because of fibre optic technology's immense potential bandwidth, 50 THz or greater. Today optical fibre cables are the backbone of the telecommunication system, which has led to high speed broadband internet and affordable long distance telephone calls. Broadband service available to a mass market opens up a wide variety of interactive communications for both consumers and businesses, bringing to reality interactive video networks, interactive banking and shopping from the home, and interactive distance learning.

1.5 Structure of Optical Fibre

A single optical fibre has the following parts:

- Core,
- Cladding,
- Buffer coating.

Fig. 1.3 illustrates the structure of optical fibre. The innermost central region of the fibre, or core, is a narrow cylindrical strand of glass used to transmit the light. Cladding is the outer optical material (or glass coating) surrounding the core that reflects the light back into the core. Buffer coating is the plastic coating that protects the fibre from damage and moisture.

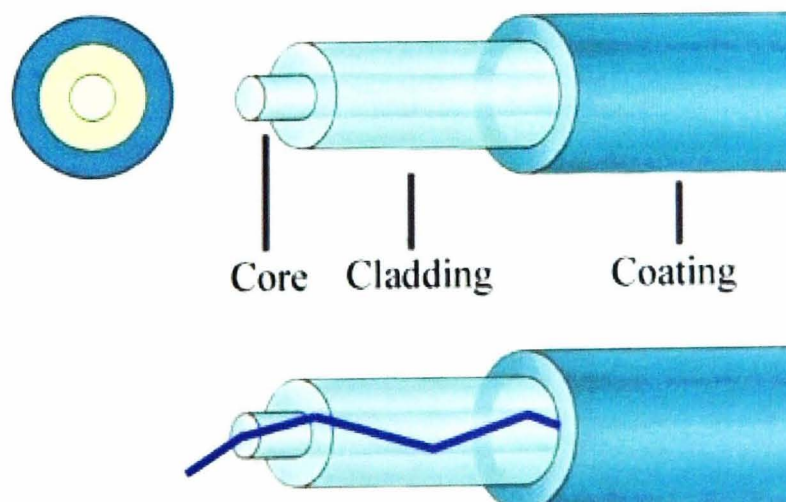


Fig. 1.3: Structure of optical fibre [University of Arizona].

Hundreds or thousands of these optical fibres are arranged in bundles, as shown in Fig. 1.4, in optical cables. The bundles are protected by the cable's outer covering, called a jacket.

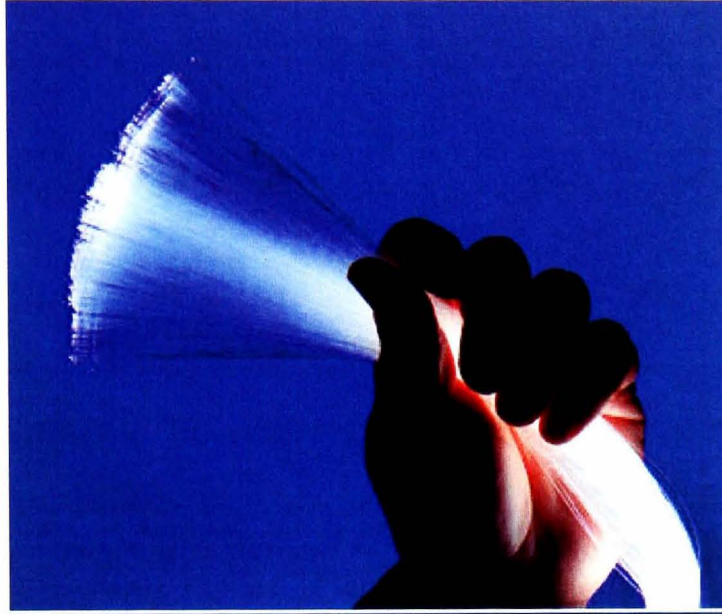


Fig. 1.4: A bundle of optical fibres [Coring Inc.]

The fibre strands, as shown in Fig. 1.5, are being prepared for splicing in a wiring closet. These few strands can collectively transmit trillions of bits per second. Theoretically, using advanced techniques such as DWDM, the modest number of fibres seen here could have sufficient bandwidth to easily carry the sum of all types of current data transmission needs for the entire planet (~100 terabits per second per fibre).

From Computer Desktop Encyclopedia
Reproduced with permission.
© 1996 Corning Incorporated

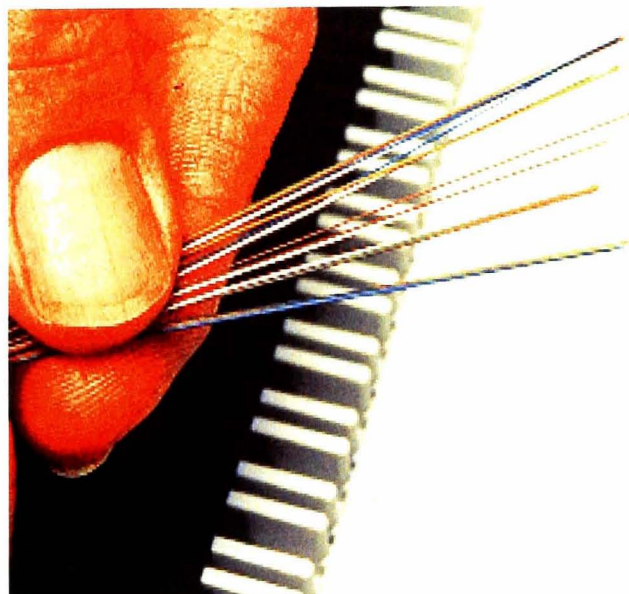


Fig. 1.5: Fibre strands [Coring Inc.].

1.6 Types of Optical Fibre

There are three types of optical fibre commonly used: single-mode fibre, multi-mode fibre and plastic optical fibre (POF). Table 1.1 briefly shows the main characteristics of single-mode and multimode fibres.

1.6.1 Single-Mode Fibre

Fibre supporting only one mode is called single-mode or mono-mode fibre. Single-mode fibre is a single strand of glass fibre with a much smaller core than a multimode fibre. The small core virtually eliminates any distortion that could result from overlapping light pulses. In single-mode fibre, light energy carried by only one mode, so no intermodal dispersion. Therefore, single-mode fibre provides the least signal attenuation and a higher transmission speed and up to 50 times more distance than a multimode fibre, but it also costs more.

1.6.1.1 Characteristics of single-mode fibre

- Single-mode fibre carries higher bandwidth than multimode fibre, but requires a light source with narrow spectral width.
- The small core diameter necessitates the use of expensive laser diodes to enable efficient light coupling and pass sufficient light into the fibre. The small core diameter needs extremely precise connectors that are expensive.
- The performance of single-mode fibre is so good that it is the only type of fibre used for long distance unrepeated transmission up to around 50 km.

Based on the index profile (refractive index of the core material), single-mode fibre has only step index profile (fibre refracts the light sharply or abruptly at the point where the cladding meets the core material). Currently, there is no commercial single-mode graded index fibre where refractive index profile changes gradually from the core to the cladding.

1.6.1.1.1 Monomode Step-index Fibre

Two principle types of step-index single-mode fibre exist:

- (a) **Matched cladding fibre:** cladding is pure fused silica; Germanium Oxide (GeO_2) is added to core to increase its refractive index.
- (b) **Depresses cladding fibre:** The core is fused silica doped with less germanium oxide than is needed for a matched cladding fibre.

In single-mode step-index fibre, the index of refraction between the core and the cladding changes less than it does for multimode fibres. Light thus travels parallel to the axis, creating little pulse dispersion. Telephone and cable television networks install millions of kilometers of this fibre every year.

1.6.2 Multimode Fibre

Fibre which supports more than one mode is called multimode fibre that only gives a reasonably high bandwidth over medium distances. Light waves are dispersed into numerous paths, or modes, as they travel through the cable's core. However, in long cable runs (greater than 3000 feet), multiple paths of light can cause signal distortion at the receiving end, resulting in an unclear and incomplete data transmission.

1.6.2.1 Characteristics of Multimode Fibre

- The fibre can capture light from the light source and pass light to the receiver with high efficiency, so can be used with low-cost light emitting diodes (LEDs).
- High precision connectors are not required because the large core diameter allows wide-tolerance on mechanics.
- Multimode fibres suffer from higher losses than single-mode fibres.

Based on the index profile multimode fibre can be classified as step-index and graded index fibre:

1.6.2.1.1 Multimode Step-index Fibre

In a multimode step-index fibre, rays of light are guided along the fibre core by total internal reflection. In multimode fibre, different modes propagate at different angle and therefore exhibit different transit times. Hence, results the pulse to spread out, phenomenon known as inter-modal dispersion, at times as it propagates along the fibre. This is the main disadvantage and it results in a limited bandwidth of this fibre. A ray, in the step-index fibre, will travel a longer distance than the actual length, because of its zig-zag path. This type of fibre is best suited for transmission over short distances, in an endoscope, for instance.

1.6.2.1.2 Multimode Graded-index Fibre

In a multimode graded-index fibre, light does not propagate by the means of total internal reflection, but by distributed diffraction. The core is composed of many different layers of glass, chosen with indices of refraction to produce a parabolic refractive index profile. The rays follow smooth curve rather than the zig-zags of step-index fibres, which reduces the inter-modal dispersion and travel distance in graded-index fibre. The shortened path and the higher speed allow light at the periphery to arrive at a receiver at about the same time as the slow but straight rays in the core axis.

1.6.3 Plastic Optical Fibre (POF)

POF is a newer plastic-based fibre which promises performance similar to glass cable on very short runs, but at a lower cost. Plastic optical fibre (POF) is commonly step-index multimode fibre, with core diameter of 1 mm or larger. POF typically has much higher attenuation than glass fibre, 1 dB/m or higher, and this high attenuation limits the range of POF-based systems.

Characteristics	Single-Mode Fibre	Multimode Fibre
Core diameter (μm)	8	62.5
Cladding diameter (μm)	125	125-400
Number of propagation mode	Only one	More than one
Dispersion path	Only one	Numerous dispersion paths
Bandwidth	Higher (up to 1000 GHz/km)	Lower (1 GHz/km)
Types	Step-index (core 8-12 μm , cladding 125 μm)	Step-index (core 50-200 μm , cladding 125-400 μm) and Graded-index (core 50-100 μm , cladding 125-140 μm)
Light Source	Laser	LED
Wavelength (nm)	1300 or 1550	850 or 1300
Transmission Rate	Higher	Lower
Transmission Distance	Long distance link (50 times more distance than multimode)	Short or medium distance link
Signal Quality	Higher	Lower
Signal Attenuation	Very low	High
Main Source of Attenuation	Chromatic Dispersion	Inter-modal Dispersion
Cost	More Expensive	Expensive
Applications	Long Transmission/Higher Bandwidth (Telecommunications lines)	Short Transmission/Lower Bandwidth (LAN, Backbone)

Table 1.1: Characteristics of single-mode and multimode fibre [Jenkins and White].

1.7 Physics of Total Internal Reflection

In an optical fibre, the light travels through the core by constantly reflecting from the cladding. This phenomenon is known as total internal reflection (TIR). TIR is an important principle for optical fibres and is dependent on the refractive indices of the two materials- in this case, the core and the cladding. There are two rules for the total internal reflection:

- Light ray must be travel from high optically dense (higher refractive index) medium (silica core) to low optically dense (lower refractive index) medium (silica cladding).
- The angle of the light is always greater than the critical angle.

Fig. 1.6 shows the behavior of the incident light ray on the interface between two dielectrics.

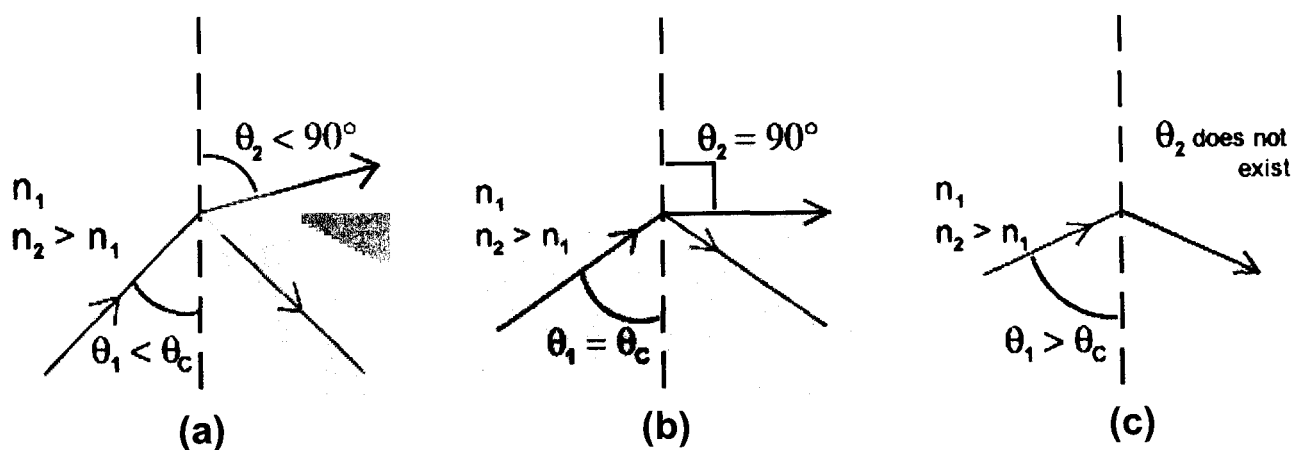


Fig. 1.6: Light rays incident on high to low refractive index interface [Rensselaer Polytech.].

In Fig. 1.6 (a), when light passes from one medium with a higher index of refraction (n_2) to another medium with a lower index of refraction (n_1), it bends or refracts away from an imaginary line perpendicular to the surface (normal line).

In Fig. 1.6 (b), as the incident angle (θ_1) through n_2 becomes greater with respect to the normal line, the refracted light through n_1 bends further away from the line. At one particular angle (when $\theta_2 = 90^\circ$), the refracted light will not

go into n_1 , but instead will travel along the surface between the two media. This particular angle is known as, critical angle (θ_c). In this case, $\theta_1 = \theta_c$.

Fig. 1.6 (c) shows, when the incident angle through n_2 is greater than the critical angle ($\theta_1 > \theta_c$) then the light is reflected entirely back into the same medium (n_2), even though n_1 may be transparent. This is known as the total internal reflection.

1.8 Fabrication of Optical Fibre

An optical fibre is manufactured from silicon dioxide by either of two methods:

- (a) The first, the crucible method, in which powdered silica is melted, produces fatter, multimode fibres.
- (b) The second, the vapor deposition process, where optical fibre is made by first constructing a large-diameter preform, with a carefully controlled refractive index profile, and then pulling the preform to form the long, thin optical fibre.

This section will focus on the vapor deposition process, where making optical fibre requires the following steps:

- Making a preform glass cylinder
- Drawing the fibres from the preform
- Testing the fibres

1.8.1 Making the Preform Blank

The glass for the preform is generally made by a process called modified chemical vapor deposition (MCVD). This section will focus on the MCVD process, the most common manufacturing technique now in use. MCVD yields a low-loss fibre well-suited for long-distance cables. In MCVD, as shown in Fig. 1.7, oxygen is bubbled through solutions of silicon chloride (SiCl_4), germanium chloride (GeCl_4) and/or other chemicals. The precise mixture governs the various physical and optical properties (index of refraction, coefficient of expansion, melting point, etc.). The gas vapors are then conducted to the inside of a synthetic silica or quartz tube (cladding) in a

special lathe, as shown in Fig. 1.8. As the lathe turns, a torch is moved up and down on the outside of the tube. The extreme heat from the torch causes two things to happen:

- The silicon and germanium react with oxygen, forming silicon dioxide (SiO_2) and germanium dioxide (GeO_2).
- The silicon dioxide and germanium dioxide deposit on the inside of the tube and fuse together to form glass.

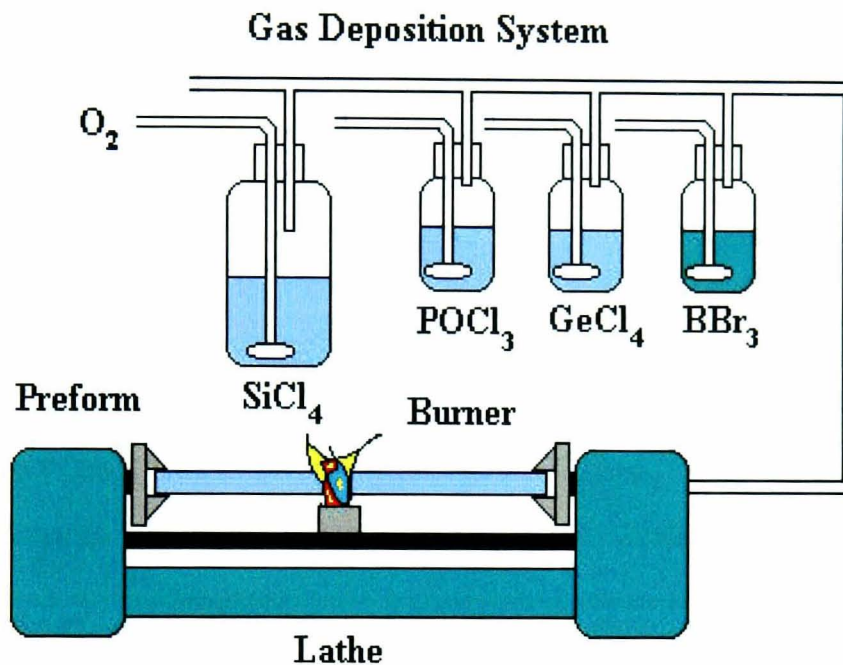


Fig. 1.7: MCVD process for making the preform blank [Fibercore Ltd.].

The torch is then traversed up and down the length of the tube to deposit the material evenly. After the torch has reached the end of the tube, it is then brought back to the beginning of the tube and the deposited particles are then melted to form a solid layer. This process is repeated until a sufficient amount of material has been deposited. For each layer, the composition can be varied by varying the gas composition, resulting in precise control of the finished fibre's optical properties. The process of making the preform blank is highly automated and takes several hours. After the preform blank cools, it is tested for quality control. A preform usually measures 10 to 25 millimeters in diameter and 600 to 1000 millimeters in length.

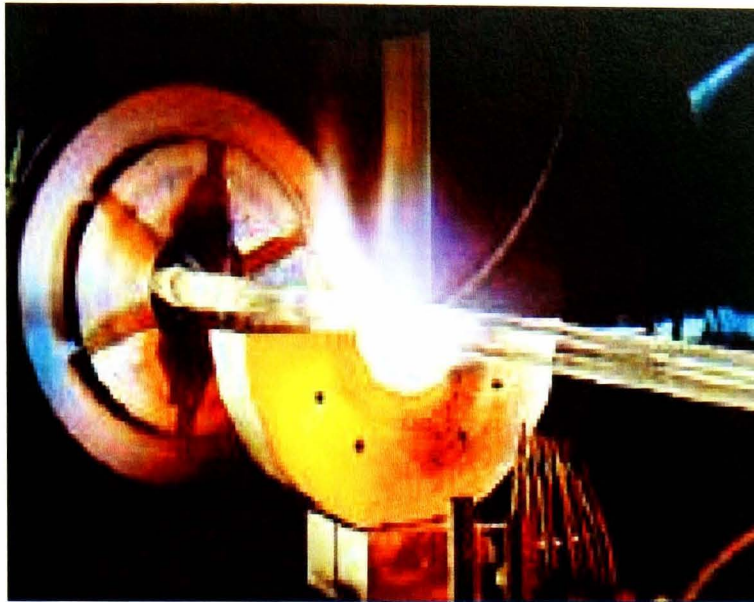


Fig. 1.8: Lathe used in preparing the preform blank [Fibrecore Ltd.].

1.8.2 Drawing Fibres from the Preform Blank

The preform, however constructed, is then placed in a device known as a drawing tower, as shown in Fig. 1.9, where the preform tip is heated into a graphite furnace (1,900 to 2,200 degrees Celsius), and the tip gets melted until a molten glob falls down by gravity. As it drops, it cools and forms a thread.

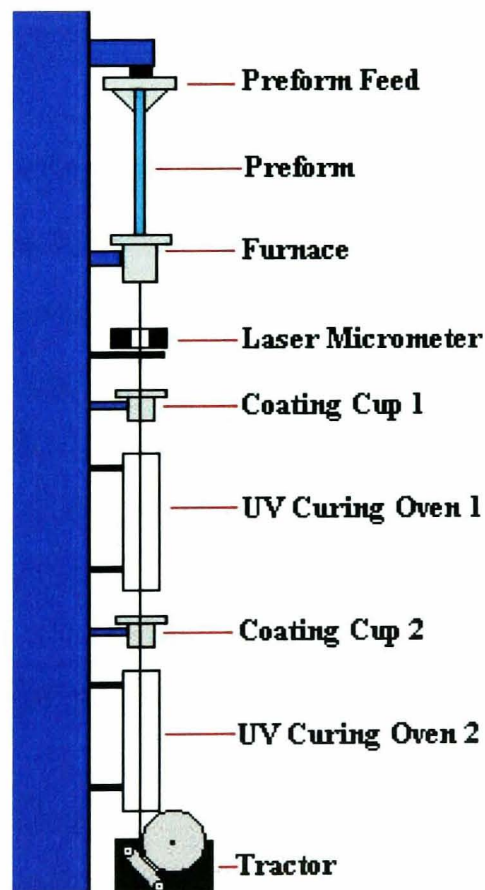


Fig. 1.9: Diagram of a fibre drawing tower used to draw optical glass fibres from a preform blank [Corning Inc.].

The operator threads the strand through a series of coating cups (buffer coatings) and ultraviolet light curing ovens onto a tractor-controlled spool. The tractor mechanism slowly pulls the fibre from the heated preform blank and is precisely controlled by using a laser micrometer to measure the diameter of the fibre and feed the information back to the tractor mechanism. Fibres are pulled from the blank at a rate of 10 to 20 m/s and the finished product is wound onto the spool. It is not uncommon for spools to contain more than 2.2 km of optical fibre. Fig. 1.10 shows the finished spool of optical fibre.



Fig. 1.10: Finished spool of optical fibre [Corning Inc.].

1.8.3 Testing the Finished Optical Fibre

The finished optical fibre is tested for tensile strength, refractive index profile, fibre geometry, attenuation, information carrying capacity (bandwidth), chromatic dispersion, operating temperature/humidity range, temperature dependence of attenuation, and ability to conduct light underwater. Once the fibres have passed the quality control, they are sold to telephone companies, cable companies and network providers.

1.9 Materials of Optical Fibre

Both the core and the cladding of an optical fibre are made of highly purified silica glass (SiO_2). Normal glass window is transparent, but the thicker the glass gets, the less transparent it becomes due to impurities in the glass. However, the glass in an optical fibre has far fewer impurities than window-

pane glass. Glass happens to be a very practical choice for optical fibre because it is reasonably strong, flexible, and has good light transmission characteristics.

Silica-based optical fibres are the most important transmission medium for long-distance and large-capacity optical communication systems. The most distinguished feature of optical fibre is its low loss characteristics. Together with such low loss properties, low dispersion is also required for signal transmission.

Glass optical fibres are almost always made from silica, but some other materials, such as fluorozirconate, fluoroaluminate, and chalcogenide glasses are used for longer-wavelength infrared applications. Like other glasses, these glasses have a refractive index of about 1.5. Typically the difference between core and cladding is less than one percent. Glasses with high fluoride content hold the most promise for improving optical fibre performance because they are transparent to almost the entire range of visible light frequencies. This makes them especially valuable for multimode optical fibres, which can transmit hundreds of discrete light wave signals concurrently.

1.10 Advantages of Optical Fibre

Fibre optic transmission systems offer a wide range of benefits not offered by traditional copper wire or coaxial cable. The small size and the fact that no electrical power is needed at the remote location give the fibre optic sensor advantages to conventional electrical sensor in certain applications.

Optical fibre offers enormous bandwidth and it takes a lot less room. Any one of the copper bundles, as shown in Fig. 1.11, can be replaced with one single fibre strand (centre of Fig. 1.11).



Fig. 1.11: Comparison between optical fibre and copper wire [Corning Inc.].

Fibre optics has several advantages [Keiser; Myabaev and Scheiner] over traditional metal communications lines, such as:

Speed: Fibre optic networks operate at high speeds - up into the gigabits.

Thinner: Optical fibres can be drawn to smaller diameters than copper wire.

Higher data rates: Fibre optic cable can support much higher data rates, and at greater distances. It can carry much more information and deliver it with greater fidelity than either copper wire or coaxial cable.

Maintenance: Fibre optic cables costs much less to maintain.

Invulnerable: Optical fibre is totally immune to virtually all kinds of interference, including lightning, and will not conduct electricity. It can therefore come in direct contact with high voltage electrical equipment and power lines.

Less expensive: Several miles of optical cable can be made cheaper than equivalent lengths of copper wire.

Less signal degradation: The loss of signal in optical fibre is less than in copper wire.

No light interference: Unlike electrical signals in copper wires, light signals from one fibre do not interfere with those of other fibres in the same cable. This means clearer phone conversations or TV reception.

Bandwidth: Fibre optic cables have a much greater bandwidth than metal cables. Optical fibres are thinner than copper wires, more fibres can be bundled into a given-diameter cable than copper wires, as shown in Fig. 1.12.

This allows more phone lines to go over the same cable. This means that fibre optic cables can carry more data.

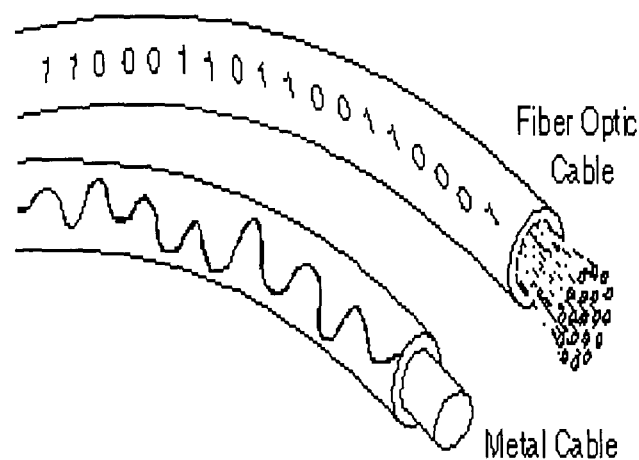


Fig. 1.12: Comparison between fibre optic cable and metal cable
[Corning Inc.].

Low power: Signals in optical fibres degrade less; therefore, lower-power transmitters can be used instead of the high-voltage electrical transmitters needed for copper wires. Again, this saves the provider and its client's money.

Digital signals: Data can be transmitted digitally (the natural form for computer data, useful in computer networks) rather than analogically.

Non-flammable: There is no fire hazard, because no electricity is passed through optical fibres. Since the only carrier in the fibre is light, there is no possibility of a spark from a broken fibre.

Lightweight: A fibre optic cable, even one that contains many fibres, is usually much smaller and lighter in weight than a copper wire or coaxial cable with similar information carrying capacity. It is easier to handle and install, and uses less channel space.

Flexible: Fibre optics are very flexible to transmit and receive light.

Resistance: Greater resistance to electromagnetic noise such as radios, motors or other nearby cables.

Secure communication: Fibre optic cable is ideal for secure communications systems because it is very difficult to tap but very easy to monitor. In addition, there is absolutely no electrical radiation from a fibre.

No chemical reaction: As the basic fibre is made of glass, it will not corrode and is unaffected by most chemicals. It can be buried directly in most kinds

of soil or exposed to most corrosive atmospheres in chemical plants without significant concern.

Table 1.2 shows the comparison among different types of transmission media.

Characteristics	Optical Fibre	Coaxial Pair	Twisted Pair
Typical distance	20 – 30 miles	2 – 3 miles	Up to 1 mile.
Typical data rate	Often 400 - 500 Mbps	10 Mbps is Common	1 - 2 Mbps for 1 Mile.
Susceptibility to Interference	Immune to electrical interference	Shielding eliminates much of the electrical interference	Electrical interference from nearby wires or motors
Applications	Commonly used in long distance phone lines. Also popular as the main communication medium in computer networks.	Often used as the primary communication medium in computer networks.	Useful where space is limited or where high data rates are not needed .i.e. behind a wall leading to a terminal.

Table 1.2: Comparison among different types of transmission media.

1.11 Applications of Optical Fibre

- The first commercial applications for fibre optics were medical. Bundled fibres can deliver illumination light to remote regions of the body, and carry understandable images back out to the doctor.
- Optical fibres are used in many flexible digital cameras for medical imaging (in bronchoscopes, laparoscopes), mechanical imaging (to

inspect mechanical welds in pipes), and plumbing (to inspect sewer lines).

- Industrial endoscopes are used for inspecting anything hard to reach, such as jet engine interiors.
- Single fibres can be inserted into blocked arteries and the laser light used to burn away the blockage.
- Telephone companies use optical fibre throughout their system as the backbone architecture and as the long-distance connection between city phone systems. The light transmitting fibre is immune to electronic noise, can carry thousands more conversations with better sound quality.
- Cable television companies have also begun integrating fibre-optics into their cable systems.
- Colleges, universities, office buildings, and industrial plants, just to name a few, all make use of optical fibre within their Local Area Network (LAN) systems.
- Most power companies already have fibre-optic communication systems in use for monitoring their power grid systems.
- An optical fibre doped with certain rare-earth elements such as erbium can be used as the gain medium of a laser or optical amplifier to provide signal amplification by splicing a short section of doped fibre into a regular (undoped) optical fibre line.
- Optical fibres can be used as sensors to measure strain, temperature, pressure and other parameters. Another use of the optical fibre as a sensor is the optical gyroscope which is in use in the Boeing 767 and in some car models (for navigation purposes).
- Optical fibres are used as hydrophones for seismic or SONAR applications.
- Fibres are widely used in illumination applications. In some buildings, optical fibres are used to route sunlight from the roof to other parts of the building. Optical fibre illumination is also used for decorative applications, including signs, art, and artificial Christmas trees.

- A single-mode fibre is used to carry just one light wave over very long distances. Bundles of single-mode optical fibres are used in long-distance telephone lines and undersea cables. Multimode optical fibres can carry hundreds of separate light wave signals over shorter distances and is used in urban systems where many signals must be carried to central switching stations for distribution.
- Fibre-optic cable can be used for audio applications (specially tuned for accurate signal transfer), yielding distortion-free sound.
- Silica fibre is typically used in applications involving high power lasers and sensors, such as medical laser-surgery.
- All-plastic fibre is useful for very short data links within equipment because it may be used with relatively inexpensive LEDs.
- Optical fibres are insensitive to Electro-Magnetism Interference and Radio-Frequency Interference (EMI\RFI), therefore, highly suitable for many military and communication applications where high signal quality, secure data transmission, and survivability are essential.

1.12 Aims and Objectives of the Thesis

The following chapters present the main aims and objectives of the research undertaken in this field which can be summarized as follows:

(1) To further develop and investigate established work on the rigorous and efficient finite element method (FEM) based on the vector \mathbf{H} -field variational formulation for the analysis of photonic crystal fibres (PCF) to understand the basic properties of photonic crystal fibres. Sequential development stages of the project will be as follows:

- Square lattice PCF with square hole,
- Square lattice PCF with rectangular hole, and
- Hexagonal lattice PCF with circular hole.

(2) To investigate several modal solution approaches for the analysis of photonic crystal fibres (PCF) with different lattice PCF. The main areas, which

will be discussed of the fundamental quasi-TE (H^y_{11}) mode, quasi-TM (H^x_{11}) mode, and higher order modes for equal and unequal air hole dimension, are:

- (a) Variation of the silica index and the effective index of the fundamental and higher order modes with the mesh, operating wavelength (λ), separation between two air holes (S), pitch (Λ), and the normalized hole diameter d/Λ and d_2/Λ .
- (b) Variation of the spot-size (σ), power confinement factor (P_s), modal hybridness, and beat length with the operating wavelength, pitch, and the normalized hole diameter d/Λ and d_2/Λ .
- (c) Variation of the group velocity dispersion (GVD) with the wavelength for H^y_{11} and H^x_{11} modes for different d_2 values and different meshes.
- (d) Characteristics of the two-dimensional (2-D) and three-dimensional (3-D) dominant and non-dominant field profiles of full structure and two-fold structure of PCF at different operating wavelength for equal and unequal air hole dimension.
- (e) Comparison between the two-dimensional field profiles, with different wavelength, pitch and different d/Λ .
- (f) Comparison results of a PCF structure with equal and unequal hole diameter.
- (h) Variations of dominant H^y field for the H^y_{11} (quasi-TE) mode along X and normalised X (X/Λ) direction.

(3) To investigate the accuracy of an existing finite element package based on the vector \mathbf{H} -field variational formulation for the analysis of modal birefringence of photonic crystal fibres. This will be carried out by performing a polarization study of different lattice photonic crystal fibres with the aim to achieve highly birefringent photonic crystal fibres. The main areas, which will be discussed, are:

- (a) Variations of the modal birefringence with the normalized diameter, d_2/Λ at the different operating wavelengths and at different pitches.
- (b) Variations of the modal birefringence with the operating wavelengths at different pitches.

- (c) Variations of the modal birefringence with the pitch at normalized diameter, d/Λ .
- (d) Comparison results of two different structural asymmetry.
- (e) Comparison results of a modal birefringence of PCF.

(4) To investigate the modal leakage losses of the photonic crystal fibres using a full-vectorial beam propagation method (BPM) based on the versatile FEM. The robust perfectly matched layer (PML) boundary condition will be introduced to the modal solution approach and polarization dependent leakage losses will be calculated, to design a single polarization PCF. The main areas, which will be discussed, are:

- (a) Variations of the confinement loss with the number of rings.
- (b) Variations of the confinement loss with the normalized diameter, d_2/Λ at different operating wavelengths.
- (c) Variations of the confinement loss with operating wavelength.

1.13 Structure of the Thesis

The work presented in this thesis is based on the research carried out by the author in the use of the versatile finite element method (FEM) and the beam propagation method (BPM) with perfectly matched layer (PML) boundary condition, mainly devoted to the study of modal solutions, birefringence and losses in photonic crystal fibre. The thesis consists of nine chapters including this chapter. The subsequent discussion gives an outline of the carefully structured thesis, beginning with an introduction of optical fibre, presented in this chapter. A thorough understanding of the principles of the optical fibre is required to investigate and develop photonic crystal fibre. Therefore, this chapter describes the fundamental theoretical background of optical fibre.

Chapter 2 describes the basic theoretical background of photonic crystal fibre.

Chapter 3 presents various numerical methods such as indirect entire-domain methods, direct sub-domain or space domain discretization methods, and field tracking methods. Comparison of different methods has also been presented in this chapter.

Chapter 4 describes the theoretical formulation of the finite element method as a powerful numerical tool in analyzing photonic crystal fibres.

Chapter 5 deals with the theoretical foundation of the beam propagation method.

Chapter 6 describes square lattice PCF with square core than with rectangular core. Several modal solutions are then presented to analyse the square, and rectangular core PCF. In this chapter, a rigorous modal solution of photonic crystal fibre is presented, to understand the basic properties of photonic crystal fibres.

Chapter 7 presents several modal solution results of the hexagonal lattice PCF with circular core for both equal and unequal air hole.

Chapter 8 performs a polarization study of hexagonal lattice photonic crystal fibres with the aim to achieve highly birefringent photonic crystal fibres. It also presents the leakage loss properties of the photonic crystal fibre.

Chapter 9 describes the conclusion and future research direction on photonic crystal fibre. A brief discussion is given on each chapter.

Appendices are provided at the end together with a list of publications by the author relevant to this work as well as a list of references cited throughout the thesis.

Photonic crystal fibre (PCF)

2.1 Brief Introduction

Photonic crystal fibres (PCFs) are a completely brand new range of optical fibres [Mortensen *et al.*] or optical waveguides [Williamson]. The photonic crystal fibre (PCF) concept is ushering in a new and more versatile era of fibre optics, with a multitude of different applications spanning many areas of science and technology [Russell, 2002].

Photonic crystal fibre marks a milestone in photonic crystal research and presents a snapshot of a remarkably dynamic field considering issues such as, losses and useful bandwidth [Krauss and Baba] mainly with a view towards the significant applications in telecommunications.

The PCF has attracted growing attention owing to its many unique properties. Increasing interest is being shown in such PCFs for a range of applications in optical communications, sensing and signal processing due to their better control and guidance of light, including unique transmission characteristics, such as large effective mode area [Knight *et al.*, 1998a], wide single-mode wavelength range [Birks *et al.*] with controllable spot sizes, anomalous dispersion at visible and near infrared wavelength [Gander *et al.*], enhanced modal birefringence [Hansen *et al.*, 2001], and many other phenomena [Wolinski *et al.*]. The optical properties of standard fibres are mostly controlled by two key parameters, the radius and the index difference between the core and the cladding. Single-mode fibre (SMF) can be designed by balancing these two parameters for a range of different applications, for example in conventional low-loss telecommunication grade single-mode fibres (SMFs) or specialized fibres such as doped fibres with a smaller spot-size. However, the adjustment of the spot-size or the group velocity dispersion (GVD) properties of these silica fibres is severely limited.

A wide range of potential applications is anticipated, exploiting the ability to adjust the spot-size, for example to create a large spot-size for high power applications and a smaller spot-size for improved nonlinear interactions and to tailor the GVD [Birks *et al.*] for various linear and nonlinear devices applications. PCF can also offer higher index contrast to facilitate their polarization maintaining properties which is useful for coherent optical communications, fibre optic sensor systems, and also to create PCFs with higher modal birefringence [Rahman *et al.*, 2006b].

2.2 Definition of PCF

Photonic crystal fibres (PCFs) may be defined as optical fibres in which the core and cladding regions consists of microstructure rather than homogeneous materials, as shown in Fig. 2.1. Therefore, PCF is also known as “Holey Fibre (HF)” [Knight *et al.*, 1996a; 1996b]. or “micro-structured optical fibre (MOF)” [Wolinski *et al.*]. In lay terms it’s called holey fibre because that’s

exactly what it look like. To industry insiders it's called photonic crystal fibre (PCF), because it uses a two-dimensional (2D) crystal structure to keep light inside the fibre [Lindstorm, 2001*b*].

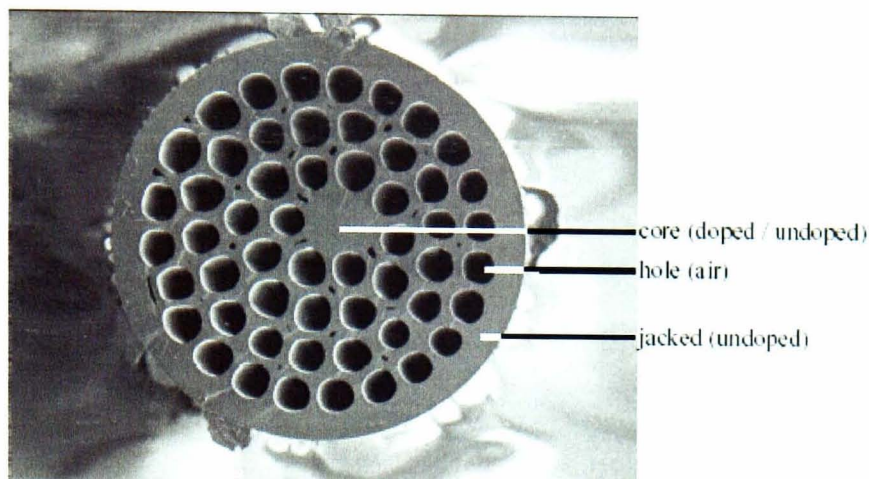


Fig. 2.1: Uniform cross-section of air-holes in a single material [Crystal-Fibre].

Although PCF is apparently similar to a conventional optical fibre, the difference is that PCF consists of a periodic or regular array [Taylor *et al.*] of microscopic holes or channels [Monro and Larkin, 2001] which give them special advantages when it comes to transmitting data. Instead of the conventional core cladding structure, the fibre traps light in its core by means of an array of tiny air holes [Lindstorm, 2001*a*] running along the waveguide length [Knight *et al.*, 2002] or the axial direction [Wolinski *et al.*] of the entire fibre length [Ferrando *et al.*, 1999].

The holes (known as cladding), as shown in Fig. 2.1, act as optical barriers or scatters, which is used to guide light within the central core. Each hole can be less than a micron in diameter. The positioning and size of the holes affect the way that light is transmitted by the fibre.

A missing hole(s) forming a defect or core [Knight *et al.*, 1996*a*] in the centre is either made of solid glass (as shown in Fig. 2.2*a*) or hollow (as shown in Fig. 2.2*b*) [Russell, 2002]. Cutting the fibre at any point and looking at its cross-section shows a solid core where the light guidance takes place [Taylor *et al.*], as shown earlier in Fig. 2.1, encircled by holes in the surrounding area (the cladding) [Monro *et al.*, 2000*a*].

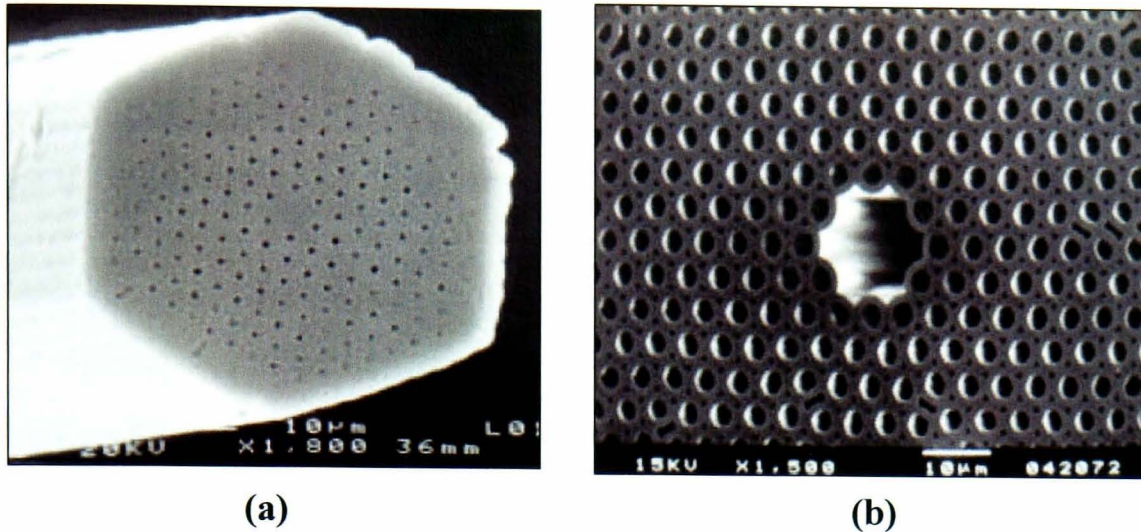


Fig. 2.2: (a) Solid-core photonic crystal fibre (b) Hollow-core photonic crystal fibre [Dettmer].

2.3 Historical Development of PCF

Back in the 1920s, John Logie Baird had the idea of using hollow tubes to transmit images in an early incarnation of television. Recently the idea of transmitting light through hollow waveguides has become cutting-edge technology once again in the form of “Holey Fibres” [Williamson]. Today, optical fibre brought about revolutionary changes in the fibre optics world. Prof. Philip Russell spent the past 16 years designing so-called holey fibre. And about 11 years ago, while as staff at England’s University of Bath, he and a team of fellow researchers built a prototype that proved that holey fibre could transmit light through a hollow, air-filled core [Lindstorm, 2001b].

Research in the field of PCF was stimulated by the prediction of photonic bandgap [Yablonovitch] which was the only guiding mechanism considered for new class of optical fibres. Later, researchers discovered that by microstructuring and including airholes in the fibre, these devices could provide revolutionary features using the simpler and more conventional principle of total internal reflection [Broeng *et al.*].

The beginning of research on PCF can be traced back over past decade that has seen PCF cut a large swath across a variety of disciplines. Many exciting phenomena have been reported since the first results on photonic crystal

fibres [Knight *et al.*, 1996a]. The most common type of PCF, which was first fabricated in 1996 by Prof. Philip Russel and his research Group, consists of pure silica core with an array of air holes running along the entire fibre length [Knight *et al.*, 1996b].

Over the past few years, photonic crystal fibre (PCF) technology has evolved from a strong research-oriented field to a commercial technology providing characteristics such as single-mode operation from the UV to IR spectral regions, large mode areas with core diameters larger than 20 μm , and highly nonlinear performance with optimized dispersion properties [Kristiansen].

A brief look at recent developments in holey fibre research

1970s: Periodic optical structures- thin film filters.

1974: Single-material fibre proposed by Kaiser *et al.*

1978: The Bragg fibre was proposed and analyzed by Yeh and Yariv.

1987: Photonic crystal concept invented [Yablonovitch], world wide research followed thereafter. The really hot topic in optics was the photonic bandgap, originally predicted by Eli Yablonovitch [Yablonovitch] and Sajeev John [John].

1991: Prof. Philip Russell first proposed the concept of photonic-crystal fibres [Freeman].

1995: Prof. Philip Russell and his research team created the world's first working photonic-crystal fibre [Freeman] that confined light by modified total internal reflection. This was an extremely interesting development, but it didn't have a hollow core and it didn't rely on a photonic bandgap for optical confinement [Dettmer].

1996: Prof. Philip Russell moved his research group to the University of Bath and reported the first working example of endlessly single-mode fibre at OFC [Knight *et al.*, 1996b]. Results were published in Optics Letters in 1996 [Knight *et al.*, 1996a], and it was their most cited letter that year [Freeman].

1997: Proposed in 1992, the first endlessly single-mode Holey Fibre was fabricated [Russell, 2002].

1998: First bandgap guiding fibre was fabricated [Knight *et al.*, 1998b].

1999: Prof. Philip Russell and his research group reported a single-mode hollow core fibre in which confinement was by a full two-dimensional photonic bandgap [Cregan *et al.*]. First prediction and realization of novel optical properties in index-guiding HF's was proposed [Williamson].

2000: DTU (Denmark) and NKT (UK) established "Crystal Fibre A/S" [Crystal-Fibre]. Prof. Philip Russell and two of his colleagues set up a spin-out business called BlazePhotonics [Freeman].

2001: BlazePhotonics spinning off from University of Bath (UK) and received \$9 m in first-round funding in March 2001. The main emphasis was on research and development of new photonic crystal fibre technologies, although it did sell a few of its fibres to research institutions and companies worldwide [Freeman].

2002: Most interesting subject on any Optical Communication conference. Breakthrough losses of 13 dB/km were reported in hollow-core photonic bandgap fibre by a team from Corning. A record-breaking supercontinuum spectrum, extending out to 2300 nm, had been demonstrated in a SF₆ glass fibre [Russell, 2002].

2003: Crystal Fibre A/S had launched four new air guiding photonic bandgap fibres (around 900 nm, 1070 nm, 1300 nm, and 1550 nm) where light was guided in the hollow core [Crystal-Fibre].

PCF is now leading to a range of new and interesting properties with a variety of applications. These are now being exploited by many companies and universities, including: Crystal Fibre A/S, INO, Alcatel, Bell Labs, and OmniGuide Communications Inc.; as well as the usual big fibre players like Corning Inc. PCF is one of the main research areas in the University of Bath and University of Southampton. Practical advances in index-guiding HF's such as improved fibre robustness, lower loss, longer lengths, device demonstrations, new materials etc. are now implementing [Williamson].

2.4 Structure of PCF

The transverse section of a photonic crystal fibre (PCF) consists basically of a two-dimensional (2D) photonic crystal, which for some specific geometries shows photonic bandgaps [Andrés *et al.*]. By making a suitable geometry of the periodic dielectric medium, a photonic crystal can be used as an optical fibre [DeHaven].

The existence of a defect in the regular structure produces the transverse localization of light in its vicinity with the consequent generation of axial guiding modes [Andrés *et al.*]. A typical PCF has a 2-D cross-sectional structure in which the solid pure-silica core region is surrounded by a cladding region that contains air holes, as shown earlier in Fig. 2.1. These holes effectively lower the index of refraction, creating a step-index optical fibre.

PCF structures vary according to its applications. The design flexibility is very large, and designers can use many different, fascinating, and odd air hole patterns to achieve specific PCF parameters. The triangular arrangement of round air holes in the cladding is typically used to create single-mode fibres. An elliptical core can create a highly birefringent fibre that is polarization maintaining.

2.5 Light-guiding Mechanism of PCF

Generally, two different kinds of PCFs exist, classified by their light-guiding mechanism, depending on its structure:

- Waveguiding by total internal reflection (index guiding PCF)
- Waveguiding by photonic bandgap effect.

2.5.1 Index-guiding PCFs

If the cladding, which is full of holes, has a lower average refractive index than the core, then light is guided by the Modified Total Internal Reflection (M-TIR)

principle which is similar to conventional fibres. Fig. 2.3 shows the high-index guiding fibres, where core has higher average refractive index than the holey cladding.

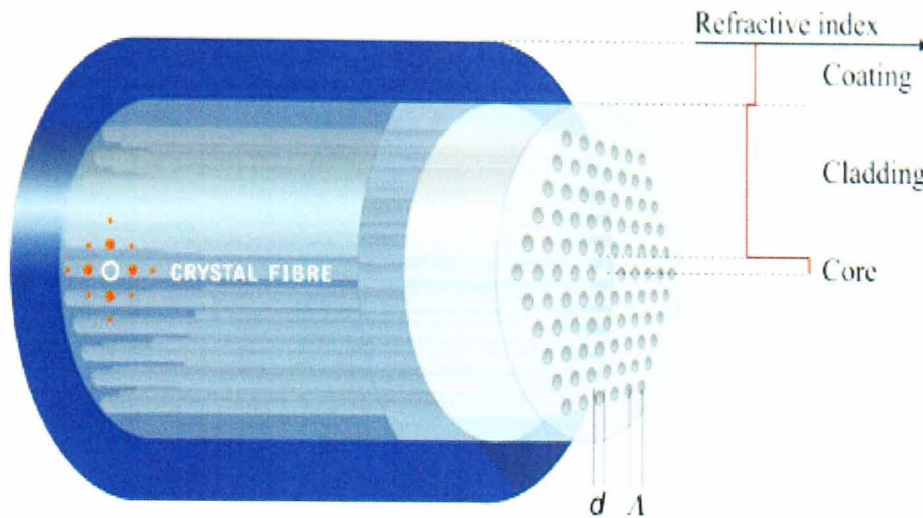


Fig. 2.3: High-index guiding fibre [Crystal-Fibre].

Some of the properties in the index-guiding case are as follows:

- Flexibility in obtaining a desired dispersion property,
- Possible to obtain single-mode operation for wide range of mode areas.

2.5.2 Photonic Bandgap (PBG) Effect

The second type of fibre provides guidance by the photonic bandgap effect where the index of the core is uncritical; it can be hollow or filled with material [Russell, 2003] such as liquids, gasses or particles [Crystal-Fibre]. A holey fibre can guide light even when the refractive index of the core is lower than that of the cladding ($n_{\text{core}} < n_{\text{cladding}}$) - if, for example, the core of the fibre comprises an air hole, as shown in Fig. 2.4. This phenomenon is known as photonic bandgap (PBG) effect.

Photonic bandgap allows for novel features such as light confinement to a low-index core. There is no material with a refractive index less than air, so this structure would not support total internal reflection; instead, the light would be contained within the hollow core by the barrier of the two-dimensional photonic bandgap formed by the array of air holes encircling the core [Dettmer].

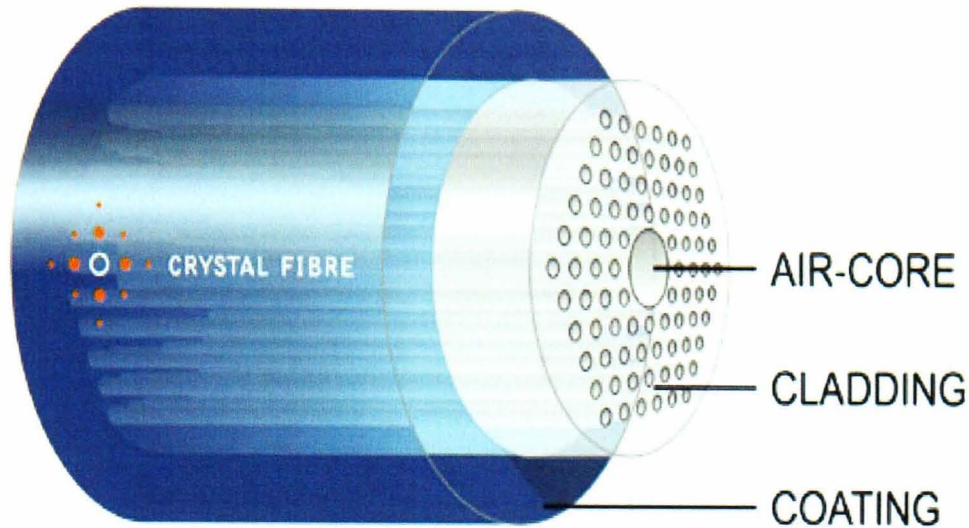


Fig. 2.4: Low-index guiding fibre [Crystal-Fibre].

Light can be controlled and transformed in these fibres with unprecedented freedom, allowing for example the guiding of light in a hollow core (as shown in Fig. 2.4), the creation of highly nonlinear solid cores with anomalous dispersion in the visible and the design of fibres that support only one transverse spatial mode at all wavelengths [Russell, 2002]. In PBG, the air holes that surround the light almost entirely eliminate dispersion, optical linearities, and reflections on the fibre. Typical applications for these fibres are high power delivery with reduced nonlinear effects and material damage, short pulse delivery, and low loss guidance in vacuum.

Table 2.1 summarizing some of the nomenclature encountered, specifically looking at the types of fibre that are formed from the different guidance methods.

Guidance Mechanism	Types of Fibre	Configuration of Fibre
Effective index guidance	-Photonic crystal fibre (PCF) -Microstructured fibre (MOF) -Holey fibre (HF)	-Solid core -Air holes act as cladding -Single material -Core has higher average refractive index than the cladding -Light is guided by total internal reflection.
Bandgap guidance	- Photonic bandgap fibre (PBG)	-Core can be hollow (air) or filled with material (liquid, gas or particles) -Air holes define cladding -Core has lower average refractive index than the cladding -Light is guided by photonic bandgap effect.

Table 2.1: Guidance mechanisms and holey fibre types.

This thesis will focus on index-guiding PCFs, as these fibres are presently most common and have less stringent requirements on structural uniformity.

2.6 Advantages over Conventional Fibre

- Due to high effective index contrast between silica and air, a much broader range of dispersion behaviour is accessible with PCFs than with standard fibre.

- The existence of two different light guiding mechanisms is one of the reasons for the versatile nature of PCFs.
- The design flexibility of PCF for tailoring a specific property is much better than that of conventional fibre. PCF has more controllable fabrication parameters than standard single-mode fibre.
- PCF technology offers many new advantages over conventional fibres, such as: insensitivity to bending, reduced fibre loss, zero dispersion, nonlinearity, polarization stability, highly adjustable effective mode area, the engineerable dispersion at visible and near-infrared wavelength, high-power delivery and many more.
- The number of holes, their sizes, shapes, orientations and placements in PCF can provide an additional degree of freedom, which is not present for conventional fibre.
- Increasing the air-hole diameter, the properties of the PCF can be enhanced which is not possible in conventional fibre.
- Single-mode operation over a wide range of wavelength [Birks *et al.*], a property that is not attainable in standard fibres.
- In conventional fibres, electromagnetic modes are guided by total internal reflection in a core region whose refractive index is raised by doping of the base materials. Where as, in PCF modes are guided by modified total internal reflection (M-TIR) in a core region whose refractive index is higher than the holey cladding.
- PCF with high-index core and air-guiding PCF (hollow core of fibre) is more flexible than conventional fibre [DeHaven], possible to make very large core area to send high power, and also possible to make very small core.

2.7 Applications of PCFs

Applications of the PCFs are emerging in many diverse areas of science and technology. Within telecommunications, PCFs have several potential applications that range from low-nonlinearity large-core transmission fibres to signal-processing fibres for terminal equipment components [Kristiansen]. This

novel fibre has a number of potential applications outside the pure transmission sphere. Some of the applications are as follows:

- Dispersion behaviour is very important for signal transmission and in many applications of nonlinear effect.
- PCF with zero dispersion at specific wavelength is used to eliminate dispersion compensation for long-haul transmission.
- PCF with extremely negative dispersion at interested wavelength for dispersion compensation [Williamson].
- The large mode-area PCFs or large spot-size has a variety of potential applications including laser/amplifier development [Monro and Larkin, 2001], transmission fibre, and low nonlinearity telecommunications [Williamson]. The large mode-area PCFs can also provide high-power delivery for applications in astronomy, lithography, materials processing, imaging, femtosecond pulse guidance [Kristiansen], general laser pigtailed [Kristiansen], and laser welding and machining [Monro and Larkin, 2001].
- The small mode area or smaller spot-size for improved nonlinear interactions, Brillouin lasers, second harmonic generation [Williamson, 2002], four-wave mixing, and polarization maintaining PCFs with higher modal birefringence etc.
- Highly birefringent PCF can be used to reduce the coupling between the orthogonal states of the fundamental mode if no higher order modes are supported. Highly birefringent PCF is also used in four-wave mixing-based applications [Watanabe and Futami], for ultrashort pulse propagation, and as polarization maintaining fibres (PMFs) etc. PMFs are essential for coherent optical communication systems and fibre sensor systems [Saitoh and Koshiba, 2003b].
- Highly nonlinear PCF with zero dispersion at wavelength, $\lambda = 1.55 \mu\text{m}$ is very attractive for a range of telecom applications such as: wavelength conversion [Lee *et al.*; Belardi *et al.*; Sharping *et al.*], Raman and parametric amplification [Hansryd *et al.*; Hansryd and Andrekson], pulse compression [Druon *et al.*], soliton generation [Sharping *et al.*], multiple clock recovery [Futami *et al.*], all optical-demultiplexing

[Oxenløwe *et al.*; Berg *et al.*], all optical switching [Williamson], and supercontinuum-based multi-channel processing [Watanabe and Futami] etc.

- PCF with high Numerical Aperture (NA) is useful for collection and transmission of high powers in situations, where signal distortion is not a problem and for the fabrication of dual-clad fibre lasers and amplifiers.
- Two-core PCF is used for strain measurement. PCF with more than one core is useful in shape-sensing applications [Russell *et al.*, www.bath.ac.uk].
- PCF is used as: optical fibre sensors, device component, fibre lasers optical transportation of the micro particles, 2R regenerators [Petropoulos *et al.*, 2001a; 2001b], optical parametric amplifiers, high-speed telecom [Omenetto *et al.*], optical sampling and reduction gear in optical clock.
- PCF is used in an optical interconnection system [Taylor *et al.*].
- Microstructured fibres can also be used to guide atoms [Monro and Larkin, 2001].

2.8 Fabrication of PCF

Fabrication of PCFs has been a highly labor-intensive and time-consuming process. The typical starting point is an array of low-index hollow capillary silica tubes, as shown in Fig. 2.5, bundled around a high-index pure silica rod replacing the centre capillary.

Low-index tubes are heated to melt onto high-index rod to form thickened solid rod or preform as shown in Fig. 2.6. Tubes are packed in a hexagonal shape with hollow, solid, birefringent, doped or tubular core elements.



Fig. 2.5: Array of hollow capillary silica tubes bundled around a pure silica rod replacing the centre capillary [Kristiansen].

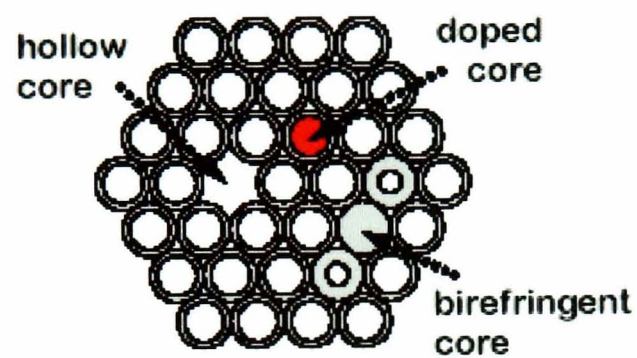


Fig. 2.6: Preform construction [DeHaven].

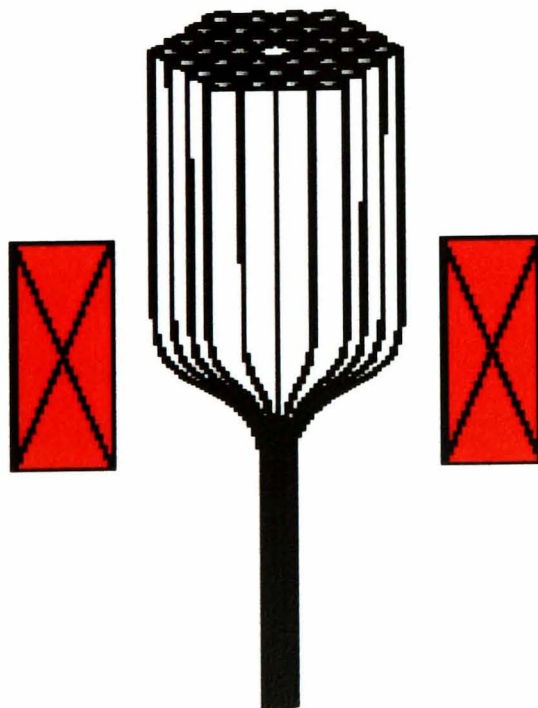


Fig. 2.7: Preform drawing down in furnace [DeHaven].

In a fibre draw tower, a standard piece of equipment in fibre creation, the manufacturer heats the preform to around 2000°C and carefully pulls the preform, using gravity and pressure, into a fibre typically 125 µm in diameter to produce a filament or fibre several kilometers long, as shown in Fig. 2.7.

Finally, a protective polymer coating (jacket) applied to the outside improves handling characteristics [Kristiansen].

2.9 Novel Properties of PCF

Photonic crystal fibres can exhibit some unusual novel and interesting optical properties not encountered in ordinary fibre. A wide range of novel optical properties are possible in holey fibres because of the following features:

- The core/cladding index contrast can be large
- Cladding design is flexible, with many different possible hole arrangements

Some of the properties are:

2.9.1 Birefringence Properties of PCF

In the PCF, the lightwave are composed of two perpendicular polarized modes (TE and TM) which travel always simultaneously at different speed. Birefringence, also known as double refraction, is the separation of a ray of light into two unequally refracted polarized rays, occurring in crystals in which the velocity of light rays is not the same in all directions. The angle of light that enters a transparent medium depends on the refractive index. Therefore, birefringence is numerically quantified as the difference between the greater and lesser refractive indices of the anisotropic crystal. Birefringence usually results from two sources:

- (a) Stress birefringence,
- (b) Shape or form birefringence.

Stress birefringence is results from bends and twists in the fibre. Shape or form birefringence results from unintentional deformation during fabrication. Other sources of birefringence are fibre strain, fibre side pressure etc [Wilson and Hawkes].

Effects of small birefringence are observed in conventional fibres, such as pulse spreading due to differential group delay. Large birefringence restricts the pulse spreading effects and the modes are not coupled together by bends and twists in the fibre. In this case, the energy in each mode remains constant along the fibre length. Therefore, effects of large birefringence are an advantage [University of Bath] in PCF. PCF can be made highly birefringent by having different air-hole diameters along the two orthogonal axis or by asymmetric core design. PCF had illustrated modal birefringence of an order of magnitude higher than that of the conventional fibres [Ju *et al.*].

Research results [Nielsen *et al.*, 2001] had shown that the form birefringence increases with wavelength as the mode increases in size and thereby overlaps the nonsymmetrical air/glass boundary.

2.9.2 Polarization Properties of PCF

Polarization maintaining fibre has a unique characteristic with its shorter beat lengths, which make it a particularly useful medium for applications in which preserving the polarization state of light is important [Lindstorm, 2001*b*]. Polarization maintaining PCF has the properties of being highly birefringence fibre. The main application of this fibre is in sensors, gyroscopes, and interferometers.

2.9.3 Dispersion of PCF

As light rays travelling in each mode travel a different distance they arrive at the output at different times. This effect is called modal dispersion and is measured in picoseconds per nanometre per kilometer (ps/nm/km). Dispersion can be broken into two components: material dispersion and

waveguide dispersion. In terms of holey fibres, waveguide dispersion is due to the wavelength-dependent change in the refractive index induced by the air holes. This can be unusually large in holey fibres if either the air holes are large or the core is small [Williamson].

When designing a nonlinear fibre, the dispersion properties are very important as it has direct impact on pulse broadening, and bandwidth for the device in which the fibre is used. For most telecommunication applications, a zero-dispersion wavelength at 1.55 μm is required and a dispersion slope as low as possible is advantageous [Hansen *et al.*, 2003]. The negative slope of the fibre is especially interesting in combination with standard nonlinear fibres with positive dispersion slope, which enables creation of nonlinear devices with near-zero slope and low dispersion in a large wavelength range [Hansen *et al.*, 2002].

Ferrando *et al.* [Ferrando *et al.*, 1999] reported the first dispersion characteristics of a photonic crystal fibre. Ferrando *et al.* [Ferrando *et al.*, 2000a] had established an original procedure to achieve PCF with ultraflattened positive or negative group velocity dispersion. For modern glass fibre, the maximum transmission distance is limited not by attenuation but by dispersion, or spreading of optical pulses as they travel along the fibre. Dispersion in glass fibres is caused by a variety of factors. Some of them are as follows:

2.9.3.1 Intermodal Dispersion

If a narrow pulse of radiation is launched into a fibre and all possible modes are excited, then after a given length, the pulse would be broadened because of the different axial velocities of the various modes present. This phenomenon is known as intermodal dispersion [Williamson]. Intermodal dispersion limits the performance of multi-mode fibre. Single-mode fibre supports only one transverse mode, and therefore, intermodal dispersion is eliminated.

2.9.3.2 Chromatic Dispersion

Chromatic dispersion, as shown in Fig. 2.8, is wavelength dependent and is caused by the core material itself and is actually negative at short wavelengths and moves positive at longer wavelengths. This creates 'magic' wavelength at which dispersion is actually zero. Single-mode fibre performance is limited by chromatic dispersion, which occurs because the index of the glass varies slightly depending on the wavelength of the light.

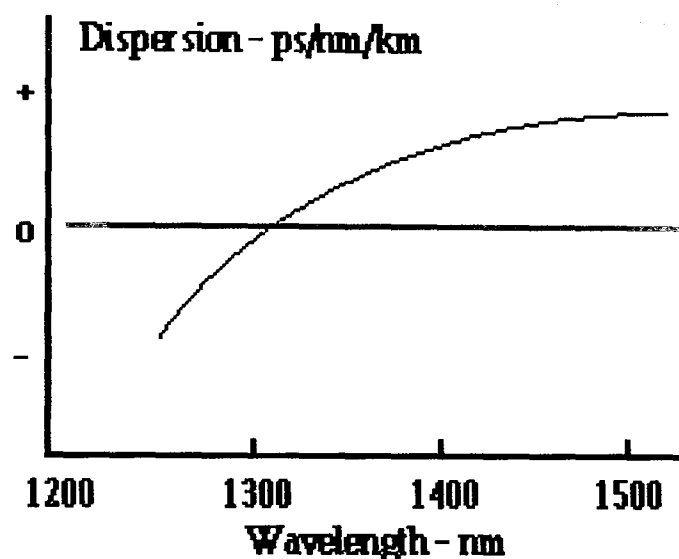


Fig. 2.8: Chromatic dispersion in single-mode fibre [Mercury Comm.].

2.9.3.3 Polarization Mode Dispersion

It can limit the performance of single-mode systems, occurs because although the single-mode fibre can sustain only one transverse mode, it can carry this mode with two different polarizations, and slight imperfections or distortions in a fibre can alter the propagation velocities for the two polarizations. Dispersion limits the bandwidth of the fibre because the spreading optical pulse limits the rate that pulses can follow one another on the fibre and still be distinguishable at the receiver.

2.9.4 Loss Mechanism

The basic loss mechanisms in PCFs are absorption by impurities [Hansen *et al.*, 2002], scattering on air/glass interfaces, structural nonuniformity, micro [Nielsen *et al.*, 2003b] and macro-bending loss and confinement loss [Finazzi *et al.*, 2002]. The confinement mechanisms can be thought of as being

produced by the existence of a homogeneous material with a specific average index [Knight *et al.*, 1998c].

Producing low-loss holey fibres requires careful thought. The effect of the confinement loss can be reduced by doping the core region, which also increases nonlinear refractive index of the glass and reduces splice loss. In single-material holey fibres, light can always leak out to the cladding, as there are no truly bound modes, only leaky ones. Increasing the number of rings of holes is one way to reduce the confinement loss [Williamson].

2.9.5 Endless Single-mode (ESM) PCF

Endlessly single-mode fibre is an unconventional property of photonic crystal fibres. In telecommunications the term 'endless single-mode' means that holey fibres can guide a single-mode over all wavelengths. Standard optical fibres become multimode as the size of the core increases relative to the wavelength. Some holey fibres can guide a single-mode regardless of the optical wavelength [Birks], referring to the absence of higher-order modes [Nielsen *et al.*, 2003a]. The cladding effective index is very important design parameter for realizing a single-mode PCF. Light at shorter wavelengths is more tightly confined to the core, so the core/cladding refractive index difference is reduced with decreasing wavelength. This strong wavelength-dependence of the cladding index can prevent the fibre from supporting more than one mode at short wavelengths [Koshiba, 2002].

Endlessly single-mode fibre [Knight, 1997] can handle many times more power than conventional single-mode fibre, according to Prof. Philip Russell. That may come in handy as vendors develop systems that can send more and more wavelengths into a fibre. Each wavelength is associated with a certain amount of power [Lindstorm, 2001b]. An undersea telecommunications link needs a single-mode operation over a wide spectral range, large bandwidth, so that it can transmit a high data rate [Monro and Larkin, 2001].

2.9.6 Nonlinear Properties of PCF

The high index difference between the silica core and the air filled microstructure enables tight mode confinement resulting in a low effective area and thereby a high nonlinear coefficient [Hansen *et al.*, 2002], as shown in Fig. 2.9. The nonlinearity of an optical fibre is proportional to the intrinsic nonlinearity of the material used to make the fibre and is also inversely proportional to the mode area of light guided by the fibre, as shown in Fig. 2.9. Therefore, nonlinearity can be minimized by increasing the mode area or by using a glass host with a low material nonlinearity, such as silica. In contrast, nonlinearity can be maximized by combining a small mode area with a high nonlinearity glass (typically found in high-index glasses such as chalcogenides) [Williamson].

Nonlinearity Tailoring

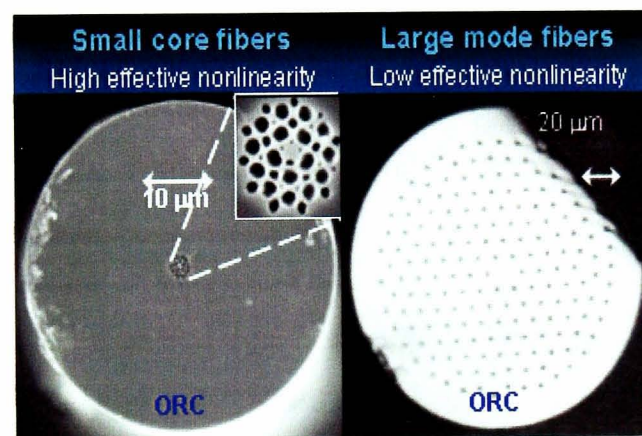


Fig. 2.9: Nonlinearity tailoring of PCF [University of Southampton].

In the last few years, experiments in photonic crystal fibres have shown nonlinear phenomena such as supercontinuum generation, third harmonic generation and efficient Raman self-frequency shift [Aceves] which were found to contribute to the formation of the continuum (such as self-phase modulation, Raman scattering, four-wave mixing etc.) depending on the type of fibre used to generate the continuum [Genty *et al.*, 2002a; 2002b].

2.10 Materials

PCF can be made with parameters impossible to achieve in standard fibres, which has led some researchers to suggest that PCFs could become the

ultimate transmission waveguide for electromagnetic fields. PCF can be made usually with fused silica or undoped pure silica (SiO_2), although dopants can be added to make active devices, just as with conventional fibre [Williamson].

PCF, made of undoped pure SiO_2 , provides very low losses, sustains high powers and temperature levels, and withstands nuclear radiation [Kristiansen]. SiO_2 is not a good conductor of heat but proton bombardment changes the characteristics of the material, increasing its resistance and hence confining the current while still providing good heat conduction. SiO_2 provides superior fibre performance for most applications with wavelengths between 200 and 2500 nm, but using other materials can enhance specific parameters like nonlinearity or waveguiding outside this spectral region.

Pure doped SiO_2 , where silica is doped with Germanium (Ge), can be used to increase refractive index of silica and Ge has very low absorption. Where as, SiO_2 doped with Fluorine can be used to reduce the refractive index of core below that of pure silica. Doped silica is now used in a variety of fibre lasers and amplifiers.

Although most PCF is formed in pure undoped SiO_2 glass, it has also recently been made using polymers [van Eijkelenborg *et al.*]. There are many other type of glasses (not SiO_2) have been used for PCF, such as: GaAs, GaAlAs, InGaAs, and InGaAsP [Kumar *et al.*].

2.11 Summary

In this chapter, a brief introduction is given to the field of photonic crystal fibre. Historical background, applications, many new advantages beyond conventional fibre, fabrication techniques, and extraordinary novel properties of photonic crystal fibre are discussed in detail.

In the next chapter, various numerical methods are discussed with their comparative advantages and disadvantages.

Numerical Methods

3.1 Introduction

The term numerical techniques describe the branch of mathematics concerned with methods of finding numerical solutions to problems. As optical technology has reached maturity, the associated devices have, themselves, become more complex. The optimization of such complex devices requires the accurate characterisation of their lightwave propagation characteristics. Unfortunately, analytical techniques are not adequate to model lightwave devices without significant approximations. Hence, there is a significant need for the development and use of numerical methods, in particular computer-aided design techniques, to simulate complex structures in order to optimize existing designs and evaluate novel devices, either prior to or instead of fabrication and experimental testing, which is time consuming and expensive.

Numerical methods are used to solve difficult and sometimes intractable problems by approximating functions to the equations that describes a process or an approximation to the process and arrive at a meaningful solution. PCF has complex structure; therefore, it is useful and meaningful to use numerical methods for the simulation and modelling of PCF. In general, numerical methods do not usually give the exact answer for a given problem, but they tend to get closer and closer towards a solution with each iteration [Champion]. There are many different types of numerical methods used these days, some of them are: the effective index method [Knox and Toulouis], the finite difference method [Schulz *et al.*], the finite element method [Rahman and Davies, 1984a] and the beam propagation method [Feit and Fleck, 1978], as being particularly important for the design process.

The field of photonic crystal fibres has by now existed for almost a decade. To date, most of the research into photonic crystal fibres has had a strong experimental basis [Knight *et al.*, 1996a], which has recently been complemented by various modal solution approaches to their characterization, but mostly using scalar formulations or being limited to specific types of structures. The strength of the scalar approach is that it is straight forward to implement and thus serve as an excellent starting point for researchers and students entering the field of micro-structured optical fibres. The scalar approach naturally gives rise to a much wider range in which the structure supports a confined mode. Although a scalar approach provides great insight to the basic physics of photonic bandgap fibres, it cannot reveal the complete picture [Riishede *et al.*].

3.2 Full-vectorial Solution

Full-vectorial solution is considered as one of the most accurate and efficient techniques. Polarisation and /or degeneracies may only be fully revealed by a full-vectorial approach. From the pioneering work in early eighties, most of the formulations used today are based on **H**-field full-vectorial formulation.

A full-vectorial approach is necessary to characterize accurately the PCF and such an **H**-field based full-vectorial approach may be extended to obtain the modal solution of PCFs [Rajarajan *et al.*, 2004]. In the literature, it is often emphasized that in general a full-vectorial approach is required for quantitative modelling of micro-structured fibres [Riishede *et al.*].

As many useful photonic crystal devices are designed around the PCFs, it is tremendously important to develop a model that is capable of accounting for the propagation mechanisms in PCFs. It is highly recognized that full-vectorial model should be adopted in the accurate analysis of propagation in PCFs [Obayya *et al.*, 2005].

3.3 Different Methods

There are many different methods for modelling the behavior of photonic crystal fibres. Several full-vectorial [Ferrando *et al.* 1999] approaches have been reported, such as localized function method [Mogilevtsev *et al.*; Monro *et al.*, 2000*b*], multipole method [White *et al.*, 2002; Kuhlmeier, *et al.*], plane wave method [Ferrando *et al.*, 1999; Johnson and Joannopoulos], finite element method [Koshiba and Saitoh, 2001]. These methods can be classified as follows:

- Indirect entire-domain techniques,
- Direct sub-domain or space domain discretization techniques, and
- Field tracking techniques.

3.3.1 Indirect Entire-domain Techniques

Indirect techniques, such as: Sinusoidal [Ferrando *et al.*, 1999], Hermite-Gaussian [Mogilevtsev *et al.*], or Cylindrical [Steel *et al.*] basis functions, usually have limitations on the shape and/or arrangement of the holes. Therefore, this report will not discuss the indirect entire-domain techniques.

3.3.2 Direct Sub-domain or Space Domain Discretization Techniques

Direct sub-domain or space domain discretization techniques can efficiently deal with arbitrarily-shaped holes and arbitrary number and arrangement of holes. In particular, the possibility of incorporating robust boundary conditions with these direct space domain techniques is quite important in order to account for the leakage losses associated with the modes propagating in PCFs. Examples of direct sub-domain or space domain discretization techniques are: Finite difference method (FDM) [Yu and Chang], Finite difference time domain (FDTD) [Lizier and Town], and Finite element method (FEM) [Cucinotta, *et al.*; Koshiba and Saitoh, 2003a].

3.3.3 Field Tracking Techniques

Field tracking techniques works in both longitudinally variant and invariant optical waveguide chips [Obayya *et al.*, 2005]. Examples of field tracking techniques are: Beam propagation method (BPM) [Feit and Fleck, 1978; Xu *et al.*; Fabrizio *et al.*, 2002], Full-vectorial finite element based beam propagation method (VFEBPM) [Obayya *et al.*, 2000a], and Imaginary distance full-vectorial finite element based beam propagation method (IDVFEBPM) [Obayya *et al.*, 2005].

3.4 Comparison of Different Methods

3.4.1 Effective Index Method

One of the simplest methods used is the effective index method [Birks *et al.*; Knight *et al.*, 1998c], which approximates the PCF as a step index fibre with the cladding index equal to the average or weighted average of the PCF in the cladding region. Although it can provide some insight into PCF operation, this reduced model is unable to predict accurately the fibre modal properties such as dispersion or birefringence, which depend critically on the arrangement and size of the air holes [Koshiba, 2002]. The effective index method is an analytical method applicable to complicated waveguides such as ridge waveguides and diffused waveguides in LiNbO_3 [Okamoto].

3.4.2 Plane Wave Expansion (PWE)

Commercial tools based on PWE are now becoming available to photonic-crystal designers. Such tools can simplify the design process for photonic crystals at multiple stages, from the initial layout and visualization of complex structures using graphical CAD interfaces to the automatic generation of band structures appropriate for the class of crystal lattice. At some point in photonic-crystal modelling, in addition to propagation studies, knowledge of the photonic band structure is indispensable. The PWE technique is ideal for this problem because it is accurate, relatively fast, and can be applied to any type of crystal structure, including irregular crystals [Kristiansen]. The plane wave method [Broeng *et al.*; Arriaga *et al.*], employing field expansion with sinusoidal basis functions, can be used for any refractive index profile if enough basis functions are used, and this is versatile, but not especially efficient and has limitation in defining PCF. Fourier transform coefficients can also be applied within a plane wave expansion method.

3.4.3 Localized Function Method

Monro *et al.* have considered vectorial approach employing the localized expansion to represent the transverse magnetic field by using Hermite-Gaussian orthogonal basis function [Monro *et al.*, 1999]. Mogilevtsev *et al.* applied localized function method as an effective tool for calculating the vector and scalar modes supported by photonic crystal fibres with localized defect. The basis of the localized function method is to expand the modal field by Hermite-Gaussian functions and to solve the governing wave equations analytically with the aid of a Fourier series representation of the refractive index profile. The principal advantage of the proposed technique is that the Fourier coefficients are found analytically that can be used directly for calculation at different wavelengths [Mogilevtsev *et al.*]. Fourier coefficients can be presented in a form that allows different materials and material dispersion to be studied without recalculation of the coefficients. Bekker *et al.*, demonstrated the extension of the method to holey fibre cross-sections with arbitrary polygon shaped holes and general hole shapes that are

approximated by linear segments [Bekker *et al.*] localized mode expansion is fast but suffers from non-uniform convergence [Kristiansen].

3.4.4 Multipole Method

White *et al.* [White *et al.*, 2002; 2001a; 2001b] have used the multipole method which involves expansion of the modal field or the dielectric constants. This method is generally inefficient in either of the following factors- computational time, defining infinite lattice or modal solution near cutoff region. This method has the limitation that it can treat only perfect circular holes [Kristiansen].

3.4.5 Supercell Lattice Method

Wang *et al.* [Wang *et al.*] used supercell lattice method which involves expansion of the modal field or the dielectric constants. This method is generally inefficient in either of the following factors: computational time, defining infinite lattice or modal solution near cutoff region.

3.4.6 Finite Difference Method (FDM)

Riishede *et al.*, applied the scalar Helmholtz equation and the finite difference approximation in index-guiding micro-structured optical fibres as well as air-core photonic bandgap fibres. The strength of this approach lies in its very simple numerical implementation and its ability to find eigenmodes at a specific eigenvalue, which is of great interest, when modelling defect modes in photonic bandgap fibres [Riishede *et al.*].

3.4.7 Finite Difference Time Domain (FDTD) Method

Finite difference time domain (FDTD) method, was originally proposed by Yee (Yee algorithm), also known as the Order-N method [Chan *et al.*]. The FDTD method works with the discretized Maxwell's equations [Bjarklev *et al.*]. The FDTD method is widely used numerical technique, which is universal, robust, methodologically simple and descriptive. FDTD is a powerful technique to analyse PCF in order to design complex structures. This straightforward method has the disadvantage of being numerically heavy and thus time

consuming since it calculates all n^2 eigenvalues. There is no simple way of calculating the position of the photonic bandgaps using the finite-difference. A full-vectorial planewave method with periodic boundary condition [Johnson and Joannopoulos] is an alternate method to calculate the bandgaps [Riishede *et al.*]. The main shortcoming of the FDTD method is its computational requirements. Consideration of three-dimensional problems requires large volumes of data to be stored and processed, which makes calculation very lengthy [Taflov].

3.4.8 Transfer-Matrix Method (TMM)

In a manner similarly to that of the FDTD method, the transfer-matrix method works with the discretized Maxwell's equations. Also in similarity with the FDTD method, proper boundary conditions should be used. The transfer-matrix method is less universal; however, it is more computationally effective than the FDTD method. Nevertheless, it suffers the same problem of drastic increase in required computational resources, when dealing with three-dimensional problems, especially with fields localized within defects. The methods can be used to model infinite periodic structures, and to find the eigenmodes and eigen frequencies, as well as transmission properties [Bjarklev *et al.*].

3.4.9 Finite Element Method (FEM)

The modal solution approach, based on the powerful finite element method [Rahman *et al.*, 1984a; 2005a] is more flexible, can represent any arbitrary cross-section of an optical waveguide more accurately and has been widely exploited to find the modal solutions of a wide range of such waveguides. In the finite element method, by using a larger number of triangular elements, which may have different shapes and sizes, any complex optical waveguide cross-section can be accurately represented [Cucinotta *et al.*]. The flexibility of the FEM to represent a cross-section of a holey fibre [Koshiba and Saitoh, 2001], with arbitrary hole sizes and placements, makes it a powerful approach where many other simpler and semi-analytical methods would otherwise be

unsatisfactory. The FEM method can be used to obtain the modal solutions of the optical waveguides with self-focusing or de-focusing nonlinearity [Rahman *et al.*, 1993] using a simple iteration loop and this approach is employed here to find the modal solutions for several photonic crystal fibres.

3.4.10 Beam Propagation Method (BPM)

The beam propagation method (BPM) is most widely used for modelling of integrated and fibre-optic photonic devices, and it has been developed to the stage of a commercial software product for this purpose. It is computationally optimal, and methodologically even simpler than FDTD [Bjarklev *et al.*]. BPM has been widely used in the last two decades as a “field tracking” technique. BPM can be three types, such as: FFT based BPM, FDM based BPM, and FEM based BPM. Since the very early pioneer work of Feit and Fleck [Feit and Fleck, 1978] in developing an FFT based BPM algorithm so many improved versions using the finite difference method and based upon scalar, semi-vector and full-vector BPM formulation have been proposed [Xu *et al.*]. BPM [Obayya, *et al.*, 2000a] can be employed to simulate the propagation of the initial field along a waveguide and more recently the imaginary axis BPM has been used [He *et al.*] to extract limited individual modes, but this approach is more computationally intensive, and time consuming. For photonic bandgap device computations, the beam propagation solutions are generally inadequate. Moreover, a major problem is the quick succession of discontinuities in a photonic crystal. BPM is generally based on slow changes, and the nature of a photonic crystal implies a large change in waveguide profile within one period, and that over and over again [Bjarklev *et al.*].

3.4.11 Full-vectorial Finite Element Based Beam Propagation Method (VFEBPM)

The full-vectorial finite element based beam propagation method (VFEBPM) [Obayya, *et al.*, 2000b] has been considered as one of the most accurate and yet efficient BPM techniques. Being formulated in terms of the transverse magnetic field components only makes it more numerically efficient [Selleri *et*

al.]. By imposing the $\text{div}\mathbf{H}=0$ and the interface boundary conditions using an elegant line integral approach [Obayya, *et al.*, 2000a], the possibility of the spurious modes to appear in the solution spectrum is totally eliminated.

3.4.12 Imaginary Distance Full-vectorial Finite Element Based Beam Propagation Method (IDVFEBPM)

Recently, a combination of the imaginary distance algorithm and the full-vectorial finite element based beam propagation method (IDVFEBPM) [Saitoh and Koshiya, 2002] has been successfully applied to the modal solution of linear [Obayya, *et al.*, 2002a] and nonlinear [Obayya, *et al.*, 2002b] optical waveguides. In order to perform an accurate modal solution of PCF, the Imaginary distance full-vectorial finite element based beam propagation method (IDVFEBPM) can be used with the robust Perfectly Matched Layer (PML) boundary condition. PML is employed at the edges of the computational window in order to account for the leakage property of the modes [Obayya *et al.*, 2005].

3.5 Summary

Research over the last decade has generated a wide variety of numerical algorithms for modelling PCFs, such as BPM, FDTM, FEM, PWE, localized mode expansion, and multipole methods. Each method has advantages and disadvantages. For example, multipole expansion produces results accurate to eight significant figures in seconds but can treat only perfect circular holes; localized mode expansion is fast but suffers from non-uniform convergence [Kristiansen]. Most of the aforementioned methods are suitable for 2-D calculations. However, the full-vectorial FEM is suitable for modal solution of PCF and full-vectorial FE-BPM is suitable for calculating the loss of the PCF. Electric and magnetic field boundary conditions and perfect match layer (PML) boundary conditions are used for FEM and BPM method, respectively. The next two chapters will describe how FEM and BPM are used in numerical methods.

Chapter 4

The Finite Element Method

4.1 Introduction

Of the different numerical approaches considered so far earlier in the previous chapter, the finite element method (FEM) [Rahman and Davies, 1984a] is now established as one of the most powerful and versatile methods in many branches of engineering. Many practical problems in engineering are either extremely difficult or impossible to solve by conventional analytical methods. The FEM is one class of numerical methods used today by many engineers to solve complicated problems. FEM is a numerical approach by which general equations can be solved in an approximate manner.

In the finite element approach, the problem domain is suitably divided into a patchwork of a finite number of subregions called elements. These elements

could be of one, two or even three-dimensions for planar waveguides, waveguides with a two-dimensional cross-section or three-dimensional guided-wave structures, respectively. For a practical optical waveguide with two-dimensional elements which are often triangular in shape and of different sizes and using many such elements, a complex waveguide cross-section can be accurately represented [Rahman *et al.*, 2005b].

The FEM are widely used for modal solutions of a wide range of optical waveguides and is able to represent any random cross-section area accurately. The flexibility and accuracy of FEM to illustrate cross-section of optical waveguides with random hole sizes makes it powerful approach to where other approach could be unsatisfactory [Rahman, *et al.*, 2004].

To accurately characterize the polarization properties of optical waveguides, a full-vectorial approach is necessary and a **H**-field based full-vectorial FEM has recently been extended to find the modal solutions of a wide range of optical waveguides [Rahman and Davies, 1984a] including PCFs [Koshihara and Saitoh, 2001]. Full-vectorial FEM is used by many authors [Montanari *et al.*; Koshihara, 2002; Obayya *et al.*, 2002b; Rahman *et al.*, 2006b] with finite cross sections [Koshihara and Saitoh, 2003c]. Saitoh *et al.* used a full-vectorial FEM with anisotropic perfectly matched layers (PML) to analyze the dispersion properties and the confinement losses in a PCF with a finite number of air holes [Saitoh *et al.*, 2003].

4.2 Historical Background

The name “finite element” was first introduced by Clough in 1960 [Clough] to describe the new technique for plane stress analysis. However, the use of piecewise continuous functions defined over a subdomain to approximate the unknown function dates back to the work of Courant (1943) [Courant], who used an assemblage of triangular elements as a way to get approximate numerical solutions. Although certain key features of the finite element can be found in the work of Courant (1943) [Courant], the formal presentation of the FEM is attributed to Turner, Clough, Martin and Topp (1956) at the Boeing

Aircraft Company [Turner *et al.*]. They used FEM to calculate the stress-strain relations for complicated aircraft structures for which no known solutions existed. With this piece of work, together with many others, an explosive development of the FEM in engineering applications began. The method was soon recognised as a general method of solution for partial differential equations, and its applicability to non-linear and dynamic structural problems was amply demonstrated. Subsequent development has been rapid, and the techniques are now extended in many other domains, such as, soil mechanics, fluid mechanics, thermodynamics, electromagnetism, biomedical engineering, etc.

4.3 The Basic Idea of the FEM

The basic idea of the FEM is that it is a numerical technique which solves the governing equations of a complicated system through a discretisation process. The governing equations can be given in differential form or be expressed in terms of variational integrals. The basic idea of the FEM is the piecewise approximation of a smooth function by means of simple polynomials, each of which is defined over a small region (element) of the domain of the function. Instead of expressing the value of the function as a whole, it is expressed in terms of the values of the functions at several points of the domain called element nodes.

The FEM can be considered as an extension to the variational methods such as the Rayleigh-Ritz and Galerkin methods or the weighted residual techniques [Zienkiewicz; Desai]. The earliest mathematical formulations for finite element models were based on variational techniques. These techniques have been applied to yield approximate solutions for variationally formulated problems in many areas in physics and engineering such as solid mechanics and fluid mechanics. The approximate solution is assumed to be a combination of given approximation functions called trial functions. The weighted residual techniques are important in the solution of differential equations and other non-structural applications. It starts with the governing

differential equation and assumes an approximate solution which in turn is substituted into the differential equation. However, these methods suffer from disadvantages which prevent them from being used in wider class of problems. The main disadvantage of the variational methods is that there is no specific way of choosing the trial functions used in the approximation and, it is difficult to construct the approximate functions for problems with arbitrary domains with changes in material properties. On the other hand, there are other difficulties suffered by the variational techniques, since the approximation is applied over the whole domain. As a result, very high degree polynomials have to be used in order to describe the unknown function accurately. This creates a more complicated problem if the domain consists of interfaces which have abrupt material changes. Also for irregular shaped boundaries, it can be really difficult to impose the boundary conditions on the complicated trial functions.

The FEM overcomes the above mentioned difficulties with two basic features which account for its superiority over other competing methods. Such as:

(i) First, a geometrically complex domain of the problem is represented as a collection of geometrically simple sub domains, called finite elements, avoiding the difficulties associated with the 'whole domain' techniques.

(ii) Second, over each finite element the approximation functions are derived using the basic idea that any continuous function can be represented by a linear combination of algebraic polynomials.

In order to implement the finite element analysis, the primary variables are replaced by a system of discretised variable over the domain of consideration. This is generally done by dividing the entire waveguide cross section into a patchwork of sub regions, called 'elements' usually triangles or quadrilaterals. The finite element mesh (discretisation) consists of elements of various shapes, such as triangles or rectangles of different sizes that are connected to each other at nodal points on the boundaries of the elements. However, the triangular elements are the basic and much preferred element when analysing electromagnetic waveguide problems, as they are easily adapted to complex shapes. Using many elements, any continuum with a complex boundary and

with an arbitrary index distribution can be approximated to such a degree that an accurate analysis can be carried out. The simplest triangular element imposes a linear interpolation between the field values of the vertices of the triangle. However the higher order polynomial interpolation functions can also be used, but the drawback is that the programming effort for those higher order elements is quite large. The unknown field functions at a nodal point are defined by a set of algebraic polynomials over each element, and the field over the guide will be determined by those nodal field values and assumed shape functions. By expressing the fields in terms of nodal values, the resulting field components can be continuous over the whole domain.

To obtain the nodal field values, the usual Rayleigh-Ritz procedure is employed for the stationary solution of the functions with respect to each of the nodal variables. This can be written in a matrix eigenvalue equation:

$$[\mathbf{A}]\{\mathbf{x}\} - \lambda[\mathbf{B}]\{\mathbf{x}\} = 0 \quad [4.1]$$

Where, $[\mathbf{A}]$ and $[\mathbf{B}]$ are real symmetric matrices, and $[\mathbf{B}]$ is also positive definite matrix. The eigenvalue λ may be k_0^2 or β^2 depending on the variational formulation and $\{\mathbf{x}\}$ is the eigenvectors representing the unknown nodal field values. It is most desirable for the resulting matrix equation to be of this canonical form, to allow for an efficient and robust solution. This equation [4.1] can be solved by one of various standard subroutines to obtain different eigenvectors and eigenvalues.

4.4 Characteristics of FEM

Several important characteristics and advantageous properties of the finite element method have contributed to its extensive use. Some of them are listed below:

- The FEM is more flexible, can represent any arbitrary cross-section more accurately. Any structure can be represented using FEM which is important for polarization issues.

- The FEM approach is a very versatile method and its strength has been the easy change of the position and size of any of the air holes, as they are required.
- In the FEM the structural and waveguide cross-section is subdivided into a finite number of elements.
- The material properties of adjacent elements need not be the same, allowing the application to bodies composed of several types of materials.
- Irregular shaped boundaries can be approximated using elements of straight edges or matched exactly using elements with curved boundaries.
- Boundary conditions such as discontinuous surface loading and mixed boundary conditions can be handled easily in a natural way.
- The size of the elements can be made smaller and consequently the mesh can be refined in regions where the unknown parameter is expected to vary rapidly.
- Various shapes, sizes, and types of elements can be used within the same region allowing the method to make optimal use of the finite elements available.
- The technique can easily lend itself to computer implementation as it involves a large number of repetitive steps.

4.5 Applications of FEM

Generality and versatility are perhaps the most outstanding features of the finite element method (FEM). The present day application of the method includes almost all physical problems that are governed by differential equations. FEM is suitable for mode analysis of optical waveguides having arbitrary refractive-index profiles and complicated waveguide structures [Okamoto].

Although this method was first developed for applications in structural mechanics, now it is widely used in many branches of science and

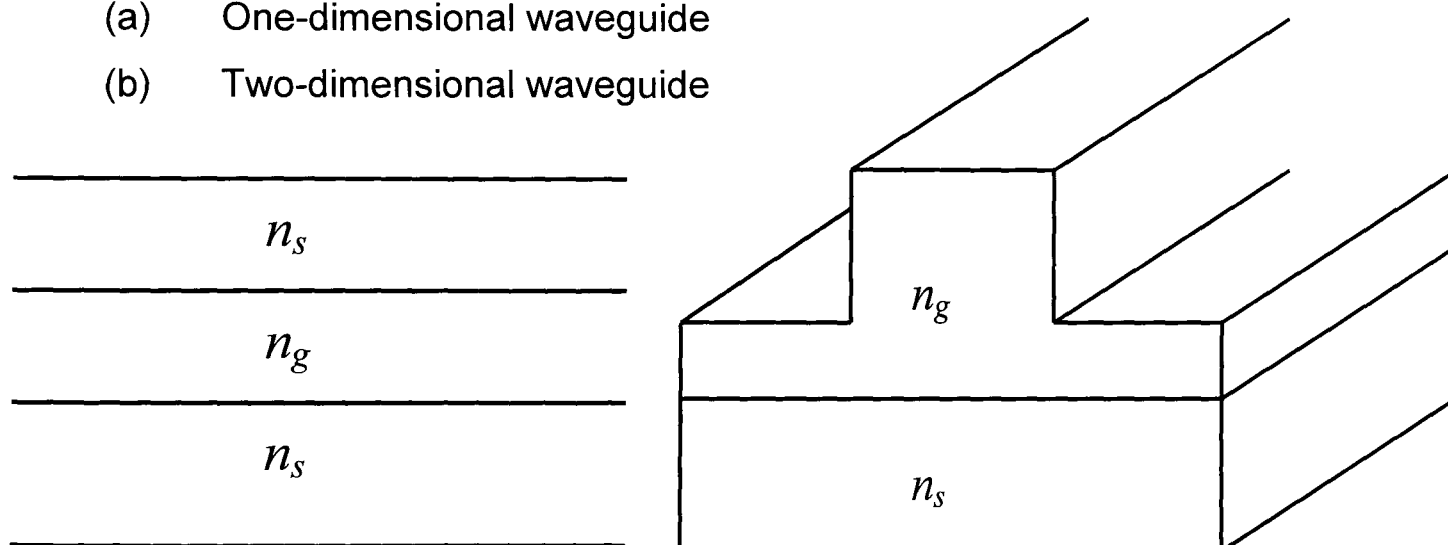
engineering. The FEM has been used to characterize accurately lightwave propagation through a wide range of practical optical waveguides, such as semiconductor ridge [Rahman, and Davies, 1985], titanium diffused LiNbO₃ [Rahman, and Davies, 1984a], and ion exchanged glass waveguides, nonlinear waveguides, MQW waveguides [Rahman, *et al.*, 1993], surface plasmon waveguides [Themistos, *et al.*], and highly-birefringent silica fibres [Liu, *et al.*, 1994]. Besides, the modal solutions of optical waveguides, over the last two decades this method has also been used to model devices based on directional couplers [Wongcharoen, *et al.*], or multimode interference couplers [Rajarajan, *et al.*, 1996.], electrooptic modulators [Rahman, *et al.*, 2002], and nonlinear optical devices [Rahman, *et al.*, 1993].

4.6 Application of FEM to Optical Waveguides

4.6.1 One and Two Dimensional Optical Waveguides

According to the cross-sectional shape of the optical waveguide, the electromagnetic waveguide problems can be classified into two groups:

- (a) One-dimensional waveguide
- (b) Two-dimensional waveguide



(a) One-dimensional planar waveguide (b) Two-dimensional waveguide

Fig. 4.1: Optical waveguide (a) one-dimensional planar waveguide (b) two-dimensional waveguide.

A planar one-dimensional waveguide or an axially symmetrical waveguide which can be treated as a one dimensional problem is shown in Fig. 4.1a. Two-dimensional waveguide is shown in Fig. 4.1b.

The eigenmode property of the waveguide is the key factor for choosing the waveguide analysis method as either scalar or vector. The scalar analysis can be employed in both one and two dimensional problems. However, for a planar structure, the scalar analysis will be sufficient, whereas, for two-dimensional problem, vector analysis is more accurate. Since, the waveguide with two-dimensional confinement supports the hybrid modes; more rigorous vector wave analysis is necessary for the precise evaluation of their polarization issues and their propagation characteristics.

4.6.2 Arbitrary Cross-sectional Shaped Optical Waveguide

Fig. 4.2 shows the arbitrary-shaped optical waveguide, composed of several different materials. These materials can be described as having arbitrary permittivity and permeability tensors ϵ and μ , respectively. These materials could be linear, nonlinear, isotropic, anisotropic, or loss less. The waveguide is assumed to be uniform along the z-axis or propagation direction. Consider light with angular frequency, ω , and propagation constant, β , propagated by such a waveguide whose structure and refractive index are constant in the direction of propagation, i.e. in the positive z direction. Assuming the time (t) and z variation are given by $\exp(j\omega t)$ and $\exp(-j\beta z)$ functions, respectively, the electric field \mathbf{E} and the magnetic field \mathbf{H} can be expressed in the form:

$$\mathbf{E}(x,y,z,t) = \mathbf{E}(x,y) \exp[j(\omega t - \beta z)] \quad [4.2]$$

$$\mathbf{H}(x,y,z,t) = \mathbf{H}(x,y) \exp[j(\omega t - \beta z)] \quad [4.3]$$

The spatial variations of the electric and magnetic fields are $\mathbf{E}(x,y)$ and $\mathbf{H}(x,y)$, respectively.

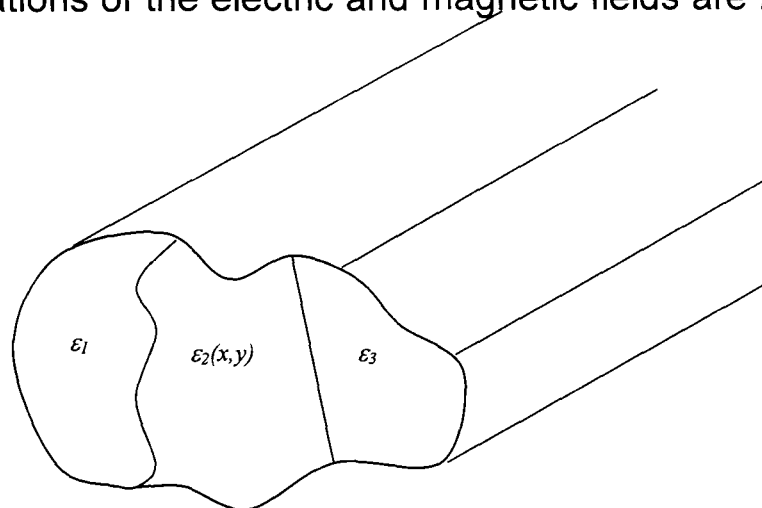


Fig. 4.2: Optical waveguide with arbitrary-shaped, with different materials.

4.7 Fundamental Electromagnetic Field Equations

The fundamental electromagnetic field equations, such as Maxwell's equations and the boundary conditions, which govern the optical waveguide phenomenon are discussed in this section. The consideration of above mentioned equations is needed to make use of the finite element method in the optical waveguide analysis problems.

4.7.1 Maxwell's Equations

Light propagation through an optical waveguide is an electromagnetic wave phenomenon which can be expressed by the Maxwell's equations. Its magnetic field is represented by four electromagnetic field vectors. These equations form a basic set of equations of the electromagnetic field theory. The equations can be written in both differential and integral forms. The differential forms of the equations are the most suitable form to be used by the finite element method. Therefore, in this thesis equations are presented only in differential form.

The differential form of Maxwell's equations in general time-varying electromagnetic fields can be expressed as:

$$\text{Ampere's law} \quad \nabla \times \mathbf{H} = \frac{\partial \mathbf{D}}{\partial t} + \mathbf{J} \quad [4.4]$$

$$\text{Faraday's law} \quad \nabla \times \mathbf{E} = -\frac{\partial \mathbf{B}}{\partial t} \quad [4.5]$$

$$\text{Gauss's law} \quad \nabla \cdot \mathbf{D} = \rho \quad [4.6]$$

$$\text{Gauss's law for magnetics} \quad \nabla \cdot \mathbf{B} = 0 \quad [4.7]$$

Where, \mathbf{H} = Magnetic field intensity (amperes/meter)

\mathbf{E} = Electric field intensity (volts/meter)

\mathbf{D} = Electric flux density (coulombs/meter²)

\mathbf{B} = Magnetic flux density (webers/meter²)

\mathbf{J} = Electric current density (amperes/meter²)

ρ = Electric charge density (coulombs/meter³)

The conservation of charge equation or the current continuity equation (holds for \mathbf{J} and the charge density, ρ) can be exposed as:

$$\nabla \cdot \mathbf{J} = \frac{-\partial \rho}{\partial t} \quad [4.8]$$

The associated constitutive relations for the medium can be exposed as:

$$\mathbf{D} = \varepsilon \mathbf{E} \quad [4.9]$$

$$\mathbf{B} = \mu \mathbf{H} \quad [4.10]$$

Where, ε = The permittivity of the medium

μ = The permeability of the medium.

For convenience lets assume the time dependence to be $\exp(j\omega t)$.

Where, j = The imaginary unit,

ω = The radian (angular) frequency, and

t = The time.

Then with this assumption, all the time derivatives may be replaced by $j\omega$ and the factor $\exp(j\omega t)$ will not be included as this factor always occurs as a common factor in all terms. Hence the differential form of Maxwell's equations becomes:

$$\nabla \times \mathbf{H} = j\omega \mathbf{D} + \mathbf{J} \quad [4.11]$$

$$\nabla \times \mathbf{E} = -j\omega \mathbf{B} \quad [4.12]$$

$$\nabla \cdot \mathbf{D} = \rho \quad [4.13]$$

$$\nabla \cdot \mathbf{B} = 0 \quad [4.14]$$

Therefore the continuity equation can be exposed as:

$$\nabla \cdot \mathbf{J} = -j\omega \rho \quad [4.15]$$

4.7.2 Boundary Conditions

Boundary conditions are the certain conditions that must be performed at the boundary between two media with different material parameters. It is necessary to focus the Maxwell's equations, as exposed above, to boundary conditions at surfaces where the refractive indices change abruptly. Fig. 4.3 shows a sketch of such a boundary between two media distinguished by the

indices 1 and 2, with the unit normal vector \mathbf{n} directed from medium 1 to medium 2.

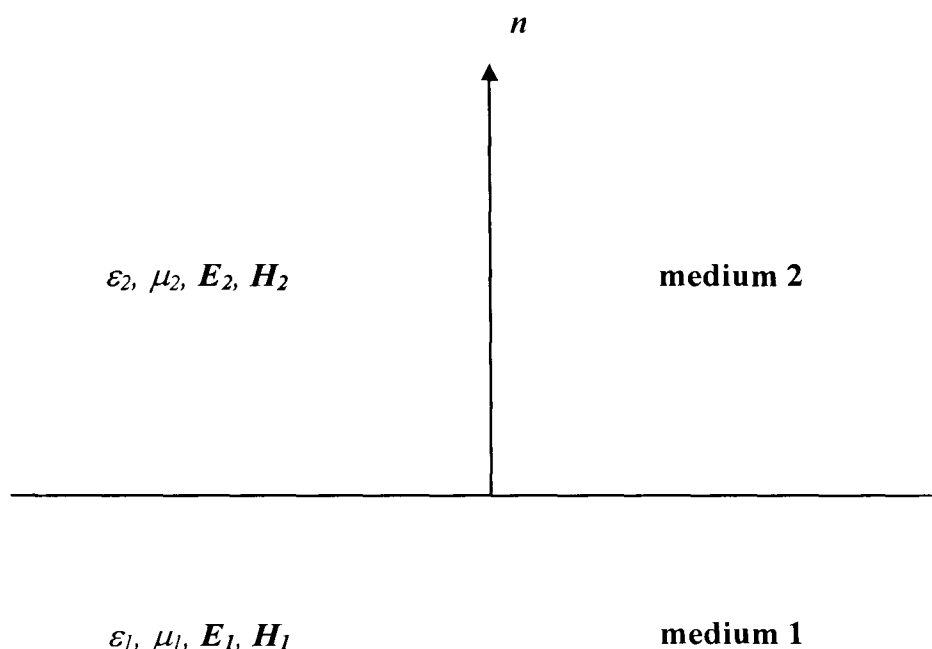


Fig. 4.3: Sketch of a boundary between two media.

In the absence of surface charges ($\rho = 0$) and surface currents ($\mathbf{J} = 0$), the boundary conditions are given as below:

- i) The tangential components of the electric field must be continuous.

$$\mathbf{n} \times (\mathbf{E}_1 - \mathbf{E}_2) = 0 \quad [4.16]$$

$$\therefore \mathbf{E}_{t1} = \mathbf{E}_{t2}$$

- ii) The tangential components of the magnetic field must be continuous.

$$\mathbf{n} \times (\mathbf{H}_1 - \mathbf{H}_2) = 0 \quad [4.17]$$

$$\therefore \mathbf{H}_{t1} = \mathbf{H}_{t2}$$

- iii) The normal components of the electric flux density must be continuous.

$$\mathbf{n} \cdot (\mathbf{D}_1 - \mathbf{D}_2) = 0 \quad [4.18a]$$

$$\therefore \mathbf{D}_{n1} = \mathbf{D}_{n2}$$

$$\therefore \varepsilon_1 \mathbf{E}_{n1} = \varepsilon_2 \mathbf{E}_{n2} \Rightarrow \therefore \mathbf{E}_{n1} \neq \mathbf{E}_{n2} \quad [4.18b]$$

- iv) The normal components of the magnetic flux density must be continuous.

$$\mathbf{n} \cdot (\mathbf{B}_1 - \mathbf{B}_2) = 0 \quad [4.19a]$$

$$\therefore \mathbf{B}_{n1} = \mathbf{B}_{n2}$$

$$\therefore \mu_1 \mathbf{H}_{n1} = \mu_2 \mathbf{H}_{n2}$$

When, μ_1 and μ_2 are the relative permeabilities in medium 1 and 2, respectively for most of the optical waveguides, $\mu_1 = \mu_2 = 1$.

$$\therefore \mathbf{H}_{n1} = \mathbf{H}_{n2} \quad [4.19b]$$

It implies equality of the magnetic field vectors at the boundary.

There is another boundary condition, which is often used in the idealised case of a perfect electric conductor. This can be considered as an 'electric wall' boundary condition:

$$\mathbf{n} \times \mathbf{E} = 0 \quad \text{or} \quad \mathbf{n} \cdot \mathbf{H} = 0 \quad [4.20]$$

This boundary condition requires that the magnetic field vector, \mathbf{H} , must vanish, and ensures the continuity of the electric field vector, \mathbf{E} , at the boundary.

When one of the two media becomes a perfect magnetic conductor, a 'magnetic wall' condition is imposed as:

$$\mathbf{n} \times \mathbf{H} = 0 \quad \text{or} \quad \mathbf{n} \cdot \mathbf{E} = 0 \quad [4.21]$$

This condition will ensure the continuity of the magnetic field component, \mathbf{H} , at the boundary and it vanishes the electric field vector, \mathbf{E} .

4.8 Finite Element Formulations

Variational [Harrington] and weighted residual approaches are the two major factors for formulating the finite element. Variational formulation has been widely used to a large variety of electromagnetic field problems, in particular to the problem of wave propagation along the arbitrary shaped waveguides with anisotropic material. Despite the fact that the weighted residual approach is more straightforward, the variational approach is more advantageous. In

variational approach, only one global parameter such as the propagation constant is needed. Moreover, most of the solutions for a wide variety of electromagnetic field problems reported in the literature have been based on the variational approach. Therefore, in this thesis only variational formulation will be discussed.

4.8.1 Types of Variational Formulation

There are mainly two types of variational formulations, which can be utilised in finite element method, such as:

- (a) Scalar formulation [Koshiha *et al.*, 1982], and
- (b) Vector formulations [Morishita and Kumagai; Rahman and Davies, 1984*b*; Koshiha *et al.*, 1985*a*].

Depending on the waveguide structure, however, there are quite a few cases in which practically acceptable solutions are obtained through the H_{mm}^y mode approximation and the H_{mm}^x mode approximation. On the basis of these observations, the scalar FEM has been developed for the analysis of two or three-dimensional optical waveguides. With this method, the number of matrix elements to be solved is reduced to 1/3 compared to the vector finite-element method [Koshiha, 1992]. For vector wave FEM analyses, complicated mathematical procedures and programming techniques are required. In contrast, spurious solutions do not appear in scalar wave FEM analyses for two or three-dimensional waveguides. Since the matrix size for scalar wave analysis is one-third smaller than that for vectorial wave analysis, required memory and CPU (central processing unit) time very small. By comparing vector and scalar wave FEM analyses, it is confirmed that a sufficiently accurate solution can be obtained via scalar wave analysis [Okamoto].

4.8.2 Characteristics of the Scalar Finite Element Method

Scalar finite element method has been applied to problems of electromagnetic wave propagation in homogenous, isotropic media, where a single potential or only one field component has been considered. It is the simplest form of the differential variational formulations. In this method, its validity becomes

apparent only in situations where the modes can be described predominantly as TE and TM modes. Koshiya *et al.* [Koshiya *et al.*, 1982] described an approximate scalar finite-element program for the analysis of anisotropic waveguides. According to Mabaya *et al.*, [Mabaya *et al.*] the scalar approximation for the TE modes is based on the following functional:

$$J(\phi) = \iint_{\Omega} \left[\left(\frac{\partial \phi}{\partial x} \right)^2 + \left(\frac{\partial \phi}{\partial y} \right)^2 + (\beta^2 - k_0^2 n^2) \phi^2 \right] dx dy \quad [4.22]$$

Where β , n , and k_0 are propagation constant, refractive index profile, and free-space wavenumber, respectively.

Here, Ω represents the cross sectional domain over which the integration is carried out. A finite element program based on the above mentioned functional yields β^2 as the eigenvalue of the matrix equation for a given k_0 . The eigenvector, $\phi(x,y)$ is the transverse field distribution, i.e. E_x component for the TE modes.

The scalar approximation for the TM modes is based on the following functional:

$$J(\psi) = \iint_{\Omega} \frac{1}{n^2} \left[\left(\frac{\partial \psi}{\partial x} \right)^2 + \left(\frac{\partial \psi}{\partial y} \right)^2 + (\beta^2 - k_0^2 n^2) \psi^2 \right] dx dy \quad [4.23]$$

$\psi(x,y)$ is the transverse field distribution, i.e. H_x field component for the quasi-TM modes. A finite element program based on this functional yields k_0^2 as the eigenvalue of the matrix equation for a given propagation constant, β .

4.8.3 Characteristics of the Vector Finite Element Method

Since the guided mode of the two or three-dimensional optical waveguide is a hybrid mode, only vector wave analysis is required so that precise and rigorous evaluation of their propagation characteristics and the dispersion characteristics can be examined. Therefore, in this thesis only vectorial formulation will be discussed in detail. In this case, the scalar formulation is inappropriate to solve and handle hybrid modes of anisotropic or inhomogeneous optical waveguide problems, vector wave analysis is

important for an accurate evaluation of the propagation characteristics. Important advantage of vector finite element method is that it offers a better solution convergence for some modal types as compared to corresponding scalar formulations. One disadvantage of any vector finite element method is the appearance of the spurious solutions or non-physical solutions, which appear mixed with the correct solutions.

4.8.3.1 Types of Vector Finite Element Method

There are many types of finite element methods for such vector wave analyses, depending on which electromagnetic (\mathbf{E} and \mathbf{H}) field components (E_z and H_z) is used for formulation. Such as:

- (1) FEM using longitudinal or axial electromagnetic field components (E_z and H_z),
- (2) FEM using the three magnetic field components (\mathbf{H}),
- (3) FEM using the three electric field components (\mathbf{E}),
- (4) FEM using the six electromagnetic field components (\mathbf{E} and \mathbf{H}),
- (5) FEM using transverse electromagnetic field components (\mathbf{E}_t and \mathbf{H}_t),
- (6) FEM using transverse electric field components (\mathbf{E}_t),
- (7) FEM using transverse magnetic field components (\mathbf{H}_t),
- (8) FEM using transverse electric field components and longitudinal magnetic field components (\mathbf{E}_t and H_z), and
- (9) FEM using transverse magnetic field components and longitudinal electric field components (\mathbf{H}_t and E_z) [Okamoto; Koshiba, 1992].

4.8.3.2 Comparison among Vector Finite Element Methods

The validity, appropriateness, and effectiveness of each of these methods have been verified and confirmed. Methods 1 (FEM using longitudinal or axial electromagnetic field components) and 2 (FEM using the three magnetic field components), in particular, are widely used for analysis and design of three-dimensional optical waveguides of almost any structure [Koshiba, 1992].

Finite element method using longitudinal electromagnetic field components is based on the axial field components (E_z and H_z), which are the least important of the \mathbf{E} and \mathbf{H} fields. The E_z and H_z formulation is one of the first formulations

used in finite element analysis [Yeh *et al.*, 1975; 1979; Mabaya *et al.*; Csendes and Silvester] and is used to solve many different types of guiding structures problems [Ahmed and Daly, 1969; Ikeuchi *et al.*, 1981; Wu and Chen, 1985]. The E_z and H_z formulation cannot treat general anisotropic problems without destroying the canonical form of the eigenvalue equation [4.1], and also some problems arise in enforcing boundary conditions for a waveguide with an arbitrary dielectric distribution.

The finite element method using transverse electric field components (\mathbf{E}_t) and magnetic field components (\mathbf{H}_t) is computationally costly as this involves additional differentiation [Ohtaka *et al.*], which in turn would be particularly disadvantageous with finite element approach.

A vector \mathbf{E} -field formulation, applied by English and Young [English and Young], is valid for general anisotropic loss-less waveguide problems and has also been applied for the solution of various types of optical waveguides [Koshiba *et al.*, 1986; Hano]. One of the limits of the \mathbf{E} -field formulation is that it needs special consideration to enforce the continuity of the tangential field components at the dielectric interface. For such a formulation, the natural boundary conditions correspond to a magnetic wall, and therefore it is essential to enforce the electric wall ($\mathbf{n} \times \mathbf{E} = 0$) as a boundary condition which is difficult to implement for irregular shaped structures.

This vector \mathbf{H} -field formulation [Koshiba *et al.*, 1985b; Rahman and Davies, 1984b; 1984c] is valid for general anisotropic problems with a non-diagonal permittivity tensor. It has the advantage over all other formulations. It is more suitable for dielectric waveguide problems, because the magnetic field is continuous everywhere, and the natural boundary conditions correspond to those of the electric wall ($\mathbf{n} \times \mathbf{E} = 0$, $\mathbf{n} \cdot \mathbf{H} = 0$), therefore no forced boundary conditions at the boundaries are required.

The total vector $\mathbf{E}+\mathbf{H}$ formulation [Svedin] does not have much advantage over the vector \mathbf{H} -field formulation since all the six components are needed for the formulation giving rise to a complicated problem.

4.8.4 The Vector H-field Formulation

The vector **H**-field formulation appears to be the most accurate and versatile method [Rahman and Davies, 1984*b*] in the case for general optical waveguide problems, where the modes are hybrid, the transverse components are the dominant and the materials have general anisotropy. The full-vector **H**-field formulation can be written as [Rahman and Davies, 1984*a*; Berk, 1956]:

$$\omega^2 = \frac{\int (\nabla \times \mathbf{H})^* \cdot \hat{\varepsilon}^{-1} \cdot (\nabla \times \mathbf{H}) d\Omega}{\int \mathbf{H}^* \cdot \hat{\mu} \cdot \mathbf{H} d\Omega} \quad [4.24]$$

Where, $\hat{\varepsilon}$ = general anisotropic permittivity of the loss-free medium,

$\hat{\mu}$ = general anisotropic permeability of the loss-free medium, and

Ω = waveguide cross section.

For an abrupt discontinuity in the permittivity in an inhomogeneous medium there is an abrupt change in the electric field, **E**. In such cases, it is advantageous to solve for the values of **H** at the nodal points. This formulation is also very important and useful when analysing various active and passive integrated optic structures.

The **E**-field as well as the **H**-field formulation, yields spurious solutions, because the divergence condition [$\text{div } \mathbf{H} = 0$] is not satisfied. Various ways of suppressing or eliminating spurious solutions have been discovered for this method. Penalty coefficient method [Rahman and Davies 1984*c*; Koshiba *et al.*, 1985*b*] have been proposed to eliminate these non-physical solutions, which will be discussed in later section.

For the solution of optical waveguide problems [Silveira and Gopinath; Lu and Fernandez 1993*a*; Hayata *et al.*, 1986*b*], most recently a variational formulation in terms of the **E**-field or **H**-field components has been proposed. In this approach, the minimum number of field components (two) is used, and the divergence condition is satisfied. It can handle accurately lossy structures [Cheung *et al.*; Lu and Fernandez 1993*b*], but it can lead to large sparse,

complex, non-symmetric matrices in the eigenvalue equation, which increase computation time, therefore effort has been made to develop efficient sparse matrix solvers [Fernandez *et al.*] in order to solve such problems.

4.8.5 Natural and Forced Boundary Conditions

The boundary condition, which is automatically satisfied in the variational procedure, is called the 'natural boundary condition'. In the case of natural boundary condition, the field decays at the boundary, therefore they can be left free. The scalar functional defined in equation [4.22] has the continuity of

$m \left[\frac{\partial \phi}{\partial n} \right]$ where $m=1$, as the natural boundary condition, and the functional

[4.23] has the continuity $m \left[\frac{\partial \phi}{\partial n} \right]$ where $m = 1/n^2$, as the natural boundary

condition, and \mathbf{n} is the outward normal unit vector. The vector \mathbf{H} -field formulation described in equation [4.24], has the electric wall as the natural boundary condition expressed as $\mathbf{n} \cdot \mathbf{H} = 0$. Therefore there is no need to force any boundary condition on conducting guide walls.

In some other cases, specially for regular shaped waveguides, and at the symmetric walls, the natural boundary condition needs to be forced to reduce the matrix problem size. However, it may be necessary to analyse the structure with complementary symmetry conditions to obtain all the modes, although the exploitation of the symmetry greatly reduces the computational cost.

4.9 Finite Element Method Formulation

To find the solution of a complicated problem by replacing it by a simpler one is the basic idea of the finite element method formulation.

4.9.1 Finite Element Discretisation

The first step in the finite element method is the discretisation of the domain into sub-regions, called elements. There are various types of elements such as one, two and three dimensional elements available for use in finite element

formulations. When the geometry and material properties can be described in terms of only one spatial coordinate, then the one-dimensional element can be used. However, when the configuration and other details of the problem can be described in terms of two independent spatial coordinates, the two-dimensional elements, as shown in Fig. 4.4, can be used.

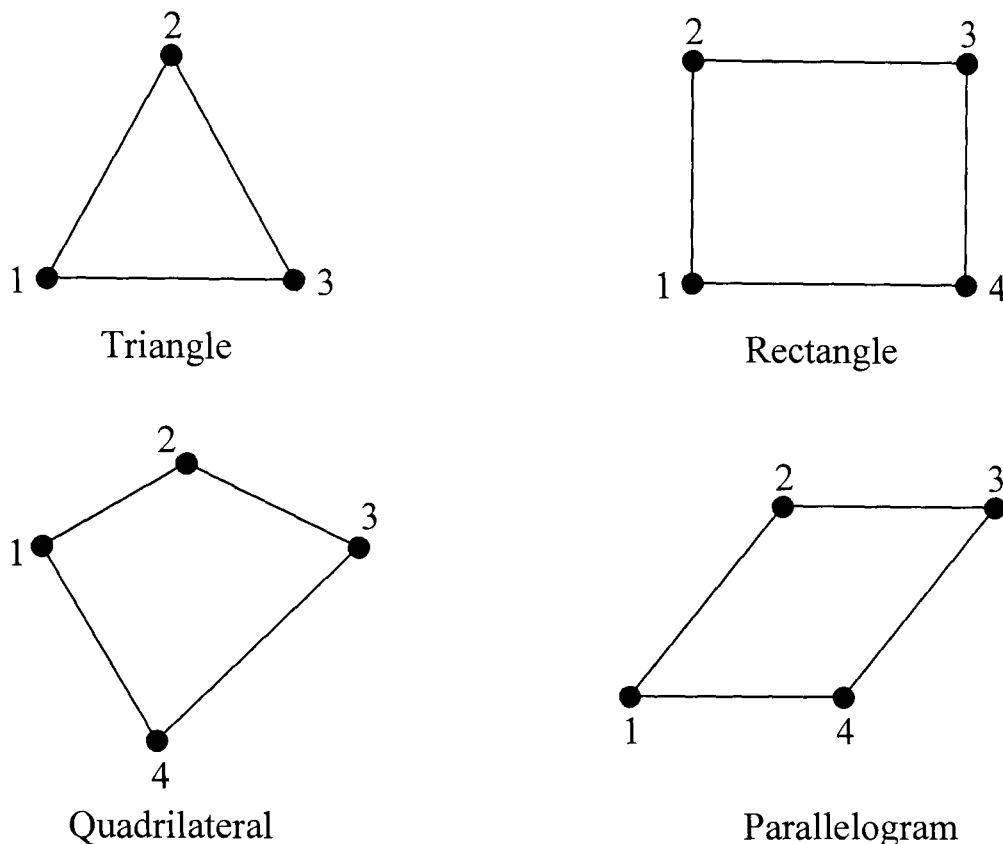


Fig. 4.4: Two dimensional finite elements.

Each element is essentially a simple unit within which the unknown can be described in a simple manner. The basic and the simplest element useful for two-dimensional analysis is the triangular element. The smaller the size of the element, the more accurate is the final solution.

Finite element discretisation of an irregular waveguide, using triangular elements is shown in Fig. 4.5. The shapes, sizes, number and configurations of the elements have to be chosen carefully such that the original body or domain is simulated as closely as possible without increasing the computational effort needed for the solution.

By dividing the waveguide cross section into triangular elements, the unknown H is also considered as to be discretised into corresponding sub-regions.

These elements are easier to analyse rather than analysing the distribution over the whole cross section.

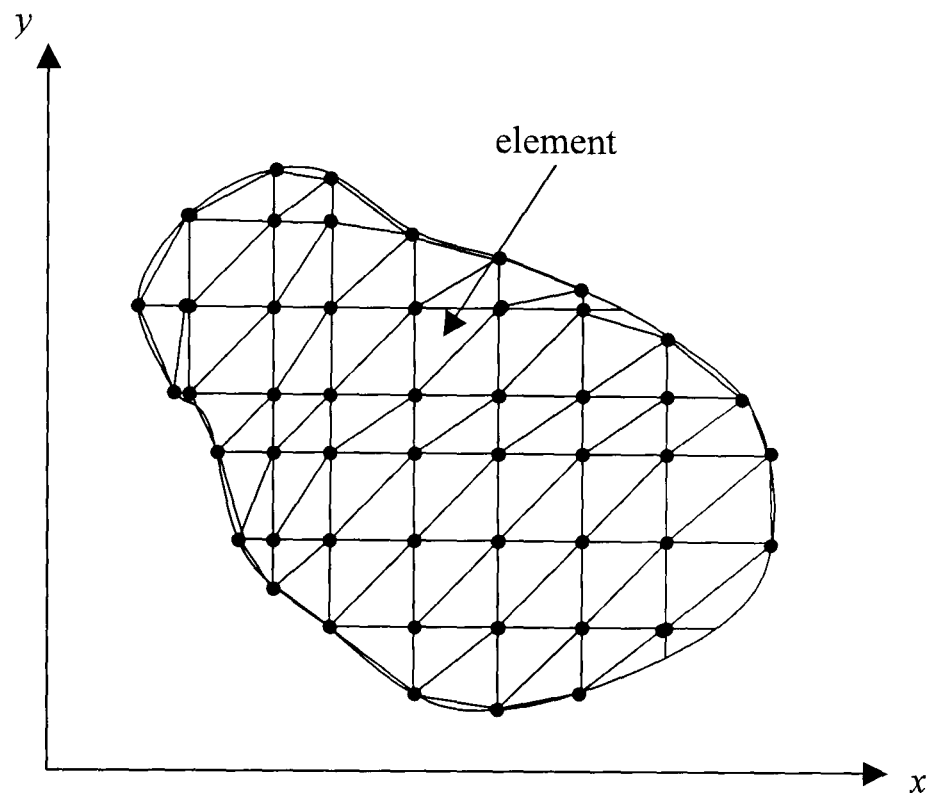


Fig. 4.5: Waveguide cross-section is subdivided into a finite number of triangular elements showing its nodes.

As shown in Fig. 4.5, the transverse plane is covered with a grid of discrete nodes which are the vertices of each triangular element. The values of H at these nodal points are the basic unknowns. The intersections of the sides of the triangular elements are called the nodal lines.

4.9.2 Shape Functions

The shape functions are a set of interpolation functions, defined in terms of complete polynomials and which are normalized over each element. For a typical element, the shape function is chosen so that it uniquely defines the field within the element under consideration.

In two-dimensional problems, the element assumes a linear interpolation between the field values at the vertices of the triangle. Within each element the unknown field H , is approximated by means of suitably chosen set of polynomials. These functions are called “shape functions”. For the simplest triangular element the interpolation polynomial should include terms

containing both x and y . In order to achieve the 'geometric isotropy', the polynomial should complete according to the Pascal's triangle, as shown in Fig. 4.6.

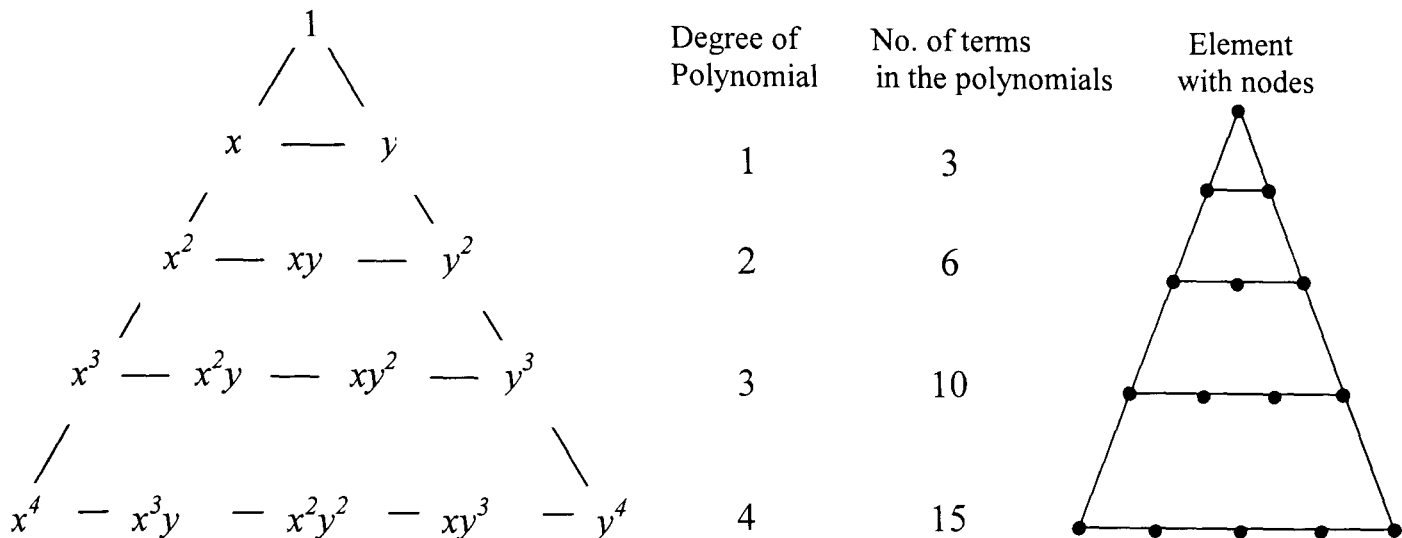


Fig. 4.6: Pascal's triangle for complete polynomials in two dimensions.

The final consideration in selecting the order of the interpolation polynomial is to make the total number of terms involved in the polynomial equal to the number of nodal degrees of freedom of the element. For example, the first degree polynomial involves three coefficients and so can be expressed in terms of three nodal values at the triangle vertices. The second degree polynomial needs six coefficients and can similarly be expressed in terms of values of six nodes as shown in Fig. 4.6.

The continuous field function $\phi(x,y)$ in the problem domain may be replaced by a set of discrete values $(\phi_i, i = 1,2,3,\dots,m)$, where m is the total number of nodes. This function will be continuous across the adjacent triangles.

A typical first order triangular element is shown in Fig. 4.7. Inside each first order triangular element ϕ is interpolated continuously. This can be achieved by introducing the interpolation functions, $N_i(x,y)$. Let $\phi_e(x,y)$ is the field inside an element. Using these interpolation functions, for $i = 3$, it can be written as:

$$\phi_e(x,y) = \sum_{i=1}^3 N_i(x,y) \cdot \phi_i \quad [4.25]$$

Where, ϕ_i are the nodal field values.

As eq. [4.25] describes the shape of an element, and therefore, the $N_i(x,y)$ are called 'shape functions'. Eq. [4.25] can also be written in matrix form:

$$\phi_e(x,y) = [N_1 \quad N_2 \quad N_3] \begin{Bmatrix} \phi_1 \\ \phi_2 \\ \phi_3 \end{Bmatrix} \quad [4.26]$$

$$\phi_e(x,y) = [N] \{\phi_e\} \quad [4.27]$$

Where, $[N]$ is the shape function matrix and the column vector $\{\phi_e\}$ is the vector corresponding to the field values at the 3 vertices of the triangular element (i.e. the nodal field values).

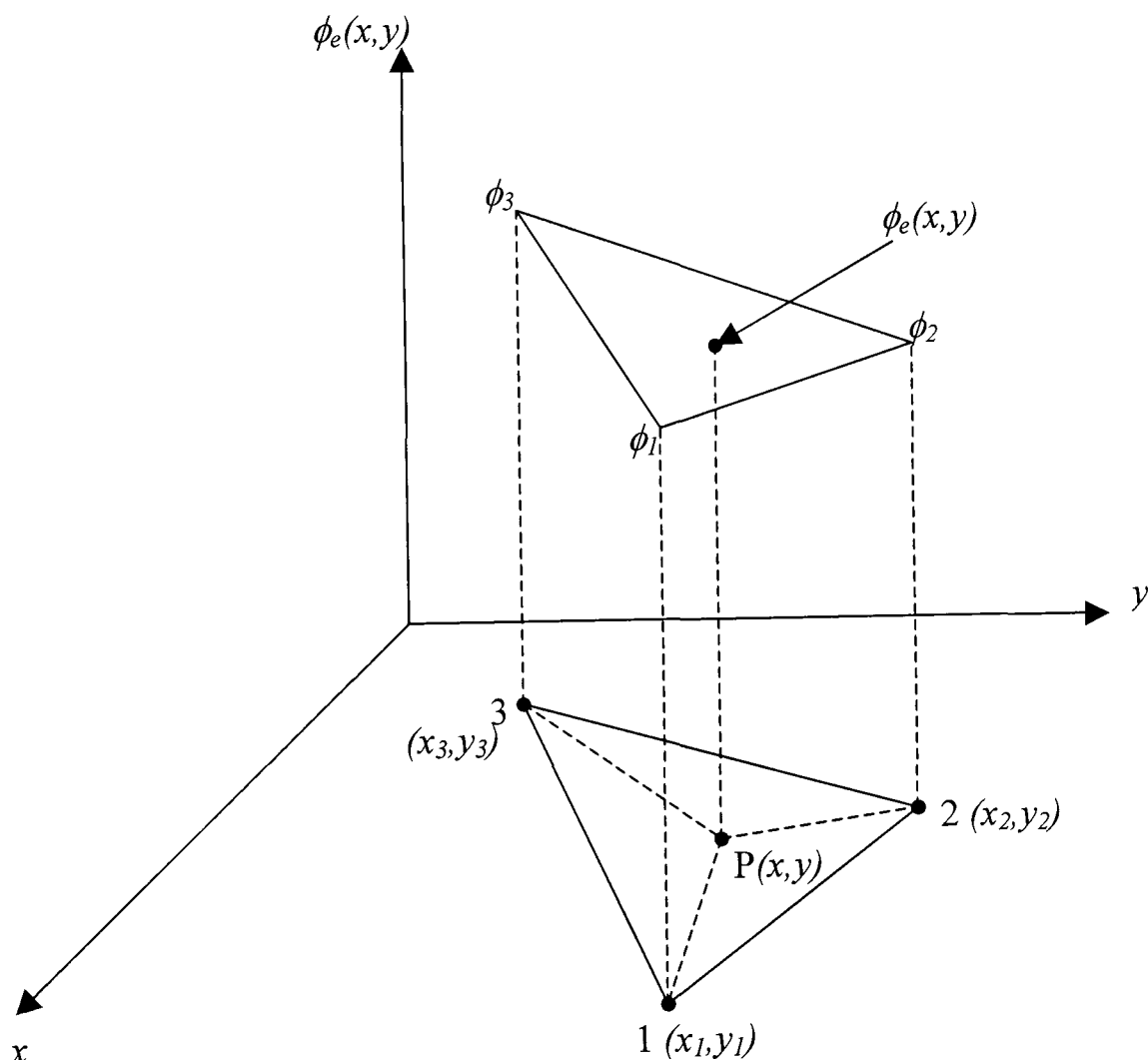


Fig. 4.7: Coordinates and node numbers of first order triangular element.

In order to obtain the shape functions, $N_i(x,y)$, $i = 1,2,3$, first a linear approximation of the field inside an element is considered:

$$\phi_e(x,y) = \alpha_1 + \alpha_2 x + \alpha_3 y \quad [4.28]$$

Where, $\alpha_1, \alpha_2, \alpha_3$ are constants.

By rewriting the approximation [4.28], such that it satisfies the conditions:

$$\phi_e(x_i, y_i) = \phi_i \quad i = 1, 2, 3 \quad [4.29]$$

Where, (x_i, y_i) ($i = 1, 2, 3$) are the (global) coordinates of the three vertices of the triangle.

Then, the nodal field values ϕ_i can be expressed as:

$$\begin{aligned} \phi_1 &\equiv \phi_e(x_1, y_1) = \alpha_1 + \alpha_2 x_1 + \alpha_3 y_1 \\ \phi_2 &\equiv \phi_e(x_2, y_2) = \alpha_1 + \alpha_2 x_2 + \alpha_3 y_2 \\ \phi_3 &\equiv \phi_e(x_3, y_3) = \alpha_1 + \alpha_2 x_3 + \alpha_3 y_3 \end{aligned} \quad [4.30]$$

In matrix form:

$$\begin{Bmatrix} \phi_1 \\ \phi_2 \\ \phi_3 \end{Bmatrix} = \begin{bmatrix} 1 & x_1 & y_1 \\ 1 & x_2 & y_2 \\ 1 & x_3 & y_3 \end{bmatrix} \begin{Bmatrix} \alpha_1 \\ \alpha_2 \\ \alpha_3 \end{Bmatrix} \quad [4.31]$$

By solving the above matrix, the constants $\alpha_1, \alpha_2, \alpha_3$ can be determined in terms of $\phi_i, i = 1, 2, 3$:

$$\begin{aligned} \alpha_1 &= \frac{1}{2A_e} [\phi_1(x_2 y_3 - x_3 y_2) + \phi_2(x_3 y_1 - x_1 y_3) + \phi_3(x_1 y_2 - x_2 y_1)] \\ \alpha_2 &= \frac{1}{2A_e} [\phi_1(y_2 - y_3) + \phi_2(y_3 - y_1) + \phi_3(y_1 - y_2)] \\ \alpha_3 &= \frac{1}{2A_e} [\phi_1(x_3 - x_2) + \phi_2(x_1 - x_3) + \phi_3(x_2 - x_1)] \end{aligned} \quad [4.32]$$

Where, A_e is the area of the triangular element given by,

$$A_e = \frac{1}{2} \begin{vmatrix} 1 & x_1 & y_1 \\ 1 & x_2 & y_2 \\ 1 & x_3 & y_3 \end{vmatrix} = \frac{1}{2} (x_2 y_3 - x_3 y_2) + (x_3 y_1 - x_1 y_3) + (x_1 y_2 - x_2 y_1) \quad [4.33]$$

Substituting for α_i from eq. [4.32] into eq. [4.28] and rearranging yields the following equation:

$$\phi_e(x, y) = N_1(x, y) \cdot \phi_1 + N_2(x, y) \cdot \phi_2 + N_3(x, y) \cdot \phi_3$$

or

$$\phi_e(x, y) = [N] \{\phi_e\} \quad [4.34]$$

Which is exactly the same matrix equation given by eq. [4.27], and $N_i(x, y)$, $i = 1, 2, 3$, are shape functions given by the matrix notation [Reddy; Davies, 1989]:

$$\{N\}^T = \begin{bmatrix} N_1 \\ N_2 \\ N_3 \end{bmatrix} = \frac{1}{2A_e} \begin{bmatrix} x_2y_3 - x_3y_2 & y_2 - y_3 & x_3 - x_2 \\ x_3y_1 - x_1y_3 & y_3 - y_1 & x_1 - x_3 \\ x_1y_2 - x_2y_1 & y_1 - y_2 & x_2 - x_1 \end{bmatrix} \begin{bmatrix} 1 \\ x \\ y \end{bmatrix} \quad [4.35]$$

Where, T denotes the transpose. This shape function matrix can also be written as:

$$\{N\}^T = \begin{bmatrix} N_1 \\ N_2 \\ N_3 \end{bmatrix} = \begin{bmatrix} a_1 + b_1x + c_1y \\ a_2 + b_2x + c_2y \\ a_3 + b_3x + c_3y \end{bmatrix} \quad [4.36]$$

and a_i, b_i, c_i ($i = 1, 2, 3$) are the constants calculated as:

$$a_1 = \frac{x_2y_3 - x_3y_2}{2A_e} \quad [4.37]$$

$$b_1 = \frac{y_2 - y_3}{2A_e} \quad [4.38]$$

$$c_1 = \frac{x_3 - x_2}{2A_e} \quad [4.39]$$

Similarly, a_2, b_2, c_2, a_3, b_3 , and c_3 can be calculated by cyclic exchange of $1 \rightarrow 2 \rightarrow 3$ in equations [4.37] to [4.39].

Consider a typical point $P(x, y)$ inside the triangular element as shown in Fig. 4.7. By carefully considering the eq. [4.35], the shape functions N_i can also be denoted by using the areas of the triangles as below:

$$N_1 = \frac{\text{area of the sub triangle P23}}{\text{area of the full triangle 123}} \quad [4.40]$$

Similarly N_2 and N_3 can be defined, and immediately it follows that N_i has the following property:

$$\sum_{i=1}^3 N_i = 1 \quad [4.41]$$

4.9.3 Assembly of Element and Global Matrices

The next stage in the finite element method is the assembly of the element matrices $[A]_e$ and $[B]_e$ into global matrices $[A]$ and $[B]$, respectively. An appropriate matrix solver is used to obtain the eigenvalues and eigenvectors of the equation. This section explains the derivation of the element and global matrices based on the full-vectorial \mathbf{H} -field variational expression eq. [4.24]. Within each triangular element, the three unknown \mathbf{H} -field components, H_x , H_y and H_z of the magnetic field can be written as:

$$H_x(x, y) = [N_1 \quad N_2 \quad N_3] \begin{Bmatrix} H_{x1} \\ H_{x2} \\ H_{x3} \end{Bmatrix} \quad [4.42a]$$

$$H_y(x, y) = [N_1 \quad N_2 \quad N_3] \begin{Bmatrix} H_{y1} \\ H_{y2} \\ H_{y3} \end{Bmatrix} \quad [4.42b]$$

$$H_z(x, y) = [N_1 \quad N_2 \quad N_3] \begin{Bmatrix} H_{z1} \\ H_{z2} \\ H_{z3} \end{Bmatrix} \quad [4.42c]$$

where, H_{xi} , H_{yi} and H_{zi} ; $i = 1, 2, 3$, represents the x , y and z components of the nodal magnetic fields. Hence, the element magnetic field vector $[\mathbf{H}]_e$ can be expressed by combining equations [4.42a]-[4.42c]:

$$[\mathbf{H}]_e = \begin{bmatrix} H_x(x, y) \\ H_y(x, y) \\ H_z(x, y) \end{bmatrix} = \begin{bmatrix} N_1 & N_2 & N_3 & 0 & 0 & 0 & 0 & 0 & 0 \\ 0 & 0 & 0 & N_1 & N_2 & N_3 & 0 & 0 & 0 \\ 0 & 0 & 0 & 0 & 0 & 0 & N_1 & N_2 & N_3 \end{bmatrix} \begin{Bmatrix} H_{x1} \\ H_{x2} \\ H_{x3} \\ H_{y1} \\ H_{y2} \\ H_{y3} \\ H_{z1} \\ H_{z2} \\ H_{z3} \end{Bmatrix} \quad [4.43]$$

Equation [4.43] can also be written as:

$$[\mathbf{H}]_e = [\mathbf{N}] \{\mathbf{H}\}_e \quad [4.44]$$

Where, $\{\mathbf{H}\}_e$ is the column vector representing the three components of the nodal field values in the element and $[\mathbf{N}]$ is the shape function matrix.

Also by substituting [4.44], the $(\nabla \times \mathbf{H})_e$ factor within the element can be written as:

$$(\nabla \times \mathbf{H})_e = \nabla \times [\mathbf{N}]\{\mathbf{H}\}_e = \begin{bmatrix} 0 & -\frac{\partial}{\partial z} & \frac{\partial}{\partial y} \\ \frac{\partial}{\partial z} & 0 & -\frac{\partial}{\partial x} \\ -\frac{\partial}{\partial y} & \frac{\partial}{\partial x} & 0 \end{bmatrix} [\mathbf{N}]\{\mathbf{H}\}_e = [\mathbf{Q}]\{\mathbf{H}\}_e \quad [4.45]$$

Where, the matrix $[\mathbf{Q}]$ can be written as:

$$[\mathbf{Q}] = \begin{bmatrix} [0] & -\frac{\partial[\mathbf{N}]}{\partial z} & \frac{\partial[\mathbf{N}]}{\partial y} \\ \frac{\partial[\mathbf{N}]}{\partial z} & [0] & -\frac{\partial[\mathbf{N}]}{\partial x} \\ -\frac{\partial[\mathbf{N}]}{\partial y} & \frac{\partial[\mathbf{N}]}{\partial x} & [0] \end{bmatrix} = \begin{bmatrix} [0] & j\beta[\mathbf{N}] & \frac{\partial[\mathbf{N}]}{\partial y} \\ -j\beta[\mathbf{N}] & [0] & -\frac{\partial[\mathbf{N}]}{\partial x} \\ -\frac{\partial[\mathbf{N}]}{\partial y} & \frac{\partial[\mathbf{N}]}{\partial x} & [0] \end{bmatrix} \quad [4.46]$$

$$\text{Where,} \quad [0] = [0 \quad 0 \quad 0] \quad [4.47]$$

$$[\mathbf{N}] = [N_1 \quad N_2 \quad N_3] \quad [4.48]$$

The following arises by using the differentiations of equation [4.36]:

$$\frac{\partial[\mathbf{N}]}{\partial x} = [b_1 \quad b_2 \quad b_3] \quad [4.49]$$

$$\frac{\partial[\mathbf{N}]}{\partial y} = [c_1 \quad c_2 \quad c_3] \quad [4.50]$$

The values of the constants b_1, b_2, b_3, c_1, c_2 and c_3 were given in equations [4.38] and [4.39].

By substituting the terms in equations [4.44] and [4.45] into the equation [4.24], the vector \mathbf{H} -field formulation functional for an element can be obtained as:

$$J_e = \int_{\Delta} \{\mathbf{H}\}_e^T [\mathbf{Q}]^* \hat{\varepsilon}^{-1} [\mathbf{Q}] \{\mathbf{H}\}_e d\Omega - \omega^2 \int_{\Delta} \{\mathbf{H}\}_e^T [\mathbf{N}]^T \hat{\mu} [\mathbf{N}] \{\mathbf{H}\}_e d\Omega \quad [4.51]$$

Δ represents the integration over the triangular element domain. T and $*$ denote the transpose and the complex conjugate transpose, respectively. ε is a scalar value for the permittivity when the material is isotropic. If ε is a tensor, then it should be represented by a 3×3 matrix and the inverse of the matrix should be implemented.

The total function, J , associated with the whole cross section of the waveguide can be obtained by summing J_e of all the individual elements,

$$J = \sum_{e=1}^n J_e \quad [4.52]$$

Where, n is the number of elements.

The minimisation of the functional given in equation [4.52] is achieved by differentiating with respect to the field nodal values and equating it to zero as below:

$$\frac{\partial J}{\partial \{\mathbf{H}\}_e} = 0 \quad e = 1, 2, \dots, n \quad [4.53]$$

This minimisation leads to the following eigenvalue equation:

$$[\mathbf{A}]\{\mathbf{H}\} - \omega^2 [\mathbf{B}]\{\mathbf{H}\} = 0 \quad [4.54]$$

Where,
$$[\mathbf{A}] = \sum_{e=1}^n [\mathbf{A}]_e = \sum_{e=1}^n \int_{\Delta} \varepsilon^{-1} [\mathbf{Q}]^* [\mathbf{Q}] d\Omega \quad [4.55]$$

$$[\mathbf{B}] = \sum_{e=1}^n [\mathbf{B}]_e = \sum_{e=1}^n \int_{\Delta} \mu [\mathbf{N}]^T [\mathbf{N}] d\Omega \quad [4.56]$$

Matrix $\{\mathbf{H}\}$ contains all the H-field nodal values over the whole cross section of the waveguide considered. $[\mathbf{A}]_e$ and $[\mathbf{B}]_e$ represent the element matrices. The assemblage of all the element matrices $[\mathbf{A}]_e$ and $[\mathbf{B}]_e$ over the whole cross section result in the so called global matrices of the eigenvalue equation,

given by $[\mathbf{A}]$ and $[\mathbf{B}]$, respectively. The calculations of the element matrices, $[\mathbf{A}]_e$ and $[\mathbf{B}]_e$, are implemented in Appendix 2.

When solving waveguide problems by using finite elements, the key factor affecting storage requirements and computational effort is the choice of algorithm to solve the matrix equation. The global matrices $[\mathbf{A}]$ and $[\mathbf{B}]$ shown in equation [4.55] and [4.56] are highly sparse. The sparsity increases with the order of the matrices and decreases with the polynomial order of the shape functions. The main advantage of using the higher order basis functions for the fields is that they give a more accurate solution for a given matrix order, but involves an increased programming effort, particularly when considering anisotropic materials, infinite elements and penalty functions. Another disadvantage when using higher order polynomials for a given matrix order is the increase in the density of the matrix.

4.10 Spurious Solution

In vector wave analysis of optical waveguides using the finite element method, spurious solutions, the most serious problems, are generated to a greater or lesser degree that prevents the applicability of FEM and creates a serious obstacle to the use of the finite-element method. The reason for the appearance of spurious modes is probably the fact that the functional is not positive definite [Csendes and Silvester]. Spurious solutions are found to spread all over the eigenvalue spectrum, some of them appearing below any true modes and some between the physical modes. A spurious solution is generated because the functional does not satisfy the boundary conditions in the original waveguide problem, although it satisfies the original vector wave equation. Some other factors that cause the appearance of spurious modes are: the positive definiteness of the operator or possibly due to the non zero divergence of the trial fields [Rahman and Davies, 1984a; 1984b]. Then a new term that compensates for the missing boundary condition must be added in the functional to eliminate the spurious solutions. Various kinds of techniques have been developed to suppress and eliminate the spurious solutions and to

contribute to the renewed appreciation of the effectiveness of the finite-element method. No effective method of suppressing or eliminating spurious solutions has been found to date for method 1 (FEM using longitudinal or axial electromagnetic field components). Furthermore, this method may be applied to an anisotropic optical waveguide whose permittivity tensor has only diagonal components, but not for nondiagonal components. On the other hand, method 2 (FEM using the three magnetic field components) was developed after method 1 and is suitable for analyzing arbitrary anisotropic optical waveguides. Various ways of suppressing or eliminating spurious solutions have been discovered for method 2. The method has recently been used as a solver for an optical waveguide analysis package and is establishing its position as a standard finite element method for vector wave analysis of optical waveguides [Okamoto; Koshiba, 1992].

The appearance of these spurious modes does not affect the calculation of the lowest propagating mode, since the lowest order mode usually corresponds to the first positive eigenvalue of the matrix equation. However, to compute higher order modes, it becomes more difficult and very cumbersome to distinguish between the spurious and the physical modes of the guide. In electromagnetic waveguide problems [Konrad; Mabaya *et al.*] spurious modes do not arise if the trial field precisely satisfies divergence-free condition ($\text{div } \mathbf{B} = 0$). In the conventional \mathbf{H} -field finite element formulation, the variational functional [4.24] is consistent with the two curl Maxwell's equations [4.11] and [4.12], but do not satisfy the $\nabla \cdot \mathbf{B} = 0$.

In the full-vector formulation it has been found [Davies *et al.*, 1982; Rahman and Davies, 1984b] that these spurious modes occur because this divergence-free condition ($\text{div } \mathbf{B} = 0$) is neither implied nor forced. Rahman and Davies [Rahman and Davies, 1984c] have utilised the 'penalty function method' in order to eliminate these spurious solutions. Mathematically, a physical mode satisfies its eigenvector condition $\nabla \cdot \mathbf{H} = 0$, which gives very easy identification of a solution as being either a physical or spurious solution by calculating the $\nabla \cdot \mathbf{H}$ for each solution over the waveguide cross section. The

solution with low values of $\nabla \cdot \mathbf{H}$ is the real modes whilst those with high values are the spurious modes.

In the penalty function method [Rahman and Davies, 1984c], an additional integral is added to the original functional [4.24] which satisfies $\text{div } \mathbf{H} = 0$. The variational formulation then becomes as:

$$\omega^2 = \frac{\int \left((\nabla \times \mathbf{H})^* \cdot \hat{\epsilon}^{-1} \cdot (\nabla \times \mathbf{H}) + \left(\frac{\alpha}{\epsilon_0} \right) (\nabla \cdot \mathbf{H})^* \cdot (\nabla \cdot \mathbf{H}) \right) d\Omega}{\int \mathbf{H}^* \cdot \hat{\mu} \cdot \mathbf{H} d\Omega} \quad [4.57]$$

Where, α = dimensionless penalty coefficient.

A separate subroutine can be introduced in order to implement the addition of the penalty term in the numerator of equation [4.57]. The value of penalty coefficient, α can be estimated to be around $1/\epsilon_g$, where ϵ_g is the dielectric constant of the core guide. Here, the divergence-free constraint is imposed in a least-squares sense, and larger the value of the penalty number the more heavily the constraint is imposed, giving a further reduction of the spurious modes from the spectrum.

The penalty function method can be used more effectively, in conjunction with the infinite elements, resulting in the reduction of some unwanted field values along the boundaries by using appropriate decay parameters and considerably improves the quality of the field eigenvectors [Rahman and Davies, 1984c]. The advantage of using the penalty term is that it does not increase the matrix order of the eigenvalue problem, does not need additional storage and additional computational time is negligible. The penalty function method [Rahman and Davies, 1984c; Koshiba *et al.*, 1984; 1985b; Young] is a useful way of imposing certain constraints on solution variables; and it has been used in structural engineering problems to impose specific boundary conditions [Bathe] in order to improve the quality of the field.

The scalar approximation does not suffer from the spurious modes difficulty, since the two scalar functionals are positive definite and therefore all the eigenvalues are positive, each one corresponding to a physical mode of the

guide. The technique of working with scalars can reduce the amount of computation and eliminate spurious modes, but at the expense of accuracy. A number of alternative ways of eliminating spurious modes from vector approximation have been suggested. A formulation in terms of the transverse \mathbf{H} -field, known as the \mathbf{H}_t , has been advanced [Hayata *et al.*, 1986a] which completely eliminates spurious modes. In this formulation, any artificial parameters such as the penalty coefficient are not included.

4.11 Infinite Element Representation

An infinite element is an element that indeed extends to infinity. The shape functions of such an element, substitutes the shape functions of the outer boundary of the orthodox elements and should decay exponentially in the direction, which the field extends to infinity.

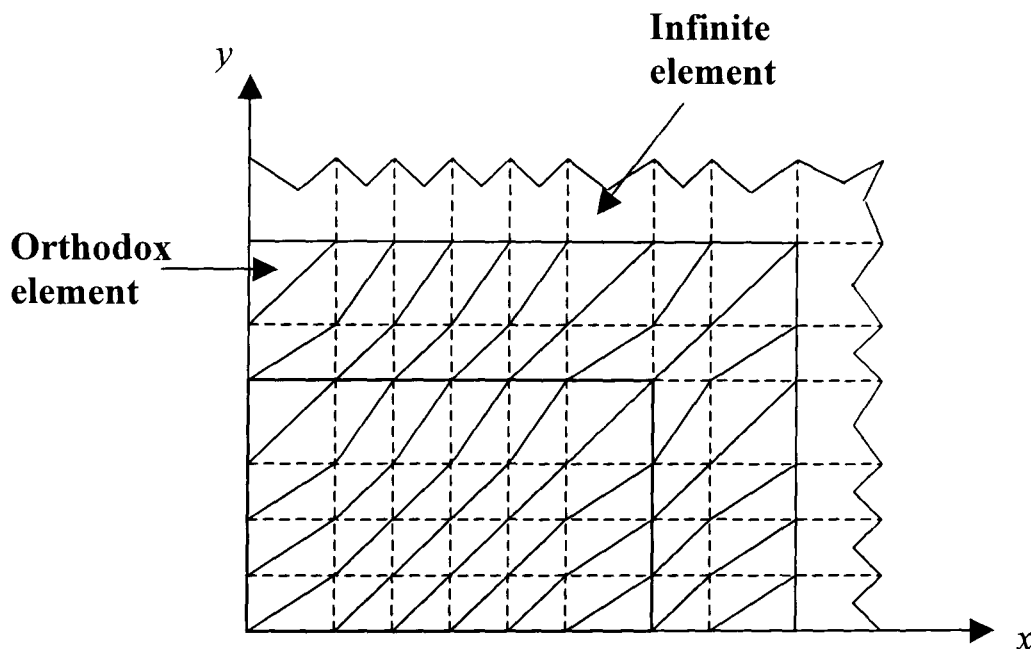


Fig. 4.8: Two-fold symmetry of rectangular dielectric waveguide cross section discretised into orthodox and infinite elements.

One common problem of the open-type optical waveguide is that finite field value exists in the region outside the guide and sometimes its decay extends to infinity in an exponential manner. The modelling of such structures, may cause problem for solutions near cut-off, where the field decays slowly and the region of significant field value can be arbitrary large. In the orthodox finite-element discretization, as shown in Fig. 4.8, the cross-section of the waveguide cannot be extended to infinity.

An artificial electric or magnetic wall boundary condition is the simplest approximation to this problem [Mabaya *et al.*], but this either introduces a significant error or needs to consider a large active domain to minimize this perturbation error. Another technique [Ikeuchi *et al.*] involves shifting the virtual boundary wall to satisfy a given criterion for the maximum field strength at that wall. Yeh *et al.* [Yeh *et al.*, 1979] have considered an exponential decay outside the core by using some boundary elements. However, because of the mixture of coordinate systems, their method lacks continuity of field over the problem domain.

An infinite element approach is developed by Rahman and Davies [Rahman and Davies, 1984*b*], which is found to be very useful when extending the domain of interest to infinity. In this approach, infinite elements are added along the outer boundary of the orthodox finite elements, as shown in Fig. 4.8, where for a typical rectangular dielectric waveguide problem, a quarter of the structure is discretized into orthodox and infinite elements, by assuming two fold symmetry. This method is quite simple to implement, and it does not increase the order of the matrices.

4.12 Summary

The finite element method based on the variational principle has been presented in this chapter, for the analysis of optical waveguiding problems. The history and the importance of the method are also described briefly. Various aspects, including different scalar and vector formulations, domain discretisation, natural boundary conditions, shape functions, element and global matrices have been discussed. Finally, the analysis of infinite elements was considered and also the important penalty function method was utilised to eliminate the spurious or non-physical solutions.

The Beam Propagation Method

5.1 Introduction

The beam propagation method (BPM) is one of the most commonly and widely used powerful methods or modelling tools for analysis and simulation of guided-wave propagation in inhomogeneous media to investigate linear and nonlinear lightwave propagation phenomena in longitudinally or axially varying waveguides, such as: S-shaped bent waveguides, tapered waveguides, curvilinear directional couplers, branching and combining waveguides [Okamoto]. The term BPM is used extensively in the optics literature. The BPM describes the evolution of the total field propagating along a waveguide and is particular useful for structures experiencing radiation waves such as leaky-mode and can show the progression of a field through a guide.

In a case, where the guided-wave structure is not uniform, but its cross-section depends on the axial distance, the modal solution approach, such as FEM, is no longer valid [Rahman *et al.*, 2005*b*]. Therefore, it is very important

to develop powerful computer-aided modelling and simulation tools. Commercial simulation tools and software have become available and are popular in the market amongst researchers, engineers and manufacturers. These tools have to be versatile, accurate, fast, robust, easy-to-use with minimum computation and memory requirement as far as possible. Researchers have developed various methods. For the case in point, the BPM has been developed. BPM is a step-by-step method which allows tracking the optical field at any point as the passing of light propagates along the guiding structures where calculations are repeated for each step in a manner of step like calculation of the propagating field.

Nowadays, BPM is considered as the most popularly used technique for modelling different three-dimensional photonic devices. Based on different numerical techniques, like fast Fourier transform (FFT), finite difference (FD), and finite element (FE), several scalar, semi-vectorial, and full-vectorial BPM approaches have been reported in the literature. The standard BPM is derived from the slowly varying envelope approximation (SVEA) [Chui and Lu]. In this thesis, for the study of leakage losses of PCF, FEM-based semi-vectorial BPM has been used, with the perfectly-matched layer (PML) boundary condition incorporated in order to effectively absorb the unwanted radiations.

5.2 Historical Background of BPM

Feit and Fleck [Feit and Fleck, 1978] first introduced the BPM in 1978, based on the Fast Fourier Transform (FFT) technique to study fibre optic devices. The BPM was first applied to a waveguide problem in 1980 [Feit and Fleck, 1980]. The early versions of BPM were only able to show the propagation of plain waves in homogeneous media with a paraxial wave equation.

Hermansson *et al.* [Hermansson *et al.*] analysed tapers in 1983 with a parabolic graded index transverse profile and various longitudinal profiles with the aid of the BPM. In 1984, Danielsen [Danielsen] succeeded in reducing the three-dimensional problem of calculating the field distribution in an integrated optic circuit to a two-dimensional problem, by applying the BPM.

One of the most critical problems with regard to guided waves occurs when the optical field spreads in half-space. For the first time, this problem was analysed by Fraunhofer, and Fresnel [März]. They tried to estimate the diffraction guided waves in their theory. Sommerfeld, in the early 1900's, presented his theory according to the diffraction in a metallic half-plane. Currently, the propagation of guided wave can be calculated numerically by BPM. The early application of this algorithm was in acoustic problems.

FFT-BPM is not suitable for commonly used semiconductor optical waveguides. Since then, many scalar, semi-vectorial, and full-vectorial BPM approaches have been reported based upon the finite difference method [Chung and Dagli; Liu and Li, 1992; Huang *et al.*, 1992]. Recently, the versatility of the FEM has been utilized in developing BPM approaches based on the scalar and full-vectorial formulations [Hayata *et al.*, 1990; Montanari *et al.*]. Although the scalar BPM approaches are numerically efficient as it solves only one field component, however, it cannot accurately model three-dimensional waveguide with hybrid fields where polarization effect is clear and polarization coupling is possible. Hence, a truly vector BPM approach is needed to rigorously characterize three-dimensional photonic devices with arbitrary index variations in all directions.

Recently, to simulate the propagation of optical waves through a z-dependent linear or nonlinear structure, the finite element based beam propagation method (FE-BPM) has been developed [Obayya *et al.*, 2000a] using a full-vectorial approach with a difference scheme along the axial directions [Rahman *et al.*, 2005b].

5.3 Applications of BPM

The BPM based on a full-vectorial FEM is used by many research groups [Tsuji and Koshihara; Obayya *et al.*, 2000b]. Being fully-vectorial, this approach is used to characterise nonlinear optical devices [Obayya *et al.*, 2000b] such as nonlinear directional couplers [Thylen *et al.*], to calculate polarization conversion along a periodically loaded semiconductor optical waveguides

[Obayya *et al.*, 2000c] and also to characterise compact bends [Rajajaran *et al.*, 2000; Baets and Lagasse]. Such an approach is particularly useful in the characterisation of tapered sections [Rahman *et al.*, 2003], Y- [Okamoto] and X- [Neyer *et al.*] junctions, gratings [Yevick and Thylen, 1982] and fibre couplers [Kaczmariski *et al.*; Lamouroux and Prade]. The method has also been utilized to accurately analyse, design, and optimize the performance of different three-dimensional photonic devices, such as leaky-mode waveguide [Obayya *et al.*, 2005].

5.4 Modelling Techniques of BPM

Modelling techniques may be classified as semi-analytical or numerical in nature, such as the effective index method, the variational method, and the coupled mode analysis. These semi-analytical methods work well for uniform optical waveguides or with coupled waveguides carrying few modes. Non-uniform structure is difficult to model accurately with such approaches and it becomes inevitable to use numerical methods [Sharma].

Modelling techniques can be vectorial, semi-vectorial or scalar in its formulation. In a dielectric waveguide, in which quasi-TE or quasi-TM modes are possible, the scalar approaches neglect the polarization effects, and the derivative of the relative permittivity with respect to the transverse directions are assumed to be negligible. In the semi-vectorial approach, the two transverse components are not coupled via the boundary through the derivative with respect to the transverse directions. Finally, in the vectorial approach, the transverse components are coupled due to the effect of the boundary and the full polarization effects are taken into consideration.

In the scalar BPM method, Helmholtz equation is the basis to solve the problems with waveguides. However, another perspective to design in the structure of modern BPM algorithms, based on the paraxial approximation, is considered. This method is called Vectorial FE-BPM Propagation Method. Since VBPM is used to solve the problems related to three-dimensional field, it requires high memory and lots of time computer to solve the problem [März].

5.5 Numerical Techniques of BPM

Various numerical techniques have been developed for modelling of optical waveguides, which treat the total field, including the guided and the radiation modes together. The BPM is classified according to the following algorithms:

- (i) Fast-Fourier transform beam propagation method (FFT-BPM)
- (ii) Finite difference beam propagation method (FD-BPM)
- (iii) Modal propagation based beam propagation method
- (iv) Finite element beam propagation method (FE-BPM)

5.5.1 Fast-Fourier Transform Beam Propagation Method (FFT-BPM)

FFT-BPM was the first method developed for beam propagation through optical waveguiding structures and was simply called the beam propagation method. The basic idea of FFT-BPM is to represent the electromagnetic field by a superposition of plane wave propagating in homogeneous media. The wave propagation in homogeneous media is modelled as an integral of these plane waves in the spectral domain and the effect of inhomogeneity of the media is accounted for as a phase correction in the spatial domain at the each propagation step.

The FFT is used to provide the link between the spatial and the spectral domains. Therefore, this method is sometimes called Split-Operator FFT-BPM and can be expressed mathematically as:

$$\psi(x, y, z + \Delta z) = PQP\psi(x, y, z) \quad [5.1]$$

Where P is the propagator and Q corrects the phase, $\psi(x, y, z)$ and $\psi(x, y, z + \Delta z)$ are field representation in two steps [März].

In FFT-BPM two concepts are considered:

- The algorithm is used by structures with an arbitrary geometry in their cross-section.
- FFT-BPM has an analytical view not only to guided waves but also to the radiated waves.

5.5.1.1 Advantages of FFT-BPM

- FFT-BPM formulations are straightforward.
- It applies to a structure with an arbitrary cross-section.
- In FFT-BPM, as long as input field is given, it is capable of tracing the wave propagation in the given structure. In this analysis, both the guided and the radiation waves are included.

5.5.1.2 Limitations of FFT-BPM

- The FFT-BPM only solves the simpler and less accurate scalar wave equations under paraxial approximation. Therefore, this method was only developed for the case of weakly guiding structures, neglecting the vectorial properties of the field.
- The FFT-BPM cannot describe the vectorial properties such as the polarisation coupling and polarisation dependence of guided-wave devices as it can only trace the scalar wave propagation.
- In FFT-BPM design method, refractive index difference in the transverse direction is considered very small. Therefore, it cannot be applied to structures with large index discontinuities which are a common feature in modern optoelectronic devices based on semiconductor materials.
- The FFT-BPM is accurate only when the beam propagates in the direction with a small angle to the z-axis. This is due to the reason that a paraxial approximation has been made in the derivation.
- Due to the inefficient discretisation, more demand of computational resources, and inaccurate description of interface boundary conditions between different dielectric media, the FFT-BPM is of limited use.

5.5.2 Finite Difference Beam Propagation Method (FD-BPM)

The beam propagation method that solves the paraxial form of the scalar wave equation in inhomogeneous medium using the finite difference method is called the finite-difference beam propagation method (FD-BPM). The early FFT-BPM was designed for analysis of structures with weakly guiding characteristics. In order to overcome the limitations of the conventional FFT-

BPM, some efforts has been made to adapt BPM to treat strongly guided waveguides [Lagasse and Bates; Yevick and Glasner, 1989; Rolland *et al.*; and Splett *et al.*]. For instance, a split-step FD-BPM has been developed by Yevick and Hermanson to simulate strongly guiding semiconductor-based rib waveguides [Yevick and Hermansson, 1989; 1990] and to solve the propagator by the finite difference method.

In order to improve the efficiency and flexibility, a FD-BPM has been developed by Hedow and Shakir [Hedow and Shakir] to solve the paraxial wave equation. The original application of the FD-BPM has been limited to cylindrically symmetric structures. Chung and Dagli introduced the FD-BPM to the Cartesian coordinate system [Chung and Dagli].

5.5.2.1 Advantages of FD-BPM

- FD-BPM formulations are straightforward. It is more accurate especially in modelling structures with large discontinuities in the refractive index.
- The advantages of FD-BPM algorithms compared to FFT-BPM become apparent, when FD-BPM uses larger propagation step size.
- Furthermore, in each step of propagation, compare to FFT-BPM the time used for calculation is reduced significantly in FD-BPM.
- The possibility of integrating wide-angle propagation and full-vector algorithms [Hadley 1992a; Al Salamed and Owais] is an additional advantage of FD-BPM.
- When computational window is reduced and the optical field reaches the computational boundaries, it is necessary to implement additional algorithms. Otherwise, the simulation of the optical devices will not be correct, because the optical field will reflect at the boundaries and will re-enter the computational window. FD-BPM can solve this problem effectively, but is cumbersome when using FFT-BPM.

5.5.2.2 Limitations of FD-BPM

- For the discretisation of the waveguide cross section, the finite difference method is inefficient. Most of the finite difference schemes

rely on uniform grids which results in high computational effort, and for curved boundaries, they present very crude approximation.

- The BPM algorithms based on FD is of limited use. This is due to the inefficient discretisation and inaccurate description of interface boundary conditions between different dielectric media.
- For vectorial propagation algorithms based on the finite differences, some authors have noticed that if an arbitrary input field is used, some unphysical gain [Kriezis *et al.*] is observed during the propagation.

5.5.3 Modal Propagation Based Beam Propagation Method

The early FD-BPM was designed for analysis of wave propagation in optical devices, but it needs a large computational effort. In order to overcome the limitations of the conventional FD-BPM, some analytical approaches have been proposed to describe the wave propagation in optical devices. One of approaches is the Least Squares Boundary Residuals (LSBR) [Rahman and Davies, 1988; El-Mikati and Davies]. The LSBR method has been used to study discontinuity parameters [Razaz and Davies; Jansen; Oraizi and Perini]. In LSBR method, the magnetic and electric field components are matched at the interface of a junction between two different sides.

The LSBR method was introduced as an alternative to point-matching (and Galerkin) methods, satisfying the boundary conditions in the usual least-square sense over the interface. The method is rigorously convergent, the error minimization being global rather than sampled, and has the flexibility of introducing an electric/magnetic-weighting factor. Other very similar approaches to LSBR have also been proposed [Reed *et al.*; Suchoski and Ramaswamy], which depend on the same principle of matching the transverse electric and magnetic field components using the conventional mode matching technique to treat problems of one and two-dimensional dielectric waveguide discontinuities. This technique can also be named Modal Propagation Method, since these approaches depend on expanding the field components in terms of the guided and/or radiation modes.

5.5.3.1 Advantages of Modal Propagation Based BPM

- Since this method of calculation requires less time and memory, it is more computationally efficient compared to FD-BPM.
- Another advantage is its capability to find the reflected rays [Hayata *et al.*, 1990], not available in most of the current FD-BPM algorithms.

5.5.3.2 Limitations of Modal Propagation Based BPM

- Modal propagation method faces problems while calculating radiation modes. Accurate characterisation of optical devices using the modal propagation methods needs the determination of all guided and radiation modes. If the problem is one-dimensional, calculations for radiation modes can be obtained by numerical methods. However, it is time consuming and labour intensive. Now if the problem expands to more than one dimension, the calculation will be very complicated.

5.5.4 Finite Element Beam Propagation Method (FE-BPM)

Recent research efforts have been directed towards the development of BPM algorithm based upon the efficient finite element method (FE-BPM). Koch and Davies introduced the first version FE-BPM [Koch *et al.*, 1989; 1991]. They used a variational method to find a solution to the scalar wave equation, using paraxial approximation. In this method, FEM is responsible for calculation in the transverse cross-section and the finite difference Crank Nicholson method is used for the longitudinal axis. Another version of FEM was presented by Hayata *et al.* [Hayata *et al.*, 1990]. The scalar wave equation is calculated by Galerkin's procedure. Special boundary conditions are required in order to avoid unphysical reflections of the guided waves from the edges of computational domain.

FE-BPM methods are not capable of determination polarisation characteristics accuracy. They also have problems in analysing and measuring the coupling property in strongly guided optical devices. FE-BPM is solved by paraxial Helmholtz equation [März]. It is believed that a full-vector FE-BPM approach is needed to accurately model 3-D photonic devices with fields of hybrid nature.

Recently, a unified FE-BPM has been reported [Tsuji and Koshiba] for both TE and TM waves propagating in strongly guiding longitudinally varying optical waveguides. Obayya *et al.* [Obayya *et al.*, 2000b] has reported a full-vectorial FE-BPM to characterise 3-D optical guided-wave devices.

5.5.4.1 Advantages of FE-BPM

- In some aspects, FE-BPM algorithm is superior to FD-BPM. For example, non-uniform discretisation ability to estimate curved boundary conditions accurately and uses them carefully.
- It solves only the transverse components of the magnetic field; hence it minimizes the computational effort and the storage requirements.
- The FEM combined with first-order Pade approximation is applied to the longitudinal direction in order to get an accurate wide-angle propagation algorithm; hence it is capable of tracing guided waves propagating off the propagation axis.

5.6 Boundary Condition of BPM

Since the computational domain in BPM calculations cannot have an infinite dimension, one of the most important parameters in implementing any BPM approach is the specification of the boundary condition. Boundary conditions must be chosen in such a way that the effect of the boundaries does not introduce errors in the propagation description of the optical field.

In the conventional FFT-BPM, the Absorbing Boundary Condition (ABC) [Lagasse and Baets; Feit and Fleck, 1978, 1980] has often been used. The idea is to artificially place a lossy medium or special material at the edges of the computational domain to absorb the possible undesired reflections at the boundary. In this case, fields at the boundary have to be zero. The major disadvantage of ABC is that it is problem dependent. ABC requires a high memory for calculations in a computer. For a specific structure, many parameters of the ABC have to be chosen carefully, such as the thickness of the lossy region and the strength of the artificial loss. Another boundary condition, called Transparent Boundary Conditions (TBC) has been proposed

[Hadley, 1992b; 1991]. Contrary to ABC, in TBC the output waves pass a specific incident angle and it does not require a high memory to carry out calculations. TBC is more robust and problem independent than the conventional ABC. In TBC, the idea is to approximate the wave near the boundary of the computational domain as a plane wave which satisfies:

$$\frac{\partial \phi}{\partial \rho} = -jk\phi \quad [5.2]$$

Where, k is the transverse wave-vector, ϕ is the field near the boundary, and ρ is the distance in the direction normal to the boundary.

However, for TBC, the plane wave approximation of the outgoing wave near the boundary is not sufficient to suppress large radiation. Moreover, when many field values inside the computational domain are involved in estimating k , some numerical instabilities has been observed [Vassallo and van der Keur, Vassallo and Collino].

5.6.1 The Perfectly Matched Layer (PML) Boundary Condition

The Perfectly Matched Layer (PML) is the latest version of boundary conditions that have shown their high efficiency and has proved to be more robust compared to the ABC and TBC. An imaginary electrical layer enables the PML boundary condition to effectively absorb the unwanted radiation waves without reflection and to attenuate the output wave at different angles and frequencies [März]. By adjusting of the PML parameters so as to have a wave impedance of exactly the same as inside the computational domain, the PML can offer a reflection less boundary to the outgoing radiation whatever its strength or angle it hits the PML-computational domain interface.

Berenger [Berenger] first introduced the concept of the PML as an alternative to the ABC or TBC, in order to synthesise an absorbing layer for the Finite Difference Time Domain (FDTD) method. The PML concept has been successfully applied in one-dimensional FD-BPM [Huang *et al.*, 1996] and needs the splitting of the field components into two sub-components. When this happens, it leads to non-Maxwell's equations, which is not the desired

form for the application of finite elements. Pekel and Mittra [Pekel and Mittra, 1995a; 1995b] had introduced a new form of the PML, for treating free space scattering problems, which does not involve the field splitting, maintaining the desired form of the Maxwell's equation for the finite element application.

Recently Obayya, Rahman and El-Mikati [Obayya *et al.*, 2000a], incorporated the robust PML boundary condition into the finite element-based BPM formulations, which considers all the three field components. The main advantage of the present formulation is that the sparsity of the global matrices is retained. Therefore, a numerically efficient sparse matrix solver is used.

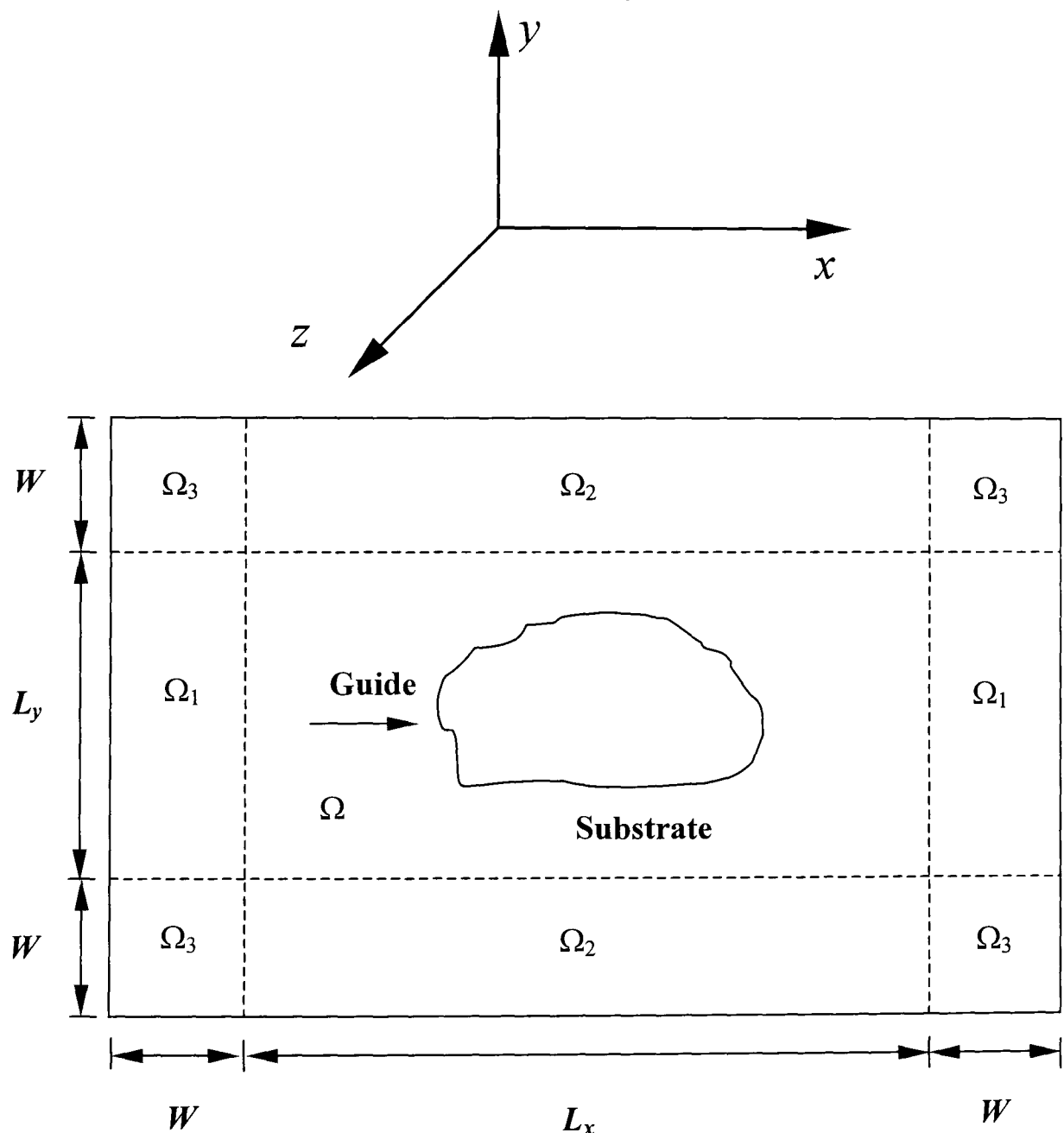


Fig. 5.1: Optical waveguide cross-section with different PML regions.

Fig. 5.1 shows the optical waveguide cross-section with different PML regions, where x and y are the transverse directions, z is the direction of propagation, regions Ω_1 and Ω_2 are the PML regions normally faced with x and y directions,

respectively, regions Ω_3 corresponds to the four corners of the PML, Ω corresponds to the computational domain region, W is the width or height of the PML, and L_x and L_y are the width and height of the computational domain in the x and y directions, respectively.

Starting with new PML form, Maxwell's curl equations can be taken the form:

$$\nabla \times \mathbf{H} = \varepsilon \frac{\partial \mathbf{E}}{\partial t} + \mathbf{J} \quad [5.3]$$

$$\nabla \times \mathbf{E} = -\mu \frac{\partial \mathbf{H}}{\partial t} \quad [5.4]$$

Where, \mathbf{E} and \mathbf{H} are the electric and magnetic field vectors, respectively.

Assuming the time dependence to be $\exp(j\omega t)$, where t is the time, ω is the radian or angular frequency, and, j is the imaginary part, for convenience purposes. Thus the differential form of Maxwell's equations can be written as:

$$\nabla \times \mathbf{H} = j\omega\varepsilon_0 n^2 \mathbf{E} \quad [5.5]$$

$$\nabla \times \mathbf{E} = -j\omega\mu_0 \mathbf{H} \quad [5.6]$$

Where, n is the refractive index, and ∇ is the modified differential operator defined as:

$$\nabla = \mathbf{x}\alpha_x \frac{\partial}{\partial x} + \mathbf{y}\alpha_y \frac{\partial}{\partial y} + \mathbf{z}\frac{\partial}{\partial z} \quad [5.7]$$

Where, \mathbf{x} , \mathbf{y} , and \mathbf{z} are the unit vectors in the x , y and z directions, respectively, and α_x , α_y and α_z are the parameters associated with the PML boundary conditions imposed at the edges of the computational window. Since the wave propagation is assumed to be along z direction, α_z will be set unity. On the other hand, α_x and α_y has to be set in such a way that the radiation waves can freely leave the computational window with almost no reflection by taking the following profile [Obayya *et al.*, 2000a]:

$$\alpha_t (t = x \text{ or } y) = \frac{1}{1 - j \frac{\sigma_e}{\omega\varepsilon_0 n^2}} = \frac{1}{1 - j \frac{\sigma_m}{\omega\mu_0}} \quad [5.8]$$

In this case, σ_e and σ_m are the electric and magnetic conductivities of the PML, respectively. The equation [5.8] shows that the PML satisfies the

impedance matching condition with an adjacent medium in the computational domain with refractive index n and wave impedance $\sqrt{\frac{\mu_0}{\epsilon_0 n^2}}$.

The values of the parameters α_x and α_y are defined in the different regions as:

- (i) region Ω (computational domain) : $\alpha_x = 1$ and $\alpha_y = 1$
- (ii) region Ω_1 : $\alpha_x = \alpha_t$ and $\alpha_y = 1$
- (iii) region Ω_2 : $\alpha_x = 1$ and $\alpha_y = \alpha_t$
- (iv) region Ω_3 : $\alpha_x = \alpha_t$ and $\alpha_y = \alpha_t$

In the PML regions, the electric conductivity profile can be assumed as:

$$\sigma_e(\rho) = \sigma_{\max} \left[\frac{\rho}{W} \right]^m \quad [5.9]$$

Where, σ_{\max} is the maximum value of the electric conductivity, ρ is the distance inside the PML which is measured from the interface of the computational domain and the PML, and m is the power of the conductivity profile and will be taken as 2. For this conductivity profile, the theoretical reflection coefficient, R , at the interface between the PML and the computational domain is [Berenger]:

$$R = \exp \left[-2 \frac{\sigma_{\max}}{cn\epsilon_0} \int_0^W \left(\frac{\rho}{W} \right)^2 \partial\rho \right] \quad [5.10]$$

Where, c is the velocity of light in free space. Performing the integrating in equation [5.10], σ_{\max} can be shown as:

$$\sigma_{\max} = \frac{3cn\epsilon_0}{2d} \ln \left(\frac{1}{R} \right) \quad [5.11]$$

Where, R is the value of the theoretical reflection coefficient.

In the case, when R is set to very small value, the maximum electric conductivity (σ_{\max}) is calculated using the equation [5.11]. Therefore, the PML parameters α_x and α_y and the electric conductivity profile $\sigma(\rho)$ will be determined for the different PML areas. Such PML arrangements will force any non-physical radiation wave leave freely the computational domain whatever the angle and/or the strength it hits the boundary of the computational domain.

5.7 Summary

The vectorial BPM combined with the powerful FEM has been presented in this chapter. The history and the application of the method are described briefly. Various aspects, including modelling technique, numerical technique, and boundary conditions have been discussed. The incorporation of the rigorous perfectly-matched layer (PML) boundary condition into the vectorial wave equations, as shown in Appendix 3, has been presented along with the implementation of divergence condition to eliminate the spurious or non-physical solutions. The proposed propagation is based upon the **H**-field components. This chapter, together with the discussion of the finite element method presented in the previous chapter, forms the basis for the work in Chapter 9 for study the leakage losses of PCF.

Modal Solutions of Square lattice Photonic Crystal Fibre

6.1 Introduction

Modal solutions of square lattice planar photonic crystal fibre with square, rectangular, and circular core have been investigated and presented in detail using a rigorous H-field based full-vectorial finite element method. Finite element based approach is particularly advantageous and is a versatile approach, which can be used to represent any arbitrary-shaped PCF with arbitrary hole shapes, sizes, orientations, materials, placement, and arbitrary refractive index profiles. The effective indices, mode field profiles, spot-sizes, power confinements, modal hybridness, beat lengths and group velocity dispersions are shown for the fundamental and higher order modes of the quasi-TE and TM polarizations. Also, with the material dispersion included, the modal chromatic dispersion has been calculated and the possibility of tailoring the PCF structure so as to achieve zero dispersion at the desired

wavelength has been shown. The influence of the hole diameter, and operating wavelength, are investigated in detail. The effects of the 2-fold symmetry and full structure are also identified. The existing two-fold symmetry has been exploited with the electric and magnetic field boundary conditions at the symmetry planes in order to reduce the computational cost and also to achieve adequate mesh refinement in the core region.

Planar optical waveguides are the key devices to construct integrated optical circuits and semiconductor lasers. Generally, rectangular waveguides consists of a square or rectangular core surrounded by a cladding with a lower refractive index than that of the core. Three-dimensional analysis is necessary to investigate the transmission characteristics of rectangular waveguides [Okamoto]. Therefore, this chapter first describes square lattice PCF with square core than with rectangular core. Several modal solutions are then presented to analyse the three-dimensional square, and rectangular core PCF.

6.2 Modelling of PCF

Sequential development stages of the project are as follows:

- Square lattice PCF with square hole
- Square lattice PCF with rectangular hole
- Hexagonal lattice PCF with circular hole

In this chapter, rigorous modal solutions of square lattice PCF with square, and rectangular hole are investigated and presented in detail. Initially, the modal properties of a square lattice PCF with an array of square holes are studied. Followed by, a PCF with rectangular holes, instead of the square holes is considered and then modal solutions are presented here.

6.2.1 Why Rectangular Hole rather than Square Hole is better?

PCF with square holes would have degenerate modes and such a waveguide would not be able to maintain a specific polarization state, due to any

structural non-uniformity or bends or stresses being present. However, when the hole shapes are not square, but rectangular in shape, the propagation constants (β) for the quasi-TE and TM modes would be different and waveguide would have a finite form birefringence.

6.3 Structure of the PCF

6.3.1 Square Lattice PCF with Square Air Holes

A schematic diagram of the planar PCF structure with the square size air hole in a homogeneous silica background is shown in Fig. 6.1. This silica area is used with its higher index value compared to the lower equivalent index in the cladding, to guide the light as does the core of a typical optical waveguide. The cladding can be another material with low index, and in this case air is considered for numerical simulations. The reason for taking air holes in a homogeneous silica background is that photonic crystal fibres work in one of two ways. In “index-guided” crystal fibres, one or more holes are missing at the centre of the array of homogeneous silica background. In this figure, a finite air cladding region ($5\ \mu\text{m}$) is considered for numerical simulation, beyond which field did not extend.

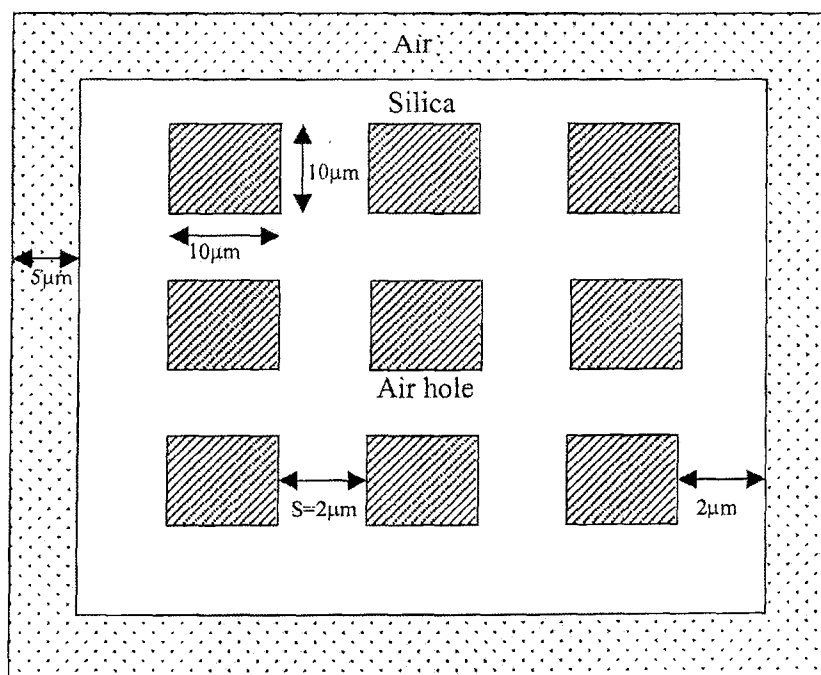


Fig. 6.1: Structure of the square size air hole in a homogeneous silica background.

A schematic diagram of the square lattice PCF with missing core at the centre surrounded by air-holes in a homogeneous silica background is shown in Fig. 6.2. Missing hole at the centre can be used to guide the light as the core of a typical optical waveguide does and the outer air holes (known as cladding), having lower refractive index than that of core, act as an optical barriers.

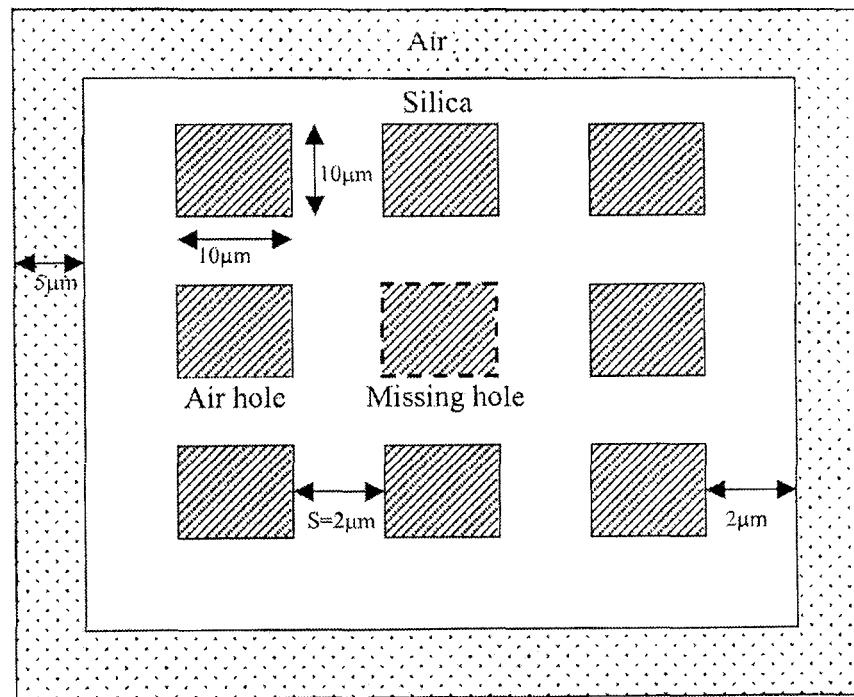


Fig. 6.2: Square lattice PCF with missing core at the centre surrounded by air-holes in a homogeneous silica background.

6.3.2 Square Lattice PCF with Rectangular Air Holes

Next, the square lattice PCF with rectangular air holes is designed in order to achieve a highly birefringent PCF. A typical planar photonic crystal waveguide with rectangular air holes in a regular periodic configuration is shown in Fig. 6.3. As mentioned earlier, rectangular air holes are arranged in a silica background. Similar to a typical PCF with circular air-holes, a missing hole at the centre can guide the light as the core of a typical optical waveguide and for integrated optical structures, holes of a square or rectangular shape would be easier to fabricate [Rahman *et al.*, 2005a] in integrated optics platform. For a regular array of holes of equal size, the hole height and width are taken as H and W , respectively with the separation between them being S in both the transverse directions. In this case the value of Λ_H and Λ_V as shown

in Fig. 6.3, are the horizontal and vertical pitches respectively. Infinite elements are also used to consider the rapidly decaying field outside the PCF structure.

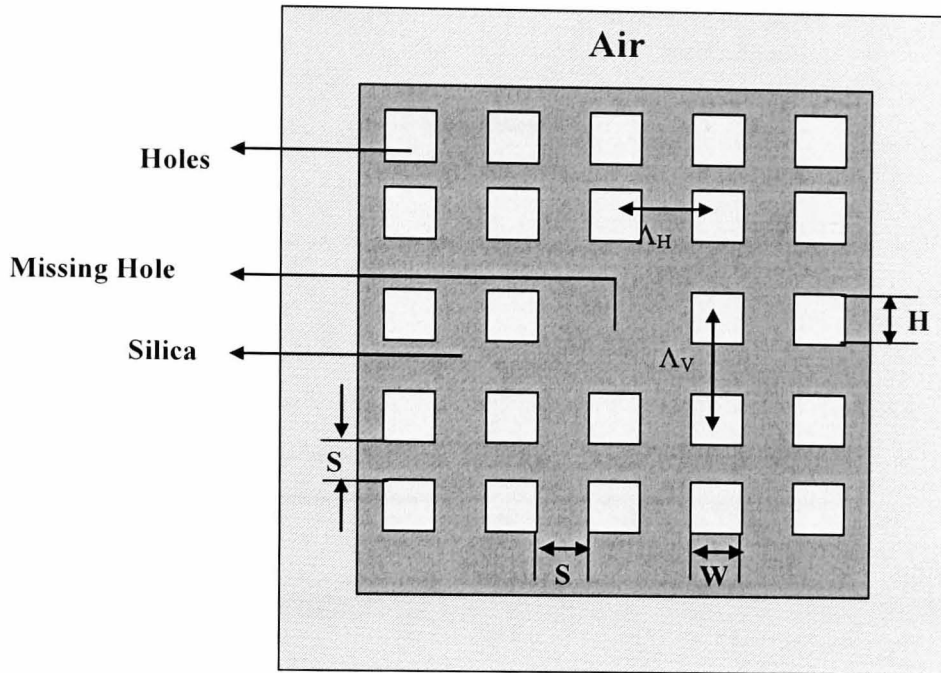


Fig. 6.3: Schematic diagram of a integrated optic PCF with rectangular air-holes where central hole is missing.

6.4 Results of Square Lattice PCF with Square Air Holes

6.4.1 Effect of Mesh Refinement in Both Full Structure and Two-Fold Symmetry

For a specific waveguide dimension, when $W = H = 10 \mu\text{m}$, and $S = 5 \mu\text{m}$, the effect of mesh refinement is studied. In this case, the silica and air indices are simply taken as 1.50 and 1.00, respectively, at the operating wavelength $1.55 \mu\text{m}$. For this numerical investigation, FEM representation of both the complete PCF cross-section and its reduced one-quarter representation by exploiting two-fold symmetry, are undertaken. Variations of the effective indices with the transverse mesh refinement for both the cases for the first three modes are shown in Fig. 6.4. In this case, identical mesh refinements have been used in both the vertical and horizontal directions to avoid structural anisotropy. Here the mesh number identifies the total number

of mesh divisions (irregular mesh discretization is used here) in each of the transverse directions.

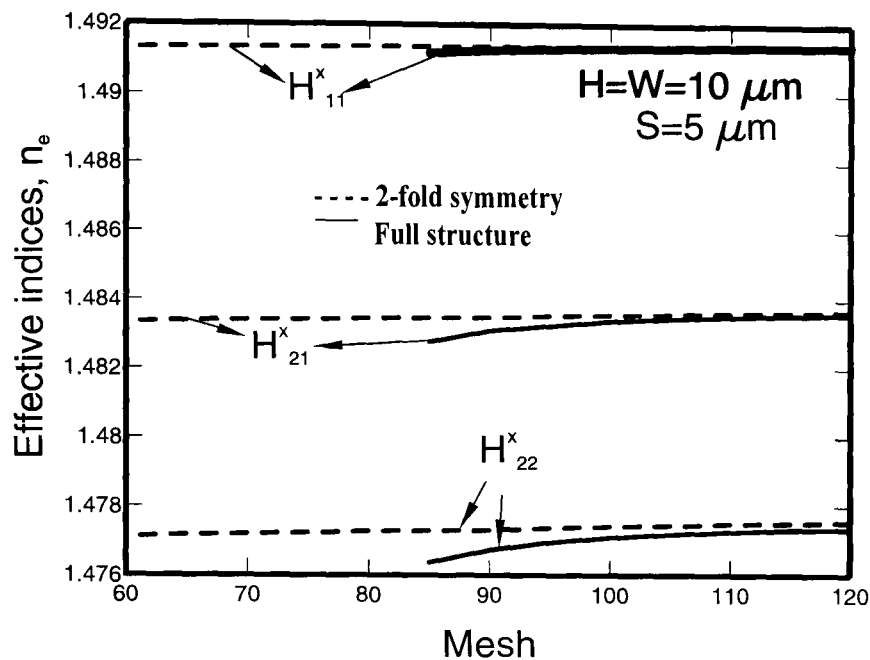


Fig. 6.4: variation of the effective indices with mesh.

It can be observed in all the cases, as the mesh refinement is increased the effective index value increases and stabilizes to their final values. It can be noted that, when the full structure is modeled, the effective indices increase slowly as the mesh is increased. However, it can also be clearly observed that when, only the quarter of the structure is used, as shown by dashed lines, effective index solutions are much more accurate compared to the full structure, for the same number of mesh divisions used in both the cases. It can be observed that the errors for higher order modes are larger for the same order of mesh refinement.

6.4.2 Effects of Operating Wavelength

Variation of the effective indices of the fundamental and higher order quasi-TE modes with the operating wavelength, λ , for a square-hole PCF is shown in Fig. 6.5. In this case, the areas of the holes are kept constant at $4.0 \mu\text{m}^2$, the width to height aspect ratio is 1:1 and the separation between two nearest air holes is $1 \mu\text{m}$. Refractive index of silica (n_0) at different operating wavelengths is calculated using Sellmeier's equation [Agrawal], shown in Appendix 1. From Fig. 6.5 it can be noticed that due to material dispersion [Agrawal], the refractive index of silica reduces monotonically with the

wavelength, which is shown as a solid line, labeled as n_g . It can be observed that the effective indices of the higher order (H^y_{21}) modes are lower than that of the fundamental (H^y_{11}) modes. As mentioned earlier, a PCF with square holes would have degenerate modes and such a waveguide would not be able to maintain a specific polarization state, due to any structural non-uniformity or bends or stresses being present. Therefore, the effective indices and modal field profiles for the quasi-TM (H^x_{mn}) modes are very similar compared to the corresponding quasi-TE (H^y_{mn}) modes for a given wavelength which are not shown here.

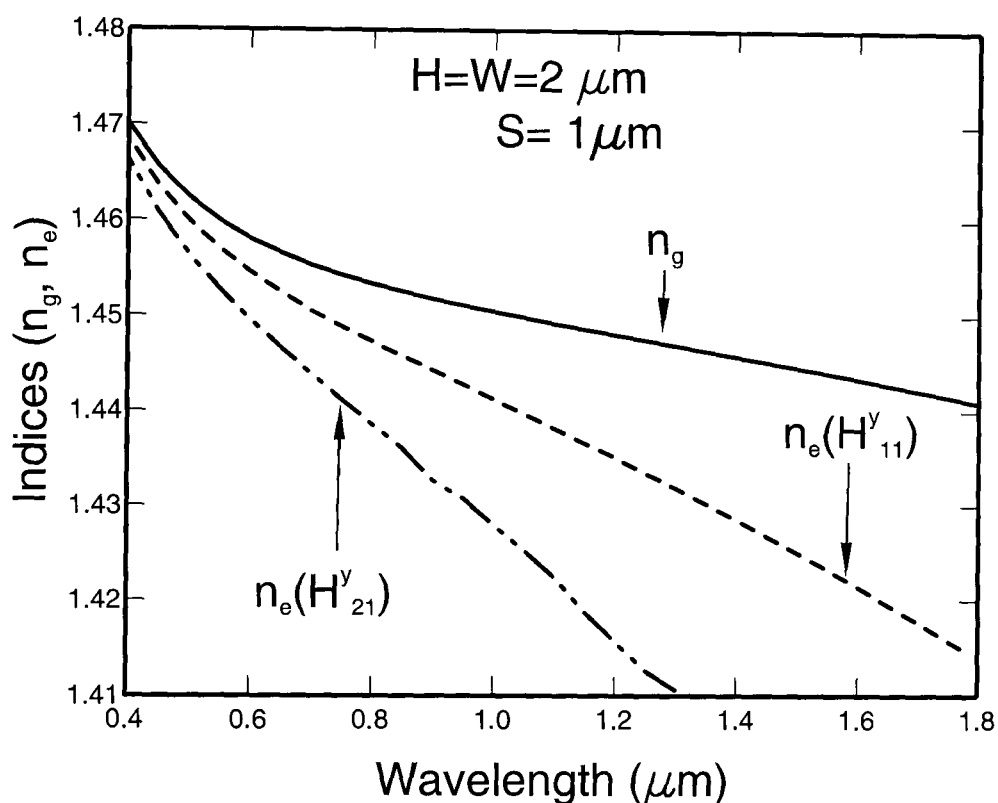


Fig. 6.5: Variation of the effective indices with the operating wavelength for a square-hole PCF.

6.4.3 Effect of Separation

Next, the effect of the separation, S , between the holes is studied. Variations of the effective indices for the fundamental and higher order quasi-TM (H^x_{mn}) modes with the waveguide dimensions are shown in Fig. 6.6. In general, the waveguide dimensions, width, W , height, H , and/or the separation between the holes, S , are varied to study the waveguide dispersion. In the first example, its overall cross-section profile is kept constant, with its height (H) and width (W) equal and the separation (S) between the holes is made one-half of these values. The silica and air indices are taken as 1.50 and 1.00,

respectively at the operating wavelength of $1.55 \mu\text{m}$. It can be noted that as the waveguide dimension is increased, the effective index values for all the modes increase and reach the core index value asymptotically. However, as the waveguide dimension is reduced, the modal cutoff points reached rapidly for all the modes. These dispersion (waveguide) curves are similar to typical integrated optical waveguides. It can be observed that the structure is multimoded when its separation is greater than $1.25 \mu\text{m}$.

The structure with square holes, as shown in Fig. 6.3, has a 90 degrees rotational symmetry and hence the TE and TM modes were degenerate. The effective indices for the quasi-TE (not shown here) modes are the same as those of the quasi-TM modes. However, in the numerical simulation since a two-fold symmetry is used with the electric and the magnetic field boundary conditions at the symmetry planes, these degenerate modes can be easily separated and the numerical interference between the degenerate modes is avoided.

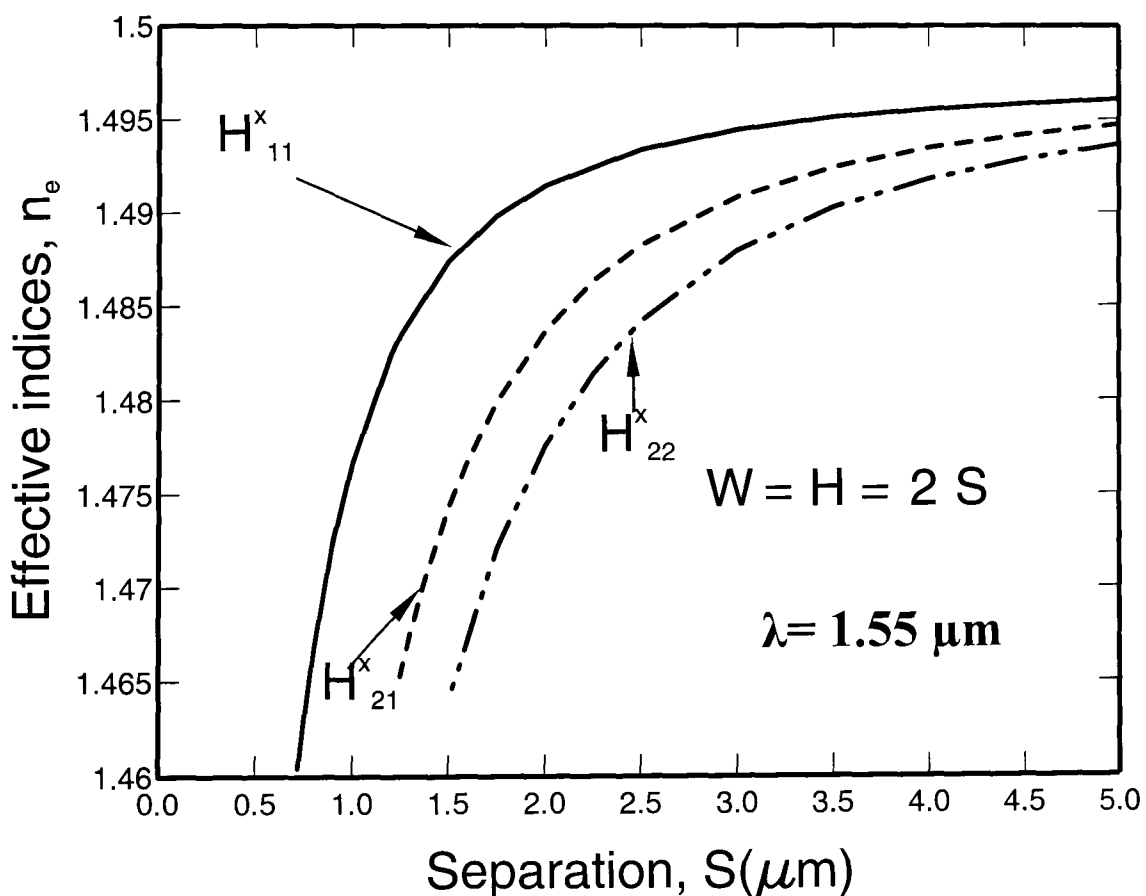


Fig. 6.6: Variation of the effective indices of quasi-TM modes with the separation between the air-holes for a square-hole PCF.

Modes in optical waveguides with two-dimensional confinement are not truly TE or TM, but hybrid in nature. For the quasi-TE (H_{mn}^y) modes, the H_y field component is dominant, however, the non-dominant field, H_x is not zero. Modal hybridness is an important parameter in the design and operation of many optical systems, particularly to identify polarization-dependent performance, the modal losses, and possible polarization conversion [Rahman *et al.*, 2005a]. The modal hybridness can be defined as the ratio of the non-dominant to the dominant field values. For the quasi-TE (H_{mn}^y) modes, the hybridness is defined as the ratio of the non-dominant H_x field over the dominant H_y field. The variations of the vector field components for the quasi-TE mode are shown in Fig. 6.7. It can be observed that as the waveguide dimension is reduced, the modal hybridness increases as the modes approach their modal cutoff. It can also be observed that as the waveguide dimension is reduced, the non-dominant H_x field is increased quickly and the dominant H_y field is decreased. As a consequence the modal hybridness, which is the H_x/H_y ratio, also increases with the waveguide dimension.

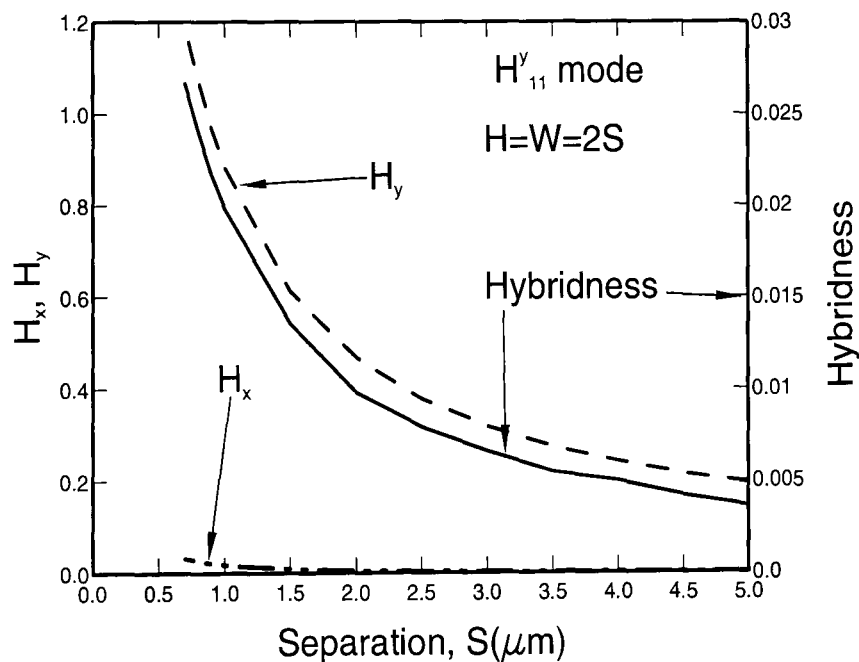


Fig. 6.7: Variation of the modal hybridness and vector field components with the separation between the air-holes.

Variations of the modal hybridness with the waveguide dimension are shown in Fig. 6.8. For the quasi-TM (H_{mn}^x) modes, the hybridness is defined as the ratio of the non-dominant H_y field over the dominant H_x field. It can be

observed that as the waveguide dimension is reduced, the modal hybridness increases as the modes approach their modal cutoff. It can also be noted that the modal hybridness for the H^y_{11} and H^x_{11} modes are identical and shown by a solid line and the modal hybridness is larger for the higher order modes than for the fundamental modes.

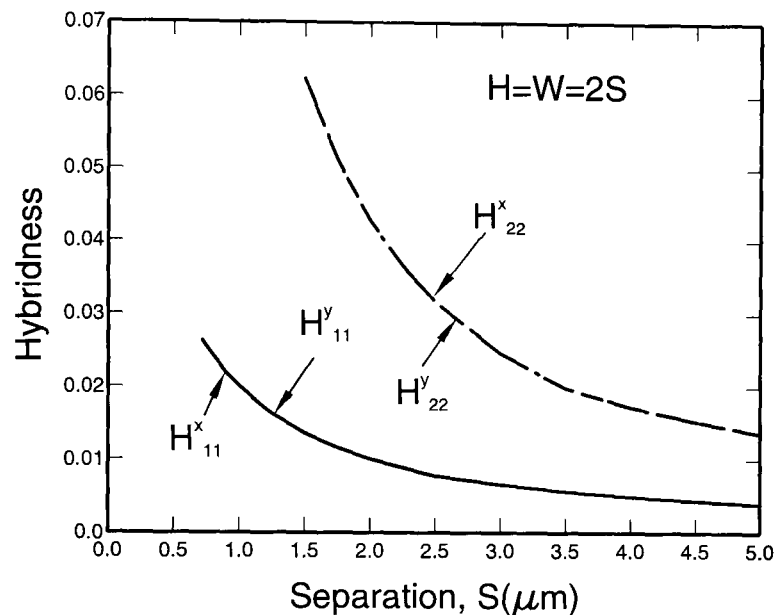


Fig. 6.8: Variation of the modal hybridness with the separation between the air-holes.

At $\lambda = 1.55 \mu\text{m}$, the dominant H_y field profile of the fundamental quasi-TE (H^y_{11}) mode when separation between the holes, $S = 1 \mu\text{m}$ and $S = 5 \mu\text{m}$ are shown in Fig. 6.9a and Fig. 6.9b, respectively. In Fig. 6.9a, the height and width of the holes are kept fixed at $2 \mu\text{m}$, where as in Fig. 6.9b, the height and width of the holes are kept fixed at $10 \mu\text{m}$. Compared to Fig. 6.9b, as the separation and waveguide dimensions are lower in Fig. 6.9a, mode is well confined in the smaller core region. In Fig. 6.9a, the field extends in the silica bridge area (in-between the holes) in both x-axis and y-axis to nearly $2.2 \mu\text{m}$ from the centre. In this case, the field expands a bit in the air hole region. Where as, in Fig. 6.9b, the field extends in the silica bridge area in both x-axis and y-axis to nearly $10.0 \mu\text{m}$ from the centre. In this case, the field hardly extends inside the air hole. Since W , H , and S are increased, modal confinement is higher. In both figures, the mode is symmetrical and in this case, the presence of 90 degree rotational symmetry is clearly visible which

means fundamental quasi-TE (H^y_{11}) and quasi-TM (H^x_{11}) mode will degenerate. Fundamental quasi-TM (H^x_{11}) mode is not shown here.

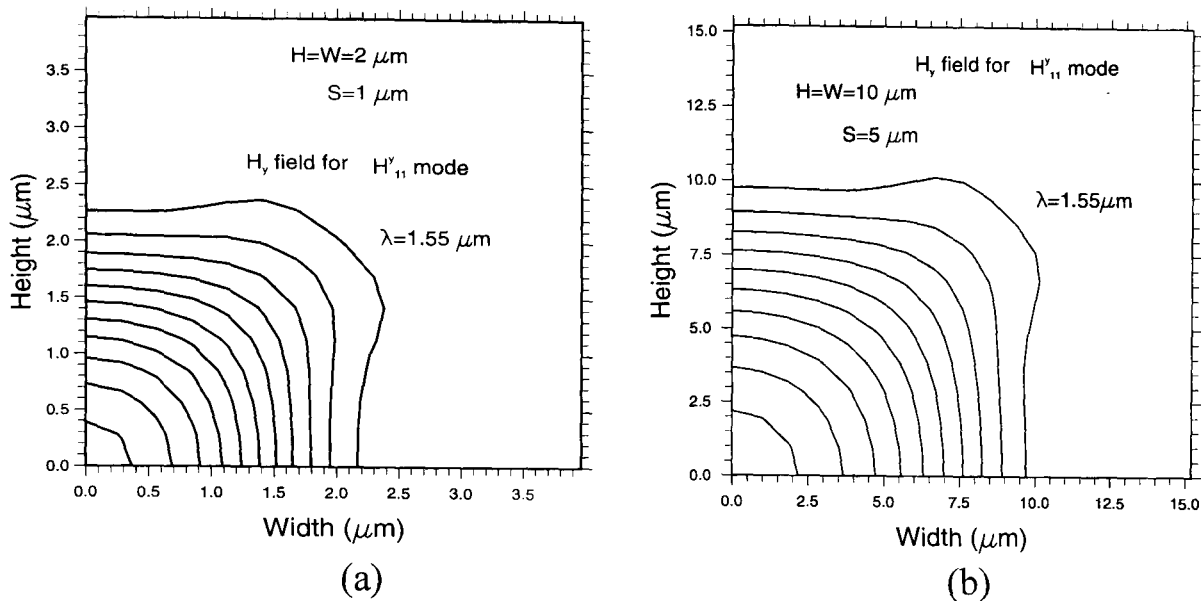


Fig. 6.9: The dominant H_y field profile of the fundamental quasi-TE (H^y_{11}) mode at $\lambda = 1.55 \mu\text{m}$, when separation between the holes (a) $S = 1 \mu\text{m}$ and (b) $S = 5 \mu\text{m}$.

Variations of the effective indices with the separation are shown in Fig. 6.10. In this case, the height and width of the holes are kept fixed at $10 \mu\text{m}$, but only their separation, S , is varied. It can be noted that as the separation (S) is increased, the effective indices are increased. This arises because, with the fixed hole size (of air), an increase in the spacing between them (made from silica) increases the fill factor, and so the equivalent index of the cladding increases. However, as the equivalent index of the cladding increases, the core index value remains constant, the index contrast between the core and cladding is reduced progressively, as the separation between the holes is increased. It can be observed that the fundamental H^x_{11} mode reaches its cutoff value when the separation (S) is $22 \mu\text{m}$, however for the H^y_{21} mode, this cutoff condition is reached when the $S = 17 \mu\text{m}$. In a qualitative way, it can be argued that at the cutoff point the spacing between the holes are too large to confine the modes inside the core region. It should be noted that for the same waveguide dimensions, a higher index contrast is needed for the higher order modes to be guided and hence for a PCF, the higher order mode reach their cutoff values at the smaller values of the S .

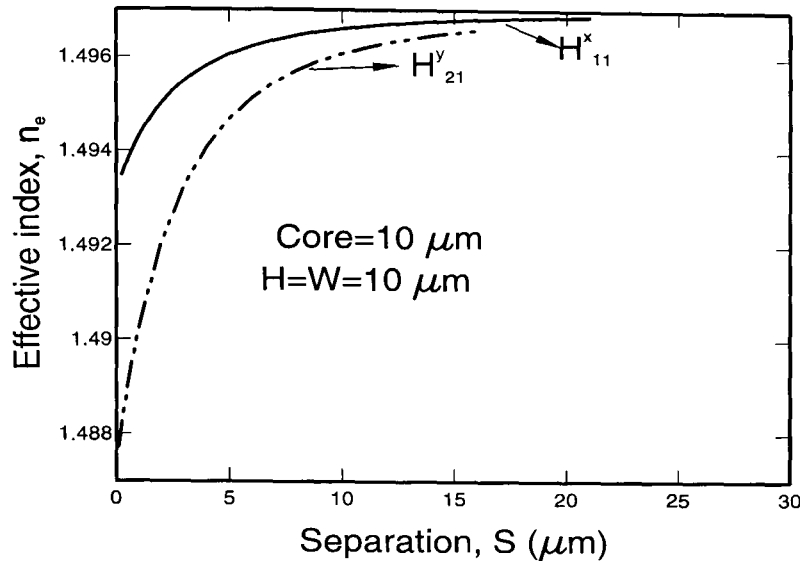


Fig. 6. 10: Variation of the effective indices with separation between the air-holes.

The dominant H_y field profile and its 3-D view for the fundamental H^y_{11} mode are shown in Figs. 6.11a and 6.11b, respectively when separation between the two nearest holes is $5 \mu\text{m}$ at wavelength $\lambda = 1.55 \mu\text{m}$. In this case, full structure of the field is considered. It can be clearly visible from these figures that core is created exactly at the centre of the structure. The optical field is well confined in the core region for a smaller value of S . Fig. 6.11b has one peak.

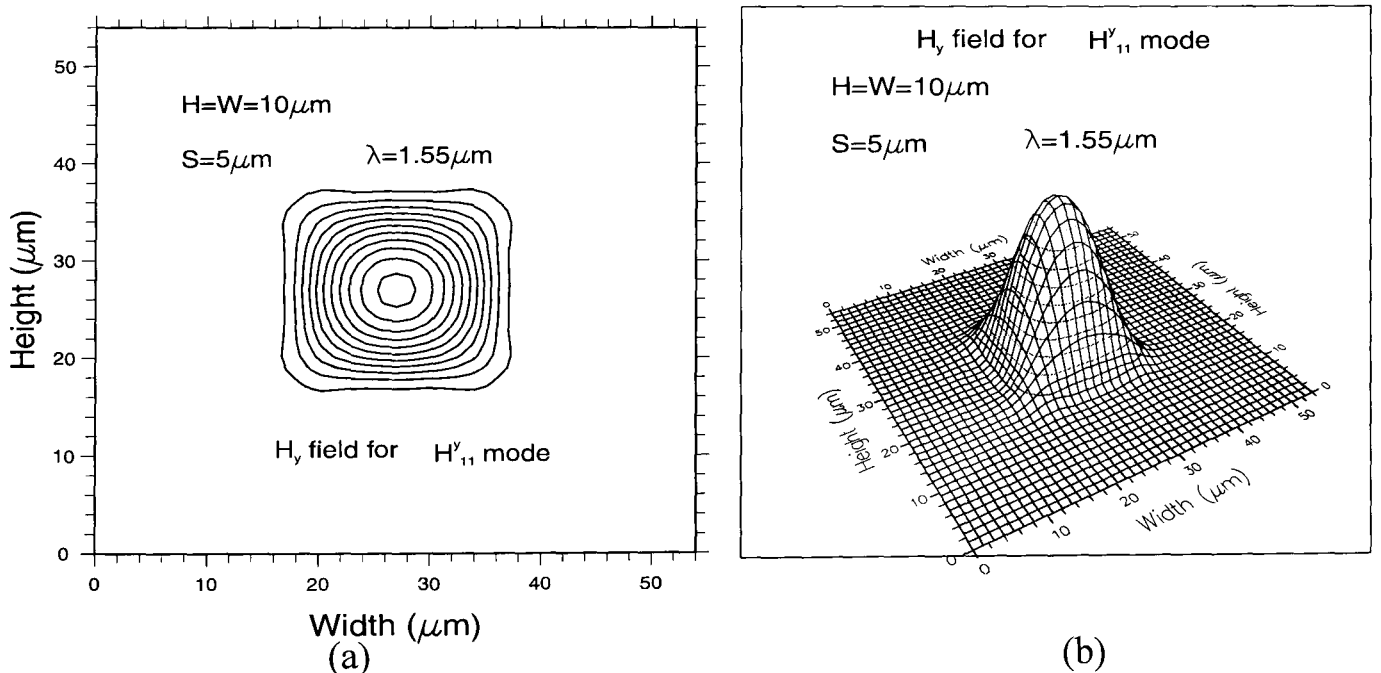


Fig. 6.11: (a) The dominant H_y field profile and (b) the 3-D view of the dominant H_y field profile of the fundamental quasi-TE (H^y_{11}) mode when separation between the holes, $S = 5 \mu\text{m}$ at $\lambda = 1.55 \mu\text{m}$.

The effect of higher separation ($S = 12.0 \mu\text{m}$) is shown in Figs. 6.12a and 6.12b for the dominant H_y field profile and its 3-D view of the fundamental H^y_{11} mode, respectively. Compared to Figs. 6.11a and 6.11b, it can be clearly noticed that the dimension of the dominant H_y field profile for the fundamental H^y_{11} mode is well confined when $S = 5.0 \mu\text{m}$. It can be observed that as the separation between the holes is increased, the optical fields are allowed to leak thorough these silica bridges. The encroachment of the field in the silica bridge, away from the core, is clearly visible in these figures.

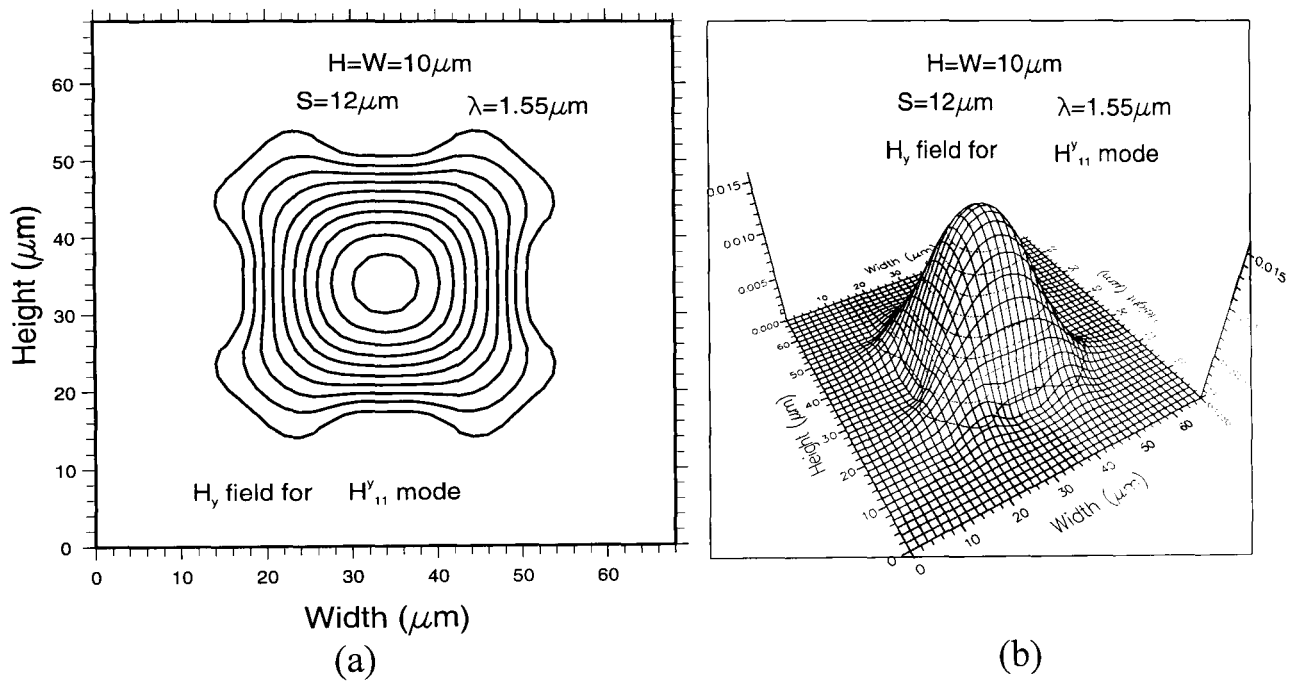


Fig. 6.12: (a) The dominant H_y field profile and (b) the 3-D view of the dominant H_y field profile of the fundamental quasi-TE (H^y_{11}) mode when separation between the holes, $S = 12 \mu\text{m}$ at $\lambda = 1.55 \mu\text{m}$.

Variation of the modal hybridness with the separation between the air-holes for the fundamental quasi-TE (H^y_{11}) and quasi-TM (H^x_{11}) modes is shown in Fig. 6.13. In this case, the height and width of the holes are kept fixed at $10 \mu\text{m}$, but their separation, S , is varied. It can be noted that as the separation (S) is increased up to $6 \mu\text{m}$, modal hybridness (non-dominant field/dominant field) is also increased. When the separation (S) is increased from $6 \mu\text{m}$ to $21 \mu\text{m}$, modal hybridness is decreased. It can also be noted that both fundamental quasi-TE (H^y_{11}) and quasi-TM (H^x_{11}) modes reach their cutoff value when $S = 21 \mu\text{m}$. Because of structural symmetry, as shown in Fig. 6.3, fundamental quasi-TE (H^y_{11}) and quasi-TM (H^x_{11}) mode degenerates.

Therefore, fundamental quasi-TE (H^y_{11}) and quasi-TM (H^x_{11}) modes show similar characteristics.

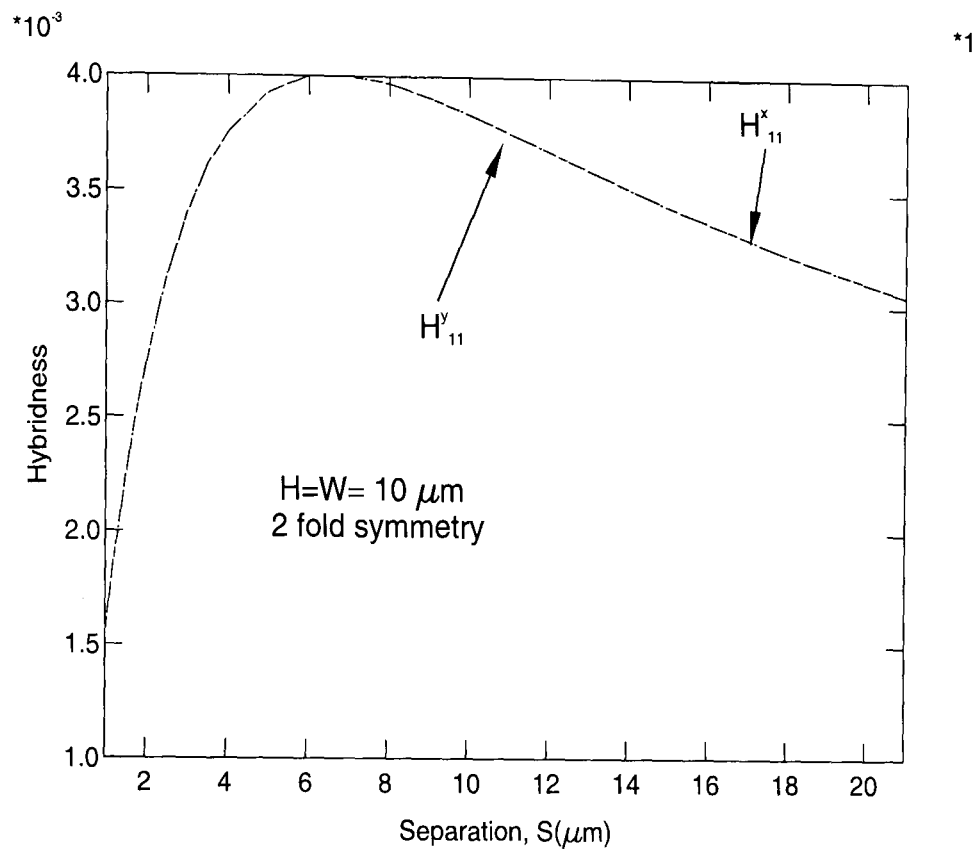


Fig. 6.13: Variation of the modal hybridness with the separation between the air-holes

6.5 Results of Square Lattice PCF with Rectangular Air Holes

6.5.1 Effects of Operating Wavelength

Next, the effect of square lattice PCF with rectangular air holes is studied. The variations of the effective indices with the operating wavelength, λ , are shown in Fig. 6.14. In this case, the height, width, and the separation of the holes are kept fixed at $1 \mu\text{m}$, $4 \mu\text{m}$, and $1 \mu\text{m}$, respectively. Due to material dispersion [Agrawal], the refractive index of silica reduces monotonically with the wavelength, which is shown a dashed line, labeled as n_g . The variations of the fundamental and higher order quasi-TE and TM modes are also shown in Fig. 6.14. It can be observed that the effective indices of the higher order modes are lower than that of the fundamental modes. It can also be noted that the effective indices for the quasi-TM (H^x_{mn})

modes are slightly lower than the corresponding quasi-TE (H_{mn}^y) modes for a given wavelength, as the width is larger than its height.

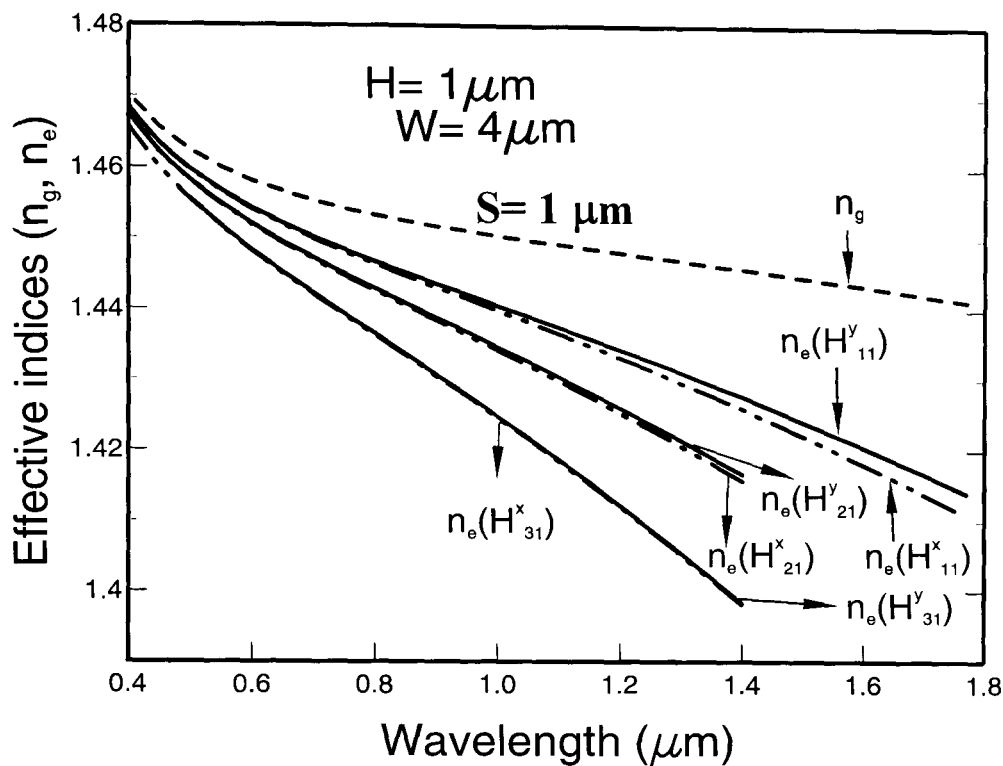


Fig. 6.14: Variation of the effective indices with the wavelength for the rectangular air-holes PCF.

The variations of the spot-size with the wavelength, for the fundamental and higher-order quasi-TM modes, are shown in Fig. 6.15. In this case, the spot-size is defined as the area where the field intensity is greater than $1/e^{\text{th}}$ of the maximum field intensity (power intensity is $1/e^2$). It can be observed that as the operating wavelength is increased, the waveguide dimensions are reduced compared to the operating wavelength and the spot-size also increases since mode approaches its cutoff condition and so expands. It can be observed that the spot-size for the higher order modes, at a given wavelength, are larger than that of the fundamental mode, as they are less confined as the mode order is increased.

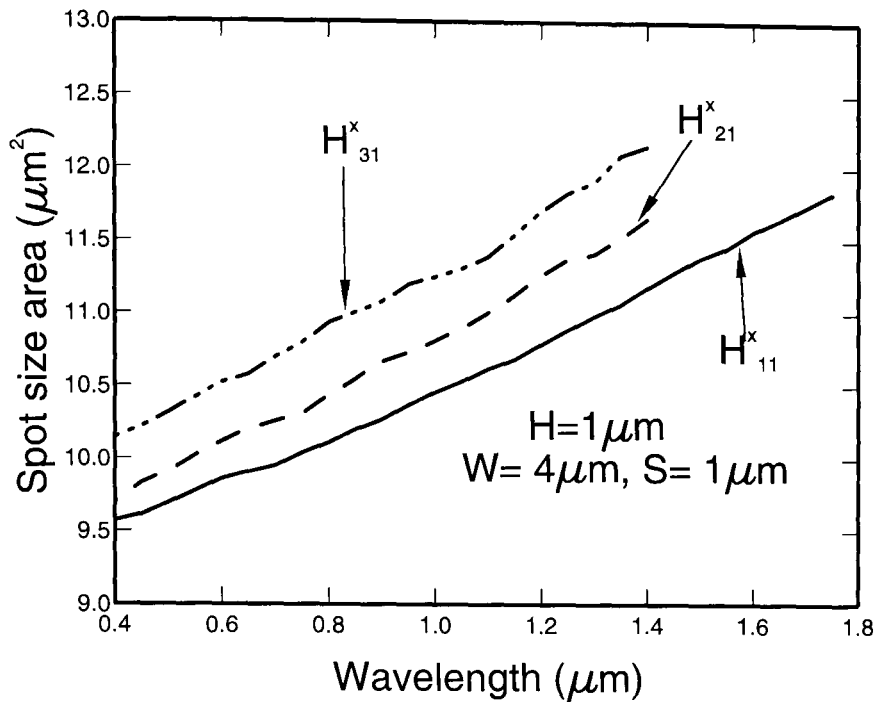


Fig. 6.15: Variation of the spot-size with the operating wavelength.

The variations of the power confinements (expressed as a percentage) in the silica region with the wavelength for the quasi-TM modes are shown in Fig. 6.16. It can be noted that as the wavelength is increased and the modes are expanded, more optical energy extends into the air-hole regions and as a consequence the modal confinement in silica is reduced. It can be observed that the power confinement for the higher order modes is smaller, compared to that of the fundamental mode as they are less confined.

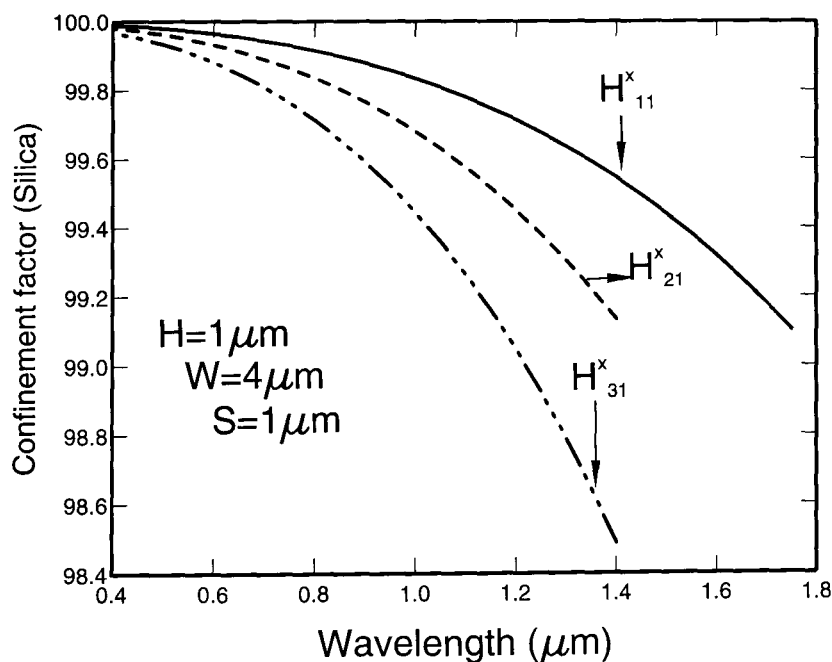


Fig. 6.16: Variation of the power confinement with the operating wavelength.

The variations of the modal hybridness with the wavelength are shown in Fig. 6.17 for the fundamental and higher order quasi-TE and TM modes. It can be noted that the modal hybridness increases as the operating wavelength is increased, since in this case the modal confinement is reduced and the modal field is more affected by the higher field strength at the core/cladding interfaces. It can be seen that the modal hybridness of the quasi-TM modes is higher than that of the quasi-TE modes. It can also be observed that the modal hybridness of the higher order modes are larger, as these modes are more extended in the air-hole regions.

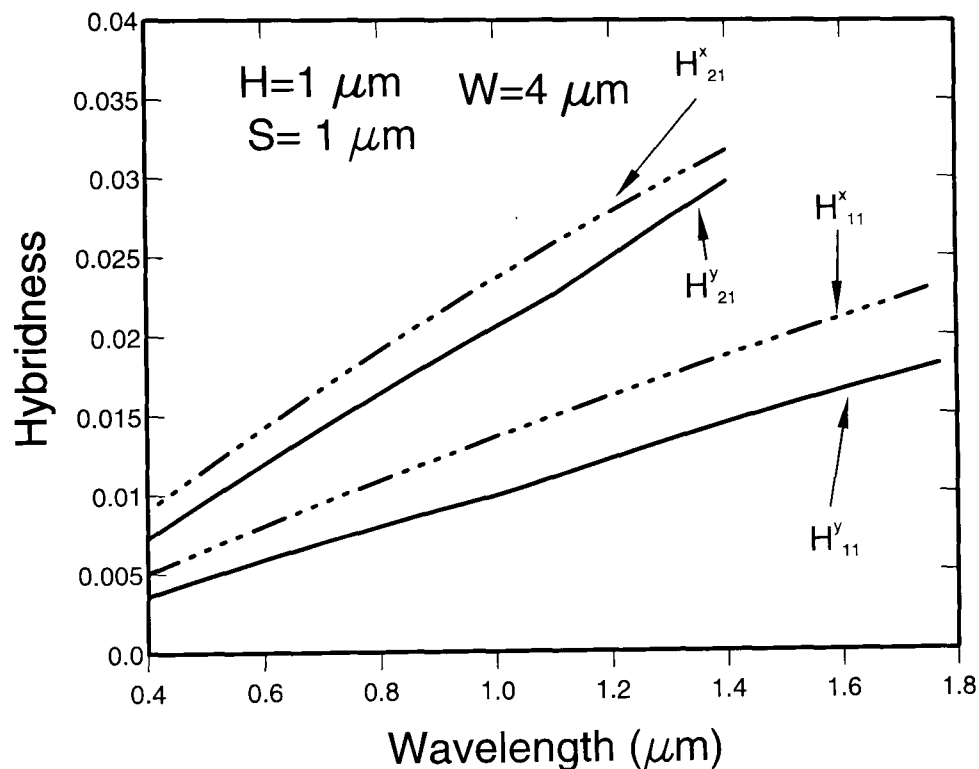


Fig. 6.17: Variation of the modal hybridness with the wavelengths.

The variation of the beat length with the operating wavelength is shown in Fig. 6.18. In this case the beat length, L_B is defined as:

$$L_B = \frac{\pi}{|\beta_y - \beta_x|} \quad [6.1]$$

Where, β_y and β_x are the propagation constants of the corresponding quasi-TE and TM modes, respectively. It should be noted that as the operating wavelength increases, the effective indices (n_e) for both the TE and TM modes reduce but Δn_e increases, where Δn_e is the difference between their effective indices. It can be observed that with increasing operating wavelength, the

beat length is reduced. This is due to the reason that beat length is inversely proportionate to the Δn_e .

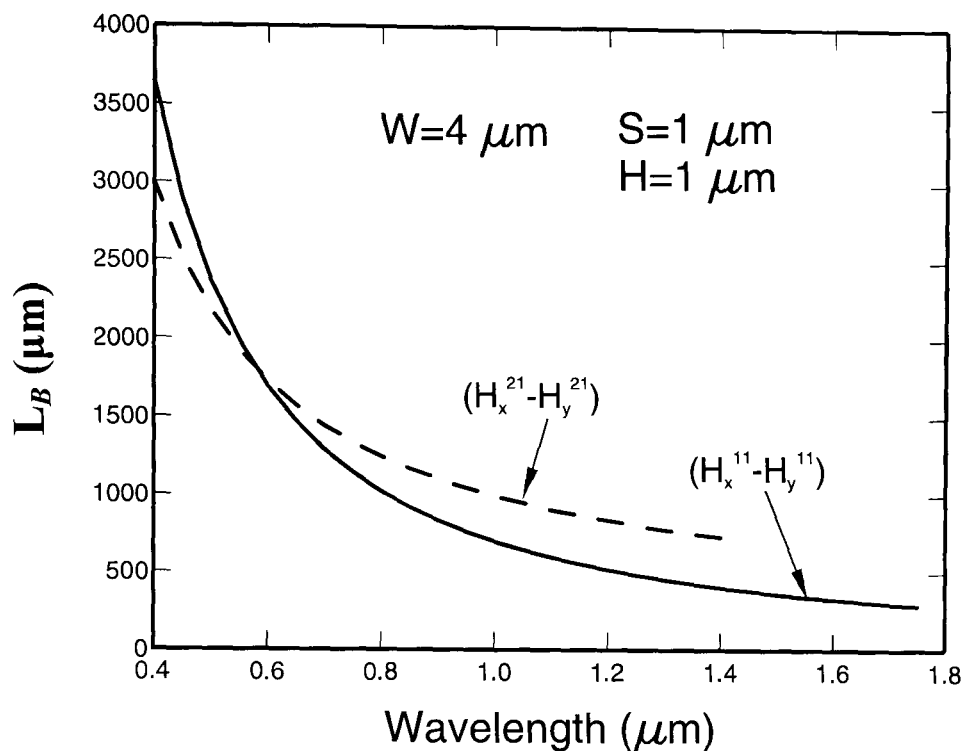


Fig. 6.18: Variation of the beat length with the operating wavelength.

6.6 Comparison Results of Square and Rectangular Air Holes

The variations of the effective indices with the operating wavelength for both square and rectangular air-holes PCF are shown in Fig. 6.19. As mentioned earlier, due to material dispersion [Agrawal], the refractive index of silica reduces monotonically with the wavelength, which is shown as dashed line, labeled as n_g . The variations of the fundamental and higher order quasi-TE modes are shown in Fig. 6.19. In this case, area of the air holes were same $4 \mu\text{m}^2$ and separation between the air holes fixed at $1 \mu\text{m}$. It can be observed that the effective indices of the higher order modes are lower than that of the fundamental modes for both square and rectangular air-holes PCF. It can also be noted that the effective indices of the quasi-TE (H_y^{11}) mode for rectangular air-holes PCF are slightly lower than the corresponding quasi-TE (H_y^{11}) modes square air-holes PCF for a given wavelength, as in rectangular air-holes the width is larger than its height.

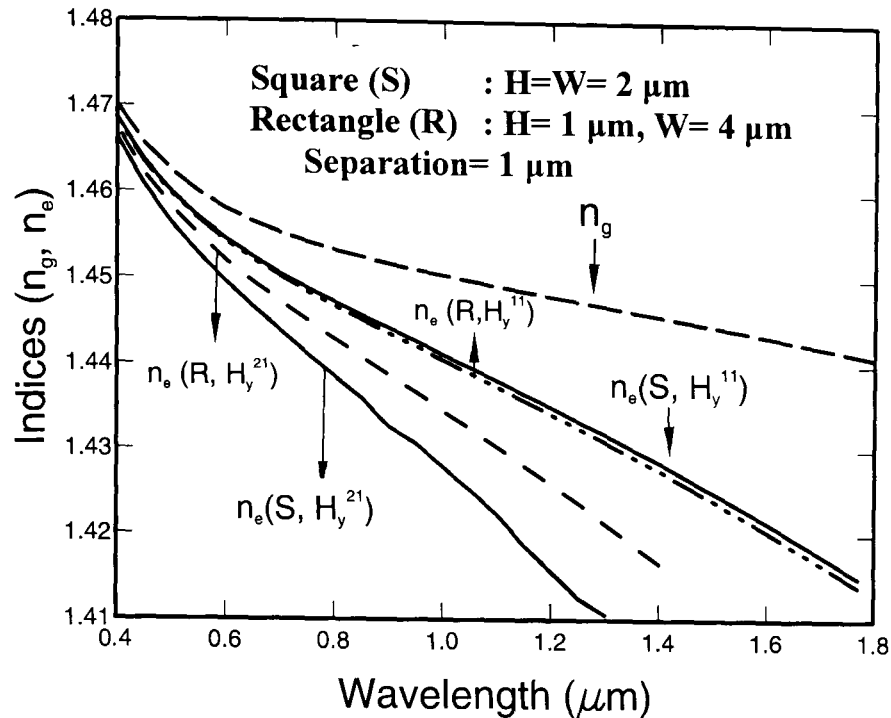


Fig. 6.19: Variation of the effective indices with the wavelength for the square and rectangular air-holes PCF.

The group velocity dispersion (GVD) is one of the most important modal properties of an optical waveguide and this parameter can be defined as:

$$D(\lambda) = -\frac{\lambda}{c} \frac{\partial^2 n_e}{\partial \lambda^2} \quad [6.2]$$

Where, n_e is the effective index of a given mode, c is the speed of light in a vacuum, λ is operating wavelength [Rahman *et al.*, 2005b].

Variations of the GVD with the wavelength for a square hole and a rectangular hole, but both with $4 \mu\text{m}^2$ hole areas, are shown in Fig. 6.20 for the dominant H_{y11}^y mode. It can be noted that the variations of the GVD with the wavelength are almost similar for the both cases, since they had exactly the same cross-sectional areas and the slight difference observed is probably due to their shapes, which are different. It can be further seen that for both cases, GVD is positive over the wavelength range 0.95 and 1.5 μm , with a maximum value of 120 ps/nm.km at $\lambda = 1.25 \mu\text{m}$.

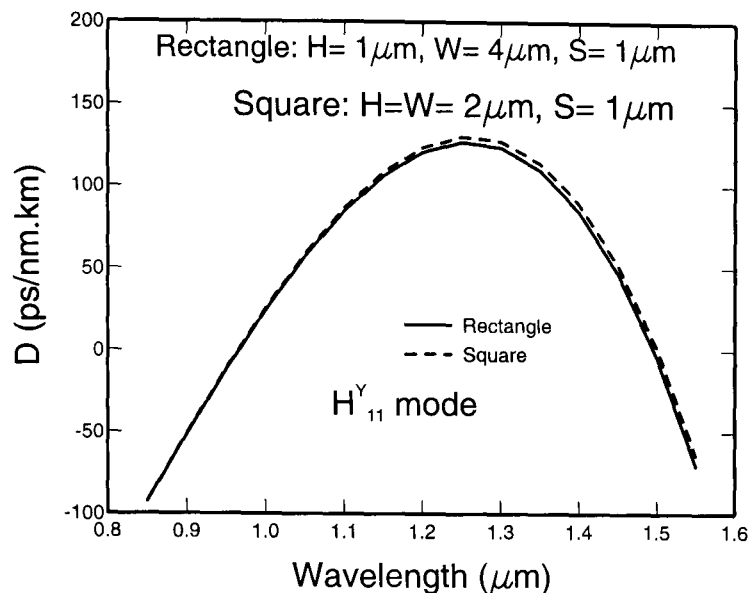


Fig. 6.20: Variation of the GVD with the wavelength for square-hole and rectangular-hole PCFs.

6.7 Summary

In this chapter, a rigorous analysis of photonic crystal fibre is presented, to understand the basic properties of planar photonic crystal fibres. Important design parameters, such as the effective indices, the modal field profile, the spot-sizes, the power confinement, the modal hybridness, beat length and the GVD are shown for planar photonic crystal fibre with square, and rectangular air holes in a square lattice, by using rigorous full-vectorial finite element based approach. The variation of the GVD, an important optical parameter, shows the effect of the hole dimension and it may be possible to design a planar PCF with a specific GVD, or other optical properties, by adjusting different fabrication parameters.

In the following chapter, the modal properties of a hexagonal lattice PCF with circular hole are studied.

Chapter 7

Characterization of Hexagonal lattice PCF

7.1 Introduction

Modal solutions of photonic crystal fibre (PCF) with symmetrical and asymmetrical circular air holes in a hexagonal matrix are presented by using a rigorous full-vectorial finite element-based approach, to understand the basic properties of photonic crystal fibres. The effective indices, mode field profiles, spot-sizes, modal hybridness, power confinements, and group velocity dispersion values have been determined and are shown and discussed. Moreover, the variations of the modal fields (H_y) in the normalized x direction are also obtained and reported in this chapter.

This research simulated a realistic photonic crystal fibre characterized by a hexagonal distribution of air holes with a central defect. The hole diameter (d), the centre-to-centre distance between two nearest air-holes or pitch (Λ), and the wavelength (λ) of light are free parameters that have changed as required.

In this case, the available two-fold symmetry has been exploited and only a quarter of the structure is shown. In this chapter, more than 28000 first order irregular size triangular elements have been used to represent only one-fourth of the PCF cross-section and a typical computational time on a 2 GHz PC is less than one minute.

7.2 Modelling of Hexagonal Lattice PCF with Circular Air Holes

Hexagonal-lattice photonic crystal fibre is designed first with symmetry air-holes then with asymmetry air-holes in order to get highly birefringence PCF.

7.2.1 Symmetry Air Holes

A typical PCF structure with holes in a hexagonal honeycomb configuration is shown in Fig. 7.1. For a regular array of holes of equal size, the hole diameter is taken as d μm with Λ , as the pitch length. A missing hole at the centre, with its higher index value compared to the lower equivalent index in the cladding region, can guide the light as does the core of a typical optical waveguide.

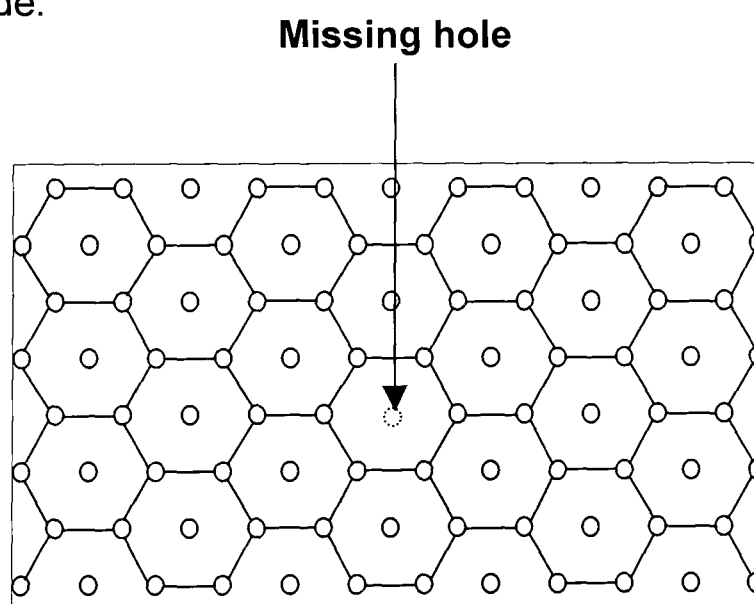


Fig. 7.1: Schematic diagram of a PCF with hexagonal array of air-holes where the middle hole is missing.

The distance between the two nearest holes from their centres is shown in Fig. 7.2. The hexagon (all sides being the same length) has taken

out from hexagonal honeycomb, as shown in Fig. 7.1, to illustrate the distance between the air-holes from their centre. In this case, the coordinates of the centre is 0, 0. First air hole on the right, with its x and y coordinates are $\Lambda, 0$.

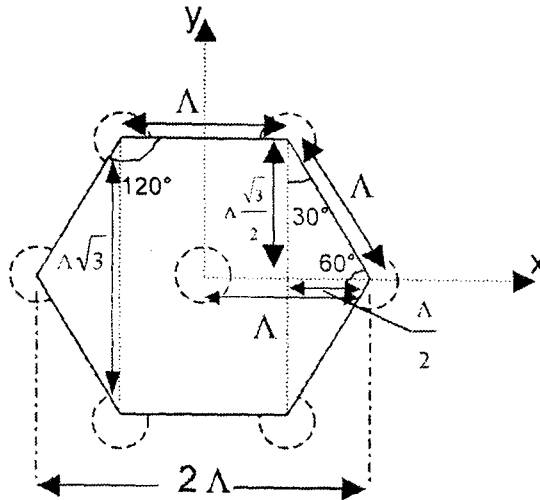


Fig. 7.2: Shows the distance between the air-holes from their centre.

7.2.1.1 Representation of Hole by Triangles

In Fig. 7.3, it is shown that a circular hole is represented by a number of triangles to form a circle. For a smaller number of mesh used, it is clear that the rectangular triangle is not adequately representing a circle.

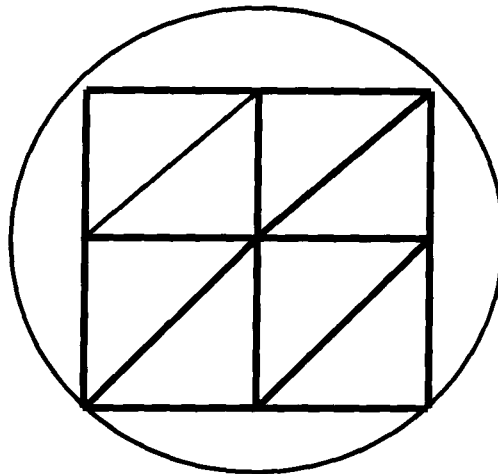


Fig. 7.3: Representation of circular hole by number of triangles.

However, when more triangles are used to represent the circle, the result improves as shown in Fig. 7.4. The representation of the circle is still approximate, however if more fine mesh size is used than the representation would get better. In the computer program, totalling in the x and y direction have been used the fine mesh of the order 120 x 120.

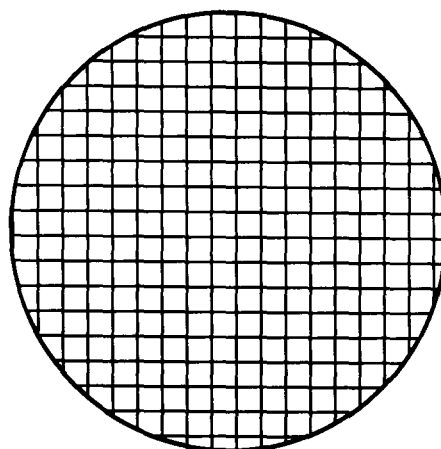


Fig. 7.4: Representation of holes by rectangular blocks (each with two triangles) using a very fine mesh.

7.2.2 Asymmetry Air Holes

The two-fold symmetry of the whole PCF structure, with its corresponding distances on both x and y directions, is shown in Fig. 7.5. In this case, all the air-holes have diameter d_1 , but only air-hole numbered 4 has diameter d_2 .

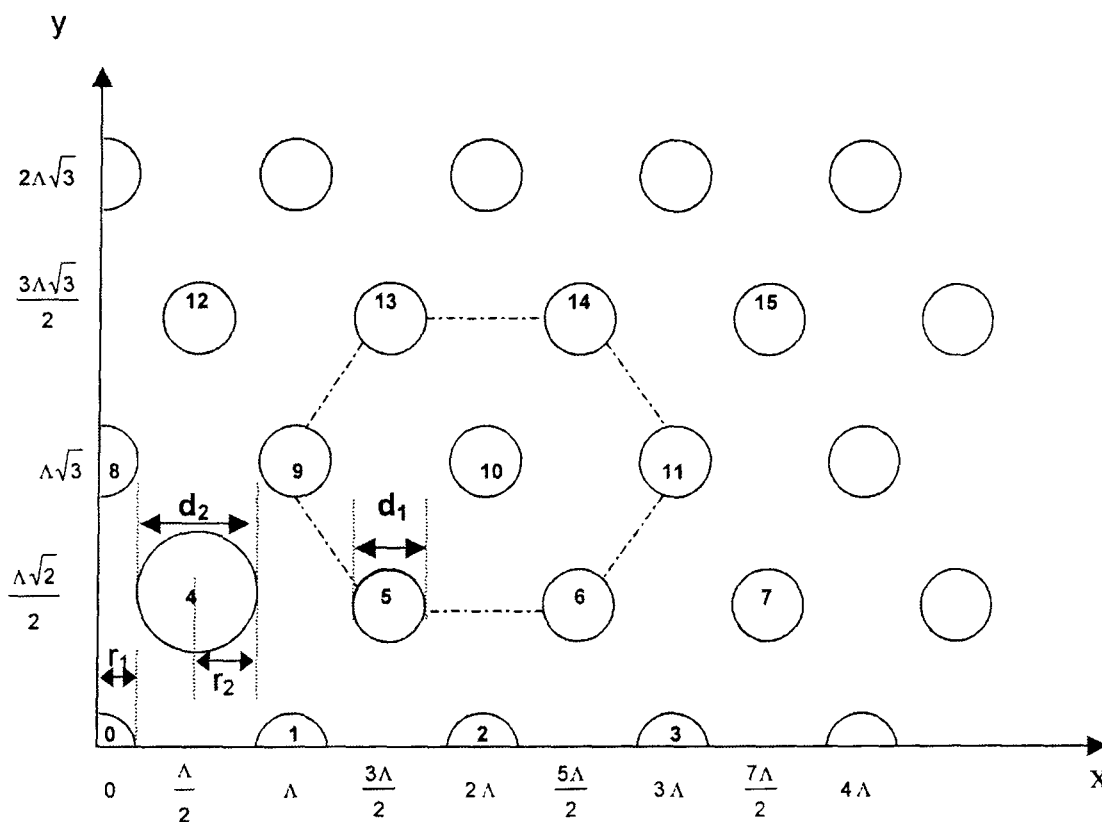


Fig. 7.5: Illustrates the two-fold symmetry of the structure of the waveguide and its corresponding distances on the x and y axis.

The difference in the hole diameter of this type of PCF have been reported [Saitoh and Koshiba, 2003b] to yield higher birefringence in these waveguides. Consequently, a similar structure is investigated later in this

project. The following x and y coordinates are introduced in the computer code to produce a hexagonal waveguide structure:

$$\begin{aligned}
 x_0=0, y_0=0 & & x_1=\Lambda, y_1=0 & & x_2=2\Lambda, y_2=0 & & x_3=3\Lambda, y_3=0 \\
 x_4=\frac{\Lambda}{2}, y_4=\frac{\Lambda\sqrt{3}}{2} & & x_5=\frac{3\Lambda}{2}, y_5=\frac{\Lambda\sqrt{3}}{2} & & x_6=\frac{5\Lambda}{2}, y_6=\frac{\Lambda\sqrt{3}}{2} \\
 & & x_7=\frac{7\Lambda}{2}, y_7=\frac{\Lambda\sqrt{3}}{2} \\
 x_8=0, y_8=\Lambda\sqrt{3} & & x_9=\Lambda, y_9=\Lambda\sqrt{3} & & x_{10}=2\Lambda, y_{10}=\Lambda\sqrt{3} \\
 & & x_{11}=3\Lambda, y_{11}=\Lambda\sqrt{3} \\
 x_{12}=\frac{\Lambda}{2}, y_{12}=\frac{3\Lambda\sqrt{3}}{2} & & x_{13}=\frac{3\Lambda}{2}, y_{13}=\frac{3\Lambda\sqrt{3}}{2} & & x_{14}=\frac{5\Lambda}{2}, y_{14}=\frac{3\Lambda\sqrt{3}}{2} \\
 & & x_{15}=\frac{7\Lambda}{2}, y_{15}=\frac{3\Lambda\sqrt{3}}{2}
 \end{aligned}$$

7.3 Numerical Results of Identical Hole PCF

7.3.1 Results of a PCF when d/Λ is Varying

Initially, the effect of the hole diameter, d , on the modal properties is investigated and the variations of the effective index and the spot-size for the fundamental quasi-TE (H_{11}^y) mode with the normalized d/Λ dimension are shown in Fig. 7.6. Here the pitch length, Λ , has been kept fixed at $2.2 \mu\text{m}$.

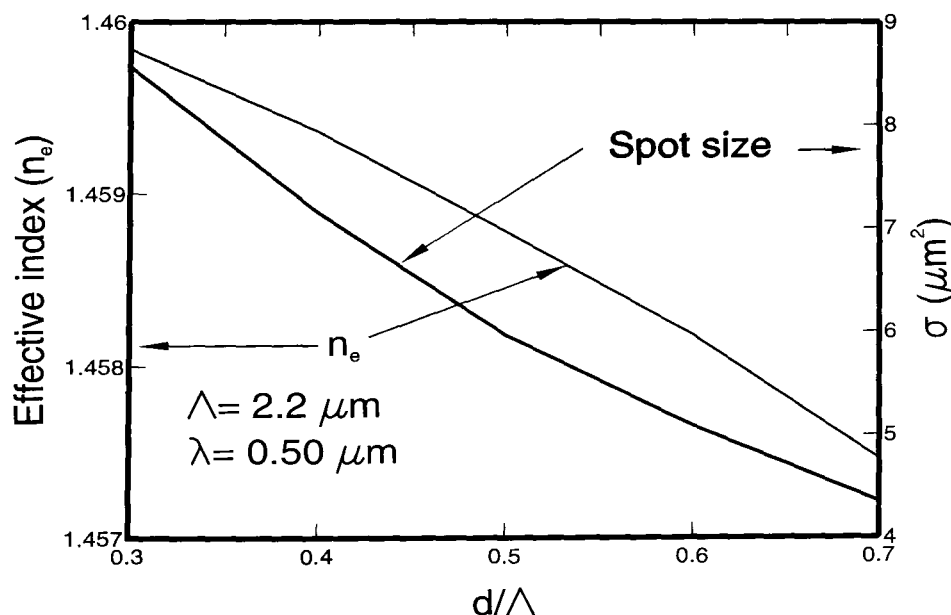


Fig. 7.6: The variation of the effective index and spot-size with the normalized hole diameter d/Λ .

In Fig. 7.6, the refractive index of the silica is taken as 1.46232 at the operating wavelength of $0.5 \mu\text{m}$. With the pitch, Λ , fixed at $2.2 \mu\text{m}$, as the hole diameter, d , is increased the equivalent index of the air-hole cladding region is reduced, which increases the index contrast between the effective cladding and the homogeneous silica core. Although the lowered cladding index also reduces the modal effective indices, the increased index difference makes the mode better confined. In this figure, it can also be observed that as the hole diameter is increased, the spot-size (σ) is reduced. This arises because the enlargement of the holes restricts the escape of the modal field out of the core area.

The dominant H_y field profile of the fundamental quasi-TE (H_{11}^y) mode for values of $d/\Lambda = 0.3$ and 0.7 at the operating wavelength of $0.5 \mu\text{m}$ are shown in Figs. 7.7a and 7.7b, respectively. In Fig. 7.7a, it can be clearly seen that for lower values of the air-hole diameter, the field extends in the silica bridge area (in-between the holes). In this case, the presence of 60 degrees rotational symmetry is clearly visible. On the other hand, for the larger air-holes, as shown in Fig. 7.7b, the field is more confined in the core, as it is restricted from the low-index air regions.

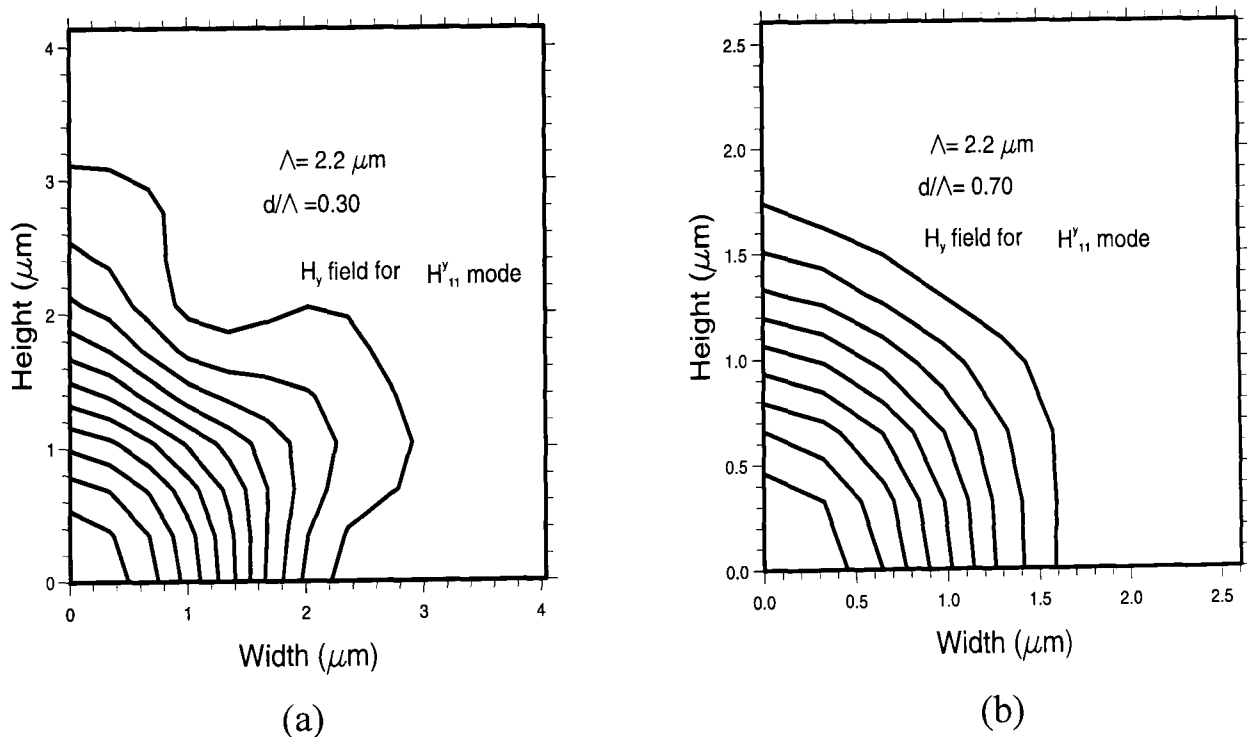


Fig. 7.7: The dominant H_y field profile of the fundamental quasi-TE mode for (a) $d/\Lambda = 0.3$ and (b) $d/\Lambda = 0.7$.

Very close observation of Fig. 7.7 reveals that the field expansion in the vertical (y) direction is larger than that in the horizontal (x) direction, which indicates that the 90 degrees rotational symmetry does not exist. The effect of the hole diameter on the spot-size is clearly visible, and its variation has been shown in Fig. 7.6.

7.3.2 Results of a PCF when Wavelength is Varying

7.3.2.1 Results of a PCF when $d/\Lambda = 0.50$

The effect of mesh refinement is shown in Fig. 7.8. In this figure, the variation of the effective indices (n_e) for 120*120 and 80*80 meshes of the fundamental quasi-TE (H_{11}^y) mode with the operating wavelength are shown by a solid line and a dashed line, respectively. It can be noted that the effective index (n_e) for both 120*120 (28800 elements) and 80*80 (12800 elements) meshes reduce with the wavelength as shown in Fig. 7.8, and then approaches the modal cutoff value. It can also be noted that the effective index of 80*80 mesh is lower (with the operating wavelength) than that of the effective index of 120*120 mesh, which yield slightly more accurate results. That means 120*120 mesh gives better modal solution results compared to 80*80 mesh. However, results are reasonably stable with mesh refinements. For 120*120 and 80*80 mesh, a typical computational time on a 2 GHz PC is less than one minute and around 30 seconds, respectively.

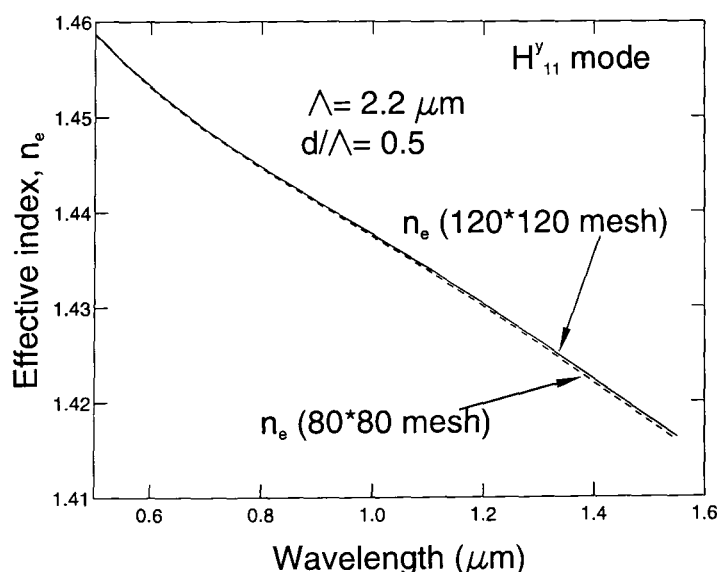


Fig. 7.8: Variation of the effective indices of the fundamental modes with the wavelength for 120*120 and 80*80 meshes.

Next, a PCF with identical holes with a pitch, $\Lambda = 2.2 \mu\text{m}$ and identical hole diameter $1.1 \mu\text{m}$ yielding d/Λ ratio of 0.50 has been investigated. The variation of the silica index (n_g) and the effective index (n_e) of the fundamental quasi-TE (H_{11}^y) and the second-order H_{21}^y modes with the operating wavelength are shown in Fig. 7.9 by a solid line, a dashed line, and a dashed-dotted line, respectively. It can be noted that the silica index (n_g), as shown by a solid line, reduces monotonically with the wavelength due to material dispersion [Agrawal], as mentioned earlier. It can also be noted that the effective index (n_e) also reduces with the wavelength, which is due to both the material and waveguide dispersions and if the rate is larger then it approaches the modal cutoff value.

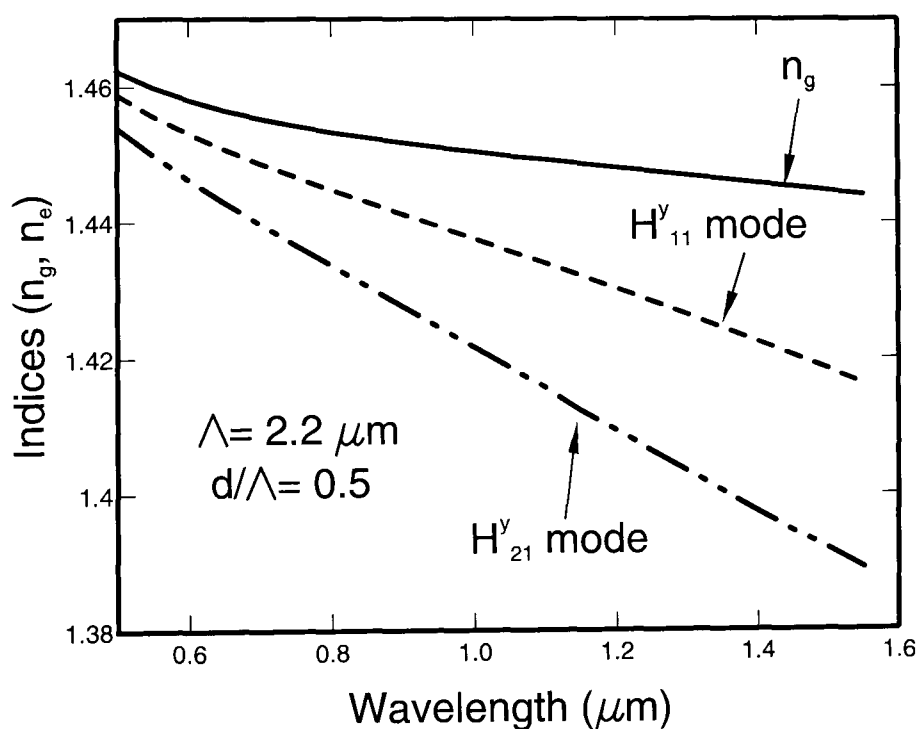


Fig. 7.9: Variation of the effective indices of the fundamental and higher order modes with the wavelength for a circular air-hole PCF.

The dominant H_y and the non-dominant H_x field profile for the fundamental quasi-TE (H_{11}^y) modes are shown in Figs. 7.10a and 7.10b, respectively, for operating wavelength of $0.5 \mu\text{m}$ and for $d/\Lambda = 0.5$. It can be seen from Fig. 7.10a that the field expands in both x and y directions, but slightly more in y direction (around $2.3 \mu\text{m}$) than that of x direction (around $1.9 \mu\text{m}$). The field profile in Fig. 7.10b is clearly shown to be lower in the core area. It has two peaks, and they are of opposite sign.

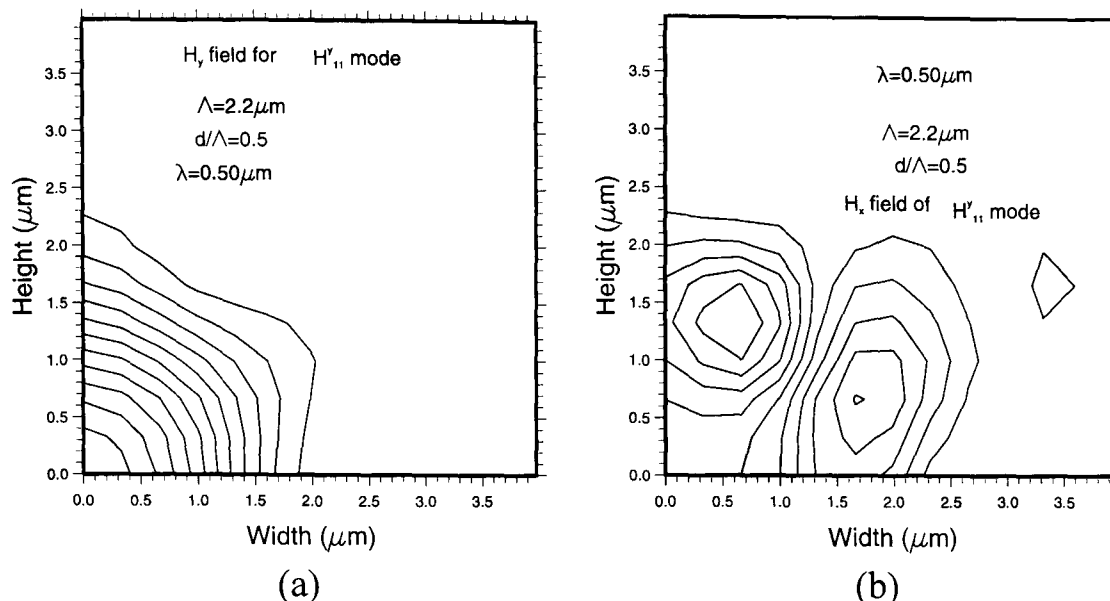


Fig. 7.10: (a) The dominant H_y and (b) non-dominant H_x field profiles of the fundamental quasi-TE mode at operating wavelength, $\lambda = 0.50 \mu\text{m}$.

Next, the effect of operating wavelength is studied. The dominant H_y field profile for the fundamental H_{11}^y mode is shown for operating wavelengths of $0.5 \mu\text{m}$ and $1.55 \mu\text{m}$, in Figs. 7.11a and 7.11b, respectively for $d/\Lambda = 0.5$.

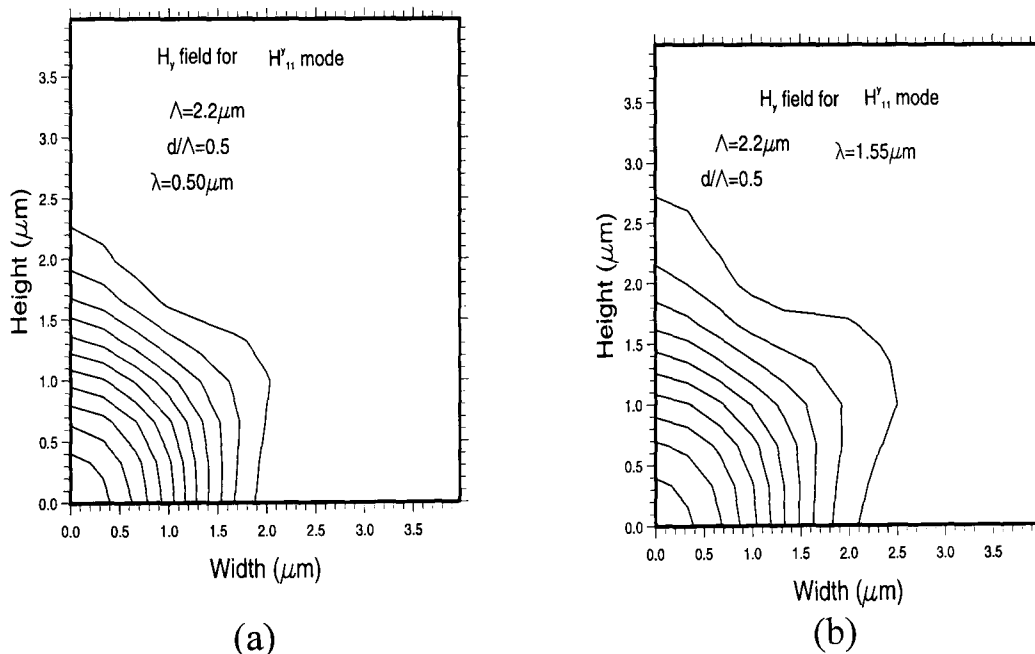


Fig. 7.11: The dominant H_y field profiles of the fundamental quasi-TE mode at operating wavelength of (a) $\lambda = 0.5 \mu\text{m}$ and (b) $\lambda = 1.55 \mu\text{m}$.

It can be seen in Fig. 7.11a, that at $\lambda = 0.5 \mu\text{m}$ for $d/\Lambda = 0.5$, the field expands more than that for $d/\Lambda = 0.7$ as shown earlier in Fig. 7.7b but less than that for $d/\Lambda = 0.3$ as shown in Fig. 7.7a. However, it can be observed that for a larger operating wavelength (in this case $\lambda = 1.55 \mu\text{m}$), the modal field profile

extends further into the air hole cladding region as the guide becomes more weakly confined. In this case, the field expands in both x and y directions more than that of at $\lambda = 0.50 \mu\text{m}$ as shown in Fig. 7.11a. It can also be observed that in both Fig. 7.10a and Fig. 7.11a for equal operating wavelength ($\lambda = 0.5 \mu\text{m}$), the modal field profile extends in both x and y directions similarly into the air-hole cladding region. In both cases, modal field is more confined.

The variation of the spot-size with the wavelength, for the fundamental quasi-TE (H_{11}^y) mode, is shown in Fig. 7.12 when $d/\Lambda = 0.50$. In this case, it can be observed that as the operating wavelength increases, the waveguide dimensions reduce compared to the operating wavelength and the spot-size also increases since the mode approaches its cutoff condition.

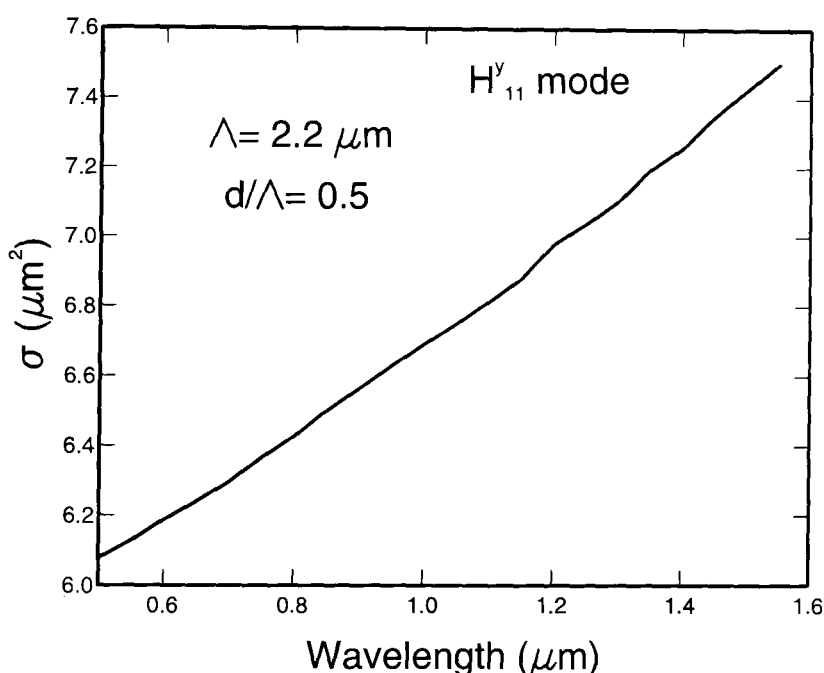


Fig. 7.12: Variation of the spot-size with the operating wavelength when $d/\Lambda = 0.50$.

The modal hybridness has been defined as the ratio of the non-dominant to the dominant field values. For the quasi-TE (H_{mn}^y) modes, the hybridness is the ratio of the non-dominant H_x field to the dominant H_y field. The variation of the field magnitude and modal hybridness with the wavelength of the fundamental quasi-TE mode is shown in Fig. 7.13, when $d/\Lambda = 0.50$. From this figure, it can be observed that as the wavelength

increases, the dominant H_y field reduces slightly (as the mode expands) but the non-dominant H_x field increases. As a consequence the modal hybridness, which is the H_x/H_y ratio, also increases with the operating wavelength. This occurs because in this case, as the modal confinement is reduced, the modal field is affected by the higher field strength at the air/silica interfaces.

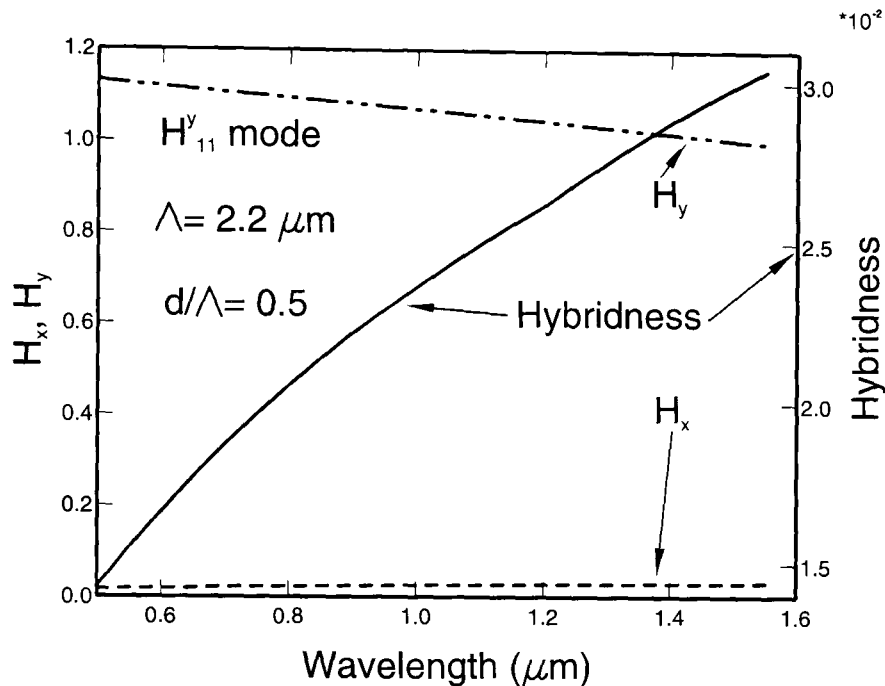


Fig. 7.13: The variation of the field magnitude and modal hybridness with the operating wavelength for $d/\Lambda = 0.50$.

As the mode expands, modal field encounters more onto the air-hole regions and the power leaking into the air-hole areas increases. This has significant effect of the modal leakage properties and also in the design of evanescent sensors, where modal properties can be influenced by introducing the sensing medium in these air-hole regions. The variation of the optical power in the silica region, P_s , with the operating wavelength is shown in Fig. 7.14 for the quasi-TE (H_{11}^y) mode when $d/\Lambda = 0.50$. It can be clearly observed that as the operating wavelength increases, the modal field expands, the spot-size increases, so the power in the air-holes increases and that in the silica region decreases. It should be noted that for the design of an evanescent sensor, the operating wavelength would be an important parameter for design optimization.

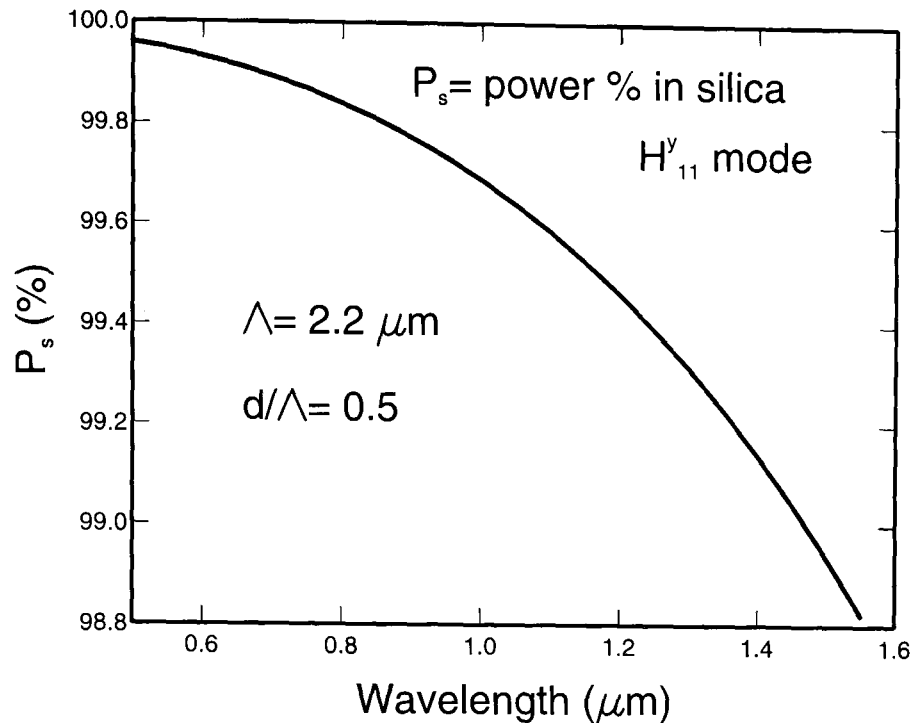


Fig. 7.14: The variation of the power confinement factor with the operating wavelength when $d/\Lambda = 0.50$.

7.3.2.2 Comparison Results of PCF when $d/\Lambda = 0.50$ and $d/\Lambda = 0.30$

The variation of the silica index and the effective index for the fundamental quasi-TE modes with the operating wavelengths are shown in Fig. 7.15. As mentioned earlier, due to the material dispersion [Agrawal], the refractive index of silica reduces monotonically with the wavelength, which is shown in this figure by a solid line and labeled as n_g . In this case the pitch, Λ , is taken as $2.2 \mu\text{m}$, with the diameter of the equal-size air holes either $0.66 \mu\text{m}$ or $1.1 \mu\text{m}$, yielding a normalized d/Λ ratio of 0.30 or 0.50, respectively. The variation of the effective index (n_e) of the fundamental quasi-TE (H_{11}^y) mode for d/Λ equal to 0.30 and 0.50 is shown by a dotted line and a dashed line, respectively. It can be noted that the reduction of the effective index is more rapid (with the operating wavelength) than that of the material index of silica, n_g , due to the additional modal dispersion besides the material dispersion (already shown by a solid line) [Rahman *et al.*, 2006b].

It can also be noted that the effective index also reduces with the wavelength, and the rate is larger and then approaches the modal cutoff value. It can be noted that when the hole diameters are larger, the effective index value is

lower, as in this case the equivalent cladding index is also lower with low silica/air fill factor due to the presence of larger size air holes.

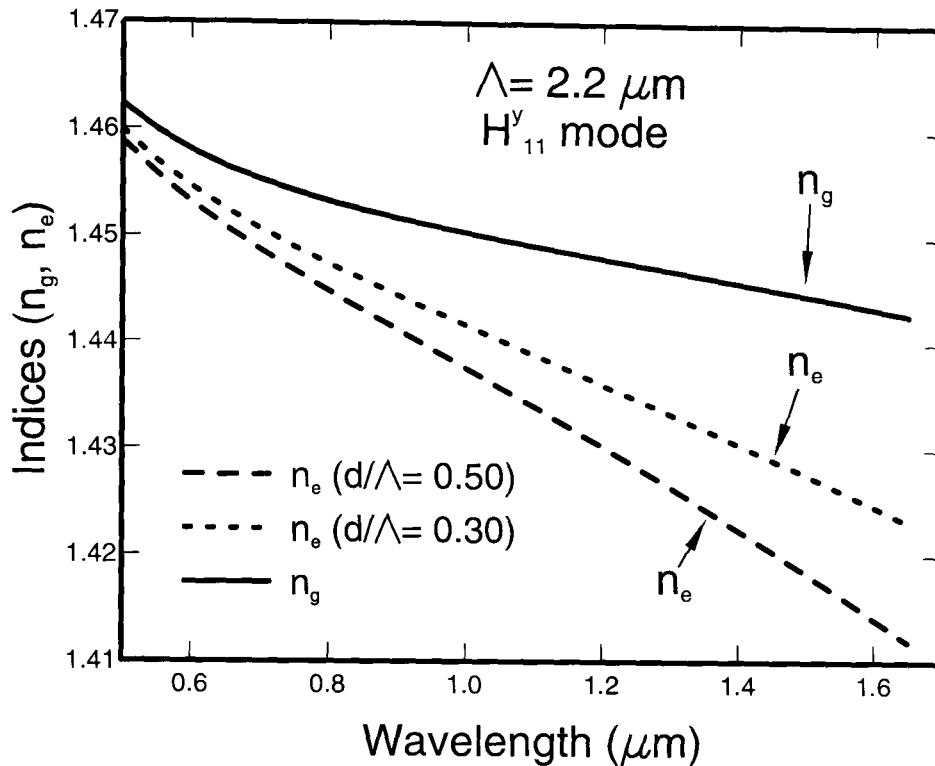


Fig. 7.15: Variation of the silica index and the effective indices with the wavelength for $d/\Lambda = 0.50$ and 0.30 .

As illustrated in Fig. 7.16 the variation of the modal hybridness (ratio of H^x and H^y) with wavelength, it can be observed that as the wavelength increases, modal hybridness also increases for both $d/\Lambda = 0.30$ and $d/\Lambda = 0.50$. As index contrast is higher for $d/\Lambda = 0.50$, hybridness is slightly higher than that of for $d/\Lambda = 0.30$. From Fig. 7.13 (for $d/\Lambda = 0.50$) it can be noticed that the value of H^y for dominant field decreases and the value of the H^x , which is a non-dominant field increases as the operating wavelength increases. However, at the same time it is also noticeable that the difference in the H^y and H^x decreases as the wavelength increases. As a result the modal hybridness, which is H_x/H_y ratio, increases with the operating wavelength. For lower λ , hybridness for $d/\Lambda = 0.30$ is larger and for higher λ , hybridness for $d/\Lambda = 0.50$ is higher. For $d/\Lambda = 0.50$, hybridness is expected to be higher as index contrast is higher. However, for a given λ , modal confinement is also higher due to large index contrast. So, overall hybridness is higher for $d/\Lambda = 0.50$, when approaches modal cutoff.

Similar study of the quasi-TM, H_{11}^x mode was also carried out, but not shown here.

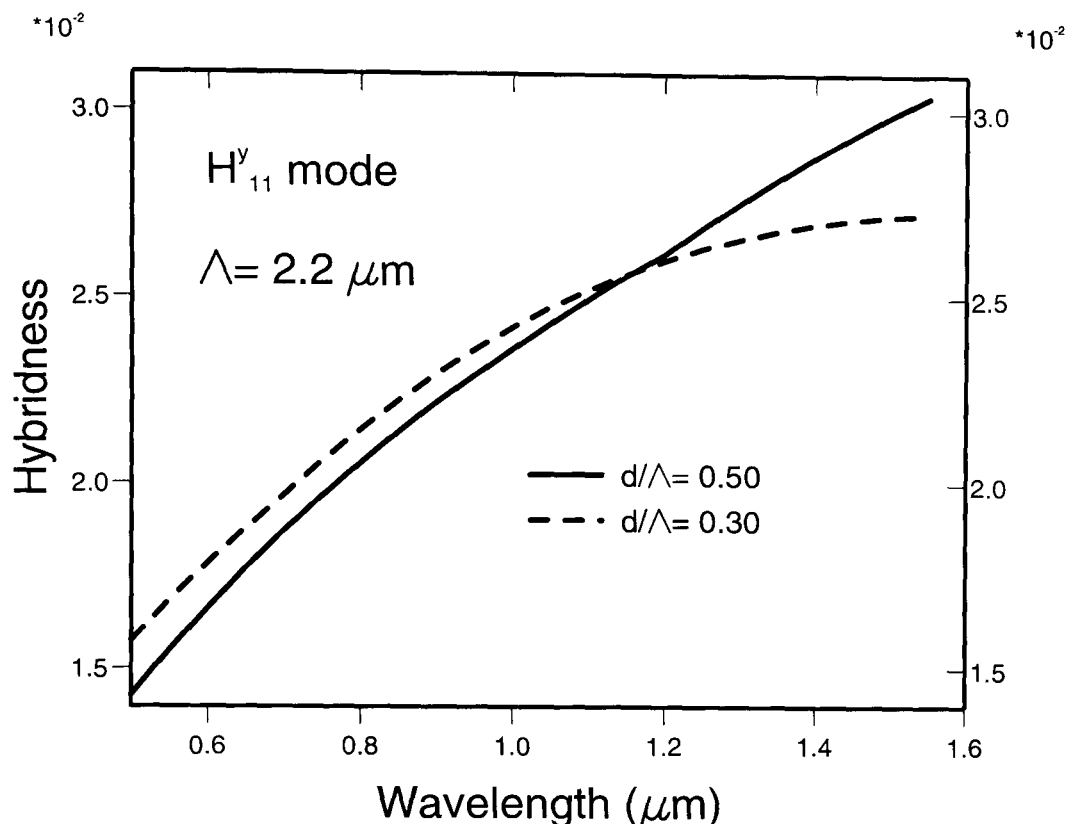


Fig. 7.16: The variation of the hybridness with the operating wavelength for H_{11}^y mode when $d/\Lambda = 0.30$ and $d/\Lambda = 0.50$.

The variations of the spot-size with the wavelength, for the fundamental quasi-TE mode, for $d/\Lambda = 0.30$ and 0.50 are shown by a dashed line and a solid line, respectively, in Fig. 7.17. It can be observed that as the operating wavelength increases, the waveguide dimensions reduce compared to the operating wavelength and the spot-size also increases since the mode approaches its cutoff condition, in a similar way to what was observed experimentally by Baggett *et al.* [Baggett *et al.*]. It can also be observed that for a PCF with a larger d/Λ value, the resulting spot-size is smaller as bigger air-holes restrict the expansion of the modal field.

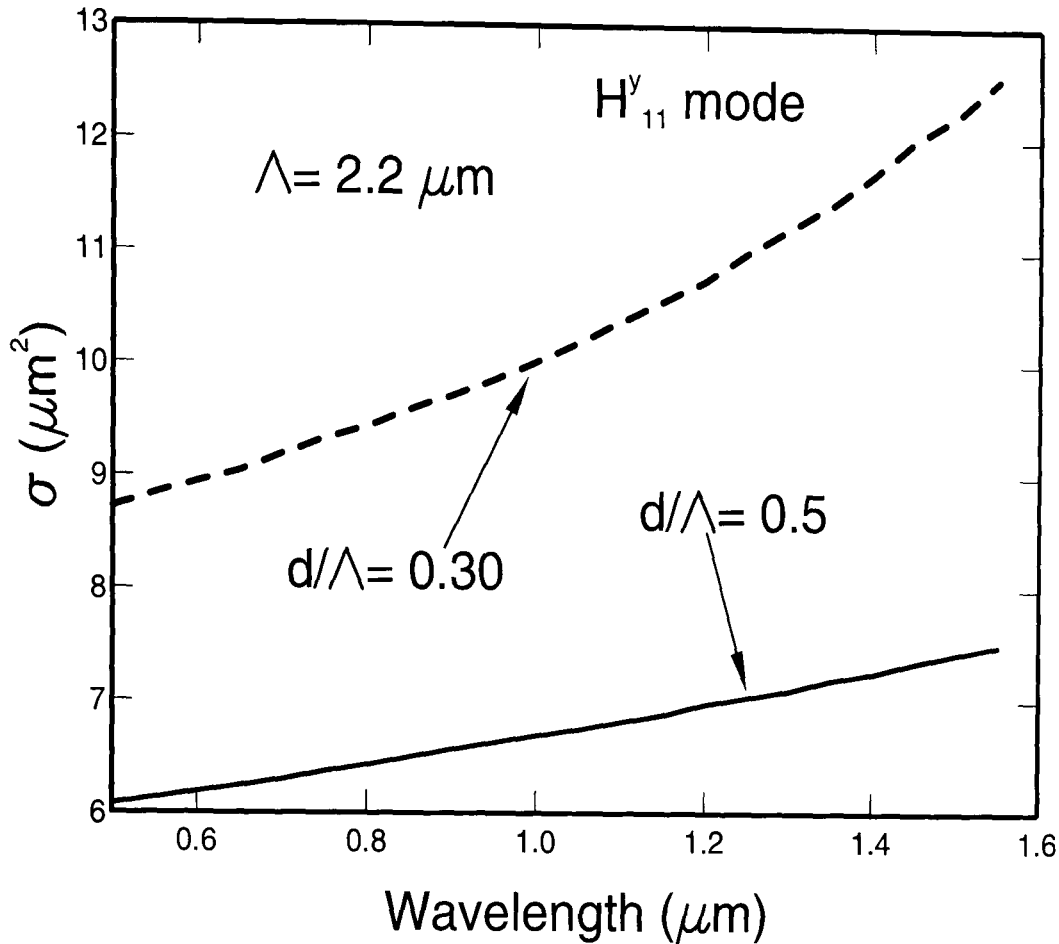


Fig. 7.17: The variation of the spot-size with the operating wavelength for $d/\Lambda = 0.50$ and 0.30 .

7.3.3 Results of a PCF when Λ is Varying

Earlier, the variations of the optical parameters with the operating wavelength and normalized hole diameter were shown only for a fixed pitch length, $\Lambda = 2.2 \mu\text{m}$. The pitch length, Λ , the operating wavelength, λ , and the normalized hole diameter d/Λ , all play key roles in the modal properties and additionally the asymmetry d_2/Λ for the birefringence properties. So, next the effect of the crystal period, Λ , is studied. For a fixed operating wavelength, the pitch length, Λ , can be used as the key controlling parameter.

The variation of the effective indices for the quasi-TE modes with the period, Λ , are shown in Fig. 7.18, when the operating wavelength is fixed at $\lambda = 1.55 \mu\text{m}$. The effective index values for $d/\Lambda = 0.50$, 0.70 and $0.90 \mu\text{m}$ are shown in this figure by solid, dashed and dashed-dotted lines, respectively. It can be observed that the effective indices reduce as the period is reduced and the fundamental H_{11}^y modes reach it cutoff condition for each case. It can also

be observed that the fundamental H_{11}^y mode reaches its cutoff condition early when $d/\Lambda = 0.50$, compared to $d/\Lambda = 0.70$ and 0.90 . It should also be noted that for higher d/Λ values, the effective index values are smaller due to their lower equivalent cladding index values and it can support a mode for a lower pitch length values due to increased index contrast.

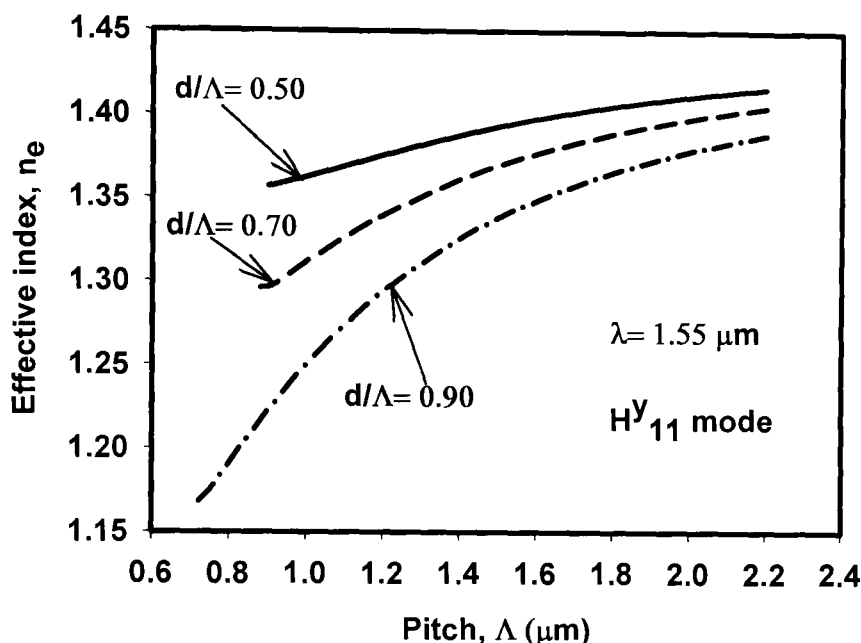


Fig. 7.18: The variation of the effective indices with the pitch when $d/\Lambda = 0.50, 0.70,$ and 0.90 .

The variations of the effective indices and spot-sizes of the fundamental quasi-TE mode with the pitch length, Λ , for different normalized hole diameters $d/\Lambda = 0.50$ and 0.90 are shown in Fig. 7.19 by a solid line and dashed-dotted line, respectively when the operating wavelength is $1.55 \mu\text{m}$. In this case, when the waveguide dimension is reduced compared to the wavelength, the modal field is extended further into the cladding region. In both the cases, the modal effective indices reduce monotonically as the pitch length, Λ , is reduced. It can be observed that the effective index values are lower for PCFs with larger d/Λ values, since in these cases the equivalent cladding indices were also lower. It should also be noted that, since for a larger d/Λ value the index contrast is higher, the cutoff value of the pitch length, Λ , is also smaller, as is shown here.

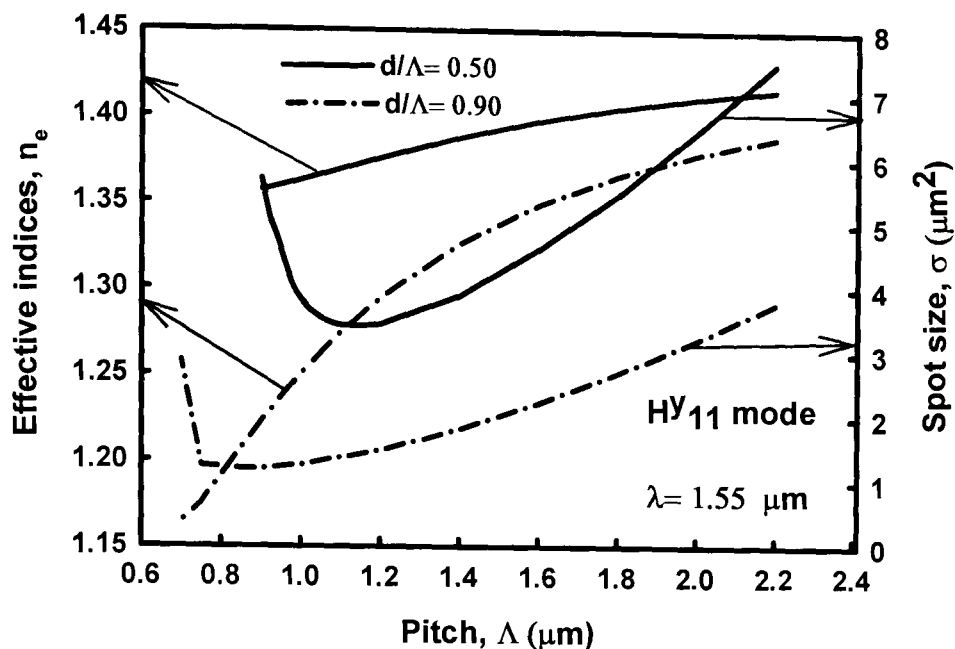


Fig. 7.19: The variation of the effective index and spot-size with the pitch when $d/\Lambda = 0.50$ and $d/\Lambda = 0.90$.

It can also be seen as the pitch length is reduced, initially the spot-size reduces and reaches a minimum value but subsequently increases sharply as the modes approach their cutoff conditions. This is due to the reason that as the pitch length, Λ , is decreased, the waveguide dimension is reduced compared to the operating wavelength, the mode approaches its cutoff condition, the modal field expands and as a consequence the spot-size also increases, in a way similar to what was observed experimentally by Baggett *et al.* [Baggett *et al.*]. It should be noted that with a larger d/Λ value, the hole diameters are large, which restricts the mode in a narrower silica region and so the spot-size is smaller. For a higher d/Λ value, the location of its smallest spot-size is also be lower. The minimum spot-size value of $3.42 \mu\text{m}^2$ can be achieved for d/Λ value 0.5, when the $\Lambda = 1.14 \mu\text{m}$ at the operating wavelength of $1.55 \mu\text{m}$. On the other hand, if the d/Λ value is increased to 0.90, the minimum spot-size could be as low as $1.20 \mu\text{m}^2$ at $\Lambda = 0.90 \mu\text{m}$, one of the lowest reported so far. It should be noted that by appropriate design combinations of the d/Λ and Λ values spot-size can be reduced below $1 \mu\text{m}^2$. For many nonlinear applications, the reduction of the spot-size is a key issue, where an example of this is the usage of sub-micron guides in supercontinuum generation [Leon-Saval *et al.*; Foster and Gaeta]. It can be

noted that for a larger d/Λ value, the cutoff condition approaches at a lower value of Λ , but more rapidly due to the larger index contrast between the silica core and the effective cladding. The higher air hole size restricts the optical field into a smaller core area.

Variations of the modal hybridness with the pitch length, Λ , for the fundamental H_{11}^y mode are shown in Fig. 7.20 for $d/\Lambda = 0.4, 0.5$ and 0.6 , by dashed-dotted, dashed and solid lines, respectively. The modal hybridness increases as Λ is reduced and reaches a maximum value when the spot-size is near to its minimum value. After reaching their peak values these values are reduced as the modes approaches their modal cutoff. For a higher d/Λ value, the location of its smallest spot-size would also be lower. It can also be noted that for a higher d/Λ value, the maximum hybridness value is also higher due to the associated higher index contrast in this case. It was also observed that for the quasi-TM modes, the patterns of the hybridness variations were similar but are not shown here.

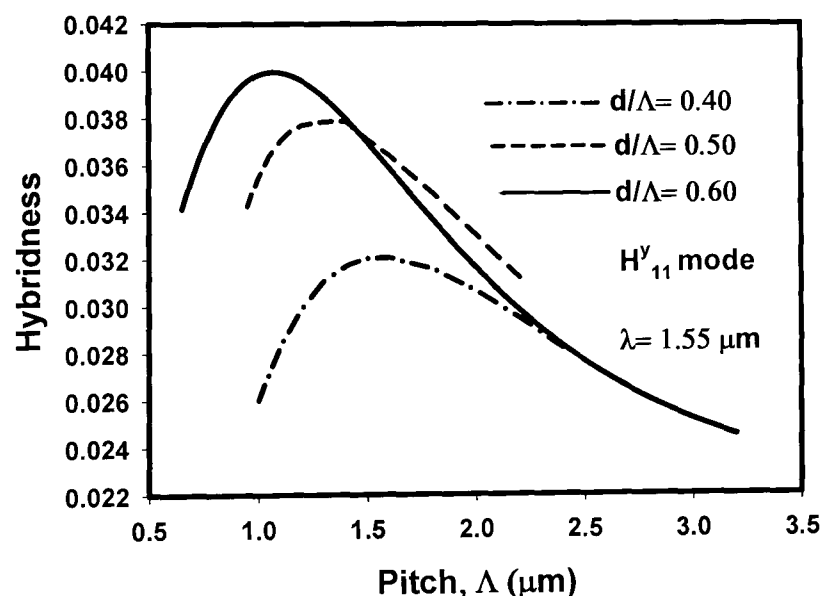


Fig. 7.20: Variations of the modal hybridness with the pitch length, Λ when $d/\Lambda = 0.40$, $d/\Lambda = 0.50$, and $d/\Lambda = 0.60$.

Earlier two-dimensional contour plots of the dominant field were shown in Figs. 7.7a and 7.7b. However, as the optical mode approaches cutoff, the field expands into the air-hole regions and to illustrate their evolutions, their variation along the x-axis is shown in Fig. 7.21. The variation of the dominant

H^y field for the H_{11}^y (quasi-TE) mode along the normalized (X/Λ) direction for $\Lambda = 2.2 \mu\text{m}$, $1.1 \mu\text{m}$ and $0.90 \mu\text{m}$ are shown by dashed, solid and dashed-dotted line, respectively. In this case, since the horizontal distance is normalized (x/Λ), the locations of the air-holes for all the Λ values appear at the same position. In these cases, the normalised hole diameter is kept constant at $d/\Lambda = 0.5$ and the operating wavelength at $1.55 \mu\text{m}$. In this normalized field, the maximum magnitude of one and three rings were considered. It can be observed that the field decays away from the PCF core and reduces substantially in the air hole region and increases locally beyond the air holes. It can also be noticed that the dashed line reduces smoothly compared to solid and dotted line. When $\Lambda = 0.90 \mu\text{m}$, 2nd and 3rd minima are clearly visible, as mode was more weakly confined and the mode being close to its cutoff, in this case the field magnitude in the cladding region is significantly large. Although, in this figure for $\Lambda = 2.2 \mu\text{m}$, the *normalized* field spread appears to be the smallest, but actually the spot-size is much larger as the pitch length is much longer.

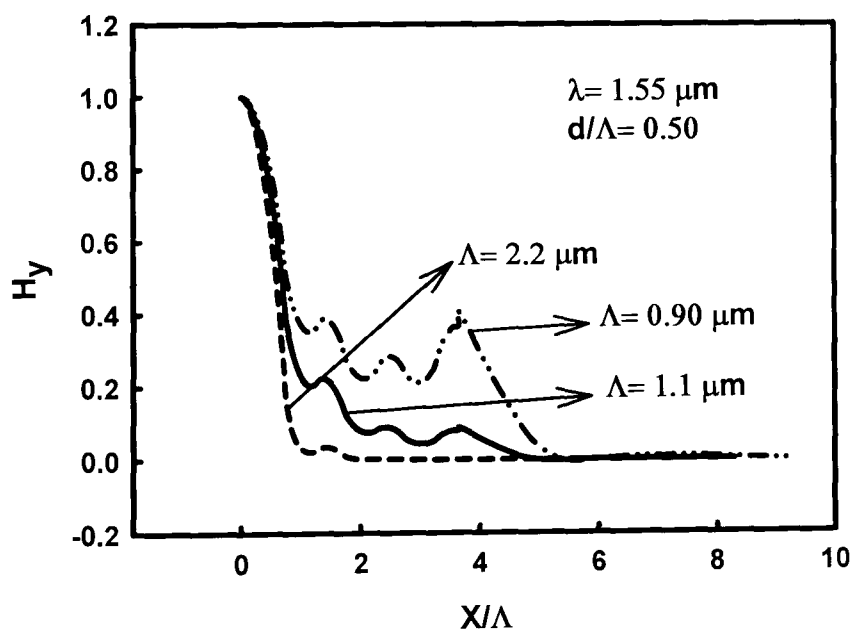


Fig. 7.21: The variation of the field with the normalized X/Λ .

In the following section, a PCF structure where hole diameters are not identical is studied.

7.4 Numerical Results of a PCF Structure with Unequal Hole Diameter

Initially, a PCF structure was studied with regular hexagonal hole arrangement with all the holes with identical diameter as illustrated in Fig. 7.1. In this hexagonal hole arrangement (as illustrated in Fig. 7.5), the diameter of the 4th hole is taken as $d_2/\Lambda=0.95 \mu\text{m}$ and the diameter of the rest of the holes remained the same as before, $d_1/\Lambda=0.5 \mu\text{m}$, where $\Lambda=2.2 \mu\text{m}$. The following results illustrate the comparison between the H_{11}^x mode and H_{11}^y modes using the structure shown in Fig. 7.5.

7.4.1 Results of a PCF when Wavelength is Varying

The variations of the silica index and the effective index for the fundamental quasi-TE and quasi-TM modes with the operating wavelengths are shown in Fig. 7.22. As mentioned earlier, the refractive index of silica reduces monotonically with the wavelength due to the material dispersion [Agrawal], which is shown in this figure by a solid line and labeled as n_g . In this case the pitch, Λ , is taken as $2.2 \mu\text{m}$, with the diameter of the equal-size air holes $1.1 \mu\text{m}$ and four unequal-size air holes $2.09 \mu\text{m}$, yielding a normalized d_1/Λ and d_2/Λ ratio of 0.50 and 0.95, respectively. The variations of the effective index (n_e) for the fundamental quasi-TE (H_{11}^y) and quasi-TM (H_{11}^x) modes are shown by a dashed line and dash-dotted line, respectively. It can be noted that the reduction of the effective index (n_e) is more rapid (with the operating wavelength) than that of the material index of silica, n_g , due to the additional waveguide dispersion besides the material dispersion [Rahman *et al.*, 2006b].

As the operating wavelength increases, the waveguide dimension reduces, compared to its wavelength and the mode approaches its modal cutoff and with that the effective index value also reduces. It can also be noted that for quasi-TM (H_{11}^x) mode, the effective index value is lower. As the wavelength is increased, the refractive index difference ($n_e^y - n_e^x$) between the H_{11}^y and H_{11}^x

modes are also increased due to the unequal air hole near the core region. As a result, birefringence is larger for larger wavelength.

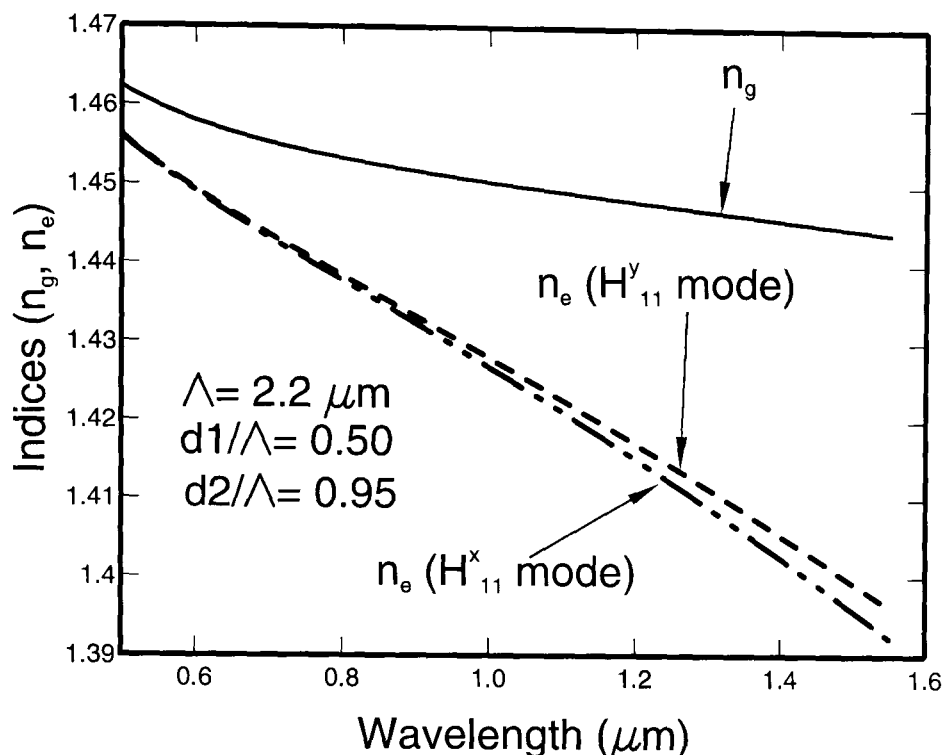


Fig. 7.22: Variation of the effective index with the wavelength for a circular air-hole PCF when $d_1 \neq d_2$.

The dominant H^x field profile of the fundamental H^x_{11} mode and the dominant H^y field profile of the fundamental H^y_{11} mode are shown in Fig. 7.23a and Fig. 7.23b, respectively for $\lambda = 0.50 \mu\text{m}$. From these figures, it can be observed that the field is not symmetrical; however its spread along the x-axis is slightly larger. From Fig. 7.23a, it can be observed that last contour line crossed the x-axis at roughly $1.7 \mu\text{m}$ and along the y-axis it is approximately $1.26 \mu\text{m}$. This is due to the reason that the diameter of the 4th air hole, as shown in Fig. 7.5, near core region is bigger (in this case $d_2 = 2.09 \mu\text{m}$) compared to the other identical air holes (in this case $d_1 = 1.1 \mu\text{m}$). Fig. 7.23b is very identical compared with the dominant H^x field profile of the fundamental H^x_{11} mode shown in Fig. 7.23a. However, it can be noticed from this figure that its spread along x-axis is slightly smaller (in this case $1.65 \mu\text{m}$).

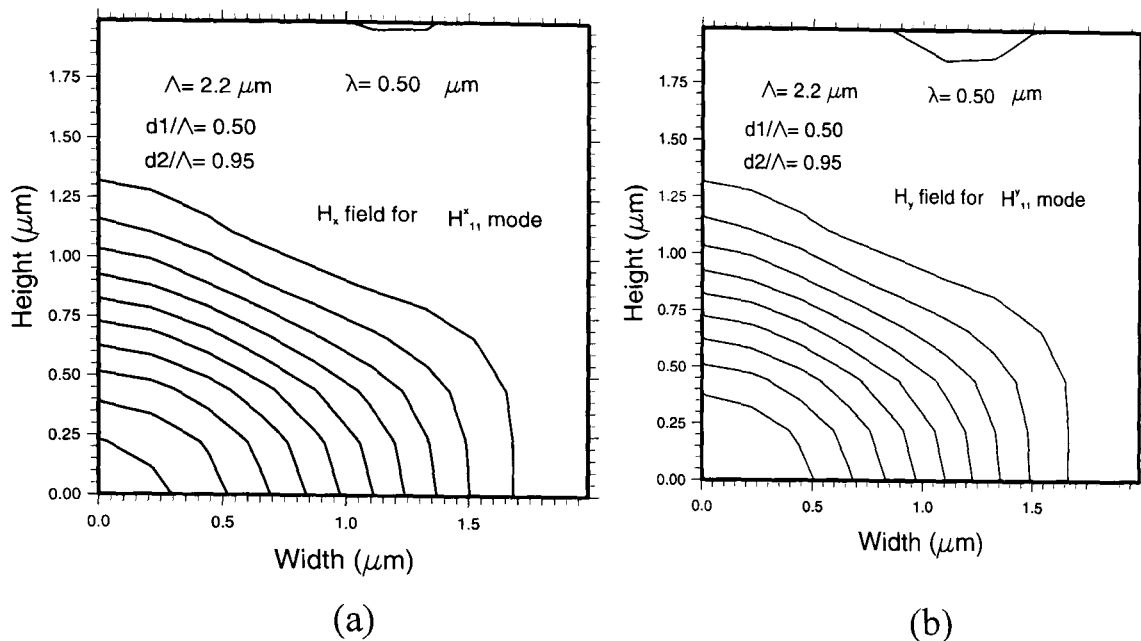


Fig. 7.23: (a) The dominant H^x field profile of H_{11}^x mode and (b) the dominant H^y field profile of the fundamental H_{11}^y mode at $\lambda = 0.50 \mu\text{m}$.

Next, the effect of longer wavelength, λ , is shown. The dominant H^x field profile of the fundamental H_{11}^x mode and the dominant H^y field profile of the fundamental H_{11}^y mode are shown in Figs. 7.24a and 7.24b, respectively for a longer wavelength of $\lambda = 1.55 \mu\text{m}$. Compared to Fig. 7.24a, it can also be clearly noticed that when wavelength is increasing from $0.5 \mu\text{m}$ to $1.55 \mu\text{m}$ mode becomes weakly confined, field spreads along both x-axis and y-axis from $1.7 \mu\text{m}$ to $1.9 \mu\text{m}$ and $1.26 \mu\text{m}$ to $1.5 \mu\text{m}$, respectively. This is due to the reason that for smaller wavelength mode is well confined and for larger wavelength mode is weakly confined. Fig. 7.24b is very identical compared with the dominant H^x field profile of the fundamental H_{11}^x mode shown in Fig. 7.24a. However, it can be noticed from this figure that its spread along y-axis is slightly larger (in this case $1.55 \mu\text{m}$). However, it should be noted that in this case the modes are better confined as shown in Fig. 7.24a for quasi-TM (H_{11}^x), compared to Fig. 7.24b for quasi-TE (H_{11}^y). As a result, for quasi-TM (H_{11}^x) mode, the effective index value is lower than that of quasi-TE (H_{11}^y) as shown in Fig. 7.22.

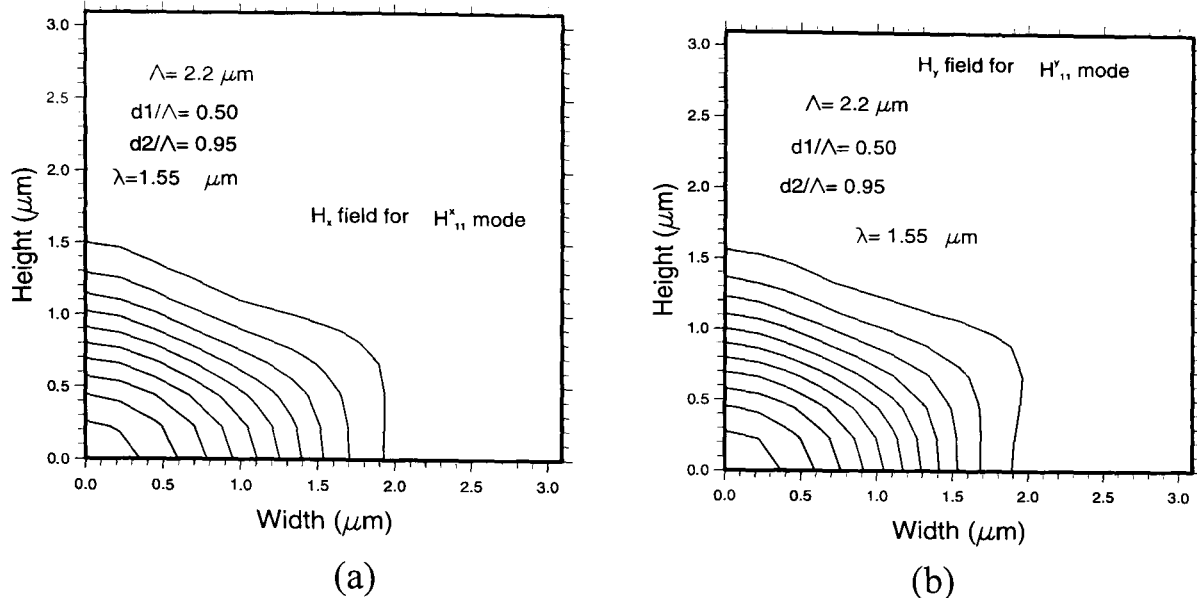


Fig. 7.24: (a) The dominant H^x field profile of H_{11}^x mode and (b) the dominant H^y field profile of the fundamental H_{11}^y mode at $\lambda = 1.55 \mu\text{m}$.

7.4.2 Results of a PCF when d_2/Λ is Varying

Next, the effect of shorter wavelength ($\lambda = 0.50 \mu\text{m}$) is shown to compare with the effect of longer wavelength ($\lambda = 1.55 \mu\text{m}$). The FEM approach is very versatile and it allows for the modelling of designs showing change of the position and size of any of the holes, as required. The modal properties of a PCF are investigated for a situation where the sizes of four air-holes in the first ring are different from that of the others. However, since the two-fold symmetry has been taken, only one air-hole, d_2 , near the core region is considered. Such a PCF would be able to maintain a specific input polarization state and the corresponding modal birefringence would also be high. In this case, the pitch, Λ , was fixed at $2.2 \mu\text{m}$, and the diameter of one air-hole (d_2) is varied and all the other hole diameters are kept fixed at $1.1 \mu\text{m}$ ($d/\Lambda = 0.5$). In this case, the operating wavelength is taken as $0.5 \mu\text{m}$. The variation of the effective indices for the fundamental quasi-TE (H_{11}^y) and quasi-TM (H_{11}^x) modes are shown in Fig. 7.25.

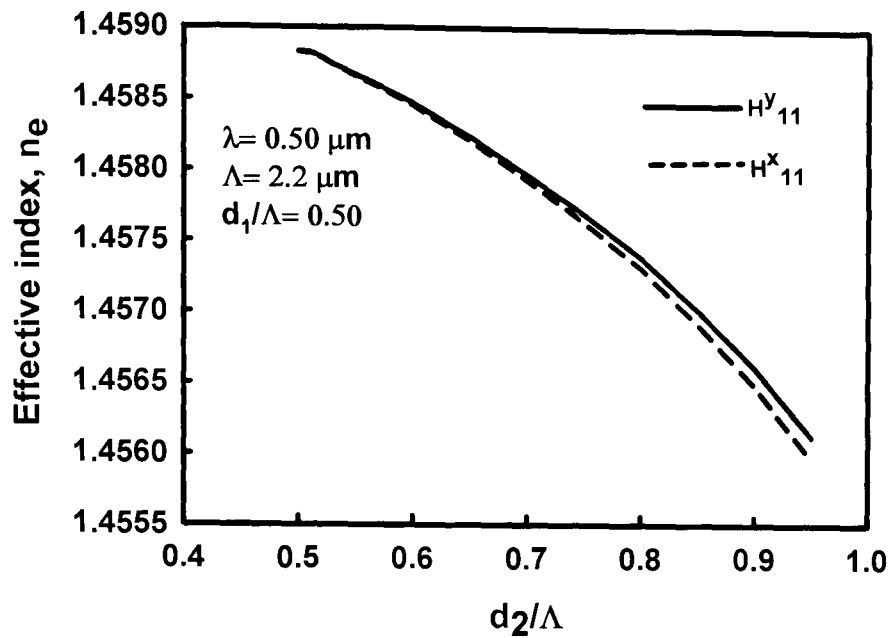


Fig. 7.25: The variation of the modal indices with the normalized diameter, d_2/Λ .

It can be observed that as the diameter of only one air-hole, d_2 , is increased, the effective index values decrease. This is due to the fact that with an increased air-hole size (even if only one is changed), the equivalent cladding index is reduced. It can be clearly observed that as the value of d_2 is increased, the modal index difference between the two fundamental TE and TM polarized mode increases. This is because of the increased d_2 diameter makes the PCF structure more asymmetric. An increased d_2 makes the vertical dimension of the effective core smaller than that of the width and as a consequence the effective index of the quasi-TE mode is higher than that of the quasi-TM mode.

The variation of the spot-size and the modal hybridness for the fundamental quasi-TE and quasi-TM modes are shown in Fig. 7.26. It can be observed that the spot-size reduces as the value of the diameter d_2 is increased. This increased air-hole diameter (even of a single hole) restricts the optical field in that air-hole region and consequently reduces the spot-size. The modal hybridness increases with the enlargement of the d_2 value, which is due to the increased interaction of the modal field with the air/silica boundaries of the air-holes, which is now closer to the core.

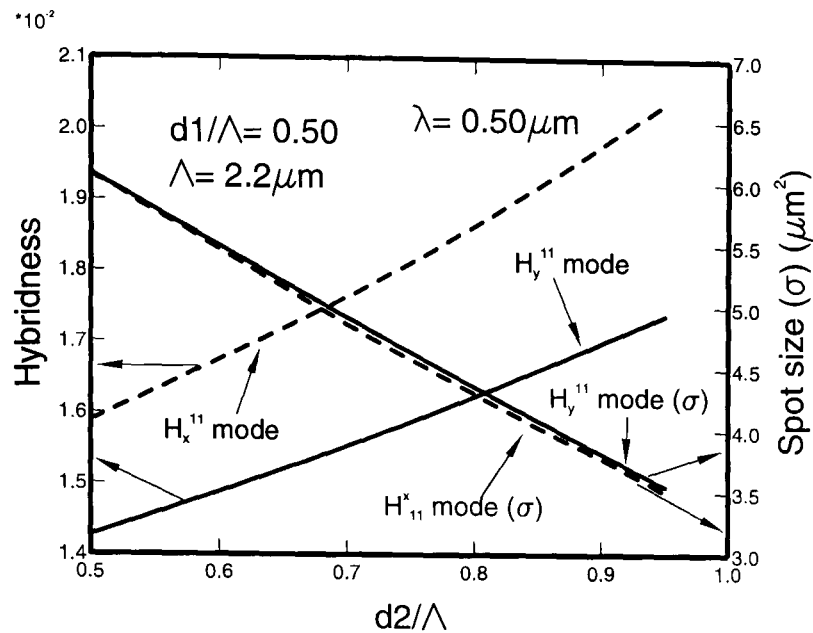


Fig. 7.26: The variation of the spot-size and modal hybridness with the normalized diameter, d_2/Λ .

As the mode expands, modal field also encounters the air-hole regions and the power leaking into the air-hole areas increases. The variation of the optical power in the silica region, P_s , with the air-hole diameter d_2 is shown in Fig. 7.27 for both the quasi-TE and TM modes. It can be clearly observed that as the air-hole diameter increases, the modal field expands, the spot-size increases, and so the power in the silica region decreases. It should be noted that for the design of an evanescent sensor, the air-hole diameter would be an important parameter for design optimization.

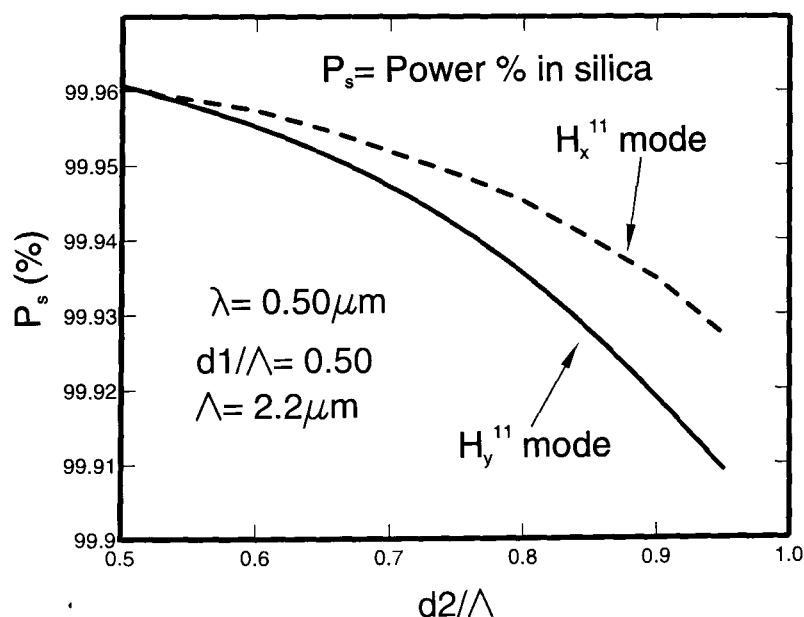


Fig. 7.27: The variation of the power confinement factor with the value of d_2/Λ .

7.5 Group Velocity Dispersion (GVD) of PCF

7.5.1 Effect of Mesh Division when Wavelength is Varying

Variations of the GVD factor, $D(\lambda)$, of H_{11}^y mode with wavelength for 120*120 mesh and 80*80 mesh are shown in Fig. 7.28 for the identical holes with a 2.2 μm pitch distance (Λ). It can be noted that the variations of the GVD with wavelength are similar for both cases. It can be further observed that in both cases, GVD is positive over the wavelength range 0.9 and 1.4 μm , with a maximum value of approximately 60 ps/nm.km at $\lambda = 1.2 \mu\text{m}$.

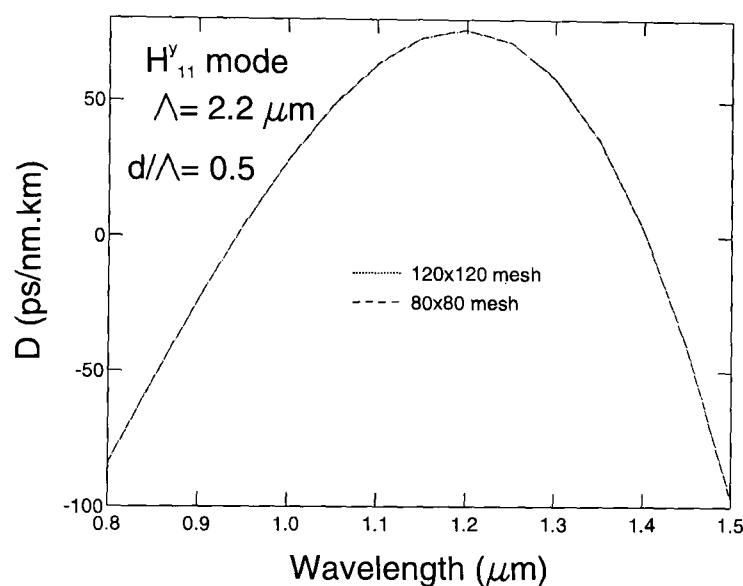


Fig. 7.28: Variation of the GVD of the H_{11}^y mode with the wavelength for $d/\Lambda = 0.5$ when mesh= 120*120 and 80*80.

7.5.2 Effect of d/Λ when Wavelength is Varying

Variation of the GVD with wavelength for H_{11}^x mode and H_{11}^y mode is shown in Fig. 7.29. It can be noted that the variations of the GVD with wavelength are similar for both cases and they are almost indistinguishable. In this case, the structure being almost symmetric, two polarized modes (H_{11}^x and H_{11}^y) were nearly identical and similarly their GVD were also almost identical. It can be further observed that in both cases, GVD is positive over the wavelength range 1.0 and 1.4 μm , with a maximum value of approximately 80 ps/nm.km at $\lambda = 1.2 \mu\text{m}$.

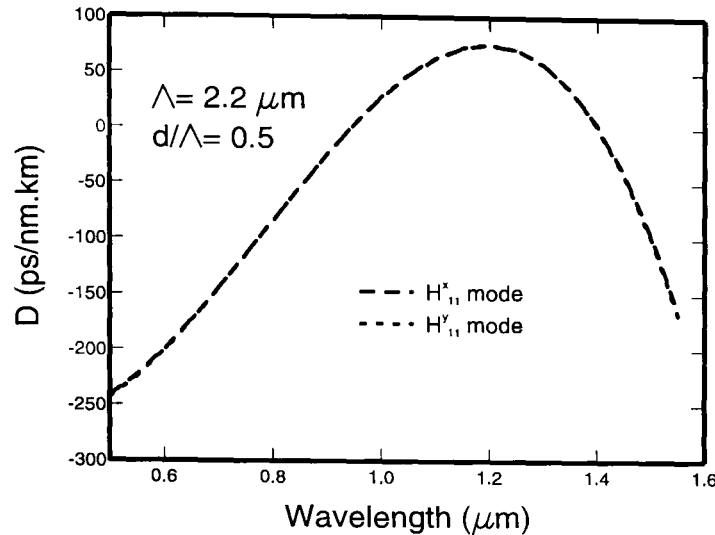


Fig. 7.29: Variation of the GVD with wavelength for H_{11}^x mode and H_{11}^y mode.

Next, two different hole diameters have been considered, where $d = 0.66 \mu\text{m}$ and $1.1 \mu\text{m}$, corresponding to d/Λ ratios of 0.3 and 0.5, respectively. Variations of the GVD with the operating wavelength are shown in Fig. 7.30. It can be observed that a low anomalous GVD can be achieved over a given operating wavelength range, and similar adjustable GVD properties cannot be achieved in the design of the less flexible telecommunication grade SMF. By adjusting the diameters of the holes, unequal air-holes within a single ring or between the rings, the range of anomalous dispersion, its maximum value and the dispersion slopes can be adjusted for a specific application.

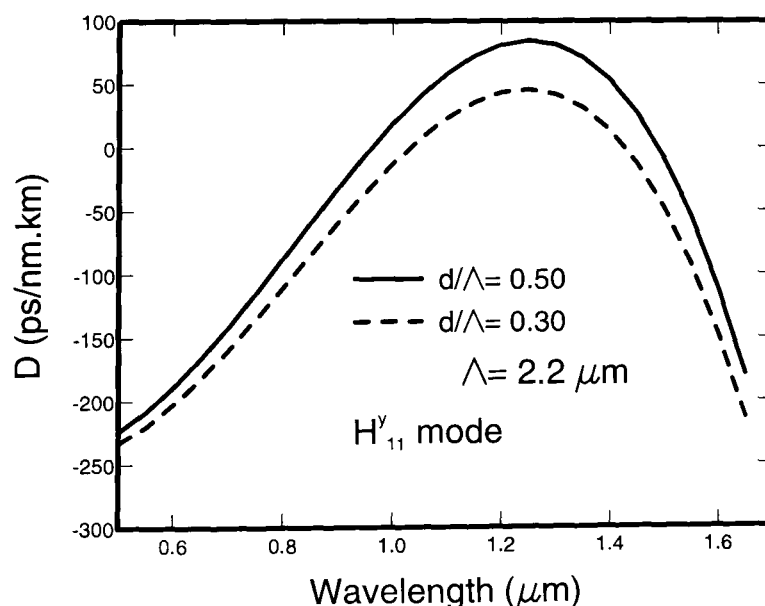


Fig. 7.30: Variations of the GVD with the wavelength for $d/\Lambda = 0.50$ and 0.30 .

7.5.3 Effect of d_2/Λ when Wavelength is Varying

In Fig. 7.5, the modal properties of a PCF were investigated for a situation where the 90 degree rotational symmetry does not exist. In this case, the size of one of the air-holes, d_2 , is different from the others. Variations of the GVD for this PCF structure are shown in Fig. 7.31. For comparison, the GVD of the degenerate PCF with $d_1 = d_2 = 1.1 \mu\text{m}$, is also shown in this figure. Again, it can be observed that by adjusting the hole dimensions of a specific group of holes, the GVD properties can be modified. It can be noted that the GVD is positive over wavelength range from 0.9 to 1.45 μm and from 0.95 to 1.4 μm for unequal and equal holes, respectively. This means unequal air holes give more positive GVD. It can also be noticed that both unequal and equal holes have a maximum value of approximately 100 ps/nm.km and 75 ps/nm.km at $\lambda = 1.2 \mu\text{m}$, respectively.

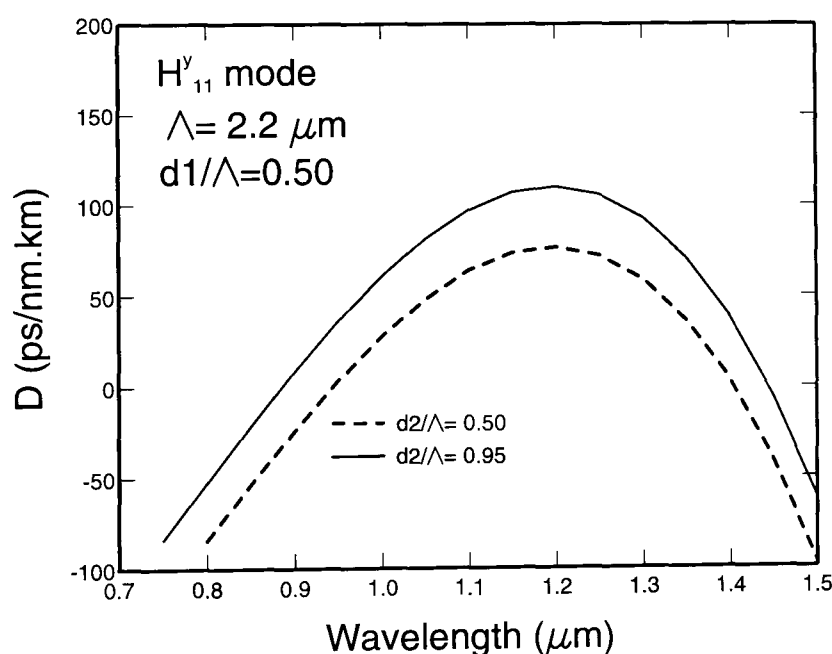


Fig. 7.31: Variation of the GVD of the H_{11}^y mode with the wavelength for $d_2/\Lambda = 0.50 \mu\text{m}$ and $d_2/\Lambda = 0.95 \mu\text{m}$ and mesh = 120×120 .

The variations of the GVD with the operating wavelength for both fundamental H_{11}^y and H_{11}^x modes are shown in Fig. 7.32 when $d_1 \neq d_2$. It can be observed that for such a highly birefringent PCF, the fundamental H_{11}^y modes have a lower positive GVD than that of the fundamental H_{11}^x modes. It

should be noted that the GVD properties of polarization maintaining PCFs are different for the TE and TM polarizations.

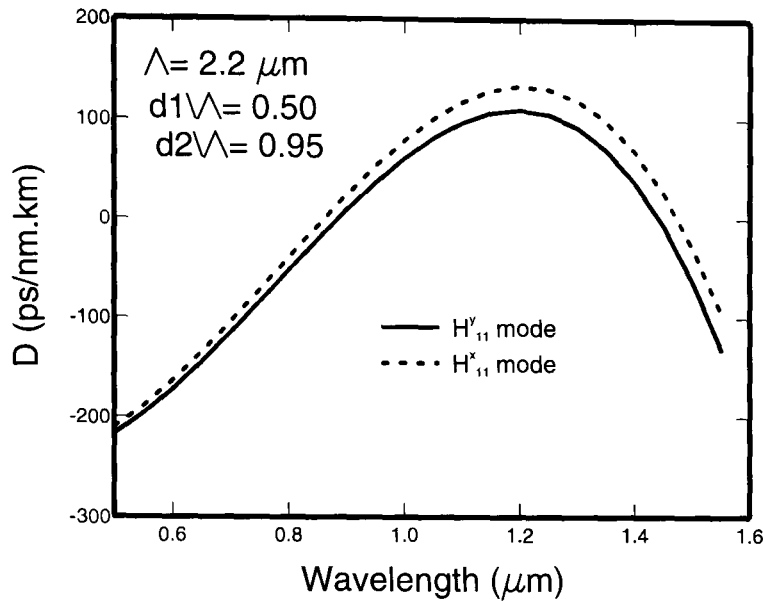


Fig. 7.32: Variation of the GVD with the wavelength for H_{11}^x and H_{11}^y when $d_1/\Lambda=0.5$ and $d_2/\Lambda=0.95$.

The variation of the GVD for polarization maintaining PCFs with various d_2 diameters is shown in Fig. 7.33. By comparison, the GVD of the degenerate PCF with $d_1=d_2=1.1\ \mu\text{m}$, is also shown in this figure. Again, it can be observed that by adjusting the hole dimensions of a specific group of holes, the GVD properties can be modified.

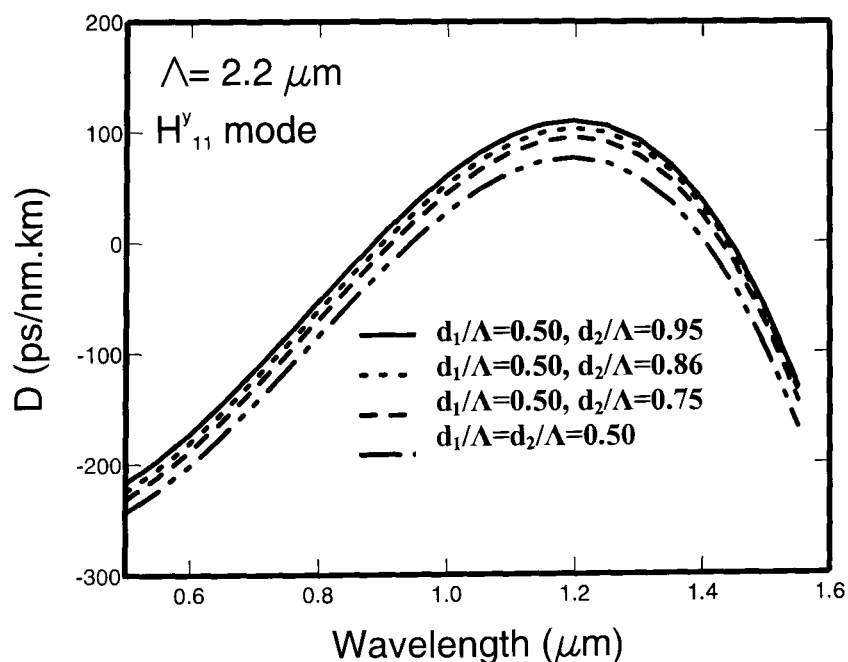


Fig. 7.33: Variation of the GVD with the wavelength for H_{11}^y modes for different d_2 values.

7.6 Summary

In this chapter, a rigorous analysis of hexagonal-lattice photonic crystal fibre with symmetrical and asymmetrical circular air-holes is presented, to understand the basic properties of photonic crystal fibres.

Important design parameters, such as the effective indices, modal field profile, spot-sizes, modal hybridness, power confinements, and the GVD are determined for equal and unequal and circular hole PCFs, by using a rigorous full-vectorial finite element-based approach. The variation of the GVD, an important optical parameter, is shown through the effect of the hole diameters and asymmetry and with the use of this modelling approach it may be possible to design a PCF with a specific GVD, or other optical properties, by adjusting the different fabrication parameters.

In the following chapter, a PCF structure where hole diameters are not identical is studied for calculating modal birefringence. Initially, four air-holes in the first ring (4th air-hole in Fig. 7.5) is enlarged to break the symmetry of the structure, so that modal birefringence can be increased. Later on, only two air-holes in the first ring (only $\frac{1}{2}$ air-hole on the x-axis) are enlarged to get birefringence. Comparisons of both of the results are discussed in next chapter.

Birefringence Study of Photonic Crystal Fibre

8.1 Introduction

Modal solutions of photonic crystal fibres with equal and unequal circular air holes in a hexagonal matrix are presented in Chapter 7, by using a rigorous full-vectorial **H**-field based finite element method. The effective indices, mode field profiles, spot-sizes, modal hybridness, power confinements, and group velocity dispersion values have been determined and presented in the previous chapter. In this chapter, modal solutions are further explored and presented. Besides the modal solutions of the effective indices, spot sizes, modal hybridness, beat length, and group velocity dispersion values; research was carried out to optimize and design highly birefringent PCF. The effects of the pitch-distance, hole diameter, structural asymmetry, air hole arrangement and the operating wavelength on the modal birefringence are also reported. It is shown that a significant value of birefringence can be achieved by using

only circular air holes, which would be easy to fabricate, and operating it close to its modal cutoff.

Holey fibres can be made from a single material, such as pure silica. Therefore, the core refractive index is the same as the index beyond the finite cladding region [Finazzi *et al.*, 2002]. The cladding region is enclosed within a circular silica jacket with a complex refractive index, which allows the jacket to absorb the portion of the mode that leaks [Finazzi *et al.*, 2003]. So every propagating mode is inherently leaky, and consequently experiences confinement loss. A variety of reasons causes the loss in holey fibres [White *et al.*, 2001*b*]: intrinsic material absorption, additional losses (water contamination, absorption due to impurities, scattering, etc.) arising during the fabrication process, and confinement [Saitoh and Koshihara, 2003*a*] or leakage loss [Saitoh and Koshihara, 2003*c*].

In this chapter, leakage loss in polarization maintaining photonic crystal fibres is also investigated and presented. Leakage loss is varying with different parameters. Comparisons of the numerical results are also discussed in detail.

8.2 Modal Birefringence of PCF

Birefringent fibres, the two orthogonally polarized modes guided in a single-mode fibre propagate at different velocities, are used to maintain polarization states in optical devices and sub-systems. By tweaking the hole geometries, as shown in Fig. 8.1, it's possible to produce level of birefringence that exceed the performance of conventional birefringent fibre by an order of magnitude.

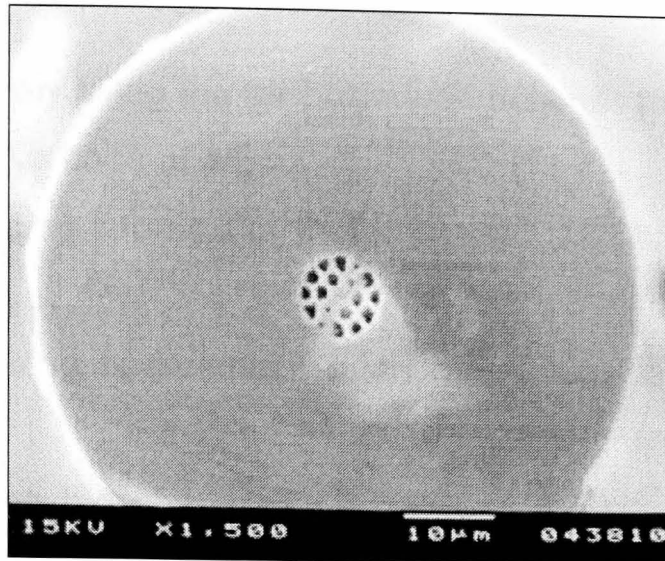


Fig. 8.1: Birefringent fibre [Dettmer, 2001].

In the axially symmetric single-mode fibre, there exist two orthogonally polarized modes, known as H_{11}^x and H_{11}^y modes in accordance with their polarization directions. If the fibre waveguide structure is truly axially symmetric, these orthogonally polarized modes have the same propagation constants and thus they are degenerate. In practical fibres, however, an axial nonsymmetry is generated by the core deformation and/or core eccentricity to the outer diameter, and it causes a slight difference in the propagation constants of the two polarizations. The difference of the propagation constants between H_{11}^x and H_{11}^y modes are intentionally made large in birefringent fibres and such fibres are also called 'polarization-maintaining' fibres [Okamoto]. Index contrast of PCFs is higher than that of conventional fibre as a result PCFs have higher birefringence than that of conventional fibre. Highly birefringent PCFs can be used as polarization maintaining fibres (PMFs) [Saitoh and Koshiba, 2003b].

8.3 Way of Making Highly Birefringent PCF

PCF can be made highly birefringent for the following reasons:

- Due to a larger index-contrast between air and silica [Hwang *et al.*].
- If polarization maintaining fibres (PMFs) employ asymmetric air hole distributions near the fibre core [Hwang *et al.*].

- By selectively filling the air holes with polymer to obtain an asymmetric structure [Kerbage *et al.*]
- By introducing two-size air holes around the fibre core [Hansen *et al.*, 2001].
- By introducing non-circular, such as elliptical air-hole [Nielsen *et al.*, 2001].
- By changing the shape of the holes or the size of some selected air holes [Rahman *et al.*, 2006a].
- By reducing the air-hole pitch, Λ [Rahman *et al.*, 2006a].

8.4 Modelling of Highly Birefringent PCF

Fig. 8.2 shows a full structure of a hexagonal lattice PCF where hole diameters are identical. In order to make highly birefringent PCF, two different size air holes around the fibre core [Hansen *et al.*, 2001] are needed. During the simulation, only two-fold symmetry has been taken.

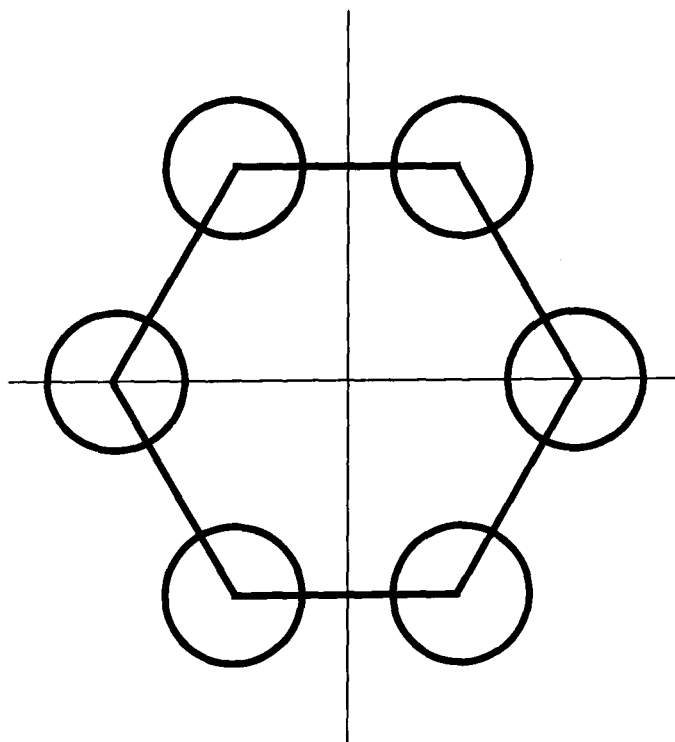


Fig. 8.2: Regular array of equal circular holes in a hexagonal lattice.

By changing the shape of the holes or the size of some selected air holes, the structural symmetry can be avoided and this yields important modal

property, the modal birefringence. Initially, two air holes are enlarged, as shown in Fig. 8.3, to get birefringence. In this case, area shown as effectively, height is greater than width, so that $n_e^x > n_e^y$.

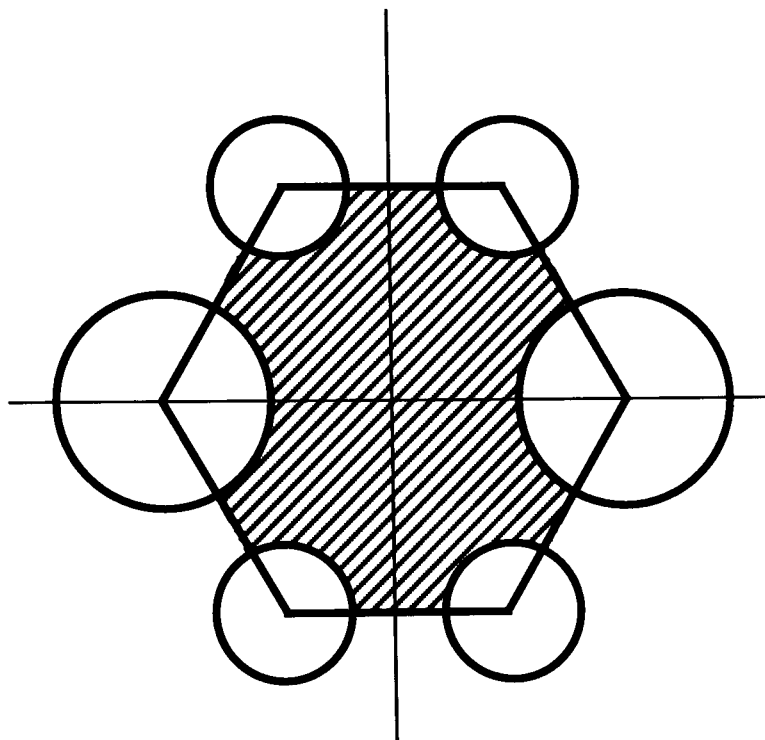


Fig. 8.3: Array of unequal circular holes in a hexagonal lattice where diameter of two air holes are increased.

Later on, four air holes, as shown in Fig. 8.4a, are enlarged to break the symmetry of the structure. Fig. 8.4a and Fig. 8.4b show full structure and quarter of full structure, respectively of a hexagonal lattice PCF where hole diameters are not identical. In Fig. 8.4b, when four air holes are enlarged, area shown as effectively, height is smaller than width, so that $n_e^y > n_e^x$.

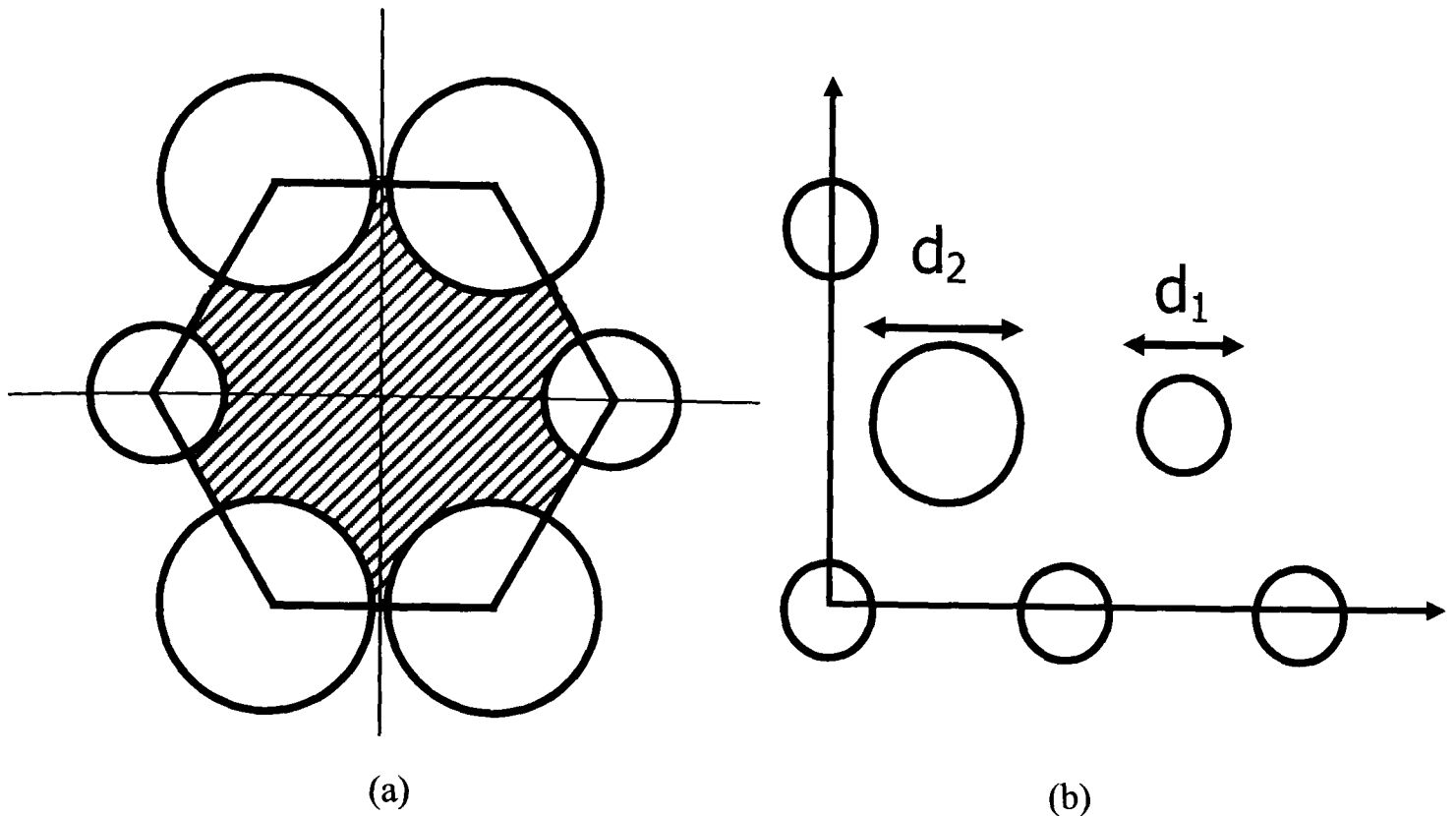


Fig. 8.4: Array of unequal circular holes of (a) full structure, and (b) quarter of a full structure in a hexagonal lattice where four air holes are increased.

8.5 Simulation Results for Birefringence

8.5.1 Results of a PCF when d/Λ is Varying

Birefringence can be controlled by introducing structural asymmetry and by changing the air-hole diameters. So, first the effect of air-hole diameter on the modal properties is studied for symmetrical PCFs. The variations of the effective index and the spot-size for the fundamental quasi-TE (H_{11}^y) mode with the normalized d/Λ dimension are shown in Fig. 8.5. The pitch length, Λ , either $2.2 \mu\text{m}$ or $2.0 \mu\text{m}$ is shown as solid and dashed line, respectively. In this case, the refractive index of the silica is taken as 1.444 at the operating wavelength of $1.55 \mu\text{m}$. As the hole diameter, d , is increased, the equivalent index of the air hole cladding region is reduced, which increases the index contrast between the effective cladding and the homogeneous silica core. Although the reduced cladding index reduces the modal effective indices, the increased index contrast also makes the mode better confined as shown earlier in Figs. 7.7b.

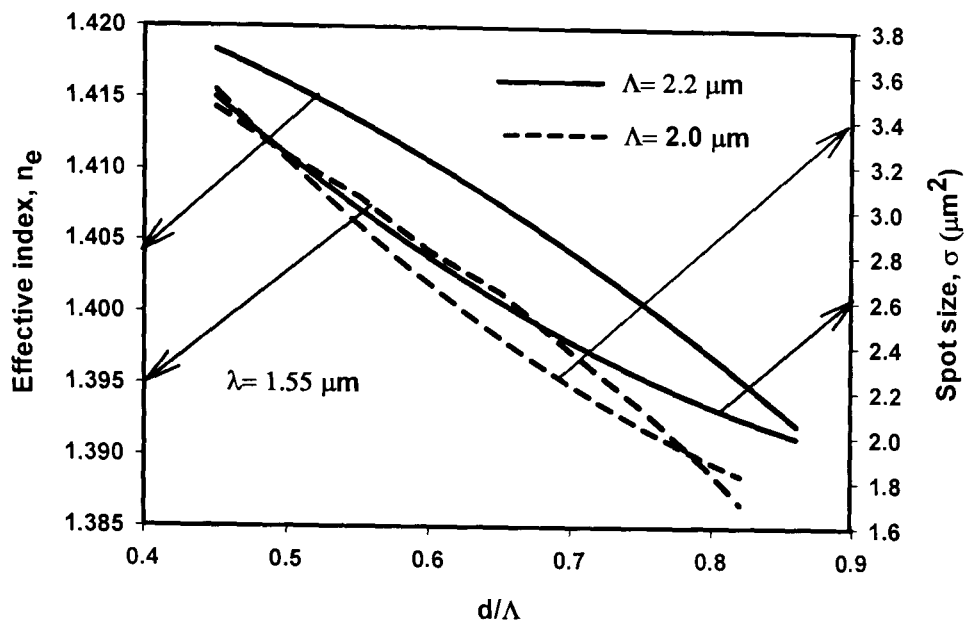


Fig. 8.5: Variations of the effective index and spot-size with the normalized hole diameter d/Λ when $\Lambda = 2.0 \mu\text{m}$ and $2.2 \mu\text{m}$.

As the hole diameter is increased, the effective index (n_e) is reduced for both pitch $2.2 \mu\text{m}$ and $2.0 \mu\text{m}$. The difference between the effective index of pitch $2.2 \mu\text{m}$ and $2.0 \mu\text{m}$ are higher when hole diameter are increased. The n_e for pitch $2.0 \mu\text{m}$ reaches early cutoff condition than that of for pitch $2.2 \mu\text{m}$. As pitch increases, effective index also increases. This is due to the reason that as Λ/λ is larger, waveguide dimension is larger compared to wavelength. For larger pitch length, mode is well confined which is not shown here.

In this figure, it can also be observed that as the hole diameter is increased, the spot-size (σ) is reduced for both pitch $2.2 \mu\text{m}$ and $2.0 \mu\text{m}$. This is because the enlargement of the holes restricts the expansion of the modal field from the core area as shown earlier in Figs. 7.7a and 7.7b. The effect of the hole diameter on the spot-size is clearly visible, and its variation is shown in Fig. 8.5. Initially, the spot size for both pitch $2.2 \mu\text{m}$ and $2.0 \mu\text{m}$ are very identical. As the hole diameter is increased, the spot-size (σ) is reduced for both pitch $2.2 \mu\text{m}$ and $2.0 \mu\text{m}$. At $\Lambda = 2.2 \mu\text{m}$, the value of the spot-size reduces from around $3.5 \mu\text{m}^2$ to $2.0 \mu\text{m}^2$. Whereas, at $\Lambda = 2.0 \mu\text{m}$, spot-size reduces from around $3.4 \mu\text{m}^2$ to $1.6 \mu\text{m}^2$. In this case, at $\Lambda = 2.0 \mu\text{m}$, the value

of the spot-size reduces more quickly. As pitch increases, spot-size also increases as waveguide dimension increases.

For a PCF with a regular hexagonal hole arrangement of fixed diameter, a 60 degree rotational symmetry exists, which makes the modes degenerate. However, strictly speaking the TE and TM modes are not degenerate as the required 90 degree rotational symmetry does not exist. For this structure with identical holes, in practice, the modal birefringence is very small and the modal properties of the fundamental quasi-TM (H_{11}^x) mode are not shown for this structure.

8.5.2 Results of a PCF when d_2/Λ is Varying

8.5.2.1 Results of a PCF where Height is Greater than Width

The birefringence of a PCF structure can be significantly increased by breaking the structural symmetry. This can be achieved by using non identical air holes in the first ring around the core. Asymmetry of the PCF can be introduced in different ways. In this case, diameters of the two air holes in the first ring, as shown in Fig. 8.6, are increased to break the rotational symmetry. The asymmetry arrangement considered here is similar as in [Kubota *et al.*], where the diameters (d_1) of the two air holes in the first ring are different from that of the other diameters (d). Since, the influence of the air holes in the first ring would be dominant; to break the structural symmetry, modification of the air hole dimensions in this ring would be more effective. For the simulation results, only a quarter of the structure is considered by exploiting the available two-fold symmetry.

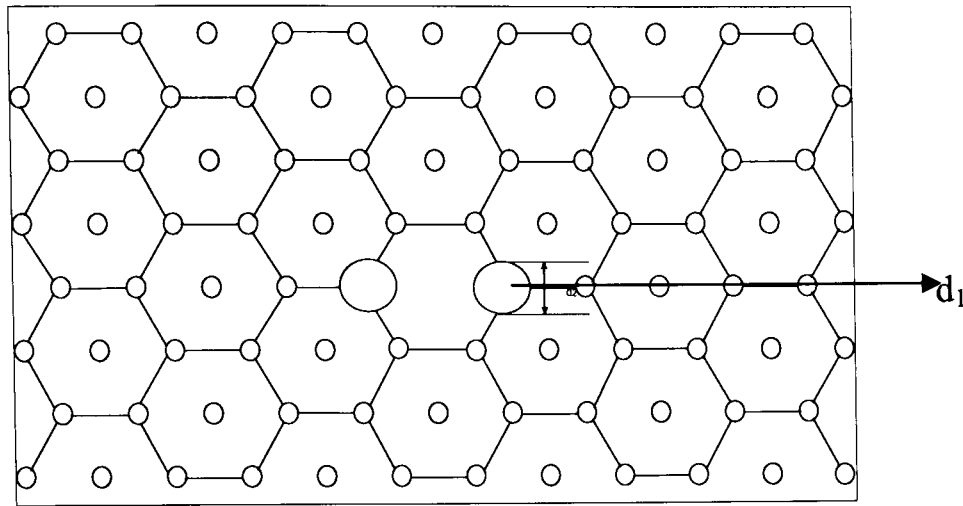


Fig. 8.6: Schematic diagram of the hexagonal lattice PCF with unequal hole sizes in the first ring where two air holes are increased.

Fig. 8.7a shows a hexagonal lattice PCF structure with circular air holes. In the hexagonal arrangements, air holes are placed in concentric rings around the core. Fig. 8.7b shows two circular air holes are increased in size. As two air holes are increased in size in the first ring, it can be clearly visible that the air region in this structure is increased. In Fig. 8.7b, it can be noticed that the height of the silica index is greater than that of width, so that $n_e^x > n_e^y$. Therefore, birefringence is expected to be lower for this structural asymmetry.

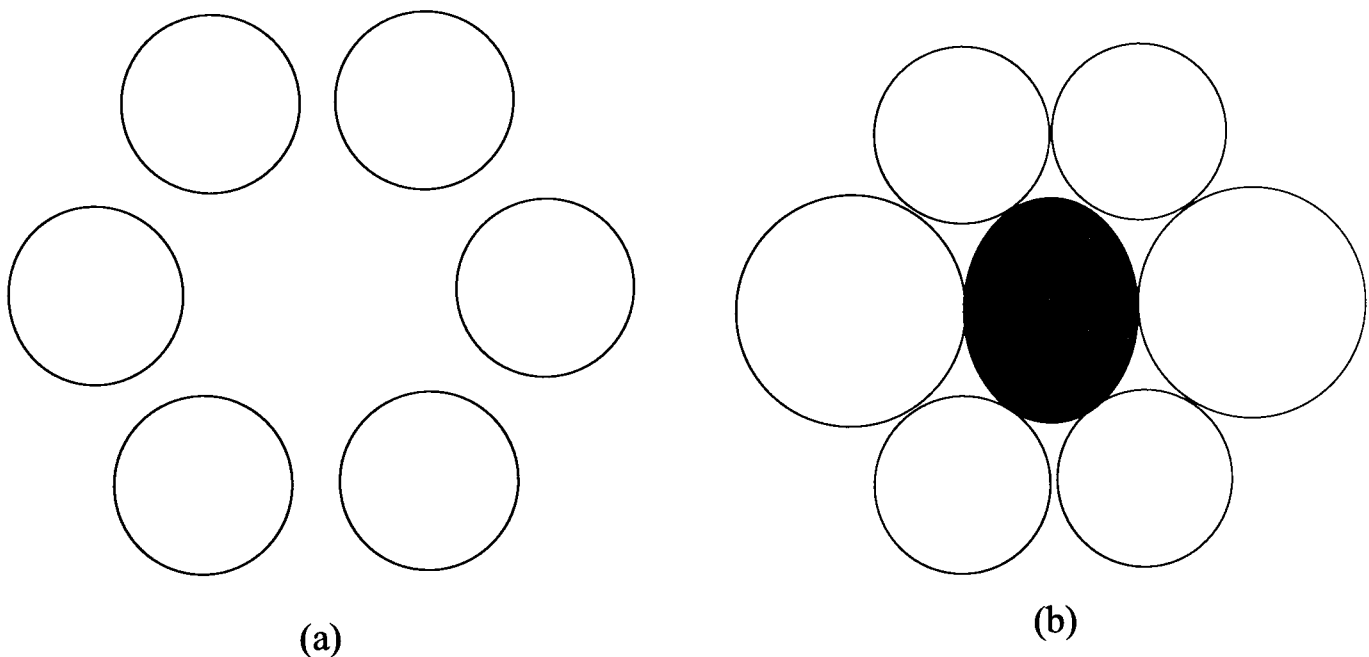


Fig. 8.7: (a) Array of hexagonal lattice, where (b) two circular air-holes are increased.

The variation of the effective indices with the normalized asymmetric air holes, d_1/Λ , is shown in Fig. 8.8 for the quasi-TE and quasi-TM modes for $d/\Lambda = 0.5$ and $\Lambda = 1.1 \mu\text{m}$. It can be observed that for lower values of d_1 , the effective indices for the quasi-TE modes are higher than those of the quasi-TM modes, as the effective height of the PCF would be smaller than their width in these cases. On the other hand when the d_1 values are higher, the effective index values of the quasi-TE modes are lower, since the effective widths are now smaller than their heights. The effective index curves cross each other when the d_1 value is similar to that of other air hole diameters, $d/\Lambda \approx 0.5$, in this case.

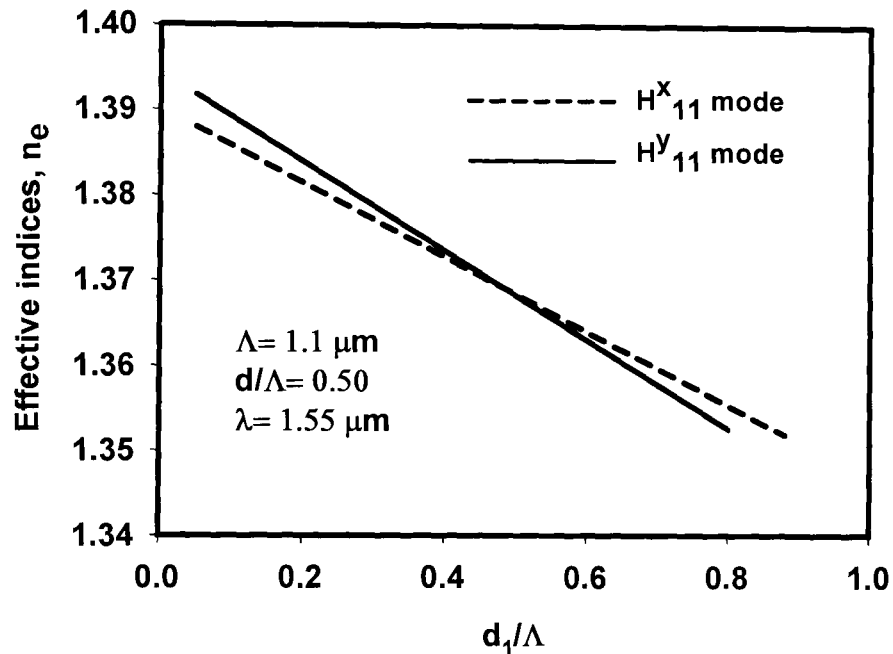


Fig. 8.8: Variation of the effective indices with the normalized d_1/Λ when $\Lambda = 1.1 \mu\text{m}$.

The variation of the spot-size with the d_1/Λ is shown in Fig. 8.9 for the quasi-TE and quasi-TM modes as a solid line and dashed line, respectively for $d/\Lambda = 0.5$ and $\Lambda = 1.1 \mu\text{m}$. It can be noted that for the polarization states, initially the spot-size is reduced for both the quasi-TE and quasi-TM modes as d_1/Λ is increased. However, when for a larger value of the d_1/Λ , the effective cross section of PCF is very small, it is unable to support the mode and the cutoff condition approaches. In this case, as the mode field expands, the spot-size rapidly increases. However, it can be noted that the quasi-TE mode

approaches its cutoff for a slightly lower value of the d_1/Λ as compared to the quasi-TM mode. This would allow the design of a single polarization PCF by fixing the d_1/Λ value between these two cutoff conditions.

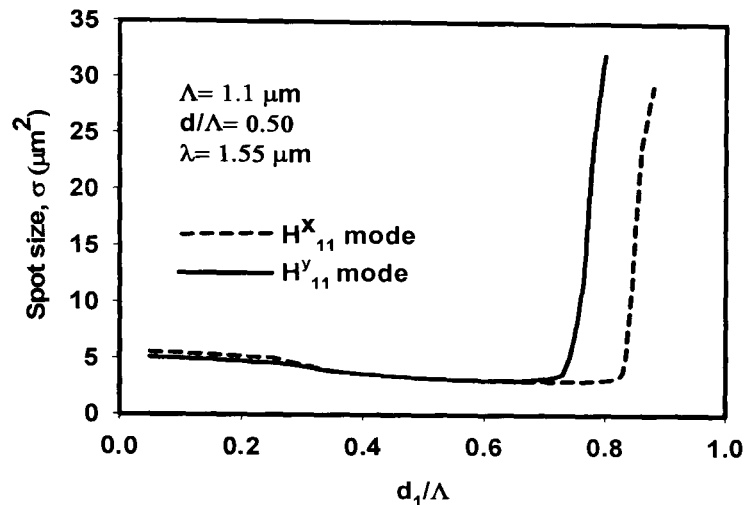


Fig. 8.9: The variation of the spot sizes with the normalized d_1/Λ when $\Lambda = 1.1 \mu\text{m}$.

8.5.2.2 Results of a PCF where Width is Greater than Height

Fig. 8.10 shows the schematic diagram of the polarization maintaining hexagonal lattice PCF with expanded unequal air holes. In this case, diameters of the four air holes in the first ring are increased to break the rotational symmetry. The asymmetry arrangement considered here is similar as in [Saitoh and Koshiba, 2003b], where the diameters (d_2) of the four air holes in the first ring are different from that of the other diameters (d).

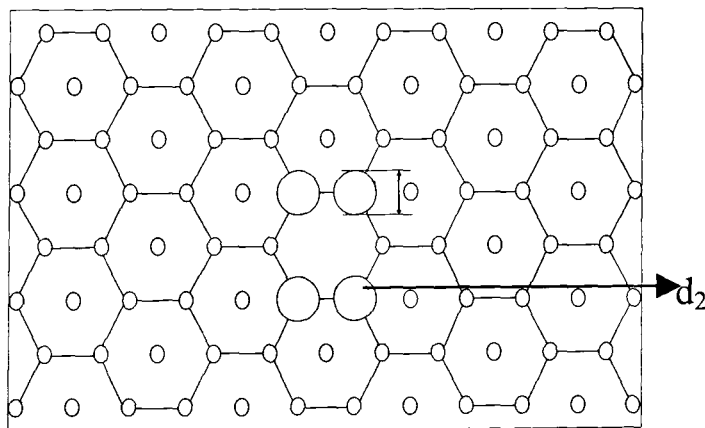


Fig. 8.10: Schematic diagram of the hexagonal lattice PCF with unequal hole sizes in the first ring where four air holes are increased.

Fig. 8.11a shows a hexagonal lattice PCF structure with equal circular air-holes and Fig. 8.11b shows four unequal circular holes. As the sizes of four air holes are increased in the first ring, it can be clearly visible that the air region in this structure is increased. Compared with Fig. 8.7b, it can be noticed from Fig. 8.11b that the width of the silica index is greater than that of height [$n_e^y > n_e^x$].

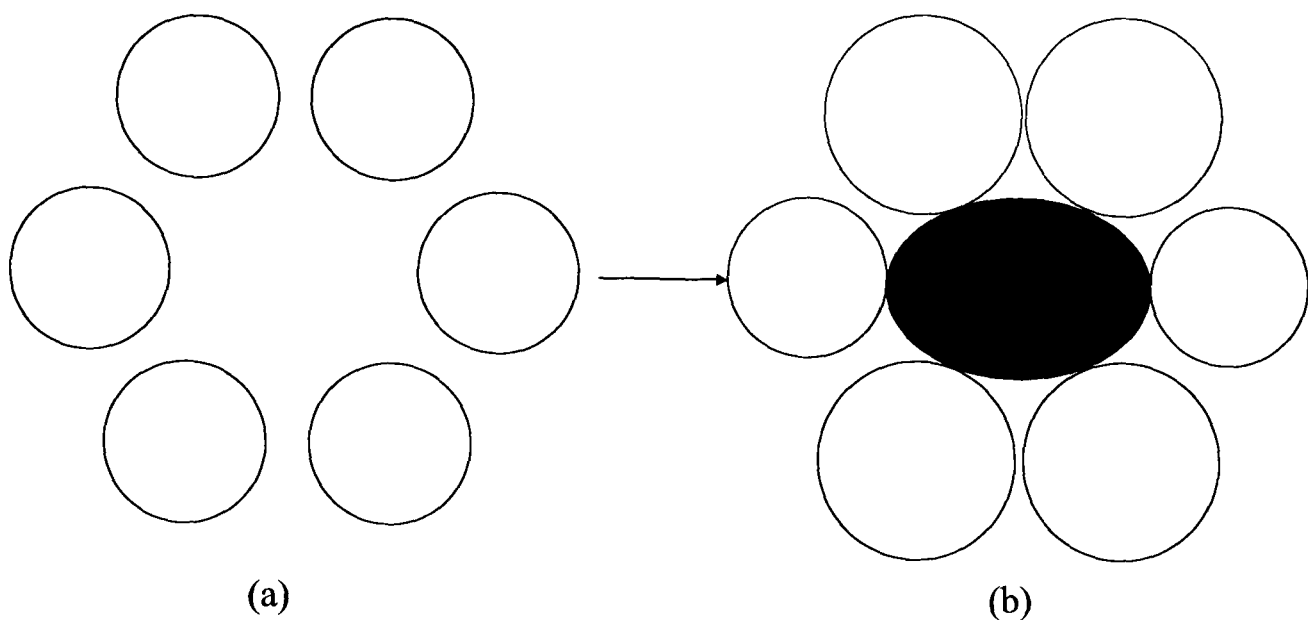


Fig. 8.11: (a) Array of hexagonal lattice, where (b) four unequal circular holes are increased.

The variations of the effective indices for the fundamental quasi-TE (H_{11}^y) and quasi-TM (H_{11}^x) and the second quasi-TE (H_{21}^y) modes with the normalized asymmetry (d_2/Λ) are shown in Fig. 8.12. An inset in Fig. 8.12 shows only a single air hole in a quarter of the cross-section used in the numerical simulations. Such an asymmetric PCF would be able to maintain a specific input polarization state and the corresponding modal birefringence is expected to be high. In this case, initially the pitch is taken as $2.2 \mu\text{m}$ with the operating wavelength as $0.5 \mu\text{m}$. In this case, since pitch is much larger than wavelength, modes are well confined. The diameter of asymmetric air hole (d_2) is varied and the diameters of all the other holes are kept fixed at $1.1 \mu\text{m}$ ($d/\Lambda = 0.5$). It can be observed that as the diameter of the air hole, d_2 , is increased, the effective index values decrease. This is due to the fact that with the increased air hole size, the equivalent cladding index is reduced. It can be

clearly observed that as d_2 is increased, the modal index difference between the two fundamental TE and TM polarized modes increases. This arises because the increased d_2 diameter makes the PCF structure more asymmetric. An increased d_2 value makes the height of the effective core smaller than that of the width (as shown in Fig. 8.11) and as a consequence the effective index of the quasi-TE mode is higher than that of the quasi-TM mode. For comparison, the effective index variation of the H^y_{21} mode is also shown in this figure. It was also observed, but not shown here, that the spot-size reduces as the d_2 diameter is increased as the increased air hole diameter restricts the optical field further in the core region.

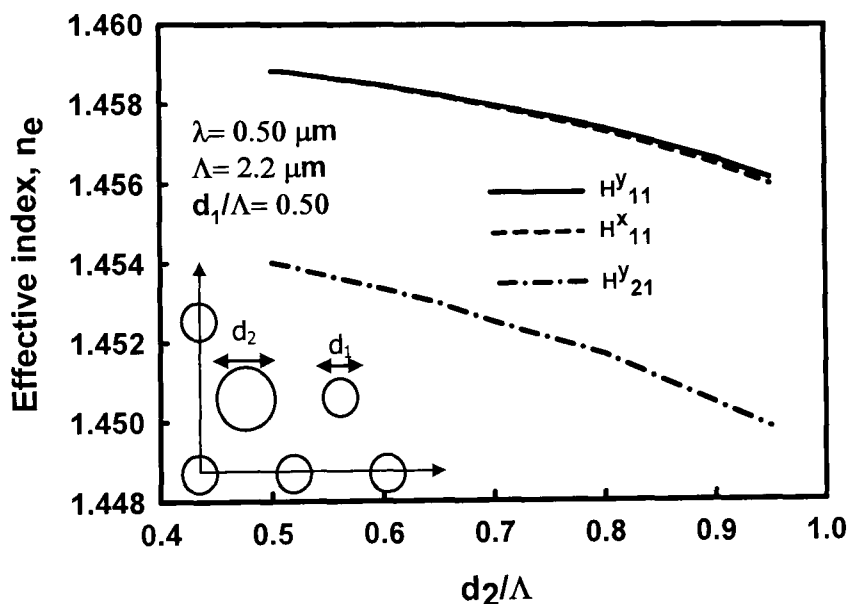


Fig. 8.12: Variation of the modal indices with the normalized diameter, d_2/Λ .

The variation of the modal birefringence, B , and beat length, L_B , at the operating wavelength $\lambda=0.50 \mu\text{m}$, are shown in Fig. 8.13. In this case the modal birefringence is defined as:

$$B = n_y - n_x \quad [8.1]$$

where n_y and n_x are the effective indices of the fundamental H^y_{11} and H^x_{11} modes, respectively.

The polarization beat length, L_B , is a measure of the birefringence and is defined as:

$$L_B = 2\pi / (\beta_y - \beta_x) = \lambda/B \quad [8.2]$$

Where, β_y and β_x are the propagation constants of the H_{11}^y and H_{11}^x modes, respectively.

It can be clearly observed that the birefringence value, as shown by a dashed line, increases as the value of d_2 is increased, since the symmetry of the PCF structure is progressively destroyed. The beat length, L_B , reduces monotonically with the d_2 hole diameter with a value of $1500 \mu\text{m}$ and a birefringence value of 1.6×10^{-4} when $d_2/\Lambda = 0.95$.

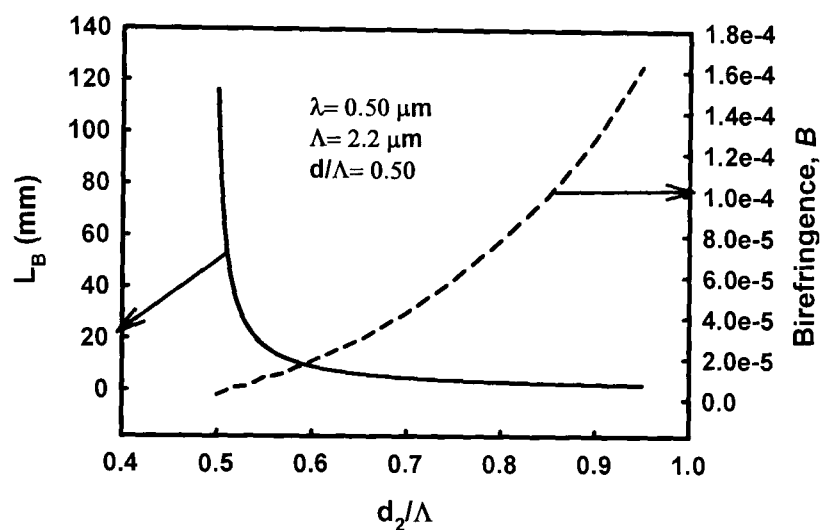


Fig. 8.13: The variation of the beat length and modal birefringence with the normalized diameter, d_2/Λ at the operating wavelength, $\lambda=0.50 \mu\text{m}$.

Next, the effect of the operating wavelength, λ , is studied, keeping the $\Lambda= 2.2 \mu\text{m}$, $d/\Lambda= 0.50$, same as the previous example. As the operating wavelength increases, the modal confinement is reduced, the optical field expands, and interacts with the silica/air interfaces around the air/hole circumferences and hence the modal birefringence increases. The variation of the birefringence, B , is shown in Fig. 8.14, by a dashed line at the operating wavelength, $\lambda=1.55 \mu\text{m}$. For comparison, the modal birefringence variation at $\lambda= 0.50 \mu\text{m}$, which was shown in Fig. 8.13, is also shown here by a solid line. It can be clearly observed that at the wavelength $\lambda=1.55 \mu\text{m}$, the maximum birefringence increases significantly to a value of 0.0039 compared to its maximum value of only 0.00016 at the wavelength $\lambda= 0.50 \mu\text{m}$.

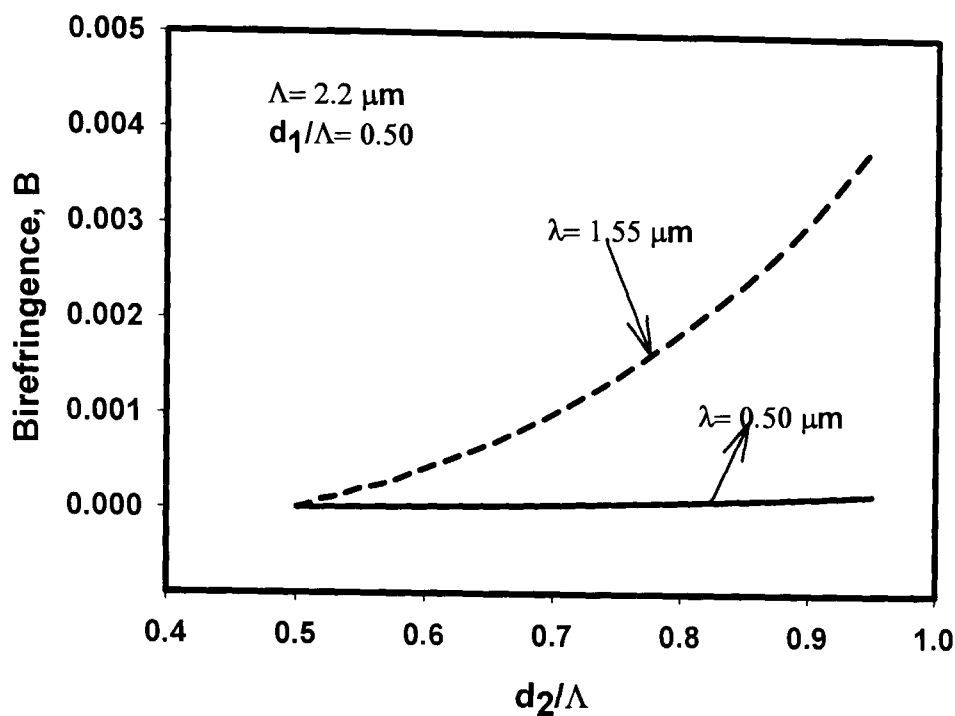


Fig. 8.14: The variation of the modal birefringence with the normalized diameter, d_2/Λ at the operating wavelength, $\lambda=1.55 \mu\text{m}$ and $\lambda=0.50 \mu\text{m}$.

It is expected that a lower pitch length, Λ , would produce a higher birefringence for a given structural asymmetry. To achieve a higher birefringence value, next, a smaller pitch length, $\Lambda = 1.1 \mu\text{m}$ is considered. In this case, only one of the air hole diameters (d_2) (in the quarter cross-section) is enlarged to increase the modal birefringence, while keeping all other normalized air hole diameters fixed at $d/\Lambda = 0.50$. The variation of the effective indices with the normalized asymmetric air holes, d_2/Λ , is shown in Fig. 8.15 for the quasi-TE and quasi-TM modes. It can be observed that for lower values of d_2 , the effective indices for the quasi-TE modes are lower than those of the quasi-TM modes, as the effective width of the PCF would be smaller than their heights in these cases. On the other hand when the d_2 values are larger, the effective index values of the quasi-TE modes are higher, since the effective widths are now larger than their heights. The effective index curves cross each other when the d_2 value is similar to that of other air hole diameters, $d/\Lambda \approx 0.5$, in this case.

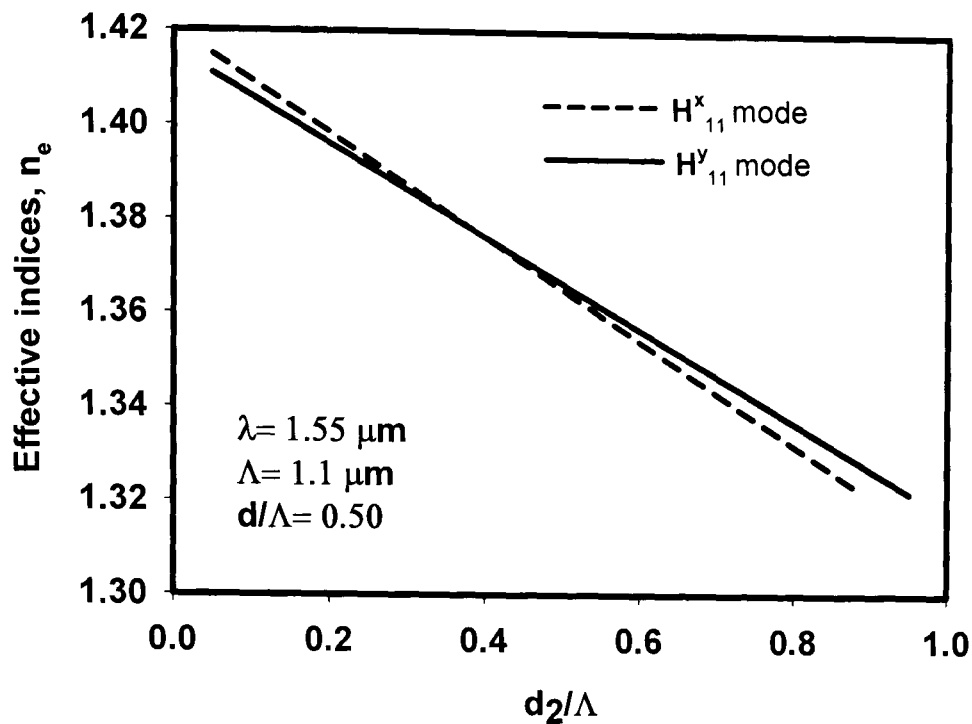


Fig. 8.15: Variation of the effective indices with the normalized d_2/Λ when $\Lambda = 1.1 \mu\text{m}$.

The variation of the spot-size with the d_2/Λ is shown in Fig. 8.16 for the quasi-TE and quasi-TM modes for $d/\Lambda = 0.5$ and $\Lambda = 1.1 \mu\text{m}$. It can be noted that for the polarization states, initially the spot-size is reduced as d_2/Λ is increased. However, when for a larger value of the d_2/Λ , the effective cross section of PCF is very small, it is unable to support the mode and the cutoff condition approaches. In this case, the spot-size increases rapidly as the mode field expands. However, it can be noted that the quasi-TM mode approaches its cutoff for a slightly lower value of the d_2/Λ as compared to the quasi-TE mode. This is due to the reason that compared to Fig. 8.9 near cutoff region $n_x < n_y$, so H_{11}^x mode approaches cutoff earlier.

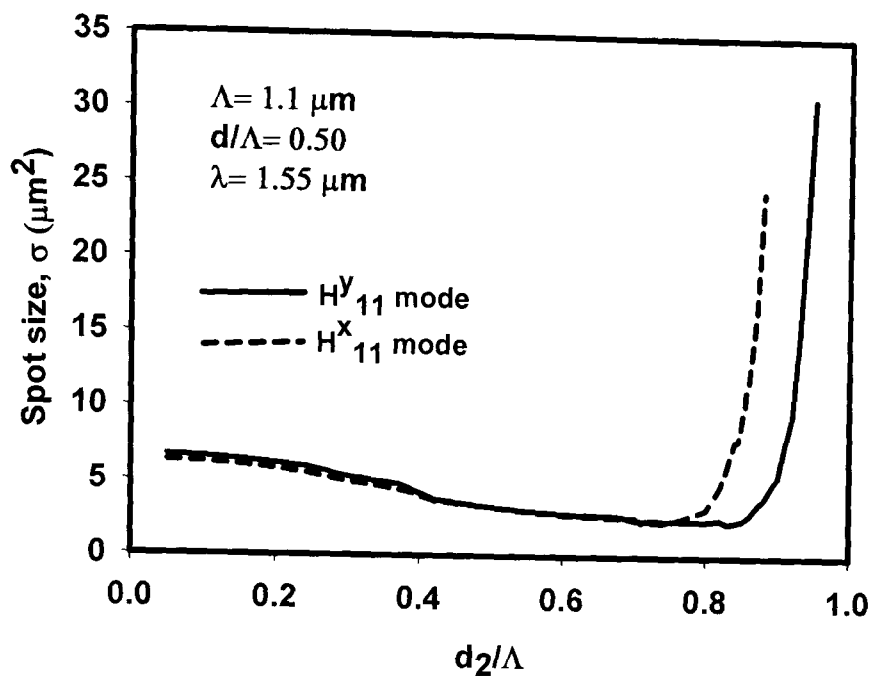


Fig. 8.16: The variation of the spot sizes with the normalized d_2/Λ when $\Lambda = 1.1 \mu\text{m}$.

The modal birefringence, B , depends strongly on the symmetry of the structure such as arises from unequal hole diameters and noncircular shapes and also on the modal confinement. Since the modal confinement is low for smaller value of the pitch, to achieve a higher birefringence value, a smaller pitch length, $\Lambda = 1.10 \mu\text{m}$ is considered. The variation of the birefringence with the normalized air hole diameter (d_2/Λ), is shown in Fig. 8.17, as a solid line, when $\Lambda = 1.1 \mu\text{m}$ at the operating wavelength $\lambda = 1.55 \mu\text{m}$. For reference, the variation of the birefringence when $\Lambda = 2.2 \mu\text{m}$ is also shown by a dashed line. It can be clearly observed that as $d_2 > d$, the birefringence is positive as the effective index value of the quasi-TE mode is higher than that of the quasi-TM mode and similarly when $d_2 < d$, the birefringence values are negative as the effective index value of the quasi-TM mode is higher than that of the quasi-TE mode. When the asymmetry is negligible, i.e. the d_2/Λ is smaller to the other air hole, which in this case $d_2/\Lambda \approx 0.50$, the modal birefringence is very small. Birefringence value increases rapidly when d_2 is much larger than d , as both the TE and TM modes approach their cutoff values and their difference increases. For $\Lambda = 1.1 \mu\text{m}$, when the d_2/Λ value is larger than 0.85, this particular PCF cannot guide the H_{11}^x mode and the PCF structure becomes a single polarization guide. It can also be clearly observed that at $\Lambda = 1.1 \mu\text{m}$,

the maximum birefringence increases significantly to a value of 0.00735 at $d_2/\Lambda = 0.85$, compared to its maximum value of only 0.0039 at $\Lambda = 2.2 \mu\text{m}$. This is one of the highest birefringence value reported so far at wavelength of $1.55 \mu\text{m}$ for an asymmetric PCF using the circular air holes. As the hole-spacing period, Λ , reduces, the spot-size initially reduces, but near $\Lambda=1.10 \mu\text{m}$ the fundamental mode approaches its cutoff condition, the optical field expands and extends more around the silica/air interfaces around the air/hole circumferences and as a result the modal birefringence increases. It is significant that the birefringence value of such a simple PCF with circular holes is high, compared to the polarization maintaining Panda or Bow-tie fibres [Liu *et al.*, 1994] and thus useful for many practical applications in optical communications and sensing.

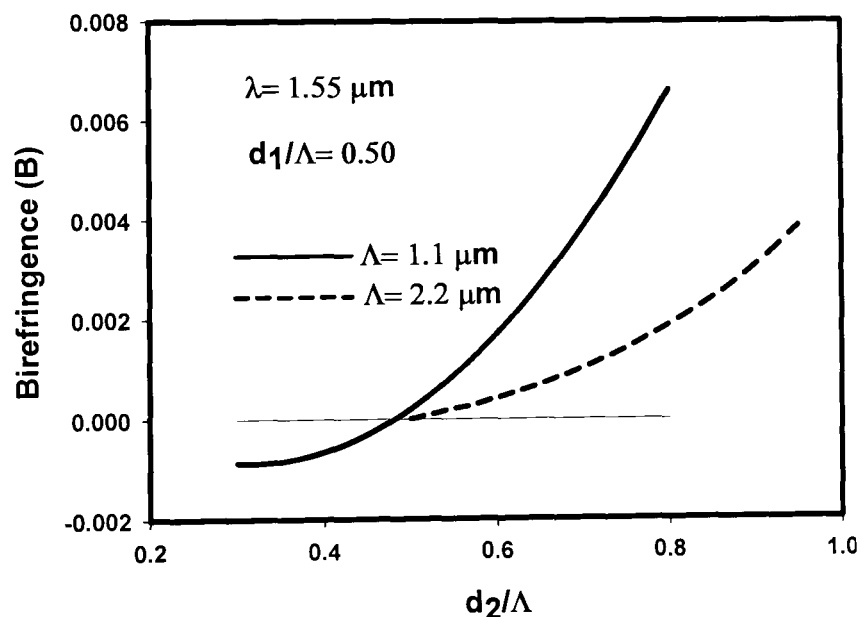


Fig. 8.17: Variation of the modal birefringence with the normalized d_2/Λ for $\Lambda = 1.1 \mu\text{m}$ and $2.2 \mu\text{m}$.

8.5.2.3 Comparison Results of Two Different Structural Asymmetry

It was mentioned earlier that diameters of either two air holes [Kubota *et al.*] or four air holes [Saitoh and Koshiba, 2003b] in the first ring could be changed to break the rotational symmetry. Although both cases have been considered separately, a comparison between the two designs is made in this work. The variations of the birefringence (B) with the normalized air hole

diameter, are shown in Fig. 8.18 for the two-hole and four-hole cases by a solid line and a dashed line, respectively when $\Lambda = 1.1 \mu\text{m}$ and the operating wavelength $\lambda = 1.55 \mu\text{m}$. Hole arrangements are also shown in this figure as an inset. It can be clearly observed that for four-hole arrangements, shown by dashed line as $d_2 > d$, the birefringence is positive and similarly when $d_2 < d$, the birefringence values are negative. It can be noted that for a higher d_2/Λ values, the effective index value of the quasi-TE mode is higher than that of the quasi-TM mode, as in this case the equivalent core width is larger than its height. Similarly, when the d_2/Λ value is lower; the effective index value of the quasi-TM mode is higher as in this case the equivalent width is smaller than its equivalent height. This birefringence value increases rapidly when d_2 is much larger than d , as both the TE and TM modes approach their cutoff values. It can be noted that in this case the maximum birefringence value is significantly higher, reaching a value of 0.00735, one of the highest reported so far at this wavelength for an asymmetric PCF using the circular air holes. When the d_2/Λ value is larger than 0.85, this particular PCF supports only the quasi-TE mode and cannot guide the H_{11}^x mode. Therefore, the PCF structure becomes a single polarization guide.

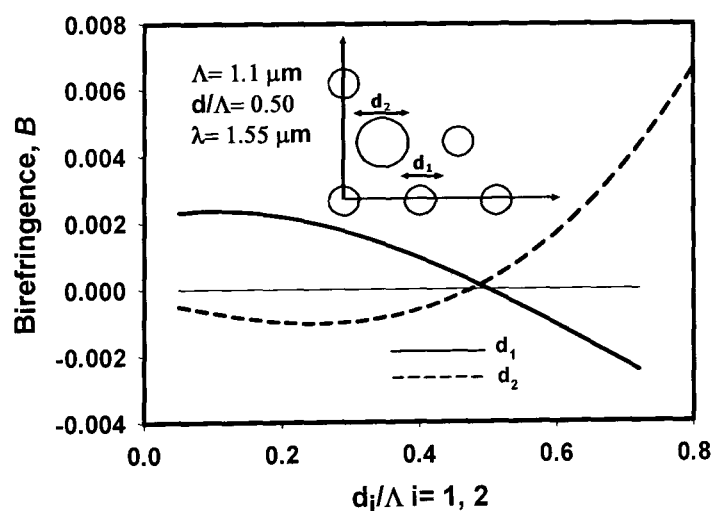


Fig. 8.18: Variation of the birefringence with two different structural asymmetry, d_i/Λ , $i = 1, 2$.

On the other hand, for the two-hole arrangement as shown by a solid line, when $d_1 < d$, the birefringence is positive as the effective width is larger than

its height. However, when d_1 is much larger than d , although the birefringence is negative, this value does not increase significantly. In this case, since the equivalent cross section is reduced only slightly, modal cutoff conditions of the two fundamental modes are not reached. It should be noted that the experimental results can be obtained for similar air hole asymmetry and modal confinement, but enlarging only two air holes [Kubota *et al.*] yielded a much lower birefringence and a value of $B = 0.00258$ was reported in the literature [Kakarantzas *et al.*] which agrees well with the result from this work.

8.5.3 Results of a PCF when Wavelength is Varying

The variation of the modal birefringence, B , with the operating wavelength, λ , is shown in Fig. 8.19. In this case the d/Λ value is kept constant at 0.5 and the asymmetric air holes with their normalized diameter $d_2/\Lambda = 0.95$. For a fixed pitch length, $\Lambda = 2.2 \mu\text{m}$, as the operating wavelength, λ , is increased, the modes become more weakly confined and modal field extends more into the air hole regions. Therefore, the difference between the fundamental quasi-TE and quasi-TM modes also increases.

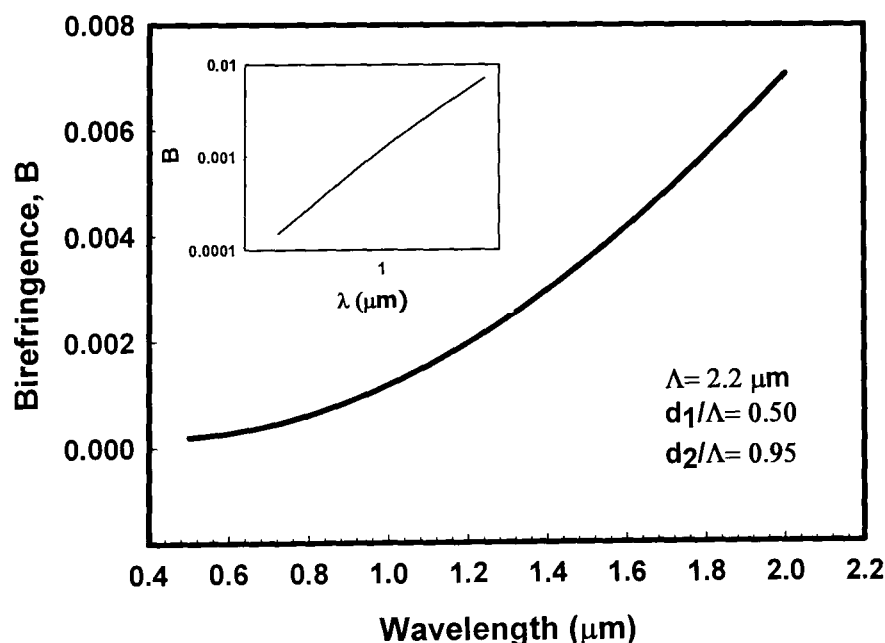


Fig. 8.19: Variation of the modal birefringence and log-log plot with the operating wavelength when $\Lambda = 2.2 \mu\text{m}$, $d/\Lambda = 0.50$, and $d_2/\Lambda = 0.95$.

It can be observed that as the operating wavelength is increased to 2.0 μm , the birefringence is increased significantly to a value of 0.0071 with the corresponding beat length, L_B , reduced to 281 μm (which is not shown here). This result agrees well with the numerically simulated result reported by Saitoh and Koshiba [Saitoh and Koshiba, 2003b] of $B = 0.00327$ at a wavelength of 1.45 μm .

It can be observed that the birefringence value increases rapidly with the operating wavelength. Earlier it has been reported that the birefringence and the operating wavelength could be related by:

$$B \propto \lambda^\kappa \quad [8.3]$$

To obtain the κ dependence, a log-log plot is also shown in Fig. 8.19 as an inset. The nearly straight line relationship demonstrates a fixed value of κ and from the slope of this line, the value of κ has been calculated as 1.6. It should be noted that the κ value depends on the specific design parameters of the PCF and values of 1.38 [Ortigosa-Blanch *et al.*] and 2.7 [Suzuki *et al.*] have been reported.

Variations of the GVD with the operating wavelength for the quasi-TE (H^y_{11}) and quasi-TM (H^x_{11}) modes for the asymmetric structure with $d_2/\Lambda = 0.95$ are shown in Fig. 8.20 by a dashed line and a solid line, respectively. Chromatic dispersion of the silica has been taken into account by calculating the refractive index of silica through the Sellmeier equation [Agrawal], as shown in Appendix 1. For comparison, the GVD of a degenerate PCF with identical air holes, $d_1/\Lambda = d_2/\Lambda = 0.5$, is also shown in this figure by a dashed-dotted line. It can be observed that by controlling the diameters of the air holes, the range of anomalous dispersion, the maximum value of the GVD and its slopes, and the locations of the zero GVD value can be adjusted and similar adjustable GVD properties cannot be achieved in the design of a less flexible telecommunication grade SMF. It can also be mentioned that when the structure being symmetric ($d_1/\Lambda = d_2/\Lambda = 0.50$), the two polarized modes

(H_{11}^x and H_{11}^y) were nearly identical and similarly their GVD were also almost identical, as shown earlier in Fig. 7.29. The polarization dependence of the asymmetric PCF can be clearly observed and so various polarization dependent linear and nonlinear devices can be designed, optimized, and fabricated by using such birefringent PCFs.

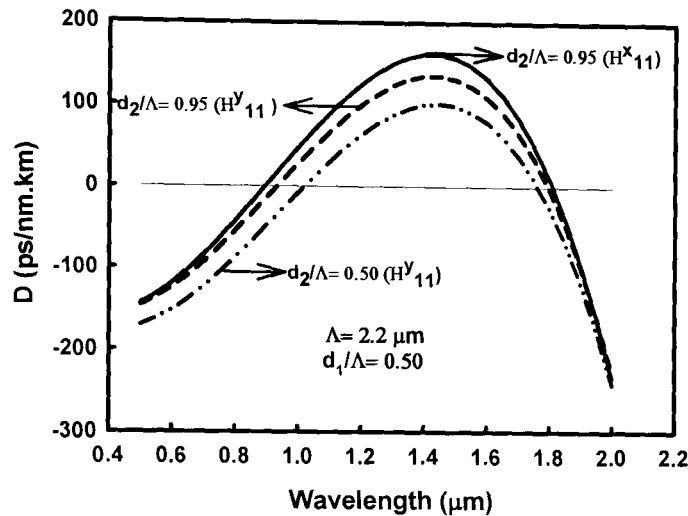


Fig. 8.20: Variation of the GVD with the operating wavelength for equal and unequal hole.

8.5.4 Results of a PCF when Λ is Varying

Earlier, the variations of the optical parameters with the operating wavelength and the normalized hole diameter were shown only for a fixed pitch length, $\Lambda = 2.2 \mu\text{m}$, and $1.1 \mu\text{m}$. The pitch length, Λ , the operating wavelength, λ , and the normalized hole diameter d/Λ , all play key roles in the modal properties and additionally the asymmetry d_2/Λ for the birefringence properties. So, next the effect of the crystal period, Λ , is studied. For a fixed operating wavelength, the pitch length, Λ , can be used as the key controlling parameter.

For a PCF with a regular hexagonal hole arrangement of a fixed diameter, a six-fold or 60 degree rotational symmetry exists, which makes the modes degenerate. There will be degenerate modes with the polarization directions rotated 60 degrees from each other. However, strictly speaking the vertically polarized TE and horizontally polarized TM modes would not degenerate as the required 90 degrees rotational symmetry does not exist. Despite very

good hexagonal symmetry in the fabricated PCFs, the existence of high birefringence in such PCFs has been measured by several groups [Peyrilloux *et al.*; Hansen *et al.*, 2004; Palavcini *et al.*; Eggleton *et al.*, 1999] but this has often been attributed to possible internal stress or to slight asymmetry, due to variations in the positioning and the diameters of the air holes. In several numerical studies, the structural representations have been systematically refined by using the finite element method [Peyrilloux *et al.*, 2003; Koshiha and Saitoh, 2001] and the plane wave method [Hwang *et al.*]. In all of these cases, a small residual birefringence remained, again probably incorrectly attributed to the intrinsic calculation error of the computational approach. However, from these reports [Peyrilloux *et al.*, Hwang *et al.*] it could be clearly observed that this residual birefringence value is larger for smaller Λ/λ values.

Variations of the birefringence with the pitch length, Λ , for a PCF with 60 degree rotational symmetry for two normalised air hole dimensions $d/\Lambda = 0.5$ and 0.4 have been studied and are shown in Fig. 8.21 by a solid line and dashed line, respectively. In this case the operating wavelength is fixed at $1.55 \mu\text{m}$.

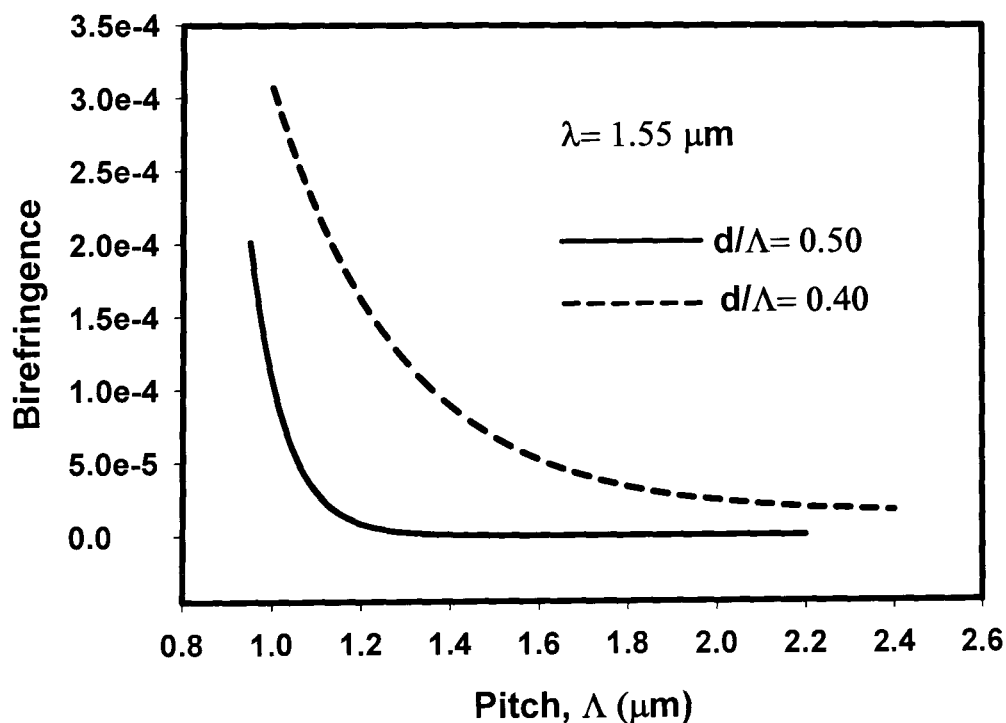


Fig. 8.21: Variation of the modal birefringence with the pitch.

For a PCF with a larger Λ/λ value, the birefringence is very small but it can also be observed that as the pitch length, Λ , is reduced, the birefringence value is increased. This is due to the reason that for lower d/Λ , field spreads more in the air hole region. For lower d/Λ , cutoff approaches slowly, and so birefringence increases slowly. In these cases, the overall birefringence values are small since PCF with identical circular air holes in hexagonal hole arrangement has a six-fold rotational symmetry, which produces degenerative modes. However, strictly speaking 90 degree rotational symmetry is not available so the propagation constants for the quasi-TE and quasi-TM modes are slightly different.

It should be noted that for some special cases the birefringence could be zero but in general this is not true for all the regular PCF structures with a six-fold symmetry, and more particularly when operating close to their cutoff points. It can be noted that for higher d/Λ values, the birefringence changes rapidly with Λ as their corresponding cutoff condition also approaches rapidly. However, this figure indicates that even with the apparent symmetry, the birefringence value can be maximised when operating close to their cutoff conditions with a smaller pitch length. One important validation of this work is the existence of the modal birefringence for PCFs with six-fold rotational symmetry.

8.6 Simulation Results for Leakage Loss

A schematic diagram of the two rings, consisting of 18 air holes, PCF is shown in Fig. 8.22. In this figure, air holes are arranged in silica background whose index of refraction is taken as 1.444 at the wavelength of 1.55 μm and where d is the hole diameter and Λ is the hole pitch. In all simulations, the computational window area $L_x/2 \times L_y/2$ has been taken as 10 $\mu\text{m} \times 10 \mu\text{m}$, which has been terminated by a PML whose width, W , is 5.0 μm and divided into 5 divisions.

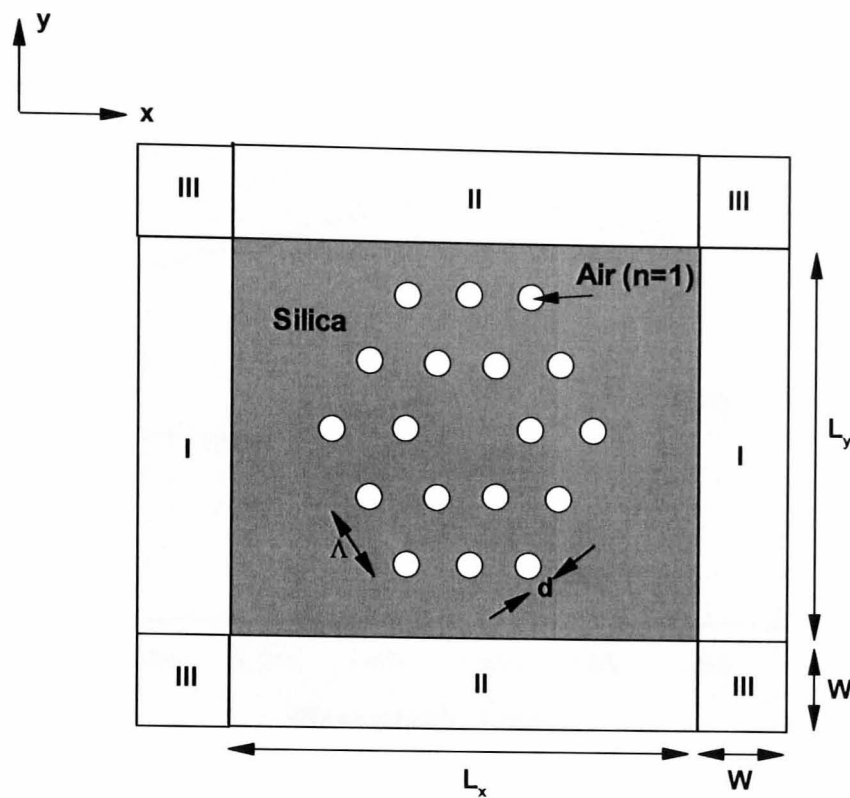


Fig. 8.22: Schematic diagram of a PCF of two rings of 18 air holes [Obayya *et al.*, 2005].

8.6.1 Result of Leakage Loss when Number of Ring is Varying

The variations of the confinement losses of a three-ring and two-ring PCF in dB/m for the fundamental quasi-TE modes in the logarithmic scale as a function of operating wavelength, λ are shown in Fig. 8.23 by a solid line and dashed line, respectively when $d/\Lambda = 0.50$, $d_2/\Lambda = 0.95$ and $\Lambda = 2.2 \mu\text{m}$. It can be noticed from this figure that for three-ring (36 air holes) PCF, the confinement loss is lowered compared to that of two-ring (18 air holes) PCF. This is due to the reason that more air holes improve the confinement value, as more air holes provide well confined modes as well as smaller spot-size values. PCF with small spot-size provides smaller leakage loss. This confinement feature of the mode to the core region is directly linked to how much the mode is “leaking” into the outer air holes region. This effect can be more clearly visible by quantitatively looking at the variation of the confinement loss with the wavelength for different number of air holes as shown in Fig. 8.23. At $\lambda = 1.30 \mu\text{m}$, the confinement loss drops from the value of around 83 dB/m to small value nearly 10 dB/m for two-rings and three-rings PCF, respectively.

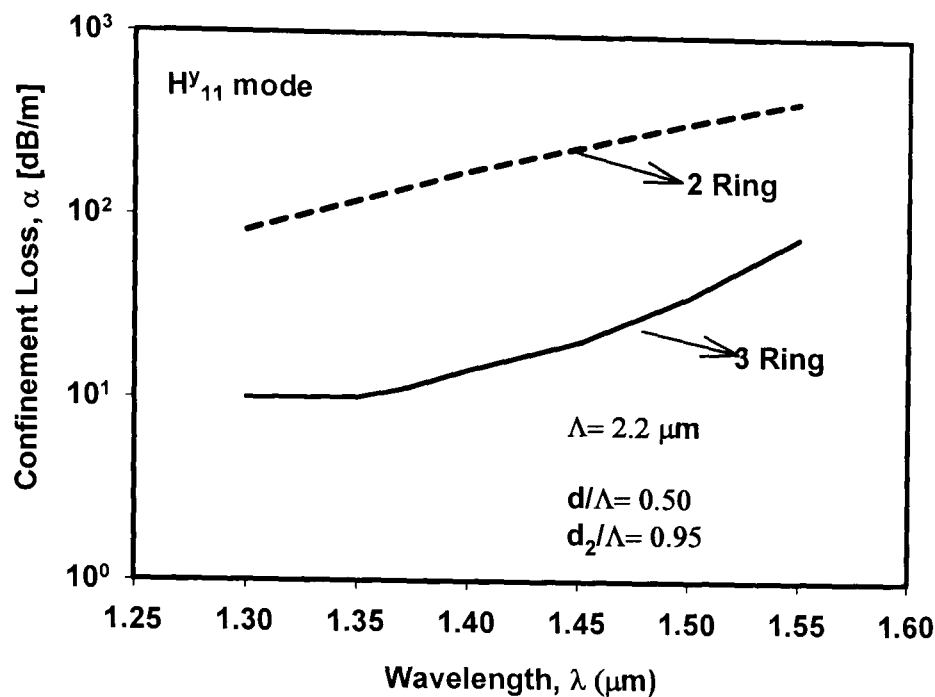


Fig. 8.23: Confinement loss of a three-ring and two-ring PCF of H^y_{11} mode in dB/m with the wavelength, λ when $d/\Lambda = 0.50$ and $d_2/\Lambda = 0.95$ at $\Lambda = 2.2 \mu\text{m}$.

8.6.2 Result of Leakage Loss when d_2/Λ is Varying

The variations of the confinement losses of a three-ring PCF in dB/m for the fundamental quasi-TE modes in the logarithmic scale as a function of d_2/Λ at the operating wavelength $\lambda = 1.55 \mu\text{m}$, $1.35 \mu\text{m}$, and $1.15 \mu\text{m}$ are shown in Fig. 8.24 by a solid line, dashed line, and dashed-dotted line, respectively when $d/\Lambda = 0.50$ and $\Lambda = 1.1 \mu\text{m}$. It can be noticed that the confinement loss for the lower operating wavelength (in this case, $\lambda = 1.15 \mu\text{m}$) is minimum compared to that of higher operating wavelength ($\lambda = 1.55 \mu\text{m}$, and $1.35 \mu\text{m}$). This is due to the reason that at smaller wavelength mode is well confined, as shown earlier in Fig. 7.11a, which leads to improving the confinement loss. For all λ values, the confinement losses decrease rapidly with the decrease in d_2/Λ . Smaller d_2/Λ value improves the confinement value, as smaller d_2/Λ value provides well confined modes as well as smaller spot-size values. PCF with large spot-size provides higher leakage loss. When $d_2/\Lambda = 0.40$, the confinement losses drop from the value of around 9261 dB/m at $\lambda = 1.55 \mu\text{m}$ to small value nearly 4195 dB/m and 598 dB/m at $\lambda = 1.35 \mu\text{m}$ and $\lambda = 1.15 \mu\text{m}$, respectively.

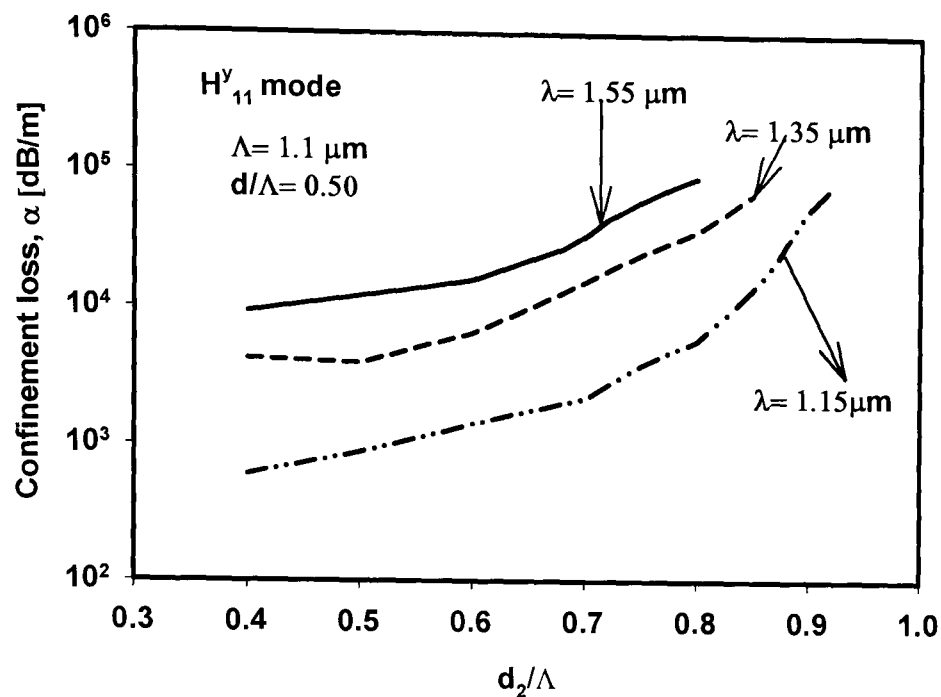


Fig. 8.24: Confinement loss of a three-ring PCF of H^y_{11} mode in dB/m with the d_2/Λ when $d/\Lambda = 0.50$ at $\lambda = 1.55 \mu\text{m}$, $1.35 \mu\text{m}$, and $1.15 \mu\text{m}$.

8.6.3 Result of Leakage Loss when Wavelength is Varying

Finally, the confinement loss of a three-ring PCF in dB/m for the fundamental quasi-TE (H^y_{11}) and the fundamental quasi-TM (H^x_{11}) modes with the operating wavelength, λ at $d/\Lambda = 0.50$ and $d_2/\Lambda = 0.80$ is demonstrated in Fig. 8.25 when $\Lambda = 1.1 \mu\text{m}$. It can be clearly noticed that the confinement loss decreases significantly for both H^y_{11} and H^x_{11} modes with the lower operating wavelength. This is due to the reason that for a larger operating wavelength (exposed in Fig. 7.11b), the guide becomes more weakly confined. As a result the confinement loss is increased. On the other hand, at smaller wavelength mode is well confined, as shown earlier in Fig. 7.11a, which leads to improving the confinement loss. The confinement loss for the fundamental quasi-TE (H^y_{11}) mode drops from a value of nearly 90155 dB/m at $\lambda = 1.55 \mu\text{m}$ to a very small value around 3101 dB/m at $\lambda = 1.1 \mu\text{m}$. Similarly, the confinement loss for the fundamental quasi-TM mode drops from a value of nearly 28069 dB/m at $\lambda = 1.55 \mu\text{m}$ to a very small value around 127 dB/m at $\lambda = 1.1 \mu\text{m}$. Which indicates, the fundamental quasi-TM (H^x_{11}) mode provides 24 times smaller confinement loss value than that of the fundamental quasi-TE (H^y_{11}) mode at $\lambda = 1.1 \mu\text{m}$.

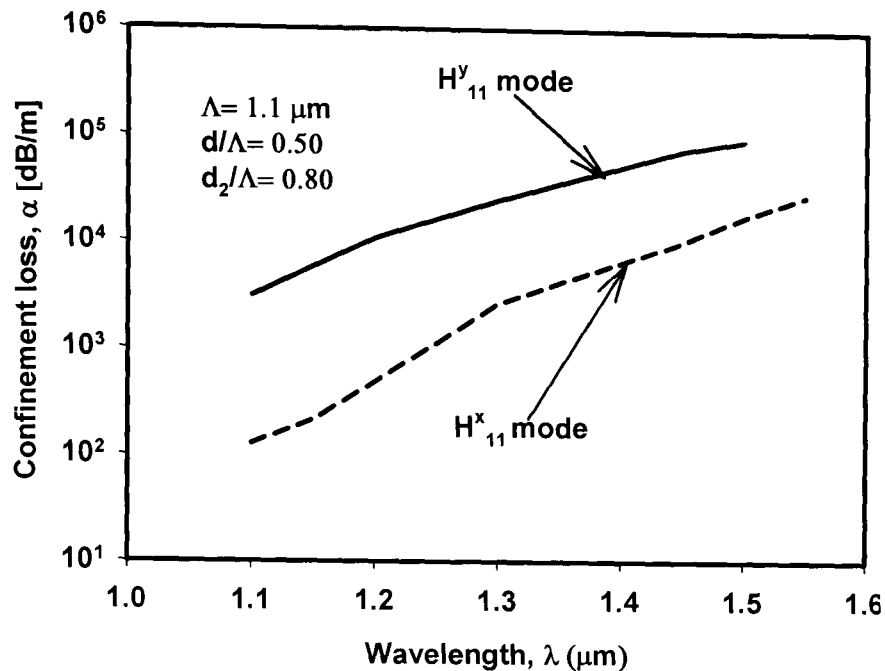


Fig. 8.25: Confinement loss of a three-ring PCF for H^y_{11} and H^x_{11} modes with the operating wavelength, λ at $d/\Lambda = 0.50$ and $d_2/\Lambda = 0.80$.

8.7 Summary

In this chapter, a rigorous analysis of hexagonal lattice photonic crystal fibre with symmetrical and asymmetrical circular air holes is presented, to understand the basic properties of photonic crystal fibres. Important design parameters, such as the effective indices, spot-sizes, modal hybridness, beat length, modal birefringence, and group velocity dispersion values are determined for equal and unequal and circular hole PCFs, by using a rigorous full-vectorial finite element based approach. The variation of the modal birefringence, an important optical parameter, is shown through the effect of the hole diameters, air hole arrangement, structural asymmetry, the operating wavelength, the pitch-distance, and with the use of this modelling approach it was possible to design a highly birefringence PCF by adjusting the different fabrication parameters.

Birefringence was enhanced by breaking the structural symmetry and this was verified by using unequal air holes. The diameter of two air holes and four air holes in the first ring was changed to break the rotational symmetry. Although

both cases have been considered separately, a comparison between the two designs is made in this work. In this work, highly birefringent PCF is designed with the higher operating wavelength, larger d_2/Λ value, lower pitch length for a given structural asymmetry. It is identified that at the wavelength $\lambda=1.55 \mu\text{m}$ the maximum birefringence increases significantly to a value of 0.0039 compared to its maximum value of only 0.00016 at the wavelength $\lambda=0.50 \mu\text{m}$. Birefringence value increases rapidly when d_2 is much larger than d . It can also be clearly observed that at $\Lambda = 1.1 \mu\text{m}$, the maximum birefringence increases significantly to a value of 0.00735 at $d_2/\Lambda = 0.85$, compared to its maximum value of only 0.0039 at $\Lambda = 2.2 \mu\text{m}$. This is one of the highest birefringence value reported so far at wavelength of $1.55 \mu\text{m}$ for an asymmetric PCF using the circular air holes. A single polarization guide PCF structure is achieved, as this particular PCF supports only the quasi-TE mode at $d_2/\Lambda = 0.85$. In this study, it is identified that for the fixed d/Λ value kept constant at 0.5 and the asymmetric air holes with their normalized diameter $d_2/\Lambda = 0.95$, as the operating wavelength is increased to $2.0 \mu\text{m}$, the birefringence is increases significantly to a value of 0.0071. It can also be identified that for higher d/Λ values, the birefringence changes rapidly with Λ as their corresponding cutoff condition also approaches rapidly.

One important validation of this work is the existence of the modal birefringence for PCFs with six-fold rotational symmetry. It is shown that the birefringence value of a simple PCF with circular holes is high, compared to the polarization maintaining Panda or Bow-tie fibre [Liu *et al.*, 1994].

In this chapter, leakage properties of photonic crystal fibres are also presented. The semi-vectorial finite element based beam propagation method has been successfully applied to perform the accurate modal analysis of PCFs. The effects of the number of air holes, d_2/Λ , operating wavelength, and the geometrical parameters of the holes on the modal properties such as the confinement loss due to the leakage nature of the modes have been thoroughly studied and explained.

Conclusion and Future Research Direction

9.1 Conclusion

Progressing from the copper wire of a century ago to today's fibre optic cable, increasing ability to transmit more information, more quickly and over longer distances has expanded the boundaries of the technological development in all areas. Optical fibres now play important role in almost everyone's life. These hair-thin strands of glass guide light from one place to another, conveying voice or data signals at the speed of light over the global networks. When optical fibres were developed in the 1970s, it opened new doors to the world of communications. The advantages of using optical fibres over conventional methods such as copper wires has led the ability of transmitting and receiving more and more data at lower cost. Fibre optics has several advantages over traditional metal communications lines which were described earlier in section 1.10. While fibre optic cable itself has become cheaper over

time, an equivalent length of copper cable cost less per foot but not in capacity.

The main drawback of optical fibre is dispersion, which limits its bandwidth and signal transmission on optical fibre wire over long distance requires expensive repeaters at distance intervals. Fibre optic cable connectors and the equipment needed to install them are still more expensive than their copper counterparts. In addition, they are more fragile than wire and are difficult to splice. The glass fibre requires more protection within an outer cable than copper. For these reasons and because the installation of any new wiring is labor-intensive, few communities yet have optical fibre wires or cables from the phone company's branch office to local customers. Despite these facts, in the long term it may be more cost effective to invest in conversion to fibre optics. This is due to the relative ease of upgrading fibre optics to higher speed and performance.

A new type of optical fibre, known as photonic crystal fibre, is one of the new possibilities, which may have the special properties to revolutionise the telecommunication industry and which can overcome the problems associated with conventional fibre. Although the principles are the same as a conventional optical fibre but photonic crystal fibre offers many advantages over conventional fibre, such as controllable dispersion and a greater bandwidth. The photonic crystal fibre can outperform conventional fibre optics in several respects. Conventional optical fibres are formed using two different sorts of glass, which have slightly different refractive indices. A higher-index core region is embedded within a lower-index cladding, so that light can become trapped within the core by total internal reflection from the core/cladding interface. In contrast, photonic crystal fibres use just a single material, such as pure silica, which has a regular pattern of tiny air holes running along its length and can transmit a wide range of wavelengths without suffering from dispersion, specially the type of PCF that was designed for this research. Photonic crystal fibre was discussed in Chapter 2.

Depending on the transverse structure design photonic crystal fibres have very different properties, including single-mode propagation regime in a broad band spectral range, large/small mode area to reduce/increase nonlinear effects, low or high bending losses, high nonlinearity for harmonic and supercontinuum generation, highly controllable polarization and group-velocity dispersion, transmission spectra, and birefringence.

The objectives set out at the beginning of the study have been successfully achieved with a detailed analysis of results during the course of the entire work. In this work, a numerical method based on the full-vectorial finite element formulation and the rigorous beam propagation method with PML boundary condition have been extensively used in order to accurately characterise the photonic crystal fibres and to study their birefringence and leakage loss properties. This thesis consists of nine chapters.

Chapter 1 had reviewed the fundamental of optical fibre, and described the ray theory. This chapter had presented information about optical fibre in areas such as: definition, optical communication system, historical background, structure, types, fabrication mechanism, light guidance mechanisms, advantages, and applications.

Chapter 2 had described the basic of photonic crystal fibre. This chapter had provided information about the definition of PCF, historical background, structure and types of PCF, advantages and applications of PCF, fabrication of PCF, and finally the novel properties of PCF.

Chapter 3 had presented the numerous types of numerical solutions for PCF analysis and had dealt with the basic principles and theory of the numerical methods. In this chapter, it had been mentioned that full-vectorial approach was necessary to characterize accurately the PCF. Comparison of different numerical methods had also been presented and finally defined why finite element method was one of the most appropriate methods for the modal solutions of PCF.

Chapter 4 had introduced the finite element method which is known as the general-purpose numerical approach for optical waveguides and is gradually being used by more researchers. In this chapter, the fundamental concepts such as the electromagnetic field equations, boundary condition, finite element formulation, discretisation of the domain, shape functions, spurious solution, the element matrices, and infinite element analysis were explained in detail. The vector **H**-field variational formulation has been implemented. However with this **H**-field formulation, the appearance of the spurious modes along with the physical modes had been a main drawback. The penalty function method was introduced in order to eliminate these spurious modes by imposing the constraint $\nabla \cdot \mathbf{H} = 0$. The research work had clearly shown that the finite element method has emerged as one of the most powerful, versatile, and accurate methods to accurately characterize the modal solutions of PCF as well as in analyzing the birefringence properties of PCF which can be used to represent any arbitrary-shaped PCF with arbitrary hole shapes, sizes, orientations and placement. The infinite elements can represent accurately the exponentially decaying optical field outside the core region. Although, if perfectly matched layers (PMLs) were used, another important parameter, the leakage loss, could be obtained but the eigenvalue equation would be complex and storage and computational time would be at least double.

Chapter 5 had reviewed the fundamental of the beam propagation method which is used to calculate the leakage loss of the PCF. This chapter had presented basic information about beam propagation method in areas, such as: historical background, underlying mathematical theory, applications, numerical techniques, and boundary conditions. This approach had been used extensively in this thesis to calculate the leakage loss of the PCF.

Chapters 6 to 8 were dealt with the numerical results, carried out during the entire research work. Chapter 6 first described square lattice planar PCF initially with square core followed by rectangular core. Modal solutions were then presented to understand the basic properties of photonic crystal fibres and to analyse the two and three-dimensional square, and rectangular core PCF. Modal solutions for the fundamental and higher order quasi-TE and

quasi-TM modes had been obtained in this work. Important design parameters, such as the effective indices, modal field profiles, variation of their spot-sizes, modal hybridism, and GVD properties had been calculated using a rigorous full-vectorial finite element based approach. In order to reduce the computational cost and also to achieve adequate mesh refinement in the core region, the existing two-fold symmetry had been exploited.

Photonic crystal fibres with a hexagonal array of holes have been widely studied by many authors and a similar structure was also considered in Chapter 7 for the further investigation. Initially, a PCF with identical holes with a $2.2 \mu\text{m}$ pitch had been investigated. Two different hole diameters had been considered here, for $d = 0.66 \mu\text{m}$ and $1.1 \mu\text{m}$, yielding a d/Λ ratio of 0.3 and 0.5, respectively. Important design parameters, such as effective indices, field profiles, spot-sizes, hybridism, power confinement factor, and the GVD properties had also been calculated in this chapter for equal and unequal circular hole PCFs. The variation of the GVD was shown through the effect of the hole diameters and asymmetry and with the use of this modelling approach it might be possible to design a PCF with a specific GVD, or other optical properties, by adjusting the different fabrication parameters. For a PCF with a regular hexagonal hole arrangement of a fixed diameter, a six-fold or 60 degree rotational symmetry exists, which makes the modes degenerate. However, strictly speaking the TE and TM modes are not degenerate as the required 90 degree rotational symmetry does not exist. For this structure with identical holes, in practice, the modal birefringence is very small. The dominant H^y field profiles of the fundamental quasi-TE (H_{11}^y) mode for $d/\Lambda = 0.30$ and $d/\Lambda = 0.70$ were shown earlier in Figs. 7.7a and 7.7b, respectively. It was clearly seen that for lower value of the air hole diameter, the field extended in the silica bridging area (in-between the air holes). On the other hand for the larger air holes with narrow bridging area, the field was more confined in the core, as they were restricted from the low-index air regions. The effect of the hole diameter on the spot-size was clearly visible, and its variation was shown in Fig. 7.6.

Next in Chapter 8, the modal birefringence properties of a PCF were investigated for a situation where the 90 degree rotational symmetry does not exist. In this case, the size of one of the air-holes, d_2 , was different from the others which was ideal for calculating modal birefringence. Initially, two air holes are enlarged, as shown in Fig. 8.3, to break the symmetry of the structure, so that modal birefringence can be calculated. Later on, four air holes, as shown in Fig. 8.4a, are enlarged to break the symmetry of the structure. Comparisons of both of the results were also discussed in section 8.5.2.3. The wave guiding properties of PCFs, such as modal index, spot-size, group velocity dispersion, and modal birefringence value strongly depend on the hole diameter and the period, for a given operating wavelength. Therefore, the variations of the modal solutions with the hole period, were shown in section 8.5.4. It was expected that a lower pitch length would produce a higher birefringence for a given structural asymmetry. To achieve a higher birefringence value, next, a smaller pitch length, $\Lambda = 1.1 \mu\text{m}$ was considered. In that case, only one of the air hole diameters (d_2) was enlarged to increase the modal birefringence, while keeping all other normalized air hole diameters fixed at $d/\Lambda = 0.50$. The variation of the birefringence (B) with the normalized air hole diameter (d_2/Λ), was shown in Fig. 8.17, when $\Lambda = 1.1 \mu\text{m}$ and the operating wavelength $\lambda = 1.55 \mu\text{m}$. It could be noted that the modal birefringence was much higher than could be achieved by simply adjusting the waveguide parameters of a SMF. So far, the highest value of the birefringence, $B = 0.00735$ at wavelength of $1.55 \mu\text{m}$, for any asymmetric PCF with circular air-holes is reported [Rahman, *et al.*, 2006b]. Finally, Chapter 8 was designed to calculate the leakage loss of photonic crystal fibre using the finite element based beam propagation method (BPM) with PML boundary condition. In this chapter, the effects of the d_2/Λ , number of holes and the geometrical parameters of the PCF on the effective index, the confinement losses, the effective mode area and the effects of the wavelengths had been thoroughly studied for the fundamental mode.

It seems clear from the great diversity and the recent progress in the area of photonic crystal fibre that this will be an important, rapidly growing and

intellectually stimulating field for many years to come. The demand for holey fibres from industry is clear. It looks likely that within the next few years they will be making a whole world of difference. There are tremendous possibilities to use this fibre to simplify the design of optical networks and do things that are very difficult or expensive today, if companies working to produce PCF can overcome the obstacles standing in the way of commercially manufacturing PCF. The cost savings potential of such an achievement is enormous, but so is difficult [Lindstorm, 2001b].

9.2 Future Research Directions

Ferrando *et al.* had shown that how the birefringence profile of the fibre can be tailored with large degree of freedom and had shown that the ordinary honeycomb and triangular [Ferrando *et al.*, 2000b] PCF had negligible birefringence. Hansen *et al.* [Hansen *et al.*, 2002] designed the microstructured region slightly elliptical (2.8%), as a result an ellipticity of the core region was giving rise to birefringence that made the fibre polarization maintaining.

It is well known that the form birefringence of silica fibre is smaller due to the smaller index contrast and additional birefringence may be introduced using stress-applying parts, with different thermal expansion coefficients, as in the design of Panda type fibres. On the other hand, the form birefringence of a PCF can be significantly higher than that of the Panda fibres because of their higher air/silica index contrasts. In Panda type fibres, due to thermal stress, both the ordinary and extraordinary indices changes, but their spatial variations are nonuniform [Liu *et al.*, 1994] and their difference, although larger than the form birefringence of solid silica fibre, are smaller relatively than the form birefringence of asymmetric PCFs. Folkenberg *et al.* have designed a polarization maintaining [Folkenberg *et al.*, 2005] and a single polarization [[Folkenberg *et al.*, 2004] PCF with the stress applying parts to increase the birefringence. Since the designs used identical air holes, with low form birefringence, the increased birefringence values due to the stress present were between 1×10^{-4} [Kubota *et al.*] and 3×10^{-4} [Folkenberg *et al.*,

2005], which is of a similar order to that in a Panda or Bow-tie silica fibre [Liu *et al.*, 1994].

The air holes of a PCF can also be selectively filled up with other materials having different refractive index values, such as polymer [Kerbage], to create a structural asymmetry. Besides obtaining a moderate birefringence value, of the order of 10^{-3} , this parameter can also be tuned with the temperature adjustment. When the refractive index change of the polymer, $\partial n/\partial T$, is taken as $-4 \times 10^{-4}/^{\circ}\text{C}$, this yields a birefringence change of the order of $\partial B/\partial T \sim 3 \times 10^{-6}/^{\circ}\text{C}$. It has also been shown that twisting or bending of the fibres also introduces additional birefringence. Under external force, a waveguide deforms and due to the elasto-optic effect, both the profiles of the ordinary and extraordinary refractive indices change. However, these birefringence changes have been modest and Zhu and Brown [Zhu and Brown] have reported of a birefringence change of 10^{-4} , for an applied force of 1000 N-m.

Although, the effects of stress applying zones, temperature changes, and applied pressure on the enhancement of the birefringence in such highly birefringent PCFs appear to have been limited, these physical parameters can however be used to tune the modal birefringence or to control the polarization degeneration of the light wave for important communications and sensor applications. The powerful finite element method can be used to represent such a complex structure accurately, and this approach is also versatile and effective specially when combined with other physical models, such as the acousto-optic, thermo-optic, elasto-optic, and electro-optic models. As a result it is extremely useful to optimize various novel PCF based components for future applications in communications and sensing in particular.

For PCFs with larger cores and positive dispersion at telecom wavelengths, the confinement loss is negligible and very low transmission loss below 0.6 dB/km has been demonstrated [Farr *et al.*]. By improvement of fabrication process, at wavelength $1.55 \mu\text{m}$, Tajima *et al.* [Tajima *et al.*] developed low-loss (0.37 dB/km) photonic crystal fibre. Hansen *et al.* [Hansen *et al.*, 2003]

showed that the PCF with nonuniform hole-distribution over the cross section of the fibre has higher confinement loss compared to the PCF with uniform hole-distribution.

Researchers from the University of Sydney, Australia, have fabricated photonic crystal fibre based on polymer optical fibre (PC-POF), which they claim is easier to manufacture than glass photonic crystal fibre [Martijin, *et al.*], as only one polymer is involved and no dopants are required, which makes it more suitable for mass-production. They have created hundreds of meters of easy-to-make polymer based photonic crystal fibre. Conventional POF is usually multimode and has high losses. PC-POF can not only be made single mode but also with reduced losses. Polymers are also known to maintain their structural uniformity throughout the fibre, whereas a collapse of internal structure is sometimes observed in a glass PC fibre [fibers.org].

Pure silica HFs can exhibit effective nonlinearities more than 50 times higher than conventional fibres, and that the confinement loss can be lowered below the loss of standard fibre types [Finazz *et al.*, 2003]. Ferrando *et al.* [Ferrando *et al.*, 2000a] showed that the tailorability of the cladding structure enables high flexibility in the design of the dispersion profile facilitating different nonlinear effects, especially by the choice of zero-dispersion wavelength (ZDW). White *et al.* [White *et al.*, 2001b] designed PCF with Ge-doped centre region core to increase the nonlinear refractive index of the core, create smaller mode field diameter and to reduce confinement loss. The novel and very flexible dispersion properties and possibility for very tight mode confinement of photonic crystal fibres makes this fibre type highly attractive as nonlinear medium. The most important parameters for nonlinear fibres are the zero-dispersion wavelength, λ_0 , and the dispersion slope. The nonlinear photonic crystal fibre with λ_0 at 1.55 μm has a many unique properties, which are different from standard nonlinear fibres [Hansen *et al.*, 2003]. Research group from Crystal Fibre A/S demonstrated a highly nonlinear PCF with zero-dispersion at 1.55 μm [Hansen *et al.*, 2002].

New PCF types, such as: elliptical hole PCF [Wu and Chao], double-core PCF [Buczynski *et al.*; Mangan *et al.*; Zhang *et al.*] in different lattice can be examined in future for comparing with existing research work. Transmission properties of double-core square and hexagonal lattice photonic crystal fibres, fabricated from multi-component glass, are measured, inter-core coupling mechanism and possible applications are discussed [Buczynski *et al.*]. Transmission properties of a double-core hexagonal lattice PCF is experimentally verified by Mangan *et al.*, [Mangan *et al.*]. Highly birefringent hexagonal lattice double-core PCF was also used as polarization splitters [Zhang *et al.*]. Taylor *et al.* [Taylor *et al.*] modelled the multi-core PCF structures using an equivalent step-index fibre model [Birks *et al.*] and coupled model theory [Ghatak and Thyagarajan]. Therefore, the demonstration of feasible multichannel communication with acceptably low crosstalk has been successfully achieved [Taylor *et al.*].

The air-holes of the microstructured optical fibres (MOFs) can be filled with various liquids to modify their optical properties. By changing the properties of the liquid, it is possible to modify the propagation properties of the fibre and hence to obtain tunable fibre devices [Wolinski *et al.*]. Eggleton *et al.* demonstrated the first fibre device with tunable transmission, where a high-index liquid was dynamically positioned in a tapered solid fibre. Liquid crystals (LCs) seem to be especially interesting substances to infiltrate MOFs, since their refractive indices can be relatively easily modified by temperature or by external fields. The PCFs with LC inclusions open up a wide range of new possibilities for light propagation tuning properties. In this way, a novel class of micro-structured fibres that can be called 'photonic-liquid crystal fibres (PLCFs)' can be obtained [Eggleton *et al.*, 2000].

Filling the hollow fibre core with gas or other materials to see the impact on light is another possibility researchers are thinking about. Beaming laser light through air has many advantages over beaming it through erbium-doped silica, according to Russell. In the first place, using air as the transport medium almost entirely eliminates optical non-linearities, dispersion and Fresnel reflections [Lindstorm, 2001*b*].

Appendix 1

Calculation of Material (SiO₂) Dispersion

Using Sellmeier's equation from G P Agrawal [Agrawal], the refractive index of silica (n_g) at different λ can be calculated.

Sellmeier's Equation:

$$n^2 - A = \sum G_K \lambda^2 / (\lambda^2 - \lambda_K^2) = G_1 \lambda^2 / (\lambda^2 - \lambda_1^2) + G_2 \lambda^2 / (\lambda^2 - \lambda_2^2) + G_3 \lambda^2 / (\lambda^2 - \lambda_3^2) + \dots$$

$n(x)$ can be obtained

Where,

$$A = 1$$

$$G_1 = 0.69617$$

$$G_2 = 0.40794$$

$$G_3 = 0.89748$$

$$\lambda_1 = 0.0684$$

$$\lambda_2 = 0.1162$$

$$\lambda_3 = 9.8962$$

$$\lambda_1^2 = 0.00467856$$

$$\lambda_2^2 = 0.01350244$$

$$\lambda_3^2 = 97.93477444$$

$$G_1 = 0.69617$$

$$G_2 = 0.40794$$

$$G_3 = 0.89748$$

To avoid all the long calculation, a small program is written to calculate n_g at different λ

```
IMPLICIT REAL*8(A-H,O-Z)

      A1=0.0684d0
      A2=0.1162d0
      A3=9.8962d0

      A1S=A1*A1
      A2S=A2*A2
      A3S=A3*A3

      G1=0.69617d0
      G2=0.40794d0
      G3=0.89748d0
      ZERO=0.0d0

110 write (6,101)
101 FORMAT('GIVE LAMDA')
      READ(5,*)AL
      IF(AL.LE.ZERO)GOTO 150

      G11=G1*AL*AL/(AL*AL-A1S)
      G22=G2*AL*AL/(AL*AL-A2S)
      G33=G3*AL*AL/(AL*AL-A3S)

      ANSQ=1+G11+G22+G33
      AN=DSQRT(ANSQ)
      write(6,102)AL,AN

102 FORMAT('LAMDA=',F10.5,'n=',F10.7)
      goto 110
150 continue
      stop
      end
```

Appendix 2

Calculation of the Element Matrices

From equation [4.55]:

$$\begin{aligned}
 [A]_e &= \varepsilon^{-1} \int_{\Delta} [Q]^* [Q] d\Omega \\
 &= \varepsilon^{-1} \int_{\Delta} \left[\begin{array}{ccc}
 -\beta^2 [N]^T [N] + \frac{\partial [N]^T}{\partial y} \frac{\partial [N]}{\partial y} & -\frac{\partial [N]^T}{\partial y} \frac{\partial [N]}{\partial x} & j\beta [N]^T \frac{\partial [N]}{\partial x} \\
 -\frac{\partial [N]^T}{\partial x} \frac{\partial [N]}{\partial y} & -\beta^2 [N]^T [N] + \frac{\partial [N]^T}{\partial x} \frac{\partial [N]}{\partial x} & j\beta [N]^T \frac{\partial [N]}{\partial y} \\
 j\beta \frac{\partial [N]^T}{\partial x} [N] & j\beta \frac{\partial [N]^T}{\partial y} [N] & \frac{\partial [N]^T}{\partial y} \frac{\partial [N]}{\partial y} + \frac{\partial [N]^T}{\partial x} \frac{\partial [N]}{\partial x}
 \end{array} \right] d\Omega
 \end{aligned}
 \tag{A1.1}$$

From equation [4.56]:

$$\begin{aligned}
 [B]_e &= \mu \int_{\Delta} [N]^T [N] d\Omega \\
 &= \mu \int_{\Delta} \begin{bmatrix} [N]^T [N] & [0]^T [0] & [0]^T [0] \\ [0]^T [0] & [N]^T [N] & [0]^T [0] \\ [0]^T [0] & [0]^T [0] & [N]^T [N] \end{bmatrix} d\Omega
 \end{aligned}
 \tag{A1.2}$$

The integrations of the shape functions in equations [A1.1] and [A1.2] can be evaluated by using the following relation for a triangular element:

$$\int_{\Delta} N_1^i N_2^j N_3^k d\Omega = \frac{i! j! k! 2!}{(i + j + k + 2)!} A_e
 \tag{A1.3}$$

Where, A_e is the area of the triangular element.

Hence the following integrals can be achieved:

$$\int_{\Delta} N_1^2 d\Omega = \int_{\Delta} N_2^2 d\Omega = \int_{\Delta} N_3^2 d\Omega = \frac{A_e}{6} \quad [\text{A1.4}]$$

$$\int_{\Delta} N_1 N_2 d\Omega = \int_{\Delta} N_2 N_3 d\Omega = \int_{\Delta} N_1 N_3 d\Omega = \frac{A_e}{12} \quad [\text{A1.5}]$$

$$\int_{\Delta} d\Omega = A_e \quad [\text{A1.6}]$$

Therefore from equation [A1.1], some of the elements of the 9×9 $[A]_e$ matrix can be calculated as:

$$[A]_{e(1,1)} = \frac{1}{\varepsilon} \int_{\Delta} -\beta^2 N_1^2 + \left(\frac{\partial N_1}{\partial y} \right)^2 d\Omega = \frac{1}{\varepsilon} \left[\frac{-\beta^2 A_e}{6} + c_1^2 A_e \right] \quad [\text{A1.7}]$$

$$[A]_{e(1,2)} = \frac{1}{\varepsilon} \int_{\Delta} -\beta^2 N_1 N_2 + \frac{\partial N_1}{\partial y} \frac{\partial N_2}{\partial y} d\Omega = \frac{1}{\varepsilon} \left[\frac{-\beta^2 A_e}{12} + c_1 c_2 A_e \right] \quad [\text{A1.8}]$$

$$[A]_{e(1,4)} = \frac{1}{\varepsilon} \int_{\Delta} -\frac{\partial N_1}{\partial y} \frac{\partial N_1}{\partial x} d\Omega = -\frac{1}{\varepsilon} c_1 b_1 A_e \quad [\text{A1.9}]$$

Matrix $[B]_e$ is also a 9×9 matrix and some of the elements are calculated as:

$$[B]_{e(1,1)} = \mu \int_{\Delta} N_1^2 d\Omega = \mu \frac{A_e}{6} \quad [\text{A1.1}]$$

$$[B]_{e(1,2)} = \mu \int_{\Delta} N_1 N_2 d\Omega = \mu \frac{A_e}{12} \quad [\text{A1.11}]$$

$$[B]_{e(1,4)} = 0 \quad [\text{A1.12}]$$

Calculation of the Wave Equations

Starting with Maxwell's curl equations [5.5] and using equation [5.6] yields [Obayya *et al.*, 2005; 2000a], the vector wave equation for the magnetic field vector, \mathbf{H} , can be derived as:

$$\nabla \times (n^{-2} \nabla \times \mathbf{H}) - k_0^2 \mathbf{H} = 0 \quad [5.12]$$

Where n is the refractive index and k_0 is the free space wavenumber and is given as:

$$k_0 = \omega \sqrt{\mu_0 \epsilon_0} = \frac{2\pi}{\lambda} \quad [5.13]$$

Where, λ is the free space wavelength.

Equation [5.12], known as full-vectorial wave equation, contains the three components of the magnetic (\mathbf{H}) field vector. This wave equation can be reduced to only the two transverse (H_x or H_y) components using the zero divergence condition:

$$\alpha_x \frac{\partial H_x}{\partial x} + \alpha_y \frac{\partial H_y}{\partial y} + \frac{\partial H_z}{\partial z} = 0 \quad [5.14]$$

Substituting [5.14] into [5.12] gives the following two coupled wave equations:

$$\begin{aligned} \frac{\partial}{\partial z} \left(n^{-2} \frac{\partial H_x}{\partial z} \right) + \alpha_y \frac{\partial}{\partial y} \left(n^{-2} \alpha_y \frac{\partial H_x}{\partial y} \right) + n^{-2} \alpha_x \frac{\partial}{\partial x} \left(\alpha_x \frac{\partial H_x}{\partial x} \right) + \\ k_0^2 H_x + n^{-2} \alpha_x \frac{\partial}{\partial x} \left(\alpha_y \frac{\partial H_y}{\partial y} \right) - \alpha_y \frac{\partial}{\partial y} \left(n^{-2} \alpha_x \frac{\partial H_y}{\partial x} \right) = 0 \end{aligned} \quad [5.15]$$

$$\frac{\partial}{\partial z} \left(n^{-2} \frac{\partial H_y}{\partial z} \right) + \alpha_x \frac{\partial}{\partial x} \left(n^{-2} \alpha_x \frac{\partial H_y}{\partial x} \right) + n^{-2} \alpha_y \frac{\partial}{\partial y} \left(\alpha_y \frac{\partial H_y}{\partial y} \right) +$$

$$k_0^2 H_y + n^{-2} \alpha_y \frac{\partial}{\partial y} \left(\alpha_x \frac{\partial H_x}{\partial x} \right) - \alpha_x \frac{\partial}{\partial x} \left(n^{-2} \alpha_y \frac{\partial H_x}{\partial y} \right) = 0 \quad [5.16]$$

In deriving the wave equations [5.15] and [5.16], the refractive index is slowly varying in the direction of propagation $\left(\frac{\partial n^{-2}}{\partial z} \right) = 0$, has been considered.

Equations [5.15] and [5.16] have less number of unknown components and also the zero divergence condition is automatically satisfied through the derivation, and hence, there is no possibility for spurious solutions to propagate. Therefore, solving equations [5.15] and [5.16] is more suitable than equation [5.12].

The fields can be separated as slowly varying envelopes and a fast-oscillating phase term by assuming the wave travels along the +z direction:

$$\begin{Bmatrix} H_x \\ H_y \end{Bmatrix} = \begin{Bmatrix} \psi_x \\ \psi_y \end{Bmatrix} \exp(-jn_0 k_0 z) \quad [5.17]$$

Where, n_0 is a reference index of refraction which should be chosen such that the envelope varies very slowly in the +z direction and ψ_x and ψ_y are the slowly-varying envelopes of the H_x and H_y components, respectively. For this purpose, n_0 should be chosen very close to the effective index of the guided modes of the concerned structures. For monomode waveguides, n_0 can be set equal to the effective index of the fundamental mode. But, for multimode waveguides, the situation will be complicated, as the effective indices of all guided modes have to be determined in order to set n_0 to the proper value. In this situation, a better approximation is to set n_0 as the average of the guide and substrate refractive indices.

When substituting equation [5.17] into equations [5.15] and [5.16], the following two coupled unidirectional wave equations can be obtained:

$$\begin{aligned}
& n^{-2} \frac{\partial^2 \psi_x}{\partial z^2} - 2jn_0 k_0 n^{-2} \frac{\partial \psi_x}{\partial z} + \alpha_y \frac{\partial}{\partial y} \left(n^{-2} \alpha_y \frac{\partial \psi_x}{\partial y} \right) + n^{-2} \alpha_x \frac{\partial}{\partial x} \left(\alpha_x \frac{\partial \psi_x}{\partial x} \right) + \\
& + k_0^2 (1 - n^{-2} n_0^2) \psi_x + n^{-2} \alpha_x \frac{\partial}{\partial x} \left(\alpha_y \frac{\partial \psi_y}{\partial y} \right) - \alpha_y \frac{\partial}{\partial y} \left(n^{-2} \alpha_x \frac{\partial \psi_y}{\partial x} \right) = 0 \quad [5.18]
\end{aligned}$$

$$\begin{aligned}
& n^{-2} \frac{\partial^2 \psi_y}{\partial z^2} - 2jn_0 k_0 n^{-2} \frac{\partial \psi_y}{\partial z} + \alpha_x \frac{\partial}{\partial x} \left(n^{-2} \alpha_x \frac{\partial \psi_y}{\partial x} \right) + n^{-2} \alpha_y \frac{\partial}{\partial y} \left(\alpha_y \frac{\partial \psi_y}{\partial y} \right) + \\
& + k_0^2 (1 - n^{-2} n_0^2) \psi_y + n^{-2} \alpha_y \frac{\partial}{\partial y} \left(\alpha_x \frac{\partial \psi_x}{\partial x} \right) - \alpha_x \frac{\partial}{\partial x} \left(n^{-2} \alpha_y \frac{\partial \psi_x}{\partial y} \right) = 0 \quad [5.19]
\end{aligned}$$

Appendix 4

List of Publications by the author

1. Rahman, B.M.A., Somasiri, N., Wongcharoen, T., Haxha, S., Obayya, S.S.A., Themistos, C., **Kabir, A.K.M.S.**, Ahmad, M.I., Rajarajan, M., and Grattan, K.T.V., "Finite element characterization of photonic devices for optical communications," *IEEE Conference on International Communication & IT-2004*, Riyadh City, Saudi Arabia, February-March, 29-4, 2004.
2. Rahman, B.M.A., **Kabir, A.K.M.S.**, Ahmed, M.I., Rajarajan, M., and Grattan, K.T.V., "Modal solutions of photonic crystal fibers by the finite element method," *SPIE Conference on Photonics Europe-2004*, Strasbourg, France, *proc. of SPIE*, vol.5450, pp. 207-216, April 2004.
3. Rahman, B.M.A., **Kabir, A.K.M.S.**, Ahmed, M.I., Rajarajan, M., and Grattan, K.T.V., "Rigorous modal solutions of photonic crystal fibers by using the full-vectorial H-field finite element method," *IEEE Conference on Wireless & Optical Communications Networks (WOCN'04)*, Muscat City, Oman, June 7-9, *The proc. Of the First IFIP international conference*, pp. 159-162, 2004.
4. Rahman, B.M.A., **Kabir, A.K.M.S.**, Ahmed, M.I., Rajarajan, M., and Grattan, K.T.V., "Full-vectorial modal solutions for photonic crystal fibers by use of the finite element method," *Roman Baths Summer School on Advanced Glass-Based Nano-Photonics (POWAG-2004)*, Bath, United Kingdom, July, 12-16,2004, Available:

www.powag.com/Papers/Rahman%20POWAG%20Poster%20July%202004.pdf.

5. Rahman, B.M.A., **Kabir, A.K.M.S.**, Ahmed, M.I., Sahota, G.S., Rajarajan, M., and Grattan, K.T.V., "Modal hybridism of polarization maintaining photonic crystal fibers by using a full-vectorial finite element method," *SPIE Conference and Symposium on Canadian and International Business and Technology Innovations in Optics and Photonics (Photonics North-2004)*, Ottawa City, Canada, September, 27-29, 2004. *Proc. of SPIE, Paper Number: 5577-36, vol. 5577, pp.293-301, 2004.*
6. Rahman, B.M.A., **Kabir, A.K.M.S.**, Alam, M. S., Somasiri, N., Ahmed, M.I., Rajarajan, M., and Grattan, K.T.V., "Rigorous analysis of photonic crystal fibers by using a full-vectorial H-field based finite element method," Invited paper, *SPIE Conference on Optical Science, Sensors and Systems-Technology, Architecture, Applications (Optics East-2004)*, *proc. of SPIE, vol. 5595, pp.54-65*, Philadelphia City, Pennsylvania, USA, October, 25-28, 2004.
7. Rahman, B.M.A., **Kabir, A.K.M.S.**, Ahmed, M.I., Rajarajan, M., and Grattan, K.T.V., "Rigorous modal solutions of photonic crystal fibers by using the finite element method," *2nd IEEE-GCC Conference on Advancing Technology in the GCC: Chalanges, and solutions*, Manama City, Kingdom of Bahrain, November, 23-25, 2004.
8. Rajarajan, M., Rahman, B.M.A., **Kabir, A.K.M.S.**, and Grattan, K.T.V., "Modal solutions of photonic crystal fibers by using the H-field finite element method," *Proc. SPIE on Smart Materials, Nano-, and Micro-Smart Systems, proc. of SPIE, vol. 5650, pp. 345-355*, Sydney, Australia, December, 12-15, 2004.
9. Rahman, B.M.A., Wongcharoen, T., Themistos, C., Ladele, E.O., Alam, M.S., Somasiri, N., Abdallah, R., **Kabir, A.K.M.S.**, Rajarajan, M., and

- Grattan, K.T.V., "Finite element characterization of photonic devices for optical communications," Invited paper, Calcutta, 2004.
10. Rahman, B.M.A., Wongcharoen, T., Somasiri, N., Abdallah, R. A., **Kabir, A.K.M.S.**, Rajarajan, M., and Grattan, K.T.V., "Rigorous design optimisation of photonic devices by using the finite element method," Invited paper, *Conference on Asia Pacific Microwave, University of Delhi South Campus, India, December, 15-18, 2004.*
 11. Rahman, B.M.A., **Kabir, A.K.M.S.**, Rajarajan, M., and Grattan, K.T.V., "Finite element modal solutions of planar photonic crystal fibers with rectangular air- holes," *Journal of Optical and Quantum Electronics*, vol. 37, number 1-3, pp.171-183, January 2005.
 12. Rahman, B.M.A., Wongcharoen, T., Themistos, C., Abdallah, R., **Kabir, A.K.M.S.**, Ladele, E.O., Somasiri, N., Alam, M.S., Rajarajan, M., and Grattan, K.T.V., "Finite element characterization of photonic devices for optical communications," *Proc. Of IEE*, vol.152, issue 5, pp. 241-246, October 2005.
 13. **Kabir, A.K.M.S.**, Rahman, B.M.A., Rajarajan, M., and Grattan, K.T.V., "Optimization of modal birefringence of photonic crystal fibres," *Proc. of SPIE on Photonic crystals: Fundamentals to Devices and 14th international workshop of optical waveguide theory and numerical simulation, proc. of SPIE*, Sydney, Australia, July, 4-8, 2005.
 14. Rahman, B.M.A., **Kabir, A.K.M.S.**, Rajarajan, M., and Grattan, K.T.V., "Modal birefringence of polarization maintaining photonic crystal fiber by using a H-field finite element method," *SPIE Conference and Symposiam on Optics and Photonics 2005*, San Diego, California, USA, July 31st- August 4th, 2005. *proc. of SPIE*, vol.5924, pp.OS1-10 [199-208] , 2005.
 15. Rahman, B.M.A., **Kabir, A.K.M.S.**, Sahota G., Vaghjiani M., Wijerante I., Somasiri N., Alam S., Obayya S., Rajarajan, M., and Grattan, K.T.V., "Modal solutions and birefringence studies of PCFs," *IEEE Seminars on*

Photonic Crystal Fibres, City University, London, United Kingdom, September 22nd, 2005.

16. Rahman, B.M.A., **Kabir, A.K.M.S.**, Vaghjiani M., Rajarajan, M., and Grattan, K.T.V., "Rigorous characterization of photonic crystal fibers by using the finite element method," *Proc. of SPIE, International Conference on Optics & Optoelectronics- ICOL 2005*, December 12th-15th 2005, Dehradun, India.
17. Rajarajan, M., Rahman, B.M.A., **Kabir, A.K.M.S.**, Wongcharoen, T., and Grattan, K.T.V., "Modal birefringence of photonic crystal fibers using the finite element method," Invited paper, *Proc. of SPIE, 4th International Conference on Optical Communications and Networks- ICOCN 2005*, December 14th-16th 2005, Bangkok, Thailand.
18. Rahman, B.M.A., **Kabir, A.K.M.S.**, Vaghjiani M.M., Wijerante I., Sahota G.S., Rajarajan, M., and Grattan, K.T.V., "Modal solutions of photonic crystal fibers by using a full-vectorial finite element method," *Proc. of SPIE*, vol.6128, pp. 114-125, *Integrated Optoelectronic Devices Photonic crystal material and devices iv*, Photonics West, San Jose, California, USA, January 21st–26th, 2006.
19. Rahman, B.M.A., Agrawal, A., Obayya, S.S.A., **Kabir, A.K.M.S.**, Namassivayane, K., Rajarajan, M., and Grattan, K.T.V., "Finite element based numerical method for photonic devices," *OWTNM- International conference on optical waveguide theory and numerical modeling*, Varese, Italy, April 20th-21st 2006.
20. Rahman, B.M.A., **Kabir, A.K.M.S.**, Vaghjiani M.M., Rajarajan, M., and Rakocevic V., "Birefringence study of photonic crystal fibers using the full-vectorial finite element method," *J. of Applied Physics B: Lasers and Optics*, vol. 84, no. 1-2, pp. 75-82, 2006.
21. Rahman, B.M.A., **Kabir, A.K.M.S.**, Namassivayane, K., Rajarajan, M., and Grattan, K.T.V., "Characterizations of photonic crystal fibres by using finite element-based full-vectorial numerical method," *IOP, Optics*

- and Photonics 2006*, University of Manchester, September 4th -7th, 2006.
22. Rahman, B.M.A., **Kabir, A.K.M.S.**, Namassivayane, K., Wijeratne, I.N.M., Rajarajan, M., and Grattan, K.T.V., "Characterizations of photonic crystal fibers by using a full-vectorial finite element method," *Proc. of SPIE*, vol.6369, Optics East 2006, Boston, Massachusetts, USA, October 1st -4th, 2006 [6369-04].
23. Rahman, B.M.A., **Kabir, A.K.M.S.**, Namassivayane, K., Wijeratne, I.N.M., Rajarajan, M., and Grattan, K.T.V., "Modal solutions of photonic crystal fibres by using a full-vectorial finite element method," 3rd International conference on computers and devices for communications (CODEC-06), Calcutta, India, pg 533-536, December 18th -20th, 2006.
24. Rahman, B.M.A., **Kabir, A.K.M.S.**, Namassivayane, K., Rajarajan, M., and Grattan, K.T.V., "Characterizations of the single-mode operation of PCF using finite element method," *Proc. of Integrated Photonics and Nanophotonics Research and Applications (IPNRA)*, paper ITuH5, OSA Technical Digest (CD), Optical Society of America, Salt Lake City, Utah, USA, July 8th -11th, 2007.
25. Rahman, B.M.A., **Kabir, A.K.M.S.**, Namassivayane, K., Rajarajan, M., and Grattan, K.T.V., "Design and optimization of photonic devices by using the finite element method," *Proc. of International Conference on Optical Communications and Networks (ICOON)*, Margala Hotel, Islamabad, Pakistan, August 7th -9th, 2007.
26. Namassivayane, K., Rahman, B.M.A., **Kabir, A.K.M.S.**, Rajarajan, M., and Grattan, K.T.V., "Single mode operation of photonic crystal fiber by using a full-vectorial finite element method," *Proc. of SPIE*, vol.6588, pp. 6588OT1-9, Prague, Czech Republic, 2007.
27. Namassivayane, K., **Kabir, A.K.M.S.**, Agrawaal, A., Rahman, B.M.A., and Grattan, K.T.V., "Characterizations of single-mode and single-

- polarization photonic crystal fibers by using a full-vectorial finite element approach," *Proc. of SPIE*, vol.6767, Optics East 2007, Boston, Massachusetts, USA, September 9th -12th, 2007.
28. Rahman, B.M.A., Namassivayane, K., **Kabir, A.K.M.S.**, Wongcharoen, T., and Grattan, K.T.V., "Single-mode and single polarization operation of photonic crystal fibres," *Proc. of 2007 Asian Pacific Conference on Communication (APCC2007)*, Bangkok, Thailand, October 18th -20th, 2007.
29. Rahman, B.M.A., Namassivayane, K., Wongcharoen, T., **Kabir, A.K.M.S.**, and Grattan, K.T.V., "Full-vectorial modal solutions of photonic crystal fibers operating at terahertz frequencies," *Proc. of 2007 Asian Pacific Conference on Communication (APCC2007)*, Bangkok, Thailand, October 18th -20th, 2007.
30. Rahman, B.M.A., Namassivayane, K., Wongcharoen, T., **Kabir, A.K.M.S.**, and Grattan, K.T.V., "Full-vectorial solutions of photonic crystal fibers by using the finite element method," *Proc. of Asian Pacific Microwave Conference (APMC2007)*, Bangkok, Thailand, December 11th -14th, 2007.
31. Namassivayane, K., Rahman, B.M.A., **Kabir, A.K.M.S.**, and Grattan, K.T.V., "Characterizations of photonic crystal fibers by using a full-vectorial finite element method," To be submitted.

References

- Aceves, A., "Pulse dynamics in nonlinear photonic crystal fibers and periodic structures," 2003 [www.ipam.ucla.edu/abstract.aspx?tid=1871]
- Ahmed, S. and Daly, P., "Finite element method for inhomogeneous waveguides," *Proc. IEE*, vol. 116, pp. 1661-1664, 1969.
- Al Salamed, M.S., and Owais, M.R., "Full wave analysis of dielectric optical waveguides by vectorial finite elements and absorbing boundary condition," *J. Optical Comm.*, vol. 24, pp 74-78, 1999.
- Andrés, P., Ferrando, A., Silvestre, E., Miret, J.J., and Andrés, M.V., "Dispersion and polarization properties in photonic crystal fibers", *IEEE Proc. of 2002 4th Int. Conf. on Transparent Opt. Networks*, vol. 2, pp. 98-103, 2002.
- Arriaga, J., Knight, J. C., and Russell, P. S. J., "Modeling the propagation of light in photonic crystal fibers," *Physica D-Nonlinear Phenomena*, vol. 189, pp. 100-106, 2004.
- Baets, R., and Lagasse, P.E., "Loss calculation and design of arbitrarily curved integrated-optic waveguide," *J. Opt. Soc. Amer. B.*, vol. 37, no. 2, pp. 177-182, 1983.
- Baggett, J.C., Monroe, T.M., Furusawa, K., and Richardson, D. J., "Comparative study of large-mode holey and conventional fibres," *Opt. Lett.*, vol. 26, no. 14, pp. 1045-1047, 2001.
- Bekker, E., Sewell, P., Benson, T., and Melnikov, L., "Numerical investigation of holey fibres with polygon shaped holes," *Proc. 11th Int. Workshop on Opt. Waveguide Theory and Numerical Modelling*, pp. 92, 2003.
- Belardi, W., Lee, J.H., Furusawa, K., Yusoff, Z., Petropoulos, P., Ibsen, M., Monroe, T.M., and Richardson, D.J., "A 10Gbit/s tuneable wavelength converter based on four-wave mixing in highly nonlinear holey fiber," *ECOC*, 2002.

- Berenger, J.P., "A perfectly matched layer for the absorption of electromagnetic waves," *J. Comput. Phys.*, vol. 114, no. 2, pp. 185-200, 1994.
- Berg, K.S., Oxenløwe, L.K., Siahlo, A., Tersigni, A., Clausen, A.T., Peucheret, C., Jeppesen, P., Hansen, K.P., and Hansen J.R., "80 Gb/s transmission over 80 km and demultiplexing using a highly non-linear photonic crystal fibre," ECOC, 2002.
- Berk, A. D., "Variational principles for electromagnetic resonators and waveguides," *IRE Trans. Antennas Propagat.*, vol. AP-4, pp. 104-111, 1956.
- Birks, T. A., Knight, J. C., and Russell, P. St. J., "Endlessly single-mode photonic crystal fiber," *Opt. Lett.*, vol. 22, pp. 961-963, 1997.
- Bjarklev, A., Bogaerts, W., Felici, T., Gallagher, D., Midrio, M., Lavrinenko, A., Mogilevtsev, D., SØndergaard, T., Taillaert, D., and Tromborg, B., "Comparison of strengths/weaknesses of existing numerical tools and outlining of modelling strategy," *Reports on PICCO deliverable D8 for WP4*, pp. 1-23, 2002, [http://intecweb.intec.ugent.be/picco/download/D8_report.pdf].
- Broeng, J., Barkou, S. E., SØndergaard, T., and Bjarklev, A., "Analysis of air-guiding photonic bandgap fibers," *Opt. Lett.*, vol. 25, pp. 96-98, 2000.
- Buczynski, R., Szarniak, P., Pysz, D., Kujawa, I., Stepien, R., and Szoplik, T., "Double-core photonic crystal fiber with square lattice," *Proc. of SPIE*, vol. 5450, pp. 223-230, 2004.
- Chan, C.T., Yu, Q.L., and Ho, K.M., "Order-N spectral method for electromagnetic waves," *Phys. Rev. B* 51, pp. 16635-16642, 1995.
- Cheung, P., Silveira, M., and Gopinath, A., "Analysis of lossy dielectric guides by transverse magnetic field finite elements method," *J. Lightwave Technol.*, vol. 13, no. 9, pp. 1873-1875, 1995.
- Chui, S.L., and Lu, Y.Y., "A Propagator- θ Beam Propagation Method," *IEEE Photon. Tech. Lett.*, vol. 16, pp. 822-824, 2004.
- Chung, Y., and Dagli, N., "An assessment of finite difference beam propagation method," *IEEE J. Quantum Electron.*, vol. 26, pp. 1335-1339, no. 8, 1990.
- Clough, R.W., "The Finite Element Method in Plane Stress Analysis," *Proc. of 2nd ASCE Conf. on Elect. Computation*, Pittsburgh, PA, 1960.

-
- Courant, R., "Variational Methods for the Solutions of Problems of Equilibrium and Vibrations," *Bull. Am. Math. Soc.*, vol. 49, pp.1-23, 1943.
 - Cregan, R.F., Mangan, B.J., Knight, J.C., Birks, T.A., Russell, P.St.J., Roberts, P.J., and Allan, D.C., "Single-mode photonic bandgap guidance of light in air," *Science*, vol. 285, pp. 1537-1539, 1999.
 - Csendes, Z. J. and Silvester, P., "Numerical solution of dielectric loaded waveguides: I – Finite-element analysis," *IEEE Trans. Microwave Theory Tech.*, vol.18, no. 12, pp. 1124-1131, 1970.
 - Cucinotta, A., Selleri, S., Vincetti, L., and Zoboli, M., "Holey fiber analysis through the finite-element method," *IEEE Photon. Technol. Lett.*, vol. 14, no. 11, pp. 1530-1532, 2002.
 - Danielsen, P., "Two-dimensional propagating beam analysis of an electrooptic waveguide modulator," *IEEE J. Quantum Electron.*, vol. 20, no. 9, pp. 1093-1097, 1984.
 - Davies, J. B., Fernandez, F. A., and Philippou, G. Y., "Finite element analysis of all modes in cavities with circular symmetry," *IEEE Trans. Microwave Theory Tech.*, vol. 30, no. 11, pp. 1975-1980, 1982.
 - Dettmer, R., "A net idea- Why photonic crystal fibre could mark the start of a new era in optical communications," *IEE Review*, pp. 19-23, 2001.
 - Druon, F., Sanner, N., Lucas-Leclin, G., Georges, P., Gaumé, R., Viana, B., Hansen, K.P., and Petersson, A., "Self-compression of 1- μ m femtosecond and pulses in a photonic crystal fiber," *CLEO*, 2002.
 - Eggleton, B.J., Westbrook, P.S., Windeler, R.S., Spalter, S., and Strasser, T.A., "Grating resonances in air-silica microstructured optical fibers", *Opt. Lett.* vol. 24, pp. 1460-1462, 1999.
 - Eggleton, B.J., Westbrook, P.S., White, C.A., Kerbage, C., Windeler, R.S., and Burdge, G.L., "Cladding-mode-resonances in air-silica microstructure optical fibers", *J. of Lightwave Technol*, vol. 18, no. 8, pp. 1084-1100, 2000.
 - El-Mikati, H.A., and Davies, J.B., "Coupling to an endfaced multicald optical fibre from a misaligned Gaussian beam or a separated multicald fibre," *Optical Quantum Electron.*, vol. 17, no. 5, pp. 297-309, 1985.
 - English, W. J. and Young, F. J., "An E vector variational formulation of the Maxwell equations for cylindrical waveguide problems," *IEEE Trans. Microwave Theory Tech.*, vol. 19, no. 1, pp. 40-46, 1971.

- Fabrizio, F., Luca, S., Paolo, B., Gaetano, B., and Stefano, T., "Full vectorial BPM modeling of Index-guiding photonic crystal fibers and couplers," *Opt. Exp.*, vol. 10, pp. 54-59, 2002.
- Farr, L., Knight, J.C., Mangan, B.J., and Roberts, P.J., "Low loss photonic crystal fiber," *Proc. ECOC*, Copenhagen, Denmark, paper PD1.3, 2002.
- Feit, M.D., and Fleck, J.A.Jr., "Light propagation in graded-index optical fibers," *Appl. Opt.* vol. 17, pp. 3990-3998, 1978.
- Feit M.D., and Fleck, J.A.Jr., "Computation of mode properties in optical fiber waveguides by a propagating beam method," *Appl. Opt.*, vol. 19, no. 7, pp. 1154-1164, 1980.
- Fernandez, F.A., Davies, J.B., Zhu, S., and Lu, Y., "Sparse matrix eigenvalue solver for finite element solution of dielectric waveguides," *Electron. Lett.*, vol. 27, no. 20, pp. 1824-1826, 1991.
- Ferrando, A., Silvestre, E., Miret, J.J., Andrés, P., and Andrés, M. V., "Full-vector analysis of a realistic photonic crystal fiber," *Opt. Lett.*, vol. 24, pp. 276-278, 1999.
- Ferrando, A., Silvestre, E., Miret, J.J., Andrés, P., and Andrés, M. V., "Nearly zero ultraflattened dispersion in photonic crystal fibers," *Opt. Lett.*, vol. 25, pp. 790-792, 2000a.
- Ferrando, A., Silvestre, E., Miret, J.J., Andrés, P., and Andrés, M. V., "Donor and acceptor guided modes in photonic crystal fibers," *Opt. Lett.*, vol. 25, pp. 1328-1330, 2000b.
- Ferrando, A., Silvestre, E., and Andrés, P., "Designing the properties of dispersion-flattened photonic crystal fibers," *Opt. Exp.*, pp. 687-697, vol. 9, no. 13, 2001.
- Finazzi, V., Monro, T.M., and Richardson, D.J., "Confinement loss in highly nonlinear holey optical fibres," *Proc. Opt. Fiber Commun. Conf.*, Paper ThS4, OFC'02, pp. 524-525, Anaheim, CA, 2002.
- Finazzi, V., Monro, T.M., and Richardson, D.J., "The role of confinement loss in highly nonlinear silica holey fibers," *IEEE Photon. Technol. Lett.*, vol.15, no.9, pp.1246-1248, 2003.
- Folkenberg, J.R., Nielsen, M.D., Mortensen, N.A., Jakobsen, C., and Simonsen, H.R., "Polarization maintaining large mode area photonic crystal fiber," *Opt. Exp.*, pp. 956-960, vol. 12, no. 5, 2004.

-
- Folkenberg, J.R., Nielsen, M.D., and Jakobsen, C., "Broadband single-polarization photonic crystal fiber," *Opt. Exp.*, vol. 30, no. 12, pp. 1446-1448, 2005.
 - Foster, M.A., and Gaeta, A.L., "Ultra-low threshold supercontinuum generation in sub-wavelength waveguides," *Opt. Exp.*, vol. 12, pp. 3137-3143, 2004.
 - Futami, F., Watanabe, S., and Chikama, T., "Simoltaneous recovery of 20x20 GHz WDM optical clock using supercontinuum in a nonlinear fiber," *ECOC*, 2002.
 - Gander, M.J., McBride, R., Jones, J.D.C., Mogilevtsev, D., Birks, T.A., Knight, J.C., and Russell, P.St.J., "Experimental measurement of group velocity in photonic crystal fiber," *Electron. Lett.*, vol. 35, pp. 63-64, 1998.
 - Genty, G., Lethonen, M, Jensen, J.R., Kaivola, M., and Ludvigsen, H., "Route to supercontinuum in photonic crystal fibers", *Conf. on Lasers and Electro-optics and Laser science, CLEO/QELS*, paper CTuU1, Long Beach , CA, 2002a.
 - Genty, G., Lethonen, M, Ludvigsen, H., Broeng, J., and Kaivola, M., "Spectral broadening of femtosecond pulses into continuum radiation in microstructured fibers", *Opt. Exp.*, vol. 10, no. 20, pp.1083-1098, 2002b.
 - Hadley, G.R., "Transparent boundary conditions for the beam propagation method," *Opt. Lett.*, vol. 16, no. 9, pp. 624-626, 1991.
 - Hadley, G.R., "Multistep method for wide-angle beam propagation," *Opt. Lett.*, vol. 17, no. 24, pp. 1743-1745, 1992a.
 - Hadley, G.R., "Transparent boundary conditions for the beam propagation method," *IEEE J. Quantum Electron.*, vol. 28, no. 1, pp. 363-370, 1992b.
 - Hano, M., "Finite-element analysis of dielectric-loaded waveguides," *IEEE Trans. Microwave Theory Tech.*, vol. MTT-32, no. 10, pp. 1275-1279, 1984.
 - Hansen, T. P., Broeng, J., Libori, S.E.B., Knudsen, E., Bjarklev, A., Jensen, J. R., and Simonsen, H., "Highly birefringent index-guiding photonic crystal fibers," *IEEE Photon. Technol. Lett.*, vol.13, no.6, pp. 588-590, 2001.
 - Hansen, K.P., Jensen, J.R., Jacobsen, C., Simonsen, H.R., Broeng, J., Skovgaard, P.M.W., Peterson, A., and Bjarklev, A., "Highly Nonlinear

- photonic crystal fiber with zero-Dispersion at 1.55 μm ," *OFC'02*, Post deadline, 2002.
- Hansen, K.P., Folkenberg, J.R., Petersson, A., and Bjarklev, A., "Properties of nonlinear photonic crystal fibers for telecommunication applications," *OFC'03*, pp. 18-19, 2003.
 - Hansen, K.P., Petersson, A., Folkenberg, J.R., Albertsen, M., and Bjarklev, A., "Birefringence-induced splitting of zero-dispersion wavelength in nonlinear photonic crystal fibers," *Opt. Lett.*, 29, pp.14-16, 2004.
 - Hansryd, J., and Andrekson, P.A., "Broad-band continuous-wave-pumped fiber optical parametric amplifier with 49-dB gain and wavelength conversion efficiency," *IEEE Photon. Technol. Lett.*, pp. 194-196, vol.13, no.3, 2001.
 - Hansryd, J., Andrekson, P.A., Hedekvist, P.O., Li, J., and Westlund, M., "Optical parametric amplifiers and their applications," *OFC'02*, pp. 123-125, 2002.
 - Hayata, K., Koshiba, M., Eguchi, M., and Suzuki, M., "Novel finite-element formulation without any spurious solutions for dielectric waveguides," *Electron. Lett.*, vol. 22, no. 6, pp. 295-296, 1986a.
 - Hayata k., Koshiba, M., Eguchi, M., and Suzuki, M., "Vectorial finite-element method without any spurious solutions for dielectric waveguiding problems using transverse magnetic-field component," *IEEE Trans. Microwave Theory Tech.*, vol. 34, no. 11, pp. 1120-1124, 1986b.
 - Hayata, K., Misawa, A., and Koshiba, M., "Split-step finite element method applied to nonlinear integrated optics," *J. Opt. Soc. Amer. B*, vol. 7, no. 9, pp. 1772-1784, 1990.
 - He, Y. Z., and Shi, F. G., "Finite-difference imaginary distance beam propagation method for modeling of the fundamental mode of photonic crystal fibers," *Opt. Comm.*, vol. 225, pp. 151-156, 2003.
 - Hendow, S.T., and Shakir, S.A., "Recursive numerical solution for nonlinear wave propagation in fibers and cylindrically symmetric systems," *Appl. Opt.*, vol. 25, no. 11, pp. 1759-1764, 1986.
 - Hermansson, B., Yevick, D., and Danielsen, P., " Propagating beam analysis of multimode waveguide tapers," *IEEE J. Quantum Electron.*, vol. 19, no. 8, pp. 1246-1251, 1983.

- Huang, W. P., Xu, C. L., and Chaudhuri, S. K., "A wide angle vector beam propagation method," *IEEE Photon. Technol. Lett.*, vol. 4, no. 10, pp. 1118-1120, 1992.
- Huang, W.P., Xu, C.L., Lui, W., and Yokoyama, K., "The perfectly matched layer (PML) boundary condition for the beam propagation method," *IEEE Photon. Tech. Lett.*, vol. 8, no. 5, pp. 649-651, 1996.
- Hwang, I.K., Lee, Y-J., and Lee, Y-H., "Birefrngence induced by irregular structure in photonic crystal fiber," *Opt. Exp.*, 11, pp. 2799-2806, 2003.
- Ikeuchi, M., Sawami, H., and Niki, H., "Analysis of open-type dielectric waveguides by the finite-element iterative method," *IEEE Trans. Microwave Theory Tech.*, vol. 29, no. 3, pp. 234-239, 1981.
- Jansen, R., "On the performance of the least-square method for waveguide junctions and discontinuities," *IEEE Trans. Microwave Theory Tech.*, vol. MTT-23, pp. 434-436, 1975.
- John, S., "Strong localization of photons in certain disordered dielectric superlattices," *Phys. Rev. Lett.*, vol. 58, pp. 2059-2062, 1987.
- Johnson, S.G., and Joannopoulos, J.D., "Block-iterative frequency-domain methods for Maxwell's equations in a planewave basis," *Opt. Exp.*, vol. 8, pp. 173-190, 2001.
- Ju, J., Jin, W., and Demokan, M.S., "Properties of a highly birefringent photonic crystal fiber," *IEEE Photon. Technol. Lett.*, vol.15, no.10, pp. 1375-1377, 2003.
- Kaczmarek, P., Lagasse, P.E., and Vandewege, J., "Propagating-beam model for single-mode fiber fused coupler," *IEE Proc. Pt. J.*, vol. 134, no. 2, pp. 111-116, 1987.
- Kakarantzas, G., Ortigosa-Blanch, A., Birks, T.A., Russell, P.St.J., Farr, L., County, F., and Mangan, B.J., "Structural rocking filters in highly birefringent photonic crystal fiber," *Opt. Lett.* vol. 28, pp. 158-160, 2003.
- Kao, K. C. and Hockham, G. H., "Dielectric fibre surface waveguides for optical frequencies," *Proc. IEE*, vol. 113, no. 7, pp. 1151-1158, 1966.
- Kerbage, C., Steinvurzel, P., Reyes, P., Westbrook, P.S., Windeler, R.S., Hale, A., and Eggleton, B.J., "Highly tunable birefringent microstructured optical fiber," *Opt. Lett.*, 27, pp. 842-844, 2002.
- Knight, J. C., Birks, T. A., Russell, P. St. J., and Atkin, D. M., "All-silica single-mode optical fibre with photonic crystal cladding," *Opt. Lett.*, vol. 21, no. 19, pp. 1547-1549, 1996a.

- Knight, J. C., Birks, T. A., Russell, P. St. J., and Atkin, D. M., "Pure silica single-mode fibre with hexagonal photonic crystal cladding," *Postdeadline Paper at OFC'96*, 1996b.
- Knight, J.C., "All-silica single-mode optical fiber with photonic crystal cladding: Errata", *Opt. Lett.*, vol. 22, no. 7, pp. 484-485, 1997.
- Knight, J.C., Birks, T.A., Cregan, R.F., Russell, P. St. J., and de Sandro, J-P, "Large mode area photonic crystal fibre", *Electron. Lett.*, vol. 34, pp. 1347-1348, 1998a.
- Knight, J.C., Broeng, J., Birks T. A., and Russell, P. St. J., "Photonic bandgap guidance in optical fiber," *Science*, vol. 282, pp. 1476-1478, 1998b.
- Knight, J.C., Birks T. A., Russell, P. St. J., and de Sandro, J-P, "Properties of photonic crystal fiber and the effective index model," *J. Opt. Soc. Am. A-Optics Image Science and Vision*, vol. 15, pp. 748-752, 1998c.
- Knight, J.C., and Russell, P. St. J., "Microstructured glass for optical fibers," *Glass and Technology Science*, vol. 75, pp. 54-62, 2002.
- Knox, R.M., and Toulouis, P.P., "Integrated circuits for millimeter through optical wave range," *Proc. MRI Symposium Submillimeter Waves*, pp.497-516, 1970.
- Koch, T.B., Davies, J.B., and Wickramasinghe, D., "Finite element/finite difference propagation algorithm for integrated optical device," *Electron. Lett.*, vol. 25, no. 8, pp. 514-516, 1989.
- Koch, T.B., Davies, J.B., Fernandez, F.A., and Maerz, R., "Computation of wave propagation in integrated optical devices using z-transient variational principles," *IEEE Trans. on Magnetics*, vol. 27, no. 5, pp. 3876-3879, 1991.
- Konrad, A., "Vector variational formulation of electromagnetic fields in anisotropic media," *IEEE Trans. Microwave Theory Tech.*, vol. MTT-24, no. 9, pp. 553-559, 1976.
- Koshiba, M., Hayata, K., and Suzuki, M., "Approximate scalar finite-element analysis of anisotropic optical waveguides," *Electron. Lett.*, vol. 18, no. 10, pp. 411-413, 1982.
- Koshiba, M., Hayata, K., and Suzuki, M., "Vectorial finite-element method without spurious solutions for dielectric waveguide problems," *Electron. Lett.*, vol. 20, no. 10, pp. 409-410, 1984.

- Koshiha, M., Hayata, K., and Suzuki, M., "Finite element formulation in terms of the electric-field vector for electromagnetic waveguide problems," *IEEE Trans. Microwave Theory Tech.*, vol. 33, no. 10, pp. 900-905, 1985a.
- Koshiha, M., Hayata, K., and Suzuki, M., "Improved finite-element formulation in terms of the magnetic-field vector for dielectric waveguides," *IEEE Trans. Microwave Theory Tech.*, vol. 33, no. 3, pp. 227-233, 1985b.
- Koshiha, M., Hayata, K., and Suzuki, M., "Vector E-field finite element analysis of dielectric optical waveguides," *Appl. Opt.*, vol. 25, no. 1, pp. 10-11, 1986.
- Koshiha, M., and Saitoh, K., "Numerical verification of degeneracy in hexagonal photonic crystal fibers," *IEEE Photon. Technol. Lett.*, vol. 13, no. 12, pp. 1313-1315, 2001.
- Koshiha, M., "Full-vector analysis of photonic crystal fibers using the finite element method," *IEICE Trans. On Electron.*, E85C(4), pp. 881-888, 2002.
- Koshiha, M., and Saitoh, K., "Polarization-dependent confinement losses in actual holey fibers," *IEEE Photon. Technol. Lett.*, vol.15, no.5, pp. 691-693, 2003a.
- Koshiha, M., and Saitoh, K., "Finite-element analysis of birefringence and dispersion properties in actual and idealized holey-fiber structures," *Applied Opt.*, vol.142, pp. 6267-6275, 2003b.
- Koshiha, M., and Saitoh, K., "Structural dependence of effective area and mode field diameter for holey fibers," *Opt. Exp.*, vol. 11, no. 15, pp. 1746-1756, 2003c.
- Krauss, T.F., and Baba, T., "Introduction to the feature section on photonic crystal structures and applications," *IEEE J. Quantum Electron.*, vol. 38, no. 7, pp. 724, 2002.
- Kriezis, E.E., Pantelakis, P., Antonopoulos, C.S., and Papagiannakis, A.G., "Full vector beam propagation method for axially dependent 3-D structures," *IEEE Trans. Magnetics.*, vol. 33, no. 2, pp. 1520-1543, 1997.
- Kubota, H., Kawanishi, S., Koyanagi, S., Tanaka, M., and Yamaguchi, S., "Absolutely single polarization photonic crystal fiber", *IEEE Photon. Technol. Lett.*, vol.16, no.1, pp.182-184, 2004.
- Kuhlmeiy, B.T., White, T.P., Renversez, G., Maystre, D., Botten, L.C., de Sterke, C. M., and McPhedran, R.C., "Multipole method for

- microstructured optical fibers. II. Implementations and results," *J. Opt. Soc. Am. B*, vol. 19, pp. 2331-2340, 2002.
- Kumar, V. V. R. K., George, A. K., Reeves, W. H., Knight, J. C., Russell, P. S., Omenetto, F.G., and Taylor, A. J., "Extruded soft glass photonic crystal fiber for ultrabroad supercontinuum generation," *Opt. Exp.*, vol. 10, pp. 1520-1525, 2002.
 - Lagasse, P.E., and Bates, R., "Application of propagating beam methods to electromagnetic and acoustic wave propagation problems: a review," *Radio Science*, vol. 22, no. 7, pp. 1225-1233, 1987.
 - Lamouroux, B., and Prade, B., "Three-dimensional beam-propagating treatment of a monomode optical-fiber half-coupler," *J. Opt. Soc. Amer. A.*, vol. 4, no. 12, pp. 2228-2232, 1987.
 - Lee, J.H., Yusoff, Z., Belardi, W., Monro, T.M., Thomsen, B., and Richerdson, D.J., "Holey fiber based tuneable WDM wavelength converter using cross-phase modulation and filtering," *ECOC*, 2002.
 - Leon-saval, S.G., Birks, T.A., Wadsworth, W.J., Russell, P.St.J., and Mason, M.W., "Supercontinuum generation in submicron fibre waveguides," *Opt. Exp.*, vol. 12, no. 13, pp. 2864-2869, 2004.
 - Liu, P.L., and Li, B.J., "Semivectorial beam-propagation method for analyzing polarized modes of rib waveguides," *IEEE J. Quantum Elec.*, vol. 28, no. 4, pp. 778-782, 1992.
 - Liu, Y., Rahman, B. M. A., and Grattan, K. T. V., "Thermal-stress-induced birefringence in bow-tie optical fibers," *Applied Opt.*, vol. 33, pp. 5611-5616, 1994.
 - Lizier, J.T., and Town, G.E., "Splice losses in holey optical fibers," *IEEE Photon. Technol. Lett.*, vol. 13, no. 8, pp.794-796, 2001.
 - Lu, Y., and Fernandez, F.A., "An efficient finite element method of inhomogeneous anisotropic and lossy dielectric waveguide," *IEEE Trans Microwave Theory and Techn.*, vol. 41, no. 6-7, pp.1215-1223, 1993a.
 - Lu, Y., and Fernandez, F.A., "Finite element analysis of lossy dielectric waveguides," *IEEE Trans. Magnetics*, vol. 29, no. 2, pp.1609-1612, 1993b.
 - Mabaya, N., Lagasse, P. E., and Vandenbulcke, P., "Finite element analysis of optical waveguides," *IEEE Trans. Microwave Theory Tech.*, vol. MTT-29, no. 6, pp. 600-605, 1981.

- Mangan, B.J., Knight, J.C., Birks, T.A., Russell, P.St.J., and Greenaway, A.H., "Experimental study of dual-core photonic crystal fiber," *Electron. Lett.*, vol. 36, no. 16, pp. 1358-1359, 2000.
- Martijin, A.E., Maryanne, C.J.L., Alexander, A., Joseph, Z., Steven, M., Nader, A.I., Ian, B., Simon, F., Ross, C.M., Martijin, C.de S., and Nicilae, A.P.N., "Microstructured polymer optical fibre," *Opt. Exp.*, vol. 9, pp. 319-327, 2001.
- Mogilevtsev, D., Birks, T.A., and Russell, P.St. J., "Localized function method for modelling defect modes in 2-D photonic crystals," *J. Lightwave Technl.*, vol. 17, no. 11, pp. 2078-2081, 1999.
- Monroe, T.M., Richardson, D.J., Broderick, N.G.R., and Bennett, P.J., "Holey optical fibres: An efficient modal model," *J. of Lightwave Technol.*, vol. 17, no. 6, pp. 1093-1102, 1999.
- Monroe, T.M., Bennett, P.J., Broderick, N.G.R., and Richardson, D.J., "Holey fibers with random cladding distributions," *Opt. Lett.*, 25, pp. 206-208, 2000a.
- Monroe, T.M., Richardson, D.J., Broderick, N.G.R., and Bennett, P.J., "Modeling large air fraction holey optical fibers," *J. of Lightwave Technol.*, vol. 18, no. 1, pp. 50-56, 2000b.
- Montanari, E., Selleri, S., Vincetti, L., and Zoboli, M., "Finite-element full-vectorial propagation analysis for three-dimensional z-varying optical waveguides," *J. of Lightwave Technol.*, vol. 16, no. 4, pp. 703-714, 1998.
- Morishita, K. and Kumagai, N., "Unified approach to the derivation of variational expression for electromagnetic fields," *IEEE Trans. Microwave Theory Tech.*, vol. 25, no. 1, pp. 34-40, 1977.
- Mortensen, N. A., Folkenberg, J. R., Skovgaard, P.M.W., and Broeng, J. "Numerical aperture of single-mode photonic crystal fibers," *IEEE Photon. Technol. Lett.*, vol. 14, no. 8, pp. 1094-1096, 2002.
- Neyer, A., Mevenkamp, W., Thylen, L., and Lagerstrom, B., "A beam propagation analysis of active and passive waveguide crossings," *J. Lightwave Technol.*, vol. 3, no. 3, pp. 635-642, 1985.
- Nielsen, M.D., Vienne, G., Jensen, J.R., and Bjarklev, A., "Modelling birefringence in isolated elliptical core photonic crystal fibers," *LEOS'01*, pp. 707-708, 2001.
- Nielsen, M.D., Folkenberg, J.R., and Mortensen, N.A., "Single mode photonic crystal fibre with effective area of $600 \mu\text{m}^2$ and low bending loss," *Electron. Lett.*, vol. 39, no. 25, pp. 1802-1803, 2003a.

-
- Nielsen, M.D., Mortensen, N.A., and Folkenberg, J.R., "Reduced micro-deformation attenuation in large-mode area photonic crystal fibers for visible applications," *Opt. Lett.*, vol. 28, pp. 1645, 2003b.
 - Obayya, S. S. A., Rahman, B. M. A., and El-Mikati, H. A., "New full-vectorial numerically efficient propagation algorithm based on the finite element method," *J. Lightwave Tech.*, vol. 18, no. 3, pp. 409-415, 2000a.
 - Obayya, S. S. A., Rahman, B. M. A., and El-Mikati, H. A., "Full-vectorial finite-element beam propagation method for nonlinear directional devices," *IEEE J. Quant. Elect.*, vol. 36, no. 5, pp. 556-562, 2000b.
 - Obayya, S.S.A., Rahman, B.M.A., and El-Mikati, H.A., "Vector beam propagation analysis of polarization conversion in periodically loaded waveguides," *IEEE Photon. Techn. Lett.*, pp.1346-1348, 2000c.
 - Obayya, S. S. A., Rahman, B. M. A., Grattan, K. T. V., and El-Mikati, H. A., "Full vectorial finite-element based imaginary distance beam propagation solution of complex modes in optical waveguides method," *J. Lightwave Tech.*, vol. 20, pp. 1054-1060, 2002a.
 - Obayya, S. S. A., Rahman, B. M. A., Grattan, K. T. V., and El-Mikati, H. A., "Full vectorial finite-element solution of nonlinear bistable optical waveguides," *IEEE J. Quant. Electron.*, vol. 38, pp. 1120-1125, 2002b.
 - Obayya, S. S. A., Rahman, B. M. A., and Grattan, K. T. V., "Accurate finite element modal solution of photonic crystal fibers," *Proc. IEE Optoelectronics*, vol. 152, Issue 5, pp. 241-246, 2005.
 - Ohtaka, M., Matsuhara, M., and Kumagai, N., "Analysis of the guided modes in slab-coupled waveguides using a variational method," *IEEE J. Quant. Electron.*, vol. QE-12, pp. 378-382, 1976.
 - Omenetto, F.G., Taylor, A.J., Moores, M.D., Arriaga, J., Knight, J.C., Wadsworth, W.J., and Russell, P.S.J., "Simultaneous generation of spectrally distinct third harmonics in a photonic crystal fiber" *Opt. Lett.*, vol. 26, pp. 1158-1160, 2001.
 - Oraizi, H., and Perini, J., "A numerical method for the solution of the junction of cylindrical waveguides," *IEEE Trans. Microwave Theory Tech.*, vol. MTT-21, pp. 640-642, 1973.
 - Ortigosa-Blanch, A., Knight, J. C., Wadsworth, W. J., Arriaga, J., Mangan, B. J., Birks, T. A., and Russell, P. St. J., "Highly birefringent photonic crystal fibers," *Opt. Lett.*, vol. 25, pp. 1325-1327, 2000.

-
- Oxenløwe, L.K., Siahlo, A., Berg, K.S., Tersigni, A., Peucheret, C., Clausen, A.T., Hansen, K.P., and Jensen, J.R., "A photonic crystal fibre used as a 160 to 10 Gb/s demultiplexer," *Post Deadline OECC*, 2002.
 - Palavicini, C., Jaouen, Y., Debarge, G., Kerrinckx, E., Quiquempois, Y., Douay, M., Lepers, C., Obaton, A.-F., and Melin, G., "Phase-sensitive optical low-coherence reflectometry technique applied to the characterization of photonic crystal fiber properties", *Optics Lett.*, vol. 30, no. 4, pp.361-363, 2005.
 - Pekel, U., and Mittra, R., "An application of the perfectly matched layer (PML) concept to the finite element method frequency domain analysis of scattering problems," *IEEE Microwave and Guided Wave Lett.*, vol. 5, no. 8, pp. 258-260, 1995a.
 - Pekel, U., and Mittra, R., "A finite element method frequency domain application of the perfectly matched layer (PML) concept," *Microwave and Opt. Technol.*, vol. 9, no. 3, pp. 117-122, 1995b.
 - Petropoulos, P., Monro, T.M., Berlardi, W., Furusawa, K., Lee, J.H., and Richardson, D.J., "2R regenerative all-optical switch based on a highly nonlinear hollow fiber," *Opt. Lett.*, vol. 26, no. 16, pp. 1233-1235, 2001a.
 - Petropoulos, P., Monro, T.M., Berlardi, W., Furusawa, K., Lee, J.H., and Richardson, D.J., "A highly nonlinear hollow fiber and its application in a regenerative optical switch," *OFC'01*, 2001b.
 - Peyrilloux, A., Chartier, T., Hideur, A., Berthelot, L., Melin, G., Lempereur, S., Pagnoux, D., and Roy, P., "Theoretical and experimental study of the birefringence of a photonic crystal fiber," *J. Lightwave Techn.*, vol.21, no. 2, pp. 536-539, 2003.
 - Rahman, B.M.A., and Davies, J. B., "Finite-element solution of integrated optical waveguides," *J. Lightwave Techn.*, vol. 2, pp. 682-688, 1984a.
 - Rahman, B.M.A., and Davies, J. B., "Finite-element analysis of optical and microwave waveguide problems," *IEEE Trans. Microwave Theory Tech.*, vol. 32, no. 1, pp. 20-28, 1984b.
 - Rahman, B.M.A., and Davies, J. B., "Penalty function improvement of waveguide solution by finite elements," *IEEE Trans. Microwave Theory Tech.*, vol. 32, no. 8, pp. 922-928, 1984c.
 - Rahman, B.M.A., and Davies, J.B., "Vector-H field finite element solution of GaAs/GaAlAs rib waveguides," *Proc. IEE-J Optoelectronics*, 132, pp.349-353, 1985.

- Rahman, B.M.A., and Davies, J.B., "Analysis of optical waveguide discontinuities," *J. Lightwave Technol.*, vol. 6, no. 1, pp. 52-57, 1988.
- Rahman, B.M.A., Liu, Y., and Grattan, K. T. V., "Finite-element modelling of One- and two-dimensional MQW semiconductor optical waveguides," *IEEE Photon. Technol. Lett.*, vol. 5, pp. 928-931, 1993.
- Rahman, B.M.A., and Haxha, S., "Optimization of microwave properties for high-speed etched and unetched lithium niobate electro-optic modulators," *J. Lightwave Technology*, vol. 20, pp.1856-1863, 2002.
- Rahman, B.M.A., Boonthittannont, W., Obayya, S.S.A., Wongcharoen, T., Ladele, E.O., and Grattan, K.T.V., "Rigorous beam propagation analysis of tapered spot-size converters in deep-etched semiconductor waveguides," *J Lightwave Technol*, vol. 21, pp.3392-3398, 2003.
- Rahman, B.M.A., Kabir, A.K.M.S., Ahmed, M.I., Rajarajan, M., and Grattan, K.T.V., "Modal solutions of photonic crystal fibers by the finite element method," *Proc. of SPIE*, vol. 5450, pp. 207-216, 2004.
- Rahman, B.M.A., Kabir, A.K.M.S., Rajarajan, M., and Grattan, K.T.V., "Finite element modal solutions of planar photonic crystal fibers with rectangular air- holes," *J. of Opt. and Quant. Electron.*, vol. 37, no. 1-3, pp. 171-183, 2005a.
- Rahman, B.M.A., Wongcharoen, T., Themistos, C., Abdallah, R., Kabir, A.K.M.S., Ladele, E.O., Somasiri, N., Alam, M.S., Rajarajan, M., and Grattan, K.T.V., "Finite element characterization of photonic devices for optical communications," *Proc. of IEE*, vol. 152, issue 5, pp. 241-246, 2005b.
- Rahman, B.M.A., Kabir, A.K.M.S., Namassivayane, K., Rajarajan, M., and Grattan, K.T.V., "Characterizations of photonic crystal fibres by using finite element-based full-vectorial numerical method," *IOP, Optics and Photonics 2006*, University of Manchester, 2006a.
- Rahman, B.M.A., Kabir, A.K.M.S., Rajarajan, M., Grattan, K.T.V., and Rakocevic V., "Birefringence study of photonic crystal fibers using the full-vectorial finite element method," *J. of Applied Physics B: Lasers and Optics*, vol. 84, no. 1-2, pp. 75-82, 2006b.
- Rajarajan, M., Rahman, B.M.A., Wongcharoen, T., and Grattan, K.T.V., "Accurate characterization of MMI devices with 2-dimensional confinement," *J. Lightwave Technol.*, vol. 14, pp.2078-2084, 1996.
- Rajarajan, M., Obayya, S.S.A., Rahman, B.M.A., Grattan, K.T.V., and El-Mikati, H.A., "Design of compact optical bends with a trench by use of finite element and beam propagation method," *Applied Optics*, vol. 39, pp.4946-4953, 2000.

- Rajarajan, M., Rahman, B.M.A., Kabir, A.K.M.S., and Grattan, K.T.V., "Modal solutions of photonic crystal fibers by using the H-field finite element method," *Proc. of SPIE*, vol. 5650, pp. 345-355, 2004.
- Razaz, M., and Davies, J.B., "Capacitance of the abrupt transition from coaxial-to-circular waveguide," *IEEE Trans. Microwave Theory Tech.*, vol. MTT-27, pp. 564-569, 1979.
- Reed, M., Sewell, P., Benson, T.M., and Kendall, P.V., "Efficient propagation algorithm for 3D optical waveguides," *IEEE Proc. Pt. J*, vol. 145, no. 1, pp. 53-58, 1998.
- Riishede, J., Mortensen, N.A., and Lægsgaard J., "A 'poor man's approach' to modelling micro-structured optical fibres," *J. Opt. A: Pure and Appl. Opt.*, vol. 5, pp. 534-538, 2003.
- Rolland, C., Mak, G., Fox, K., Adams, D., Thorpe, A., Yevick, D., and Hermansson, B., "Analysis of strongly-guiding rib waveguide S-bends: theory and experiment," *Electron. Lett.*, vol. 25, no. 18, pp. 1256-1257, 1989.
- Russell, P.St.J., "Photonic crystal fibres", *Department of Physics, University of Bath*, Bath, pp. 1-59, 2002.
- Russell, P.St.J., "Photonic crystal fibers," *Science*, vol. 299, pp. 358-362, 2003.
- Russell, P.St.J., Knight, J.C., Birks, T.A., Mangan, B.J., and Wadsworth, W.J., "Recent progress in photonic crystal fibres," *Optoelectronics group, University of Bath*, [www.bath.ac.uk].
- Saitoh, K., and Koshiba, M., "Full-vectorial imaginary-distance beam propagation method based on a finite element scheme: Application to photonic crystal fibers," *IEEE J. of Quant. Electron.*, vol. 38, no. 7, pp. 927-933, 2002.
- Saitoh, K., and Koshiba, M., "Confinement losses in air-guiding photonic bandgap fibers," *IEEE Photon. Technol. Lett.*, vol.15, no. 2, pp. 236-238, 2003a.
- Saitoh, K., and Koshiba, M., "Single-polarization single-mode photonic crystal fibers," *IEEE Photon. Technol. Lett.*, vol. 15, no. 10, pp.1384-1386, 2003b.
- Saitoh, K., and Koshiba, M., "Leakage loss and group velocity dispersion in air-core photonic bandgap fibers," *Opt. Exp.*, vol. 11, no. 23, pp. 3100-3109, 2003c.

- Saitoh, K., Koshiba, M., Hasegawa T. and Sasoka E., "Chromatic dispersion control in photonic crystal fibers: application to ultraflattened dispersion," *Opt. Exp.*, vol. 11, no. 8, pp. 843-852, 2003.
- Schulz, N., Birewith, K., Arndt, F., and Koster, U., "Finite-difference method without spurious solutions for the hybrid mode analysis of diffused channel waveguide," *IEEE Microwave Theory Tech.*, vol. 38, pp. 722-729, 1990.
- Selleri, S., Vincetti, L., Cucinotta, A., and Zoboli, D.M., "Complex FEM modal solver of optical waveguides with PML boundary conditions," *Opt. Quant. Electron.* vol. 33, pp. 359-371, 2001.
- Sharping, J. E., Fiorentino, M., Kumar, P., and Windeler, R. S., "All-optical switching based on cross-phase modulation in microstructure fiber," *IEEE Photon. Technol. Lett.*, vol. 14, pp. 77-79, 2002.
- Silveira, M., and Gopinath, A., "Analysis of dielectric guides by transverse magnetic field finite element penalty method," *J. Lightwave Technol.*, vol. 13, no. 3, pp. 442-446, 1995.
- Splett, A., Majd, M., and Petermann, K., "A novel beam propagation method for large refractive index steps and large propagation distances," *IEEE Photon. Tech. Lett.*, vol. 3, no. 5, pp. 466-468, 1991.
- Steel, M.J., White, T.P., de Sterke, C.M., McPhedran, R.C., and Botten, L.C., "Symmetry and degeneracy in microstructured fibres," *Opt. Lett.*, vol. 26, pp. 488-490, 2001.
- Suchoski, P.G., and Ramaswamy, V., "Design of single mode step-tapered waveguide sections," *IEEE J. Quantum. Electron.*, vol., 23, no. 2, pp. 205-211, 1987.
- Suzuki, K., Kubota, H., Kawanishi, S., Tanaka, M., and Fujita, M., "Optical properties of a low-loss polarization-maintaining photonic crystal fiber", *Opt. Exp.*, vol. 9, no. 13, pp.676-680, 2001.
- Svedin, J. A. M., "A numerically efficient finite element formulation for the general waveguide problem without spurious modes," *IEEE Trans. Microwave Theory Tech.*, vol. 37, no. 11, pp. 1708-1715, 1989.
- Tajima, K., Zhou, J., Nakajima, K., and Sato, K., "Ultralow loss and long length photonic crystal fiber," *J. Lightwave Technol.*, vol. 22, no. 1, pp. 7-10, 2004.
- Taylor, D.M., Bennett, C.R., Shepherd, T.J., Michaille, L.F., Nielsen, M.D., and Simonsen, H.R., "Demonstration of multi-core photonic crystal fibre in an optical interconnect," *Electron. Lett.*, vol. 42, no. 6, pp. 331-332, 2006.

- Themistos, C., Rahman, B.M.A., and Grattan, K.T.V., "Finite element analysis of lossy surface plasmon modes using perturbation technique," *Applied Opt.*, vol. 34, pp. 7695-7701, 1995.
- Thylen, L., Wright, E.M., Stegeman, G.I., Seaton, C.T., and Moloney, J.V., "Beam-propagation method analysis of a nonlinear directional coupler," *Opt. Lett.*, vol. 11, no. 11, pp. 739-741, 1986.
- Tsuji, Y. and Koshiba, M., "A finite element beam propagation method for strongly guiding and longitudinally varying optical waveguides," *J. Lightwave Technol.*, vol. 14, no. 2, pp. 217-222, 1996.
- Turner, M.J., Clough, R.W., Martin, H.C., and Topp, L.C., "Stiffness and deflection analysis of complex structures," *J. Aeronaut. Sci.*, vol. 23, no. 9, pp. 805-806, 1956.
- van Eijkelenborg, M. A., Large, M. C. J., Argyros, A., Zagari, J., Manos, S., Issa, N. A., Bassett, I., Fleming, S., McPhedran, R. C., de Sterke, C. M., and Nicorovici, N. A. P., "Microstructured polymer optical fibre," *Opt. Exp.*, vol. 9, pp. 319-327, 2001.
- Vassallo, C., and Collino, F., "Highly efficient absorbing boundary conditions for the beam propagation method," *J. Lightwave Technol.*, vol. 14, no. 6, pp. 1570-1577, 1996.
- Vasallo, C., and van der Keur, J.M., "Highly efficient transparent boundary conditions for finite difference beam propagation method at order four," *J. Lightwave Technol.*, vol. 15, no. 10, pp. 1958-1965, 1997.
- Wang, Z., Ren, G., Lou, S., and Jian, S., "Supercell lattice method for photonic crystal fibers," *Opt. Exp.*, vol. 11, pp. 980, 2003.
- Watanabe, S., and Futami, S., "Optical signal processing using nonlinear fibers," *ECOC*, 2002.
- White, T. P., McPhedran, R. C., Botten, L. C., Smith, G. H., and de Sterke, C. M., "Calculations of air-guided modes in photonic crystal fibers using the multipole method," *Opt. Exp.*, vol. 9, pp. 721-732, 2001a.
- White, T.P., McPhedran, R.C., de Sterke, C.M., Botten, L.C., and Steel, M.J., "Confinement losses in microstructured optical fibers," *Opt. Lett.*, vol. 26, no. 21, pp. 1660-1662, 2001b.
- White, T.P., Kuhlmeij, B.T., McPhedran, R.C., Maystre, D., Renversez, G., de Sterke, C.M., and Botten, L.C., "Multipole method for microstructured optical fibers. I. Formulation," *J. Opt. Soc. Am. B*, vol. 19, pp. 2322-2330, 2002

- Wolinski, T.R., Szaniawska, K., Ertman, S., Lesiak, P., Domanski, A.W., Dabrowski, R., Nowinowski-Kruszelnicki, W., and Wojcik, J., "Influence of temperature and electrical fields on propagation properties of photonic liquid-crystal fibres," *Meas. Sci. Technol.*, vol. 17, pp. 985-991, 2006.
- Wongcharoen, T., Rahman, B.M.A., and Grattan, K.T.V., "Accurate characterization of optical filters with two-dimensional confinement," *J. Lightwave Technol.*, pp.2596-2603, 1996.
- Wu, R. B. and Chen, C. H., "A variational analysis of dielectric waveguide by the conformal mapping technique," *IEEE Trans. Microwave Theory Tech.*, vol. MTT-33, no. 8, pp. 681-685, 1985.
- Wu, T.-L., and Chao, C.-H., "Photonic crystal fiber analysis through the vector boundary-element method: effect of elliptical air hole", *IEEE Photon. Technol. Lett.*, vol.16, no.1, pp. 126-128, Jan 2004.
- Xu, C.L., Huang, W.P., and Chaudhuri, K.S., "Efficient and accurate vector mode calculations by beam propagation method," *J. Lightwave Technol.*, vol. 11, pp. 1209-1215, 1993.
- Yablonovitch, E., "Inhibited spontaneous emission in solid state physics and electronics," *Phys. Rev. Lett.*, vol. 58, pp. 2059-2062, 1987.
- Yeh, C., Ha, K., Dong, S.B., and Brown, W.P., "Arbitrary shaped inhomogeneous optical fiber or integrated optical waveguides," *J. Appl. Physic.*, vol. 46, no. 5, pp. 2125-2129, 1975.
- Yeh, C., Ha, K., Dong, S.B., and Brown, W.P., "Single-mode optical waveguide," *Appl. Opt.*, vol. 18, no. 10, pp. 1490-1504, 1979.
- Yevick, D., and Thylen, L., "Analysis of gratings by the beam propagation method," *J. Opt. Soc. Amer. B*, vol. 72, no. 8, pp. 1084-1089, 1982.
- Yevick, D., and Glasner, M., "Analysis of forward wide-angle light propagation in semiconductor rib waveguide and integrated optic structures," *Electron. Lett.*, vol. 25, no. 23, pp. 1611-1613, 1989.
- Yevick, D., and Hermansson, B., "Split-step finite difference analysis of rib waveguides," *Electron. Lett.*, vol. 25, no. 7, pp. 461-462, 1989.
- Yevick D., and Hermansson, B., "Efficient beam propagation techniques," *IEEE J. Quantum Electron.*, vol. 26, no. 1, pp. 109-112, 1990.
- Young, T. P., "Design of integrated optical circuits using finite elements," *IEE Proc.*, pt. A, vol. 135, no. 3, pp. 135-144, 1988.

- Yu, C.-P., and Chang, H.-C., "Applications of the finite difference mode solution method to photonic crystal structures," *Opt. Quant. Electron.* vol. 36, pp. 145-163, 2004.
- Zhang, L., and Yang, C., "Polarization splitter based on photonic crystal fibers", *Opt. Exp.*, vol. 11, no. 9, pp. 1015-1020, 2003.
- Zhu, Z., and Brown, T.G., "Stress-induced birefringence in microstructured optical fiber," *Opt. Lett.*, vol. 28, no. 5, pp. 2306-2308, 2003.

Bibliography

- Agrawal, G.P., "Nonlinear Fibre Optics," *Academic Press*, 3rd Ed., 2001.
- Bathe, K., "Finite element procedure in engineering analysis," *Prentice-Hall*, Englewood Cliffs, NJ, 1982.
- Champion, E. R., "Numerical Methods for Engineering Applications," *Marcel Dekker, INC*, 1993.
- Coring Incorporated: www.answers.com; www.webopedia.com.
- Crystal-Fibre A/S: www.crystal-fibre.com.
- Davies, J. B., "The finite element method," *Numerical techniques for microwave and millimeter-wave passive structures*, Edited by T. Itoh, New York: Wiley, pp. 33-132, 1989.
- DeHaven, S., "The LaRC fiber draw tower,"
[www.pcs.cnu.edu/~fos/StanDeHavenNASA.ppt].
- Desai, C. S., "Elementary finite element method," *Prentice-Hall Inc.*, New Jersey, 1979.
- Fibrecore Ltd: www.webopedia.com
- Fibers.org: <http://fibers.org/articles/news>.
- Freeman, T., "Innovations in holey fiber", *FiberSystems America & Asia*, pp. 24, 2003, [<http://optics.org/articles/news/5/4/1/1>].
- Ghatak, A., and Thyagarajan, K., "Introduction to fiber optics," CUP, Cambridge, UK, 1998.
- Goff, D.R., "Fiber Optic Reference Guide," *Woburn*, 3rd ed., Massachusetts, 2002.
- Harrington, R.F., "Field computation by moment methods," *Florida, R. E., Krieger Publishing Company*, 1968.

-
- Hecht, J., "City of Light: The Story of Fiber Optics," *Oxford University Press*, New York, 1999.
 - Jenkins, F.A., and White, H.E., "Fundamentals of optics," *McGraw-Hill Inc.*, New York, 1967.
 - Keiser, G., "Optical fiber communications," *McGraw-Hill*, 3rd ed., Int. Ed., 2000.
 - Kolimbiris, H., "Fiber optics communications," *Pearson prentice Hall*, 2004.
 - Koshiya, M., "Optical waveguide analysis," *English language ed.*, 1992.
 - Kristiansen, R.E., "Guiding light with holey fibers", *Spie's Oemagazine*, pp. 25-28, 2002.
 - Lindstrom, A., "Holey fiber!: Optical advancements swamping slowdown pessimism," *Issue of Broadband^{Week}.com*, 2001a, http://www.broadbandweek.com/news/010402/010402_news_ofc.htm.
 - Lindstrom, A., "Hole-way to heaven: Hollow core fiber could lead the way to much lower cost networks," *Issue of Broadband^{Week}.com*, 2001b [www.broadbandweek.com].
 - März, R., "Integrated Optics," *Artech House*, London, chapt. 1-4, pp. 1, 9-25, 39-45, 80-82, 87-129, 1995.
 - Mercury Communications Ltd.: www.gare.co.uk/technology_watch/fibre.htm.
 - Monro, T.M., and Larkin, A., "Holey fibers could revolutionize telecommunications," *UniSci-Daily University Science News*, 2001, [<http://unisci.com/stories/20011/0321014.htm>].
 - Myabaev, G.K., and Scheiner, L.L., "Fiber-optic communications technology," *Pearson Education (Singapore)*, 2nd ed., 2002.
 - Okamoto, K., "Fundamentals of Optical Waveguides", *Academic Press*, Optics and Photonics, 2000.
 - Reddy, J. N., "An introduction to the finite element method," *McGraw-Hill Inc.*, New York, 1984.
 - Rensselaer Polytechnic Institute: www.rpi.edu.
 - Senior, J.M., "Optical fiber communications," *Prentice-Hall of India*, 2nd ed., 2001.

- Sharma, A., "Guided wave optics," *Selected Topics*, Viva Books Private Ltd., First ed., 2005.
- Taflov, A., "Computational electrodynamics: The finite-Difference Time-Domain Method," Norwood, MA: Artech House, 1995.
- University of Arizona, Optics.arizona:
www.optics.arizona.edu/Pictures/optical-fiber-basics.jpg
- University of Bath: www.bath.ac.uk
- University of Southampton, Optoelectronics Research Center:
www.orc.soton.ac.uk.
- Williamson, C., "Holey fibers!" *Light Reading- Networking the Telecom Industry*, Nov 21, 2002, [<http://www.lightreading.com>].
- Wilson, J., and Hawkes, J.F.B., "Optoelectronics: An Introduction," *Prentice Hall International (UK) Ltd*, 2nd Edition, 1989.
- Zienkiewicz, O.C., "The finite element method," *McGraw-Hill*, 3rd edition, UK, 1977.